Heat transport of suspended graphene and 2D materials : from diffusive to ballistic regime

Priyank Singh

To cite this version:

Priyank Singh. Heat transport of suspended graphene and 2D materials : from diffusive to ballistic regime. Materials Science [cond-mat.mtrl-sci]. Université Grenoble Alpes [2020-..], 2022. English. NNT : 2022GRALY016 . tel-03827201

HAL Id: tel-03827201
https://theses.hal.science/tel-03827201

Submitted on 24 Oct 2022

Heat transport of suspended graphene and 2D materials: from diffusive to ballistic regime

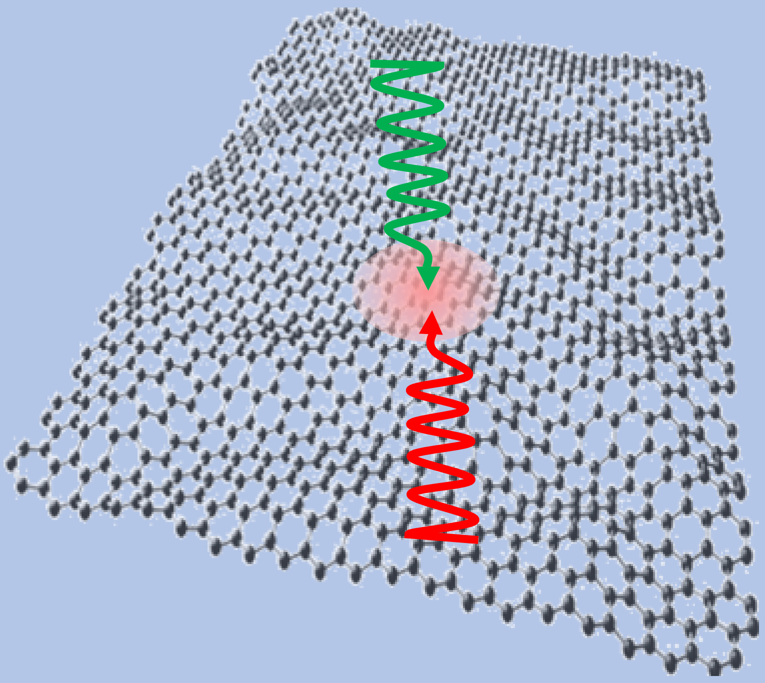

Priyank Singh

THÈSE

Pour obtenir le grade de

DOCTEUR DE L'UNIVERSITÉ GRENOBLE ALPES

Spécialité : NANOPHYSIQUE

Arrêté ministériel : 25 mai 2016

Présentée par

Priyank SINGH

Thèse dirigée par **Nedjma BENDIAB**, Maîtresse de conférences HDR, Université Grenoble Alpes
et co-encadrée par **Laëtitia MARTY**(Chargée de recherche HDR, Université Grenoble Alpes
et **Michele LAZZERI**, Directeur de recherche, CNRS Délégation Paris Centre

préparée au sein du **Laboratoire Institut Néel**
dans **l'École Doctorale Physique**

Transport thermique dans le graphène et les matériaux 2D suspendus : du régime diffusif vers le balistique

Heat transport of suspended graphene and 2D materials: from diffusive to ballistic regime

Thèse soutenue publiquement le **31 mars 2022**
devant le jury composé de :

Monsieur PASCAL PUECH
Maître de conférences HDR, UNIVERSITE TOULOUSE 3 - PAUL SABATIER, Rapporteur
Monsieur KONSTANTINOS TERMENTZIDIS
Directeur de recherche, CNRS DELEGATION RHONE AUVERGNE, Rapporteur
Madame GEORGIA FUGALLO
Chargée de recherche, CNRS BRETAGNE ET PAYS DE LA LOIRE, Examinatrice
Monsieur JULIEN PERNOT
Professeur des Universités, UNIVERSITE GRENOBLE ALPES, Président
Monsieur OTAKAR FRANK
Docteur en sciences, Ustav Fyzikalni Chemie J. Heyrovského, Examinateur
Monsieur OLIVIER BOURGEOIS
Directeur de recherche, CNRS DELEGATION ALPES, Examinateur

Abstract

This thesis investigates the fabrication and study of the thermal properties of different 2D materials under the formalism of existing literature and beyond. The thesis can be broadly divided in three parts. The first part discusses sample fabrication involving making of see-through holes in substrates followed by integrating CVD grown graphene over the patterned holes. It also discusses the mechanical exfoliation of different 2D materials on substrates. The process of standard transfer for suspending graphene is optimized and characterized using Raman spectroscopy, atomic force microscopy and scanning electron microscopy. We successfully suspend graphene on hole size of 2-10 µm radius. Second part of thesis discusses the estimation of thermal conductivity of different 2D materials on substrates using 1 laser Raman thermometry. It presents an attempt to understand the role of temperature and optical power on the evolution of optical phonon frequencies with the electronic structure of the material. In the final part, it discusses the characterization of the suspended graphene using 1 and 2 laser Raman thermometry. It shows the effect of geometry on the parameters of 1 laser Raman thermometry and thereby discusses the possibility of non-diffusive thermal transport in suspended graphene. It presents the first thermal transport spatial imaging of suspended graphene using the 2 laser Raman thermometry setup by heating the graphene at the center of the suspended region. The experiments show a deviation from linearized Fourier law in suspended graphene, which has not been reported experimentally up to our knowledge. A phenomenological model using nonlocal nonlinear term is proposed to successfully fit the observed thermal transport behavior in suspended graphene. Using this model, this work reports a thermal conductivity of 550 W/m.K for suspended graphene, which is one of the highest among existing materials. Such approach presents a better formalism to correctly estimate the thermal conductivity of 2D materials by incorporating a generalized Fourier law.

Résumé

Cette thèse étudie la fabrication et l'étude des propriétés thermiques de différents matériaux 2D dans le cadre du formalisme de la littérature existante et au-delà. La thèse peut être globalement divisée en trois parties. La première partie traite de la fabrication d'échantillons impliquant la réalisation de trous traversants dans des substrats, suivie de l'intégration de graphène synthétisé par CVD sur les motifs de trous. Il aborde également l'exfoliation mécanique de différents matériaux 2D sur des substrats. Le processus de transfert standard pour la mise en suspension du graphène est optimisé et caractérisé à l'aide de la spectroscopie Raman, de la microscopie à force atomique et de la microscopie électronique à balayage. Nous avons suspendu avec succès le graphène sur des trous de rayons de 2 à 10 µm. La deuxième partie de la thèse traite de l'estimation de la conductivité thermique de différents matériaux 2D sur des substrats à l'aide de la thermométrie Raman 1 laser. Elle présente une tentative de comprendre le rôle de la température et de la puissance optique sur l'évolution des fréquences des phonons optiques avec la structure électronique du matériau. La dernière partie traite de la caractérisation du graphène suspendu à l'aide de la thermométrie Raman à un et deux lasers et notamment de l'effet de la géométrie sur les paramètres de la thermométrie Raman à 1 laser. Les résultats sont discutés à la lumière de la possibilité d'un transport thermique non diffusif dans le graphène suspendu. Ce travail présente pour la première fois des cartes de transport thermique du graphène suspendu en utilisant la thermométrie Raman à 2 lasers (un laser chauffant et un laser de détection). La mesure de ces cartes par spectroscopie Raman sur graphène suspendu montre un écart à la loi de Fourier linéaire qui n'avait pas été mesuré ainsi à notre connaissance. Afin de comprendre cet écart, un modèle phénoménologique utilisant la loi de Fourier généralisée a été utilisé pour ajuster les cartes obtenues. Ce modèle indique un transport thermique non local et non linéaire. Cette nouvelle méthodologie expérimentale couplée a ce modèle phénoménologique, a permis une estimation de la conductivité thermique du graphène suspendu de 550 W/m.K. cette conductivité est l'une des plus élevées parmi les matériaux existants. Cette nouvelle approche a ainsi permis d'estimer plus finement la conductivité thermique du graphène suspendu en incorporant une loi de Fourier généralisée, ouvrant la voie à une meilleure compréhension de la propagation de la chaleur dans les matériaux 2D.

Contents

Acknowledgments **vii**

List of Figures **xi**

List of Tables **xv**

List of abbreviations **xvii**

Outline of the thesis **xxi**

1 Introduction **1**
- 1.1 State of the art 1
- 1.2 Motivation of the project 4
- 1.3 2D materials 5
  - 1.3.1 Graphene 5
    - 1.3.1.1 Thermal properties 6
  - 1.3.2 Transition Metal DiChalcogenides (TMDCs) 7
  - 1.3.3 other 2D materials 8
- 1.4 Measurement of thermal properties in 2D materials 9
  - 1.4.1 Electrical methods 9
    - 1.4.1.1 Thermal Bridge method 9
    - 1.4.1.2 Scanning thermal microscopy 11
  - 1.4.2 Spectroscopic methods 13
    - 1.4.2.1 Raman scattering 13
    - 1.4.2.2 Raman spectroscopy of 2D materials 16
    - 1.4.2.3 1-laser Raman thermometry 18
    - 1.4.2.4 2-laser Raman thermometry 22
- 1.5 Conclusion 25

2 Suspending 2D materials **27**
- 2.1 Substrate preparation 28
  - 2.1.1 Geometrical requirements for thermal study 28
  - 2.1.2 Material requirement of the substrate 29
  - 2.1.3 Fabrication of see-through holes 30
    - 2.1.3.1 Some challenges and solutions 31
- 2.2 Graphene and 2D materials 35
  - 2.2.1 Mechanical exfoliation of 2D materials 35

2.2.2 CVD growth of 2D materials 37
2.3 Transferring 2D materials on desired substrates 37
2.3.1 Stamping of exfoliated 2D materials 37
2.3.2 Transfer of CVD grown graphene on substrates with holes . 39
2.3.2.1 Drying graphene 40
2.3.3 Optimization for cleanliness of transferred graphene 41
2.3.3.1 1. Avoiding critical point drying step 42
2.3.3.2 2. Replacing the acetone for etching PMMA 45
2.3.3.3 3. Replacing the etchant for Copper 47
2.3.3.4 4. Avoiding PMMA/graphene interface 48
2.3.4 Strain and doping study in suspended samples 49
2.4 Conclusion 55

3 Thermal conductivity of 2D materials extracted by 1 laser Raman thermometry 57
3.1 Raman thermometry on semiconductors 58
3.1.1 Effect of global heating 58
3.1.2 Effect of local heating 61
3.1.3 Thermal conductivity 63
3.2 Raman thermometry on insulators 63
3.2.1 Effect of global heating 64
3.2.2 Effect of local heating 66
3.2.3 Thermal conductivity 68
3.3 Raman thermometry: semi-metals and metals 68
3.3.1 The case of semi-metal: graphene 68
3.3.1.1 Global heating 68
3.3.1.2 Local heating: suspended graphene 69
3.3.1.3 Exfoliated graphene on different substrates 70
3.3.2 The case of metals: 2H-TaSe$_2$ 71
3.3.2.1 Global heating 71
3.3.2.2 Local heating 73
3.3.3 Thermal conductivity 74
3.4 Electronic structure and thermal response 74
3.5 Conclusion 76

4 Effect of geometry on heat response of suspended graphene 77
4.1 Effect of global heating in suspended graphene 79
4.1.1 Evolution of G and 2D bands 80
4.1.2 Strain analysis 82
4.2 Effect of local heating on suspended graphene 84
4.2.1 Case 1: Dependence of G and 2D mode with hole size 85
4.2.1.1 Evolution of G and 2D bands with laser power . . 87
4.2.1.2 Strain analysis 89
4.2.2 Case 2: Dependence G and 2D mode with spatial location of hot spot 93
4.2.2.1 Analysis of case 1 and 2 94
4.3 Extraction of thermal conductivity 96

4.4 Temperature determination by optical phonons 98
4.5 Conclusion 100

5 Thermal transport beyond Fourier regime 101
5.1 Measurement scheme 103
5.1.1 Wavelength of heating laser 103
5.1.2 Motion stage 105
5.2 2 Laser Raman thermometry in suspended graphene 106
5.2.1 Observations 106
5.2.2 Extracting the temperature profiles 109
5.2.3 Analysis under Fourier's formalism 112
5.2.4 Phenomenological theory of non-local and non-linear thermal transport 116
5.2.5 2LRT by heating the substrate 121
5.3 Conclusion 123

6 Conclusions and perspectives 125

Appendix A 129

Appendix B 131
.1 Holesize: Radius 3.6 μm 131
.2 Holesize: Radius 5.3 μm 132
.3 Holesize: Radius 8.3 μm 133
.4 Temperature profiles 134

Appendix C 135
.5 Razor blade technique 135
.6 Piezo scan method 137

Bibliography 139

Acknowledgments

The journey of PhD can never be encapsulated in few pages, however, I would try to attempt acknowledging visible and invisible contributions. This journey of nearly 3.5 years has shaped itself by several memories at play.

I would like to start by thanking F. Pois, A.L. Jaussent, S. Gadal for their kind help during the administrative tasks. In this series, I would like to mention that the personals at the reception of A building were very helpful. I would like to extend my thanks to Armelle for her help for acquiring the books from the institut's library. She was kind to extend my borrows according to my need.

I would like to thanks my family 'away from home' but in India, specifically Disha, Mahima, Vamsee, Danish, Priyanka, Divya, Ankush, Shreya, Sucheta, Parul, Saumita, Diwas, Nikita, Abhiroop, Vaishali, Jyoti, Ginni, Aarati, Srishti^2 (Srivastava and Dang), Siddharth, Aditi, Nancy, Meenakshi, Pragati, Vivek, Vijaya, Ekta, Goldi, Jilin and many more. The little interactions with them once in a while was helpful. I would also like to apologize, if I am missing some names, but certainly they are there in part of my brain.

I would like to thank Dr. Yamijala for inspiring me to apply in EU for PhD studies. I would like to thank all the technical staff for helping me through this journey. I would like to thank A. Claudel, L. del Rey, B. Fernandez, D. Jegouso, C. Felix, J. Motte, L. Abbassi, P. Giroux, P. Lachkar, V. Reita and G. Julié, who have been helpful in technical work, specially the optical alignment, obtaining graphene, mechanical workshop and nanofabrication. I would also thank Patrick for his kind help for IT related issues.

The work presented in the thesis has different contributions from collaborators. I would like to thank J. Chaste, H. Shin, K. Ma, T. Goislard, M.A. Méasson, P. Bouvier, J. Maire, R. Swami, O. Arcizet, B. Pigeau for the efforts made in making the scientific quest possible. In this series I would like to extend my thanks to all the NAWA family which was very supportive during my stay at NAWATECHNOLOGIES for 2.5 months of internship.

PhD journey cannot be completed without the important and integral guidance of the supervisors. I was lucky to have three great supervisors and sweetest human beings. Nedjma has always inspired me to know that I can go one step further. I am specially thankful to her for her enormous efforts despite her illness. I have learnt a lot from my mistakes during this period. She always took time from her busy schedule of University teaching and labwork, to guide me through different experiments and discussions. She along with Laëtitia has always mentioned my mistakes in most sweetest way possible. Moreover, they have been extremely patient with me despite my silly mistakes. I would like to extend my thanks to

Michele as well. He is very kind human being, who traveled several times from Paris to Grenoble to support me during my work. Despite the CoViD19 situation, all three of them were cautious to guide me through the toughest times.

The personality of Laëtitia has touched me philosophically as well as practically. She has been kind to me during this entire period of PhD not because it was necessary but it is how she is, in general. Her personality has helped me to remind myself about the very culture I come from. I have taken hours of her life for scientific and philosophical discussions by starting a conversation 'Can I ask a small question?' or 'Do you have 5 minutes?'. If being honest, I would miss this part of my PhD throughout life. She has always been very sweet and supportive throughout the PhD.

I would also like to thank my labmates for providing a family like environment around me. I never felt as an outsider in Grenoble, thanks to Estelle, Ana, Guilliam, Enzo, Goutham, Roberto, Riadh, Wei-Lei, Pauline, Andrej, Nicolas, Anike, Suzanne, Simone, Thanasis, Suman, Alois, Will, Julia, Maria and Brice. The environment of lab was never much stressful. The spirit of seeking was kept in a way that research was never profession but more like fun activity. It helped me during the days experiments weren't going smoothly. I was lucky to have an office member like Guilliam. I had a lot of fun discussing science, philosophy and bit geopolitics with him. We had some hiking and climbing training as regenerative activities post office hours. I am very thankful to all these memories created during the stay.

Not all the time was spent at lab, my sincere thanks to my circle at my stay at RHB. Certainly the deserving thanks to the administrative and other staff of RHB. Special thanks to Vivekanand, Ujjwal, Madhav, Purbayan and others for their kind interaction during weekends. We enjoyed going for short walks to discuss and have some social circle familiar enough to speak in mother tongue. Though this circle was made during the end of PhD, I enjoyed a lot during this interaction. Philosophical discussions with them were intriguing to trigger the ATHATO BRAHM JIGYASA. I would like to specially thank Richa for her kind support throughout the journey. She was patient and kind enough to provide me with a friendly environment when I needed some discussions. In fact, probably she was one person who has closely known my status of work schedule and mindset more closely. I had several innovative ideas during this period and I got into critical discussions with her regarding the practicality and applicability of them.

At the heart of my life, my parents have been source of inspiration throughout the entire journey. The very background of them have kept me inspired with high ethical values. The very interest in nature and physics was nurtured well by them. Despite the colonized hangover in the typical mind of middle class family, they supported my thirst for learning more than me to be an administrative officer. I would never be able to thank them enough. My very first circle of interaction is my brother Mayank and sister Saumya. Though I had little interaction with my sister, I am thankful to her for her efforts during old days while I was trying to be a kid experimentalist. My brother has been fulfilling the family obligations to keep me going without having to worry about them. I can never thank him enough for this. Thanks to my bhabhi Pooja and niece Garvita for being there when I needed them. I am very thankful to my grand parents and thereon ancestors for sacrificing to make me possible.

मां और पिताजी आप दोनों के त्याग और तपस्या के परिणाम स्वरूप ही, मैं ये कार्य पूरा कर पाया हूं। आपका आभार सदैव रहेगा। अपने आशीर्वाद में मुझे हमेशा रखने हेतु सहृदय धन्यवाद। पिताजी अपना शरीर छोड़ चुके हैं परन्तु उनके एवं आपके सिखाये हुए मूल्यों पर चलकर ही मैं अपना जीवन व्यतीत करूँगा। सादर नमन।

I hope I have not missed anyone in this list of acknowledgments. If anyone is missed in this mention I would like to apologize as well.

At the end I would like to thank the UNIVERSE for being the way it is, for example thanks to electrons to have the properties and behaviors they have.

List of Figures

1.1 Graphene lattice 6
1.2 Graphene energy dispersion 6
1.3 Periodic table with TMDCs 7
1.4 $MoSe_2$ structure and energy dispersion 8
1.5 Thermal bridge method 9
1.6 Thermal conductance and conductivity with temperature 10
1.7 SThM instrumentation 11
1.8 Dependence of thermal resistance 12
1.9 Schematic of Raman process in molecules 14
1.10 Feynman diagram of Raman process in solids 15
1.11 Typical Raman spectra of graphene 16
1.12 Schematic of Lee plot 17
1.13 Schematic of hotplate experiment 19
1.14 Schematic of 1 laser Raman thermometry 19
1.15 Local temperature profile for suspended graphene in Corbino geometry 21
1.16 Schematic of 2 laser Raman thermometry 22
1.17 Temperature profile of suspended thin film of Si 23
1.18 Thermal conductivity estimation of graphene using different methods 25

2.1 Existing geometry of see-through holes in our lab 28
2.2 Design of see-through holes 29
2.3 See-through holes using DRIE 30
2.4 Successful creation of SiO_2 membranes with see-through holes . . . 31
2.5 Optical focusing of strained SiO_2 membranes 32
2.6 Impurity of the SiO_2 membrane 32
2.7 Success with clean substrates 33
2.8 Drilling of holes using wet etching 33
2.9 Substrates from wet etching 34
2.10 Misalignment issue 34
2.11 Mechanical exfoliation 35
2.12 Mechanical exfoliation of graphene 36
2.13 Mechanically exfoliated samples 36
2.14 Schematics of stamping 37
2.15 Suspended graphene 38
2.16 hBN thin film with FIB hole 39
2.17 Wet transfer 40
2.18 Schematic of CO_2 phase diagram 40

2.19 SEM image of the suspended graphene by standard transfer 41
2.20 Sample annealed at 400^{o}C 42
2.21 Sample annealed in the steps of 300^{o}C - 400^{o}C - 200^{o}C 43
2.22 Sample annealed at 350^{o}C 43
2.23 Comparison of sample resulting from three different methods 44
2.24 Removing PMMA using toluene treatment for 3 hrs 46
2.25 Overnight toluene treatment 46
2.26 Removing PMMA using different methods 47
2.27 Sample annealed at 400^{o}C 47
2.28 Aluminium mediated suspended samples 48
2.29 Gold mediated suspended samples 49
2.30 Raman spectra of graphene resulted from different preparation methods 49
2.31 Lee plot for samples resulted from different methods 50
2.32 Strain and doping with corresponding G band frequency for different processes 51
2.33 Statistics of strain and doping 52
2.34 Raman map for gold mediated transfer 53

3.1 Characterization of exfoliated $MoSe_2$ 58
3.2 Characterization of exfoliated $MoSe_2$ on SiO_2/Si 59
3.3 Temperature dependence of optical properties 60
3.4 Temperature dependence of PL intensity 60
3.5 Laser power dependence of optical phonons of exfoliated $MoSe_2$ . . 62
3.6 Raman spectra of CVD grown h-BN on sapphire 64
3.7 Global heating of CVD grown hBN on sapphire 65
3.8 Local heating of CVD grown h-BN on sapphire 66
3.9 Optical absorption of CVD grown h-BN on sapphire 67
3.10 Temperature evolution for optical phonons of suspended graphene . 69
3.11 Local heating of suspended graphene 69
3.12 Raman spectrum of graphene on different substrates 70
3.13 Local heating of mechanically exfoliated graphene on different substrates 71
3.14 Mechanically exfoliated 2H-$TaSe_2$ 72
3.15 Temperature dependent Raman modes of mechanically exfoliated 2H-$TaSe_2$ 72
3.16 Local heating of mechanically exfoliated 2H-$TaSe_2$ using different excitation 73
3.17 $\partial\omega/\partial$T and $\partial\omega/\partial P_{laser}$ with electronic structure 74

4.1 Thermal conductivity of suspended graphene using optothermal methods 77
4.2 Frequency *vs* temperature for different radius of suspended graphene 79
4.3 Linearly fitted G band frequency with temperature for different radius 80
4.4 Linearly fitted 2D band frequency with temperature for different radius 80
4.5 Radius dependence for global heating 81

4.6 Radius dependent slope ratio of 2D band to G band 82
4.7 Temperature dependent strain evolution for different hole size . . . 83
4.8 $\partial\epsilon/\partial$T dependence on radius of hole size 84
4.9 Strain during the cool down 85
4.10 Schematic of transport during local heat under diffusive model . . . 86
4.11 Laser power dependent evolution for different radius of suspended graphene 86
4.12 Interdependence of $\delta\omega_G$/dP, initial G band frequency and radius . . 87
4.13 Interdependence of 2D band slope, initial 2D band frequency and radius 88
4.14 Initial G and 2D band frequency for different hole size 88
4.15 Radius dependence of $(\partial\omega_{2D}/\partial\mathrm{P}_{laser})/(\partial\omega_G/\partial\mathrm{P}_{laser})$ 89
4.16 Lee plot and strain estimation for different hole size 90
4.17 Initial strain for different hole size 91
4.18 Dependence of $\partial\epsilon/\partial\mathrm{P}_{laser}$ on radius of hole size 92
4.19 Effect of substrate on optical phonon frequency with laser power . . 93
4.20 Spatial dependence of $\partial\omega_{G/2D}/\partial\mathrm{P}_{laser}$ 94
4.21 Transmission for 532.1 nm laser through suspended graphene 96
4.22 Thermal conductivity of suspended graphene using optothermal methods 97
4.23 Temperature estimation 98

5.1 Schematic of 2-laser Raman thermometry 103
5.2 Transmission profile of edge filter and dichroic mirror 104
5.3 Sample stage for 2LRT 105
5.4 Optical image of suspended graphene 105
5.5 Initial strain and doping of suspended graphene 107
5.6 2D band frequency map of suspended graphene in 2LRT configuration 107
5.7 AFM profile of the suspended sample 108
5.8 Estimated temperature maps of suspended graphene in 2LRT configuration 109
5.9 Temperature profile (T(r)) for different wedges 110
5.10 Representative profile of T(r) with distance 111
5.11 Representative logarithmic profile for T(r) 113
5.12 Schematics for different W(r) behaviors and our observation 115
5.13 Representative profile of T(r) with distance 118
5.14 Fits with proposed model for T(r) profile of different wedges 119
5.15 Estimated temperature maps of suspended graphene in 2LRT configuration while the hotspot is on the substrate 121
5.16 Temperature profile with distance 122

1 Phonon dispersion in graphene 129
2 Raman processes in k space 130

3 2D band frequency maps of suspended graphene with radius 3.6 μm 131
4 Estimated temperature maps of suspended graphene with radius 3.6 μm 132

5 2D band frequency maps of suspended graphene with radius 5.3 μm 132
6 Estimated temperature maps of suspended graphene with radius 5.3 μm 133
7 2D band frequency maps of suspended graphene with radius 8.3 μm 133
8 Estimated temperature maps of suspended graphene with radius 8.3 μm 134
9 Averaged temperature profile for 2.3 mW heating power 134

10 Razor edge method 135
11 Spot size of heating laser using razor edge technique 136
12 Spot size of heating laser by using linear scan of piezo stage 137

List of Tables

2.1 **Empirical parameters from annealing processes** 44

2.2 **Raman modes for different processes**: The G and 2D band frequency parameters for different processes as observed in Raman spectroscopy 50

3.1 **Different thermal parameters of various materials** : Thermal conductivity of different materials using Balandin *et al.* formalism (o.e.- overestimation and u.e.- underestimation). *, †, + show the SiO_2/Si, sapphire and 10 nm Au/Si substrates, respectively. 75

5.1 The extracted parameters from the proposed model (κ_{3D} is in $Watt/K/m$, l_1 is in μm). 120

List of abbreviations

PL	Photoluminescence
HOPG	Highly oriented pyrolytic graphite
PMMA	Polymethyl methacrylate
PDMS	Polydimethylsiloxane
2D	2 dimensional
CVD	Chemical vapor deposition
1LRT	1 Laser Raman thermometry
2LRT	2 Laser Raman thermometry
NA	Numerical Aperture
TDTR	Time dependent thermoreectance
MFP	Mean free path
SThM	Scanning thermal microscopy
TMDC	Transition Metal DiChalcogenides
SOI	Silicon on insulator
RIE	Reactive ion etching
TMAH	Tetra-methylammonium hydroxide
FIB	Focused ion beam
SEM	Scanning electron microscope
FWHM	Full width at half maximum
TEC	Thermal expansion coefficient
HRTEM	High Resolution Transmission Electron Microscopy
CDW	Charge density wave

CCD	Charge-coupled device
AFM	Atomic force microscope

Outline of the thesis

2D materials have shown very promising electronic and physical properties. Owing to their limiting thickness of atomic scale, the estimation of physical quantities such as thermal conductivity are not straightforward, when compared to their bulk counter part. There has been several approaches for such estimation which provide wide range of values for graphene alone. Some of such techniques are scanning thermal microscopy (SThM), thermal bridge method and Raman optothermal techniques. The thermal conductivity predicted by these methods ranges from 60 to 5000 $W/m.K$ [1, 2, 3, 4, 5, 6]. Despite the progress made in the quest of estimating the thermal conductivity of 2D materials, the fundamental questions remain untouched such as the applicability of linear Fourier law in these limiting thicknesses.

The reports estimating the thermal conductivity of 2D materials apply the diffusive thermal transport equation for estimation. Moreover, the temperature estimation is made only at the hotspot which puts the estimation in question due to limited applicability of energy conservation. The questions mentioned here, put an open debate to find a generalized experimentation to test the applicability of linear Fourier law and establish a formalism to estimate the thermal conductivity for such materials.

The objective of this PhD project was to develop a first 2 Laser Raman thermometry experiment [7] in our laboratory applied for the first time to suspended graphene membranes and to explore the physics of suspended graphene with optical tools, namely Raman spectroscopy and opto-thermal measurements. Using the 2 laser Raman thermometry we present a direct and reliable experimental way to access the thermal conductivity of 2D materials and provide a phenomenological theory for generalized Fourier law applicable for materials with limiting thicknesses. The findings of this study will be presented in this manuscript which is structured as follows:

The first chapter gives an overview of 2D materials properties, along with the state of the art for estimating their thermal conductivity. We then discuss the optical techniques such as Raman spectroscopy used to characterize the 2D materials. The chapter ends with an emphasis on different techniques to measure the thermal conductivity with special emphasis on Raman optothermal techniques.

In chapter two, we discuss the sample fabrication. The chapter consists of two parts: one discussing the details of substrate fabrication with specially designed holes to suspend graphene. Second part discusses the 2D material integration with different substrates. While discussing the samples, we discuss about mechanical exfoliation and CVD grown samples, graphene in particular. We discuss the issues of a systematic integration of CVD grown graphene over see-through holes by modifying the existing standard processes. We then characterize the optimized transfer using Raman spectroscopy for different strain and doping contributions to the transferred graphene samples.

Third chapter discusses the thermal conductivity of different 2D materials using the formalism of the first reported optothermal Raman experiments by Balandin *et al.* [6]. We try to compare thermal parameters of different 2D materials on the basis of their electronic structure. We also focus on exfoliated graphene on different substrates and address the laser power dependent studies G mode which is not yet reported.

Fourth chapter discusses about 1-laser Raman thermometry for different radius of the hole sizes. With basic diffusive formalism, we attempt to understand the observations. We also demonstrate that the 2D frequency of graphene can be used as a thermometer mode and present the thermal conductivity of suspended graphene using the formalism of Balandin *et al.* and discuss its limitations. At the end we show the way to directly estimate the local temperature of the suspended graphene for our calibration.

In the fifth chapter we describe the 2-laser Raman thermometry experiment which allows measuring spatial evolution of the Raman mode frequency for graphene, subjected to a temperature gradient. We then convert these data into temperature maps of the suspended graphene and discuss the temperature profiles from the hot spot to the thermal sink. We present a phenomenological theory to go beyond the Fourier law and explain our findings. Here, we try to settle the question of applicability of Fourier law in suspended graphene for estimating the thermal conductivity and provide a better way to estimate the thermal conductivity for graphene. The general conclusion deals with applicability of our temperature mapping technique to 2D materials in general, and discusses future prospects.

Chapter 1

Introduction

Thermal physics is one of the fundamental concepts to our understanding of materials. Concept of heat can be traced back to one of the oldest systematic literature known to human kind such as Rigveda [8, 9]. Thermal properties remains central to modern understanding of materials ranging from quantum to cosmological systems [10]. Modern day dependence on electronic devices requires the study of heat management in such devices since the heat dissipation remains a central bottleneck for energy conservation. The more thorough investigation of heat transfer dates back to Joseph Fourier in his book 'Théorie analytique de la chaleur' [11]. His treatise details about the heat transfer in 3D materials, setting the basis for the concept of diffusive thermal transport.

The diffusive nature of thermal transport induces major heat losses leading to device efficiency compromise. With recent material advancements (such as thin films and low dimensional materials), non-diffusive transport has been discussed [12, 13]. Investigating and opening the possibility to access more easily the ballistic thermal transport highlights the fundamental understanding of heat and could also contribute to heat management in electronic devices. Recent developments of low dimensional materials such as 2D materials have shown greater possibilities in this regard. Moreover, phonon engineering is one of the prospects where the nanostructuring of the 2D materials can be used to tune the thermal properties [12, 14, 15, 16]. Even though phonon engineering is applicable to almost all the materials, low dimensional materials have shown great potential in thermal management [14]. For instance, the thermal conductivity of carbon nanotubes have been shown to be very high (3000 W/m.K), which makes them potential candidates to be used as heat sink in device applications [17, 18]. This chapter presents an overview for the low dimensional materials and different ways of measurement for estimating their thermal properties.

1.1 State of the art

Thermal properties of thin films started to draw attention of physicists with the advent of microelectronic devices. Before, discussing the details of state of the art we can remind ourselves the Fourier law. The total heat transfer (ϕ) for a system is given by the Fourier law:

$$\phi = \kappa \nabla T \tag{1.1}$$

where κ is the thermal conductivity of the material and ∇T shows the gradient of the temperature. The estimation of ∇T, requires us to measure the temperature and the cross section of the system at different locations. One can readily notice that under the Fourier model of heat transport, the total heat transfer is inversely related to thickness of a material [11], it in turn affects the thermal conductivity estimation with liming thickness of samples. Due to inverse relation, the measurements seem to show singularity in case of thinner samples, which results in huge values of thermal conductivity. This issue became much more relevant with the discovery of 2D materials which are usually one or few atoms thick. With such thicknesses, the in-plane thermal transport is much more relevant than the out of plane thermal transport [19]. In fact, the classical setups for measuring thermal conductivity were no longer useful, since they were capable of measuring out of plane thermal conductivity, owing to bulk nature of samples. This inadequacy gave rise to different methods for measuring thermal conductivity of thin films.

First such report was done by Schafft *et al.*, where they measured the thickness and temperature dependence of thin SiO_2 films, heating by Joule effect (4-probe measurement of the resistance that they calibrated with a hot chuck) [20]. They observe that in the sub-micrometer thickness the thermal conductivity is different than the one reported for bulk SiO_2. They also observed that the thermal conductivity varies directly with thickness whereas it varies inversely with temperature. They explain these observations with phonon boundary scattering which increases with decreasing thickness thereby reducing the conductivity. The boundary scattering is also temperature dependent and hence it affects the temperature evolution. These measurements were done on SiO_2 grown on Si$\langle 111 \rangle$ substrates, which opens a crucial question *i.e.* how much does the substrate affect the thermal properties in such cases. Due to sub-micron thickness of thin films, a substrate is readily used for fabricating the electronic devices, which becomes a significant parameter in the heat propagation problem. In fact for the case of 2D materials, the device fabrication is mostly done on a substrate which is why the same question can be extended in that case as well.

To understand the effect of substrates there could be different approaches to study the system. In this line of thought suspending samples are one of the possibilities. Another important prospect is the way to heat the sample. The idea of using point or linear heater instead of plane heater was initiated by J. Krempaský in 1964 [21]. This idea can be considered to be the foundation for studying the heat transport from local heating point of view. Much of the progress is based on the formalism provided by Krempaský. Such approach presents a crucial question of interface thermal resistance, which has been explored in detail by number of reports for different materials in 1 and 2 dimensional materials [22, 23, 24].

On the experimental part, there have been several reports for estimating the thermal conductivity of graphene. Balandin *et al.* was the first to report the thermal conductivity of exfoliated graphene using Raman thermometry, where the laser is used as point heater [6]. Using optical phonons they estimated the thermal conductivity for their suspended 3 μm-large ribbon of graphene to be around 5000 W/m.K. This was the highest reported thermal conductivity for any material. Two years later, Faugeras *et al.* presented a similar study using Raman opto-thermal and Stokes anti-Stokes intensity ratio to estimate the temperature profile of CVD grown suspended graphene over a hole of 44 μm diameter. Using such methodology they estimated the thermal conductivity to be around 600 W/m.K. This number was one order of magnitude less than Balandin *et al.*, suggesting a wide range of thermal conductivity depending on the graphene nature.

In the same year Ruoff *et al.* presented another approach using similar technique but different model (See section 1.4) and estimate the thermal conductivity of CVD grown suspended graphene to be around 2500 W/m.K (400 W/m.K when supported). In their report they particularly questioned the approach of Balandin *et al.*, since the power used for heating the graphene was assumed to be 100 % absorbed, which is not correct considering the 3.3±1.1 % reported absorption of graphene [1]. The power absorbed by the suspended graphene was obtained as the difference between the power transmitted through an empty hole and that transmitted through a graphene flake. In addition, Ruoff *et al.* justified the number estimated by Faugeras *et al.* to the high laser power (6.2 mW) used in the experiment, which raised the temperature of graphene. Considering such wide range of thermal conductivity even for the case of CVD grown graphene raises concern over the applicability of diffusive equation to estimate the thermal conductivity.

Alternatively, Bae *et al.* in 2013, presented a set of study using the heater-sensor approach of thermal bridge to estimate the thermal conductivity of graphene. Since they used graphene exfoliated on substrate, they measured rather low value of conductivity of around 500 W/m.K, which was in close agreement to the study of Ruoff *et al.* Their estimation also claimed to have reached a phonon mean free path of nearly 100 nm. This estimation is inspired from the report of Prasher (2008), which was dedicated for estimating the thermal conductivity of CNTs in the temperature range of 10-100 K [25]. It is important to mention that the relations taken for the estimation are based on phonon dispersion relation of Kumatsu, which predict the specific heat of graphite only up to 100 K [25, 26]. Hence, this estimation of the mean free path can be severely off from the real intrinsic numbers.
Another approach using scanning thermal microscopy to estimate the thermal conductivity for different sized suspended graphene was presented by Hwang and Kwon in 2016 [3]. Interestingly, even on their suspended samples, they estimated the conductivity to be around 600 W/m.K. This estimation was low, compared to all other reports in the suspended samples. However, they show that contribution of thermal contact resistance of probe and sample could severely affect the estimation for smaller samples, since the thermal probe itself has spatial limitation. Despite their careful approach, the technique they used cannot estimate the thermal conductivity for large area of suspended samples owing to instrumental issues

(largest size of hole- 3.7 μm).

All these reports present a range of values for thermal conductivity of suspended and supported graphene. Despite using same approaches, a consistent estimation of thermal conductivity for the case of supported graphene is noticed whereas the estimations for suspended graphene yield wide range of values [2, 1, 6, 27]. One of the possible reasons could be that the supported graphene measurements do not yield the intrinsic numbers due to the thermal coupling with substrate [28]. The question of consistent methodology, to estimate the thermal conductivity of 2D materials for intrinsic properties, is still open. In fact it would not be an exaggeration to say that this wide range of thermal conductivity values cannot be justified only to sample quality. Rather, the problem must be looked at from fundamental point of view such as to test the applicability of Fourier model in one or few atom thick materials. We shall be establishing the motivation for such study in the next section.

1.2 Motivation of the project

To sketch the motivation of the manuscript, we will focus on the fundamental point of view for understanding thermal physics in low dimension.

Despite the progress made in the field of thermal physics in low dimensions, the question of the applicability of Fourier's law of heat diffusion in 2D limit remains an open one, as well as the thermal transport regime in these materials : is it diffusive, quasi-ballistic, ballistic or hydrodynamic, as predicted theoretically? [4, 29, 30, 31]. The thermal transport regime is determined by the mean free path of the phonons and the size of the concerned device [30]. Even though there are several reports of extracting thermal conductivity in 2D materials [1, 32, 33], the direct measurement of mean free path in such systems remains an open question. Often, the estimations made for mean free path come from mathematical relation between thermal conductivity (κ), specific heat (C) and the mean free path (Λ) ($\kappa=\frac{1}{2}$ CvΛ, v being the average phonon velocity). However, since the methodology of estimating the thermal conductivity is already debated, one cannot rely on these numbers. For instance, the applicability of heat equation is never tested in 2D materials, but it is presumed to be applicable, which can severely affect the estimated thermal conductivity, other parameters and conclusions thereon. Such assumption is very strong for extracting thermal conductivity considering the limiting thickness. Furthermore, there are theoretical predictions about the mean free path in freestanding graphene (100 μm) but the experimental verification shows a large range of smaller values (few nm to 775 nm) [4, 29, 32, 34].

Owing to the fundamental questions mentioned above, it becomes debatable to model the thermal conductivity estimation in experiments without answering these questions. It could be argued that this ambiguity might be the reason for the wide range of thermal conductivity value reported for graphene. For example, the MD simulations have predicted the lattice thermal conductivity to be around 10000 W/m.K, however, these simulations may suffer the deviations owing to high computational cost for long range interactions, which has been discussed in recent reviews [35, 36]. On the other hand, calculation by solving Boltzmann transport equation predicts the in-plane lattice thermal conductivity to be around 4000 W/m.K [29]. Moreover, different experimental approaches have resulted in numbers ranging from 600- 5000 W/m.K [5, 1, 3, 6].

With an open debate about the consensus of reliable estimation of thermal conductivity of suspended graphene, there is ample room for understanding the subject from scratch. We will try to answer one of the very fundamental question of applicability of diffusive model in 2D limit, in order to contribute positively to the debate. In addition, we might be able to provide a consistent or more reliable way to estimate the thermal properties for 2D materials, which may take us beyond Fourier model.

1.3 2D materials

Working with microscopic systems in early 20^{th} century was pretty much considered ‘impossible’. By the mid-20th century, the works of W. Paul (1958) led to the foundations for trapping and experimenting with single atoms or ions [37]. Pretty much similarly, the idea of ‘stable 2D systems’ was heavily debated in late 20^{th} century [38]]. In early 21^{st} century, Novoselov and Geim disproved the hypothesis of instability of 2D systems by the discovery of mechanically exfoliated graphene to be stable in ambient conditions [39]. The isolation of graphene lead to several 2D materials down to few atoms thickness originating from different layered materials such as h-BN, transition metal dichalcogenides etc. The wide range of chemical and physical properties of such systems guides researchers to use them in electronics, optics, mechanics and different applications [40]. The electronic structure in 2D materials range from insulator to direct or indirect semiconductors to semimetals and metals as well [41]. Along with rich electronic structures, they present interesting thermal properties, which could in turn be utilized for heat dissipation in electronic devices. Here we would like to briefly discuss physical properties of some of these materials.

1.3.1 Graphene

Graphene is also known as ”mother of all the 2D materials”. Soon after it’s isolation from bulk graphite in 2004, it drew attention of scientific community owing to its unique electronic properties [39]. The mechanical exfoliation of graphene was done using scotch tape followed by transfer onto a SiO_2/Si substrate [39]. Graphene has honeycomb lattice with two carbon atoms in its unit cell as depicted in figure 1.1. The carbon atoms are sp^2-hybridized forming rings of strong covalent bonds with a delocalized electron gas arising from the overlapping p_z-orbitals throughout the lattice (called π-bonds). Thus the sp^2-bonds are responsible for both graphene’s extreme mechanical stiffness and high electrical conductivity [42, 43].

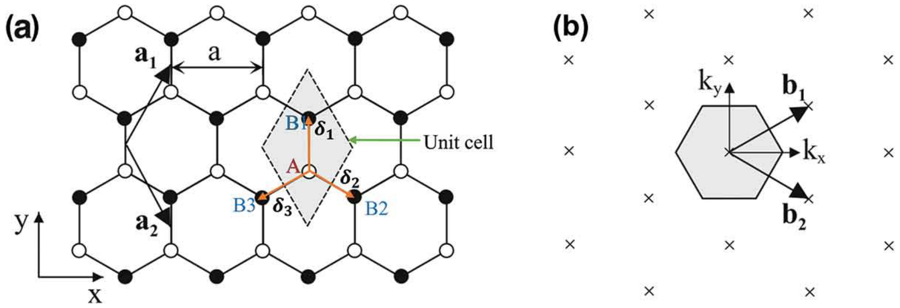

Figure 1.1: **Description of graphene [42]:** (a) Crystal structure of graphene and corresponding (b) Reciprocal space : The direct space in (a) has two carbon atoms represented by white and black circles. A primitive unit cell is shown by the rhombus structure enclosed by dashed line. In reciprocal space, k_x and k_y represent the unit vectors in (b).

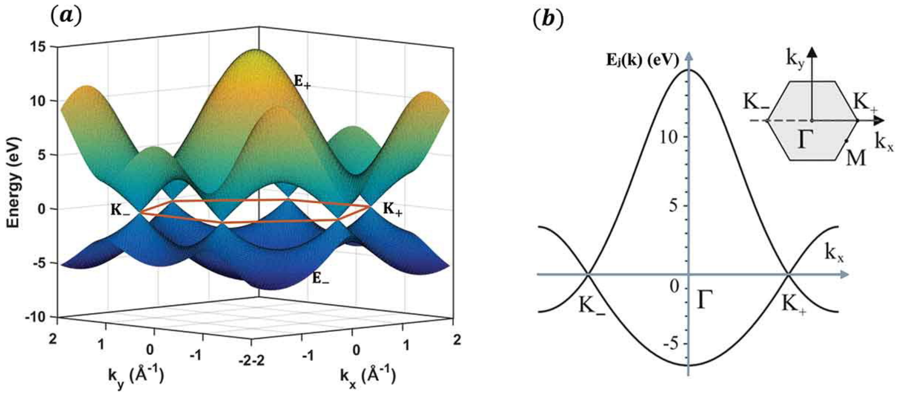

Figure 1.2: **Energy diagram of graphene [42]:** (a) 3D representation of energy dispersion in k space and (b) A cut along y-z plane to observe the energy dispersion along k_x axis. (a) shows the hexagonal unit cell of the reciprocal space showing all K-points whereas (b) shows the two K points along the k_x axis with the linear dispersion near two K points with k_y=0.

The first Brillouin zone is hexagonal with two inequivalent consecutive corners denoted K^- and K^+, shown in figure 1.2. These specific points are called Dirac points, since electron energy bands show linear dispersion near these points, as depicted in figure 1.2(b). Owing to this linear dispersion, electrons near the Fermi level show massless behavior equivalent to photons, which are also particles with linear energy dispersion. With such properties, we can imagine to use graphene as platform for interesting physics using the peculiar tuneability of the electronic structure [44].

1.3.1.1 Thermal properties

The thermal properties of graphene are particularly interesting owing to it being an ideal 2D material (with single atom thickness). Thermal conductivity has two main contributions arising from lighter electrons and heavier ions (collective ion vibrations which are referred to as phonons). The contribution from electron can be estimated by the Wiedemann-Franz law. However, it was shown in recent years that the contribution from electrons is calculated to be very small relative to the phonon contribution [45, 46]. Interestingly, an experimental observation to estimate the contribution from electrons was found to be in the order of 10 W/m.K in suspended graphene. Despite the theoretical calculations showing the violation of Wiedemann-Franz law, it was validated in the experimental observation.

It was shown that the thermal conductivity of graphene is driven by phonons since the conductivity contribution from electrons is very small (10 W/m.K) compared to phonon contribution (6600 W/m.K) [47]. The phonon contribution can be estimated via Raman thermometry. Balandin *et al.* estimated the thermal conductivity of graphene, using the Raman thermometry, to be in the range of 5000 W/m.K, which is indeed very high compared to the electron contribution. However, different measurements report range of different thermal conductivity for graphene [1, 27]. We will discuss the different approaches used to estimate the thermal conductivity of graphene in forthcoming sections (section 1.4).

1.3.2 Transition Metal DiChalcogenides (TMDCs)

Transition metal dichalcogenides are 2D materials with chemical composition of MX_2, where M is a transition metal and X is a chalcogen. As shown in figure 1.3 the transition metals are highlighted in colors along with the chalcogens S, Se and Te. The combination of the two in the MX_2 format gives rise to several layered compounds with wide range of optical and electronic properties. This vast range of properties makes them suitable candidates for electronic and opto-electronic applications [48].

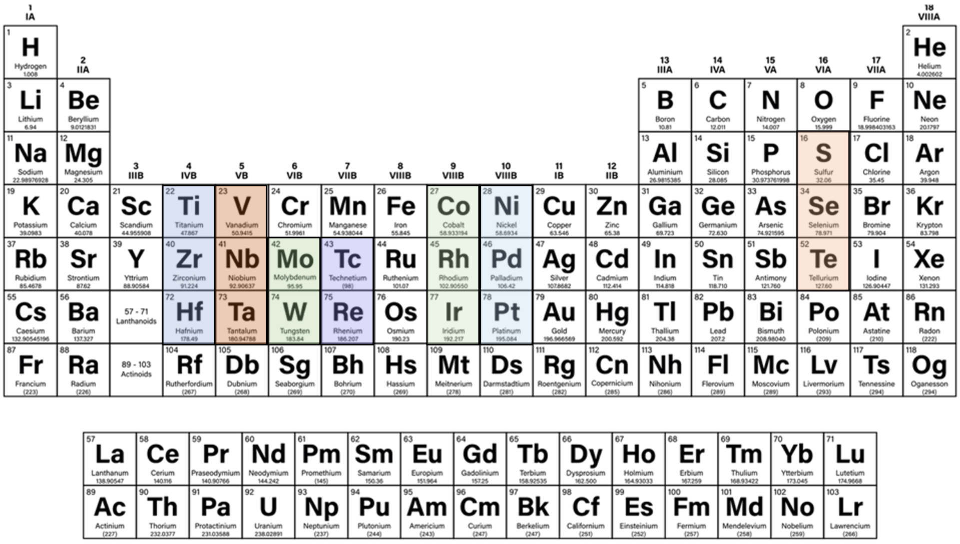

Figure 1.3: **Periodic table** [Adapted from google]: The transition metals are highlighted in colors (orange and shades of blue , green) along with the chalcogens S, Se and Te (light orange), which constitute the MX_2 TMD material.

Interestingly, it has been shown that bulk TMDCs with indirect bandgap semiconductors show direct bandgap semiconducting properties when observed at their monolayer, such as, $MoSe_2$. The direct bandgap of $MoSe_2$ (monolayer) has been shown to be 1.58 eV [49]. The structure of $MoSe_2$ is such that it is three atom thick material where the Mo atom is sandwiched between two Se atoms, as shown in figure 1.4, blue and tangerine color represent the Se atoms and lavender color shows the Mo atom.

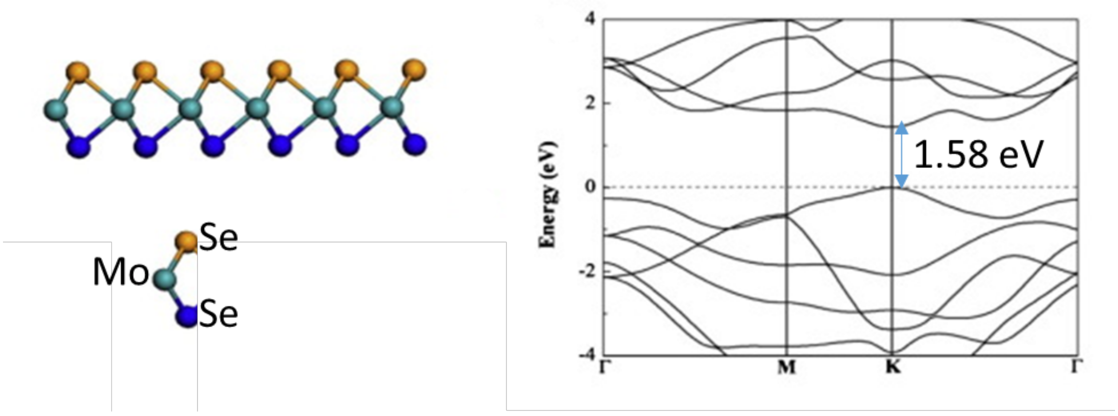

Figure 1.4: **Structure of monolayer $MoSe_2$** [50]: (left) Blue and tangerine colors show the top and bottom Se atoms and lavender color shows the Mo atom, (right) Electron band dispersion of monolayer $MoSe_2$, at K point the direct band gap of 1.58 eV is shown.

As depicted in the band structure of monolayer $MoSe_2$ (figure 1.4), the direct band gap of 1.58 eV is at K point of the reciprocal space. It has been shown that the electronic structure can be modified by various means such as interfacing with other materials, strain, temperature etc [50]. With such tunability, TMDC materials present wide range of possible applications in opto-electronics [48]. However, one bottleneck for such application is the thermal properties of these materials. Literature has shown that these materials show poor thermal conductivity for electronic applications [51]. Interestingly, these studies have used suspended samples but in applications the devices are made on a substrate. We can estimate the thermal properties using the optical phonons of these materials. We will elaborate our measurements of exfoliated samples on substrate in chapter 3.

1.3.3 other 2D materials

There are several other members of the 2D family. One such example is h-BN, hexagonal boron nitride, which shares same lattice structure with graphene. Since the substrate effect is very pronounced in case of 2D materials, It is important to have an insulating substrate for realizing them into electronic devices. It is shown that graphene encapsulated in few layer h-BN gives the best electrical properties of graphene. h-BN from this point of view becomes an interesting platform to test out thermal properties and how it could be used to dissipate the heating effect from the encapsulated 2D material being used as an electronic device [52]. h-BN can be realized by replacing two carbon atoms from graphene unit cell with boron and nitrogen atoms, respectively. Moreover, the lattice mismatch of graphene and h-BN is only 4 % [52]. Unlike graphene, h-BN is an insulator with a band gap of 6.4 eV. Such a large band gap in comparison to earlier discussed 2D materials, makes it perfect for being used as a dielectrics for 2D materials. However, thermal isolation is not achieved by this method leading to the choice of suspending the 2D material over a hole.

1.4 Measurement of thermal properties in 2D materials

With the need to measure the thermal conductivity in 2D materials, there have been several approaches to reach to thermal conductivity values via different experimental approaches. We will be discussing some of these experimental approaches here.

1.4.1 Electrical methods

1.4.1.1 Thermal Bridge method

Thermal Bridge method was first devised by Kim *et al.* to measure the thermal conduction in carbon nanotubes [5]. The design of the technique allows it to be used in measuring the thermal properties of 2D materials as well.

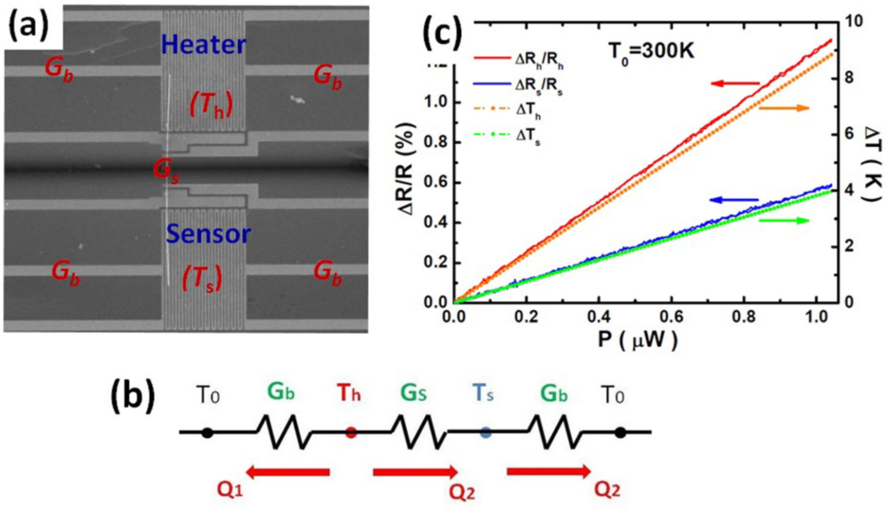

Figure 1.5: **Measurements in thermal bridge method** [53]: (a) SEM image of an insulating nanowire suspended by MEMS for thermal measurement. This measurement can provide information on the thermal conductivity, thermopower and electrical resistance in a single device. (b) Schematics of the thermal flow circuit. (c) Resistance change and corresponding temperature change in the heater/sensor .

Thermal bridge method uses nano-lithography to suspend the samples between two microscopically designed islands which can be used as heater and sensor (see figure 1.5). A nano-manipulation systems is used to detect and change the temperature across the sample which later can be used to extract the thermal conductivity of the sample. It is important to mention here that this method uses complicated nano-fabrication in order to achieve the microelectromechanical system (MEMS).

In principle the temperature is calibrated by measuring the resistance of the heater and sensor metal lines. Thermal bridge method was used by Bae *at al.* to measure the thermal conductivity and conductance of exfoliated graphene samples supported on SiO_2/Si substrates. Keeping the length of the device same (260 nm), they varied the width of the graphene nano-ribbons from 45 to 130 nm (Figure 1.6(a)). It was shown that with decrease in the width of the nano-ribbon, the contribution of ballistic transport should increase but due to increased edge scattering the overall effect is suppressed. Maximum of 35% theoretical ballistic heat flow limit was reported for the larger (260 nm) sample. However, smaller width samples showed smaller thermal conductance owing to increased edge scattering contributions.

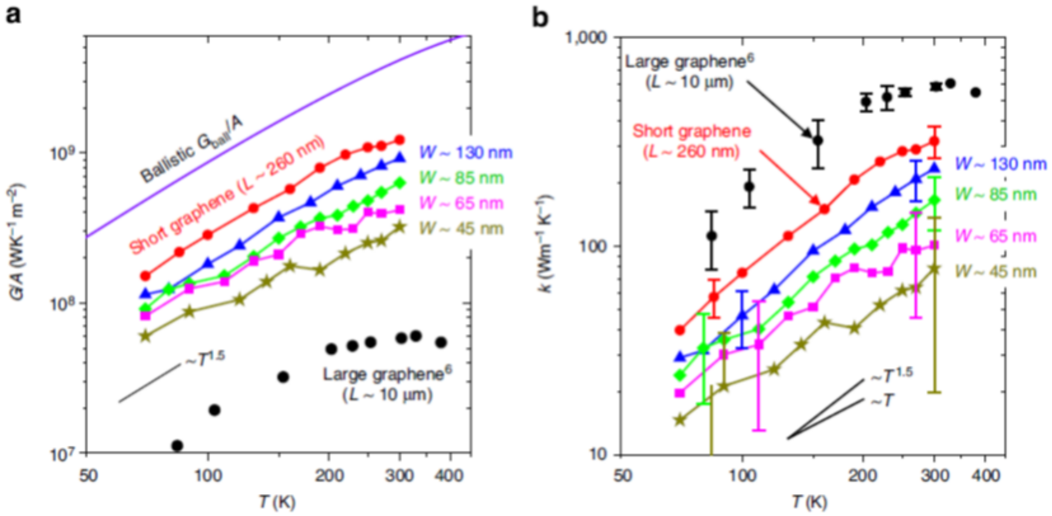

Figure 1.6: Measurements done in [4] for different width of exfoliated graphene on SiO_2/Si : (a) Thermal conductance *vs* temperature, (b) Thermal conductivity *vs* temperature.

The thermal conductance and conductivity scale with temperature as $T^{1.5}$, as shown in figure 1.6. However, the thermal conductivity scales as $W^{1.8 \pm 3}$ (W being width). The interesting observation of thermal conductivity scaling with width of the sample was attributed to the edge phonon scattering events. It was shown that with reduced edge scattering contribution the transport regime shifts towards quasi-ballistic regime.

Despite the modelling of the heat flow and deconvoluting the interface contributions for these reports, it can be argued that the prominent substrate effect w.r.t. doping and strain cannot be ruled out, which would directly impact the intrinsic thermal properties of the graphene [28]. Interestingly, it can be said that this study hints towards the possibility of non-diffusive thermal transport in case of suspended graphene. However, the nano-fabrication involved in suspending graphene for thermal bridge method makes it extremely challenging. However, such experiment could be an interesting platform to study the thermal transport regime, for example an in-situ Raman mapping could be performed for different heating powers, to observe the thermal transport using the principles of Raman thermometry.

1.4.1.2 Scanning thermal microscopy

Scanning thermal microscopy (SThM) is a variation of Atomic force microscopy technique. The technique was developed by Williams and Wickramasinghe in late 1980s [3]. The working mechanism of SThM is similar as the scanning tunneling microscopy (STM). The main difference between the two is the constant use of heat flux to maintain the distance between the sample and the tip instead of tunneling current. Owing to the nanometer spatial resolution of SThM technique it is suitable for thermal characterization at nanometer scale. Typically, the tip is made of Pt-Cr and the junction is used as thermocouple.

The experimental setup, as shown in figure 1.7, consists of a function generator, a preamplifier, a notch filter, a signal access module (SAM), a Wheatstone bridge circuit, a SThM probe, and a scanning probe microscope (SPM). The function generator is used to apply a high-frequency ac bias to heat the thermocouple of the SThM probe. The Wheatstone bridge is used to remove the dominant ac voltage and thereby improve the sensitivity of the measurement of the dc thermoelectric voltage generated from the thermocouple junction of the SThM probe. The dc thermoelectric voltage from the thermocouple junction is fed into the SAM and became available simultaneously with the topography signal of the SPM [3, 54].

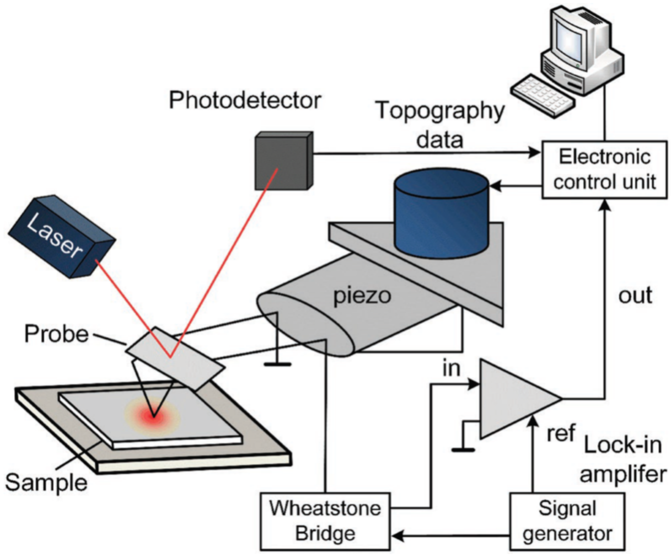

Figure 1.7: **Schematic of SThM instrument [3]**: Typical measurement scheme of the SThM setup, where the probe is made in contact with sample and it is connected to a feedback system for sensing the local temperature.

$$T_s = T_{c1} + \frac{T_{c2} - T_{c1}}{T_{j1} - T_{j2}}(T_{c1} - T_{nc1}) = T_{c1} + \phi(T_{c1} - T_{nc1}) \tag{1.2}$$

where T$_s$ ia the unperturbed temperature of sample; T$_c$ is the temperature measured by the SThM probe in contact mode; T$_{nc}$ is the temperature measured in the nonthermal contact mode; T$_j$ is the temperature jump, which is defined as (T$_c$-T$_{nc}$) and subscripts 1, 2 represent the powers at two different heating powers of the thermocouple junction of the SThM probe.

This equation was used in order to use null point SThM in order to measure the unperturbed temperature (T$_s$) of the membrane along with the local spreading thermal resistance which can be done by monitoring ϕ. Using the SThM probe scan across the suspended membrane, one can measure T$_{c1and2}$ and T$_{nc1and2}$ for two different heating powers and optimized signal to noise ratio. Using these measured values in equation 1.2 one can estimate ϕ and T$_s$ profiles across the diameter of suspended membrane. As shown in figure 1.8, the value of ϕ_{center} decreases linearly for samples with diameter 1.56-3.68 μm.

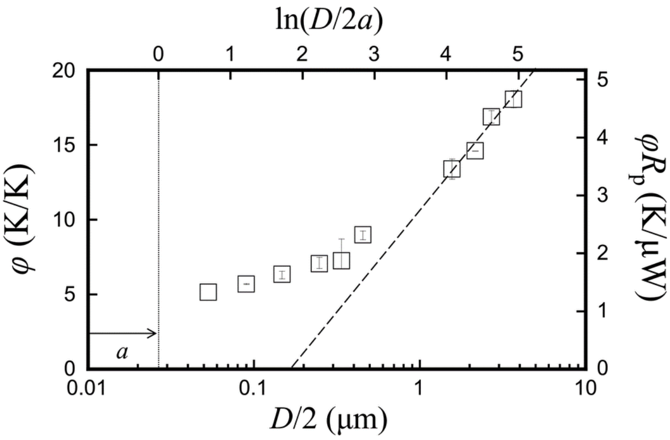

Figure 1.8: **Measurements done in [3] for different width of exfoliated graphene on SiO$_2$/Si** : Thermal resistance against ln(D/2a), a is the thermal resistance of the tip sample interaction, the radius of such interaction for [3] is 25 nm.

As shown in figure 1.8, the extrapolation of linear graph leads to negative value of thermal resistance which is consistent with the observation made by Ruoff *et al.* [1]. Such observation is attributed to the ballistic resistance increase as ln(D/2a) gets relatively smaller than the mean free path (MFP) of phonons, a parameter being the radius of tip sample thermal contact resistance (around 25 nm). Such observation is consistent with the predictions made by Chen [55]. He showed that when the radius of a heat-generating particle embedded in a medium gets much smaller than the heat carrier (phonons in this case) MFP, very few scattering events occur near the heated sphere and the heat carrier transport becomes ballistic or nonlocal [55]. The samples with smaller diameter than 1.56 μm, show a deviation from the linear dependence , which can be attributed to the ballistic transport regime owing to its smaller size and increase in ballistic resistance.

This experimental study demonstrates that the thermal conductivity follows a linear variation with ln(D/2a) which verifies the Klemens' theory [56] for a narrow range of diameter (1.56-3.68 μm). However, it is important to mention that Klemens' theory does not take into account the ballistic resistance, whereas the experimental study claims to have included this contribution. The extracted thermal conductivity in this work is about 600 W/m.K, which is relatively small as compared to other reports for suspended graphene. However, such value is in agreement with reported value for supported graphene. It is worth pointing out that the thermal conductivity does not show any size dependence with change in diameter, which was attributed to the linear dependence with ln(D/2a). This is despite the fact that the change in size would change the contribution from ballistic resistance.

On the other hand, due to small size samples (largest diameter- 3.68 μm) it limits the significant effect of ballistic resistance contribution to the thermal conductivity. It is important to mention that since the tip sample interaction is a very crucial component of this study, for larger diameter samples the technique would suffer drawback of rupturing the sample. Such issue was reported at the edge of the suspended graphene. It has been shown that for large diameter suspended graphene membranes, graphene at the center occupies lower topography than the edge, which can be a cause of critical problem with this technique and hence it is difficult to apply for larger suspended samples. In order to avoid such problems, non contact techniques allowing to probe the phonons directly, are interesting to get insights on thermal transport. We will now discuss Raman spectroscopy as a power tool to try to reach such a goal.

1.4.2 Spectroscopic methods

There are several methods reported in literature for measuring the thermal conductivity by using light matter interaction. Time dependent thermoreflectance (TDTR) and Raman optothermal methods are some of the examples. However, since TDTR is not applicable to 2D materials thinner than 20 nm, we shall not be discussing them here. We will focus on Raman thermometry using 1 and 2 lasers in the following subsections.

1.4.2.1 Raman scattering

Light matter interaction can take place in several possible ways, for instance the out-coming light photon has different energy than the input light photon. Such inelastic scattering was first described by Indian physicist C.V. Raman in 1928, for which he was awarded Nobel prize in 1930. To understand Raman scattering, we can discuss the light matter interaction for a molecular system as follows:
When the system is excited to a virtual electronic state, it can relax in three possibilities (as shown in figure 1.9).

- Process 1- A system in ground vibrational state of the ground electronic state accepts a photon and relaxes back to the same vibrational state of the ground electronic state. (Rayleigh scattering)

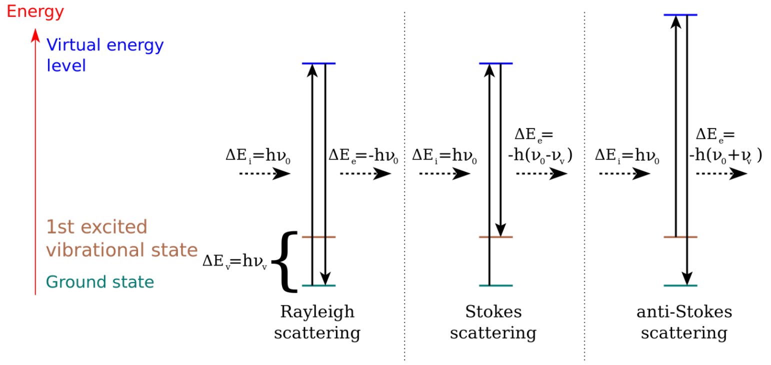

Figure 1.9: **Schematic of scattering process in molecules**: The excitation from ground state to a virtual state can result in three possible radiative relaxations, when the energy of scattered photon is same as incident photon it is called as Rayleigh scattering. When the scattered photon has energy smaller than that of incident photon it is known as Stokes Raman scattering while in reverse case it would be anti-Stokes Raman scattering. [57]

- Process 2- A system in ground vibrational state of the ground electronic state accepts a photon and relaxes back to the 1^{st} excited vibrational state of the ground electronic state. (Stokes Raman scattering)
- Process 3- A system in 1^{st} excited vibrational state of the ground electronic state accepts a photon and relaxes back to the same vibrational state of the ground electronic state. (Anti-Stokes Raman scattering)

We can associate the process 2 as annihilation of a phonon and process 3 as creation of a phonon in case of solid state systems undergoing Raman scattering. A typical Feynman diagram is shown in figure 1.10. The top figure shows the Stokes process where the incoming photon gives up the energy to the system (resulting in creation of phonon) resulting in lower energy scattered photon (ω_s=ω_l -ω_0), while the bottom figure represents anti-Stokes process, where incoming photon takes up the energy of the phonon from the system (resulting in annihilation of phonon) higher energy scattered photon (ω_s=ω_l +ω_0).

$$I \propto |\sum_{n*,n} \frac{\langle \omega_s, ph, i|H|0, ph, n*\rangle\langle 0, ph, n*|H|0, 0, n\rangle\langle 0, 0, n|H|\omega_l, 0, i\rangle}{[\hbar\omega_l - E_n - E_i].[\hbar\omega_i - \hbar\Omega_0 - (E_{n*} - E_i)]}|^2.\delta(\omega_i - \Omega_0 - \omega_s) \tag{1.3}$$

The mathematical description of the whole process can be represented by proportionality relation 1.3. The three Hamiltonians can be explained as follows:

- $\langle$0,0,n$|$H$_{e-photon}|\omega_l$,0,i$\rangle$ The system takes up the photon of incident laser energy and is excited to a state n from initial state i.
- $\langle$0,ph,n*$|$H$_{e-phonon}|$0,0,n$\rangle$ The system creates a phonon or annihilates a phonon and goes from energy state n to n*.

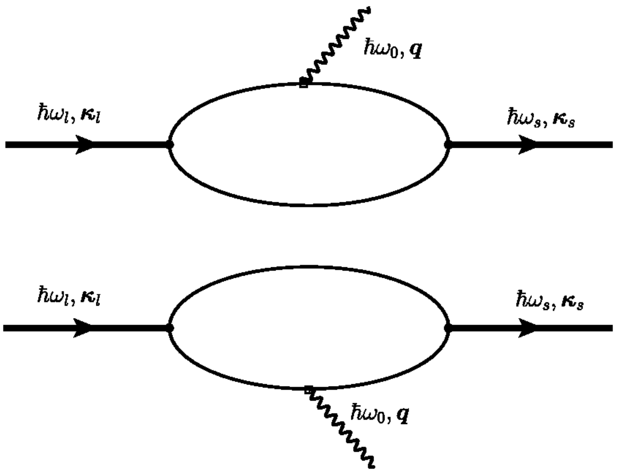

Figure 1.10: **Feynman diagram of Raman process in solids [58]**: The top figure shows the Stokes process and the bottom figure represents anti-Stokes process. Phonon energy is represented by $\hbar\omega_0$, scattered photon energy is $\hbar\omega_s$ and $\hbar\omega_l$ is laser energy.

- $\langle \omega_s$,ph,i$|$H$_{e-photon}|$0,ph,n$^*\rangle$ The system emits the resulting scattered photon and relaxing back to the ground state i.

The individual terms mentioned above decide the strength of Raman scattering presented by a system and hence is called as scattering cross section. The scattered photon when compared to incident photon can give the information about the phonons of the system. The phonons with energy equal or larger than 10 cm^{-1} are optical phonons which are readily detected in a Raman spectrometer [59]. The increase in laser power to a system can increase the absorption and thereby increase the overall temperature of the system which can then be detected by the optical phonon energy, due to the coupling between acoustic and optical phonons. Another way to detect the temperature is to use the Boltzmann distribution of phonons by monitoring the Stokes to anti-Stokes intensity ratio. We would be discussing both the approaches in following sections which can be used to make thermometry applications *via* Raman scattering.

We use WITec alpha Raman spectrometer in the lab for measuring Raman signals. The spectrometer consists of two different gratings 600 and 1800 grooves/mm. We use motorized piezoelectric stage for controlling the fine movement of samples. 600 grooves/mm grating can be used to record photoluminiscence (PL) of different samples. The optics of the setup is configured in different boxes associated for different wavelengths of excitation. Sample is located by using objective turret fitted with different magnifications (10x, 50x, 100x). Setup is configured in back-scattered geometry where the Raman signal is collected via an optical fiber (0.22 NA) coupled to the collection optics. Data presented in the manuscript are corresponding to the same Raman spectrometer unless stated.

1.4.2.2 Raman spectroscopy of 2D materials

Raman spectroscopy is an inelastic light scattering based tool for characterizing the vibrational modes of a sample. It helps to probe the optical phonons of the system. A system with N atoms in the unit cell would have 3 acoustic phonon modes and 3N-3 optical phonon modes. Raman scattering results from spatial change in polarizability of the system. Since such change does not appear from all the symmetries, not all the vibrations lead to Raman scattering. The vibrations which does not result in polarizability change, are often termed as Raman inactive mode. It is why, the symmetry of a system gives crucial information about Raman active modes of a system. Symmetry of a 2D material should be discussed to gain insight of Raman scattering. The point group symmetry of monolayer graphene is D_{6h} at the Γ point [60]. The vibration associated with Γ point vibration results in the G band of Raman scattering whereas the D_{3h} symmetry at K point leads to double phonon mode of D band which is frequently called 2D mode.

A typical Raman spectra of graphene collected with the setup is presented in figure 1.11.

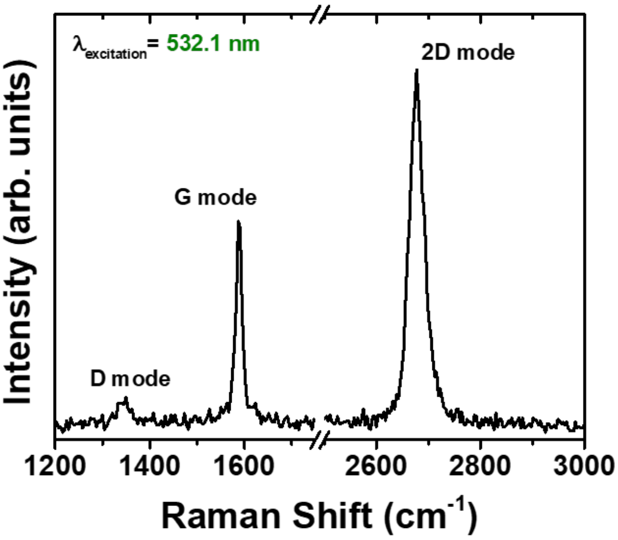

Figure 1.11: **Raman spectrum of suspended monolayer graphene**: The in-plane vibration at Γ-point results in the G mode whereas the 2 phonon process at the K point results in the 2D mode in Raman measurements.

The G band presented in figure 1.11 corresponds to in-plane vibration and it's doubly degenerate with E_{2g} symmetry. Whereas, 2D band is 2-phonon process at K point (see appendix A for details of phonon dispersion in graphene and different Raman processes involved in graphene contributing to 2D band) [61, 62].

The optical phonons (G and 2D bands) carry very rich information about the local lattice parameter. Since strain affects the lattice parameter directly, hence the strain information can be extracted using the frequencies of G and 2D bands. Lee *et al.* presented a correlation analysis to deconvolute the strain and doping using the frequency of G and 2D band [63]. The behavior of G and 2D band

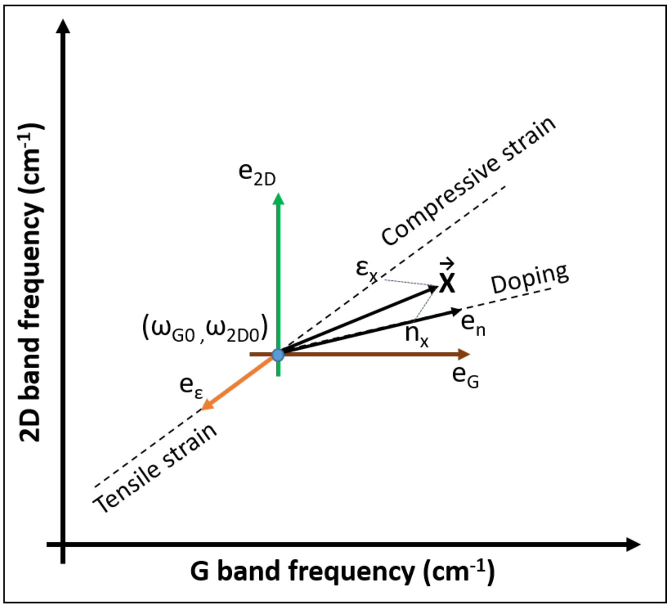

Figure 1.12: **Schematic of Lee plot**: The Lee plot has G band frequency as x axis and 2D band as y axis, this plane can be used to express the coordinates as strain and doping. The blue dot shows the undoped and unstrained G and 2D band frequency. The e$_G$ and e$_{2D}$ coordinates are orthogonal to each other which can be projected to another non-orthogonal coordinate system namely strain (ϵ_x) and doping (n$_x$). Such projection would result in strain and doping of the sample.

induced by doping is studied by Das *et al.* [64, 65]. It was shown by Das *et al.* that the ratio of Raman shift of 2D and G band ($\Delta\omega_{2D}/\Delta\omega_G$) is 0.7 for hole doping up to a hole surface charge of 2 x 10^{13} cm^{-2} [64, 65]. However, such number is found slightly lower in case of electron doping. Another study observing the same ratio $(\Delta\omega_{2D}/\Delta\omega_G)_{biaxial}$ for a biaxial strain was found to be 2.8 for both tensile and compressive strain [66]. Since, we would be suspending graphene over a hole, it would be a fair assumption for biaxial strain. Hence, we will be using the same number for further analysis.

With each measurement of Raman scattering we obtain a value of G and 2D band frequency, which can be treated as a $\vec{X}$ in a 2D plane with abscissa as G and ordinate as 2D band frequency (figure 1.12). Strain and doping can be used as non-orthogonal axes with origin as the strain-free and doping free point as shown by ω_{G0},ω_{2D0} (figure 1.12). In order to access the strain an doping we need to project the $\vec{X}$ onto the strain and doping axes. We can achieve this following the coordinate transformation shown by equation 1.4.

$$\begin{bmatrix} \epsilon_\epsilon \\ \epsilon_n \end{bmatrix} = \begin{bmatrix} s_G & s_{2D} \\ p_G & p_{2D} \end{bmatrix} \cdot \begin{bmatrix} \epsilon_G \\ \epsilon_{2D} \end{bmatrix} \tag{1.4}$$

where the matrix elements denote the shifts of the G and 2D modes positions as a function of biaxial strain and hole doping and are given by [67].

$$\begin{bmatrix} s_G & s_{2D} \\ p_G & p_{2D} \end{bmatrix} = \begin{bmatrix} \frac{\Delta\omega_G}{\Delta\epsilon} & \frac{\Delta\omega_{2D}}{\Delta\epsilon} \\ \frac{\Delta\omega_G}{\Delta n} & \frac{\Delta\omega_{2D}}{\Delta n} \end{bmatrix} = \begin{bmatrix} -57.3(cm^{-1}/\%) & -160.3(cm^{-1}/\%) \\ 10^{-12}(cm^{-1}/cm^{-2}) & 0.7.10^{-12}(cm^{-1}/cm^{-2}) \end{bmatrix} \tag{1.5}$$

With these numbers and inverting the equation 1.4, we can express

$$\begin{bmatrix} \epsilon_G \\ \epsilon_{2D} \end{bmatrix} = \frac{1}{p_{2D}.s_G - s_{2D}.p_G}. \begin{bmatrix} p_{2D} & -s_{2D} \\ -p_G & s_G \end{bmatrix} . \begin{bmatrix} \epsilon_\epsilon \\ \epsilon_n \end{bmatrix} \tag{1.6}$$

Using the transformation of equation 1.6, we can express the G and 2D frequency in terms of strain and doping axes. We can, now simplify a randomly measured $\vec{X} = \mathrm{x}_G\mathrm{e}_G + \mathrm{x}_{2D}\mathrm{e}_{2D}$, in terms of strain and doping as follows:

$$\vec{X} = \frac{x_G.p_{2D} - x_{2D}.p_G}{p_{2D}.s_G - s_{2D}.p_G}.e_\epsilon + \frac{x_{2D}.s_G - x_G.s_{2D}}{p_{2D}.s_G - s_{2D}.p_G}.e_n \tag{1.7}$$

Such a formalism, is very helpful in extracting strain and doping using Raman measurements of graphene [68]. We would be using this formalism in next chapters, in order to ensure the strain contribution to the thermal transport part. It can also be extended to another 2D material such as MoS_2, however, to our knowledge it can not be claimed to be a general formalism for all the family of 2D family. For instance in case of h-BN, due to existence of single Raman active mode, such formalism is not applicable.

1.4.2.3 1-laser Raman thermometry

1-laser Raman thermometry is a non-invasive spectroscopic method, used to estimate the thermal conductivity of 2D materials. Balandin group devised this methodology for the first time to estimate the thermal conductivity of single layer graphene [6]. This method was later used for different 2D materials such as TMDCs [69, 70, 51]. With Raman spectroscopy one can monitor all the vibrational modes of a 2D material and we can select one of the modes which responds to the heating. Since the temperature dependence causes phonon-phonon anharmonic interactions along with the lattice dynamics, the vibrational mode adds more information to thermal physics. This vibrational mode can be used as a thermometer mode and hence can be used to determine the thermal conductivity.

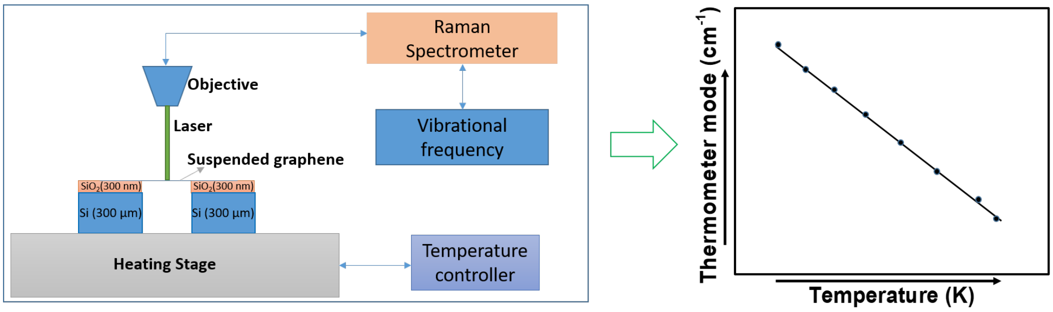

Figure 1.13: **Schematic of hotplate experiment**: (left) The schematics of hotplate experiment-the sample is placed directly on the heating stage which is connected with a temperature controller, this assembly is in the connection with Raman spectrometer, (right) A schematic of graph produced by such experiment, As the temperature is increased the thermometer mode shows a redshift.

The approach of Balandin involves two different experiments, one involving a heating stage (Fig 1.13) to heat the sample, while the other experiment uses the laser power to heat the sample (Fig 1.14). In both of these experiments, the thermometer mode is followed in order to monitor the heat. The data from two experiments are linearly fitted and then can be used to estimate the thermal conductivity according to the relation 1.8.

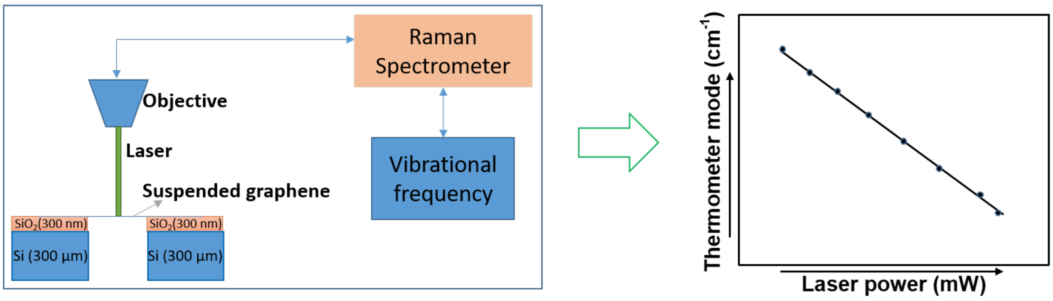

Figure 1.14: **Schematic of 1 laser Raman thermometry**: (left) The schematics of 1 laser stage and the connection with Raman spectrometer, here the heater laser is same as the probe laser, (right) A schematic of graph produced by such experiment, As the laser power is increased the thermometer mode shows a redshift.

Using a laser to excite the vibrational modes one can estimate the effect of heat absorbed by the system due to the coupling between optical and acoustic phonons. The slope obtained by plotting the vibrational frequency against the laser power (Fig 1.14) is key to estimate the thermal conductivity by the following relation.

$$\kappa = \frac{\chi}{2\pi h} \frac{\partial P_{laser}}{\partial \omega} \tag{1.8}$$

where χ is temperature coefficient obtained from the hotplate experiment (fig 1.13), h denotes the thickness of the material and P$_{laser}$, ω represents the laser power and the frequency of the thermometer mode, respectively. With this technique, Balandin *et al.* reported the thermal conductivity of mechanically exfoliated suspended graphene to be around 5000 W/m.K. The above mentioned relation is reduction of a uniform radial heat flow equation for two different powers [71]. It is crucial to mention that the radial heat flow equation used here assumes the Fourier diffusive thermal transport model.

Another important point to mention is that the relation 1.8 mentioned by Balandin *et al.* in their report of the model did not assume the P$_{laser}$ to be the absorbed laser power, which causes the wrong estimation of the thermal conductivity. To correct the relation we must insert the absorbance of the material w.r.t. to the used wavelength for collecting the Raman signal. This would modify the relation as:

$$\kappa = \frac{\chi}{2\pi h}\frac{\partial P_{abs}}{\partial \omega} \tag{1.9}$$

However, Ruoff *et al.* proposed another way of making optothermal Raman for extracting the thermal conductivity. They used two different spot sizes for heating lasers (experiment mention in figure 1.14). Using the radial heat flow equation, they extracted two parameters in order to calculate the thermal conductivity by applying the following relation:

$$\frac{\partial^2 \theta}{\partial z^2} + (\frac{1}{z})(\frac{\partial \theta}{\partial z}) - \theta = \frac{q''}{g}\exp^{\frac{z^2}{z_0{}^2}} \tag{1.10}$$

where q'' is the peak absorbed laser power per unit area, θ = (T-T$_{ambient}$) and z = (g/(κ_st))$^{1/2}$.r, with κ_s is thermal conductivity of graphene, r being the radial position and g represents the thermal interface conductance per unit area.

With the solution of differential equation 1.10, they deduce two parameters which can be found by using the observations of experiment shown in figure 1.14 and 1.13 [1]. This approach has advantage of using the absorbed laser power. Using such approach Ruoff *et al.* estimated the thermal conductivity to be around 2500 W/m.K [1]. This value is nearly half the value estimated by Balandin *et al.*. The discrepancy can be attributed to the fact that the model of Balandin *et al.* suffers a major set back of using the injected power whereas Ruoff's proposition eliminates this drawback.

Another approach was used by Faugeras *et al.*, where they used Corbino geometry of suspended graphene over a hole of 22 μm radius in 2mm thick copper plate [27]. They used Stokes and anti-Stokes intensity ratio of G band frequency to estimate the temperature of the graphene membrane. They used a blackbody like tungsten radiation source and a two-color pyrometer for calibration of estimation of temperature. The relation used is as follows:

$$\frac{I(\omega_{exc} - \omega_G)}{I(\omega_{exc} + \omega_G)} = exp^{\frac{\hbar\omega_G}{k_B T}} \tag{1.11}$$

where I(x) represents the intensity, k_B is the Boltzmann constant, $\hbar$ is reduced Planck's constant and T is the estimated temperature. Using the relation 1.11 they estimated the local temperature of the graphene while moving the laser spot across the center to the edge of the suspended graphene. They observed that it was easier to heat the membrane in the center than the edge, which was attributed to closeness of the heat sink. Using the heat diffusion equation they could estimate the thermal conductivity of graphene. They assumed a Gaussian profile of the laser spot in order to estimate the heat generated in the membrane as was done by Ruoff *et al.*.

Now a similar equation of heat transport (as equation 1.10) can be applied to the temperature profile created by using equation 1.11 (the profile is shown in figure 1.15) to estimate the thermal conductivity of the membrane.

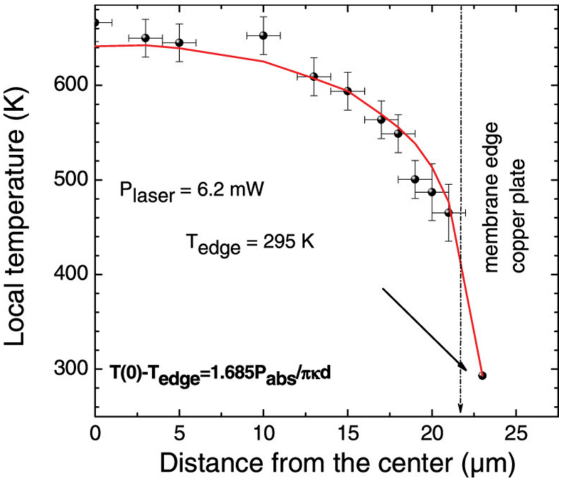

Figure 1.15: **Local temperature profile for suspended graphene in Corbino geometry** [27]: The temperature estimation was done using the ratio of Stokes and anti-Stokes intensities measured during Raman spectroscopy, such profiles can be utilized to estimate the thermal conductivity.

Using the profile presented in figure 1.15, a thermal conductivity value of 632 W/m.K was estimated. This estimation was nearly $(1/10)^{th}$ of the estimation done by Balandin *et al.*. Even though the smaller value of thermal conductivity was attributed to difference in optical absorption of graphene by Faugeras *et al.*, Ruoff *et al.* attributed it to the high laser power (6.2 mW) used for temperature estimation of the graphene membrane. They argued that the use of high laser power raises the temperature of graphene to 600 K, which lowers the thermal conductivity.

Despite such efforts, one major limitation in all the approaches is the fact that they assume a diffusive model of thermal transport, which is not experimentally justified. One must verify experimentally that the diffusive transport in suspended graphene is a good approximation, which cannot be done using this approach.

In this way of extracting thermal conductivity, we use the same laser to heat and probe the sample. In order to understand the thermal transport in a system, it is important to know the propagation of the heat, away from hotspot. To do so, we have to separate the heater and probe lasers, which can be achieved by using two different lasers. We would be discussing about the 2 laser Raman thermometry in following part of discussion.

1.4.2.4 2-laser Raman thermometry

The idea to monitor the heat propagation in suspended 2D materials was initiated by Reparaz *et al.* [7]. They investigate a novel technique with two lasers, using one of the lasers to heat the thin film of Si (250, 1000, 2000 nm thicknesses) and the other laser to probe the thermometer mode via Raman scattering. A schematic of the setup is shown in figure 1.16. The advantage in such a scheme is the freedom of making a Raman map by keeping the heater laser fixed with the sample while moving the probe laser to scan the sample. A schematic of Raman map is shown on the right hand side of the figure 1.16.

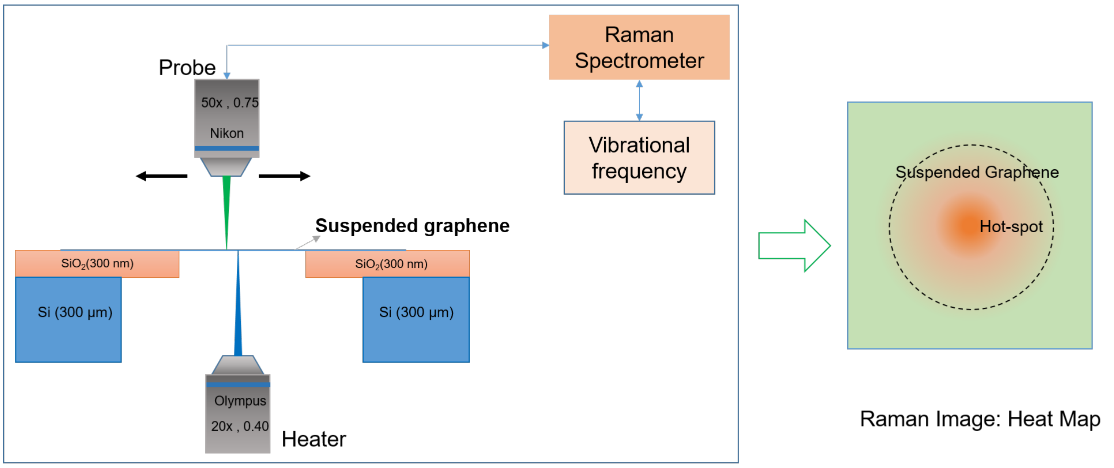

Figure 1.16: **Schematic of 2 laser Raman thermometry**: (left) The schematics of 2 laser stage and the connection with Raman spectrometer, here the heater laser is fixed with the sample stage and the probe laser is moved relative to the sample-heater assembly, (right) A typical thermal transport map generated out of such experimentation, where dotted line depicts the holes of the samples so that the inner side would be suspended graphene while outer part would represent supported graphene.

In case of Fourier's transport, the energy flux is directly proportional to the gradient of temperature:

$$\phi \propto \nabla T \tag{1.12}$$

where ϕ is the energy flux and T represents the temperature of the system. The proportionality constant for such relation gives the thermal conductivity of the material, which is shown in equation 1.1.

Solving the equation 1.1 for radially symmetric system, we can obtain

$$T = Aln(r) + B \tag{1.13}$$

where A and B are constants.

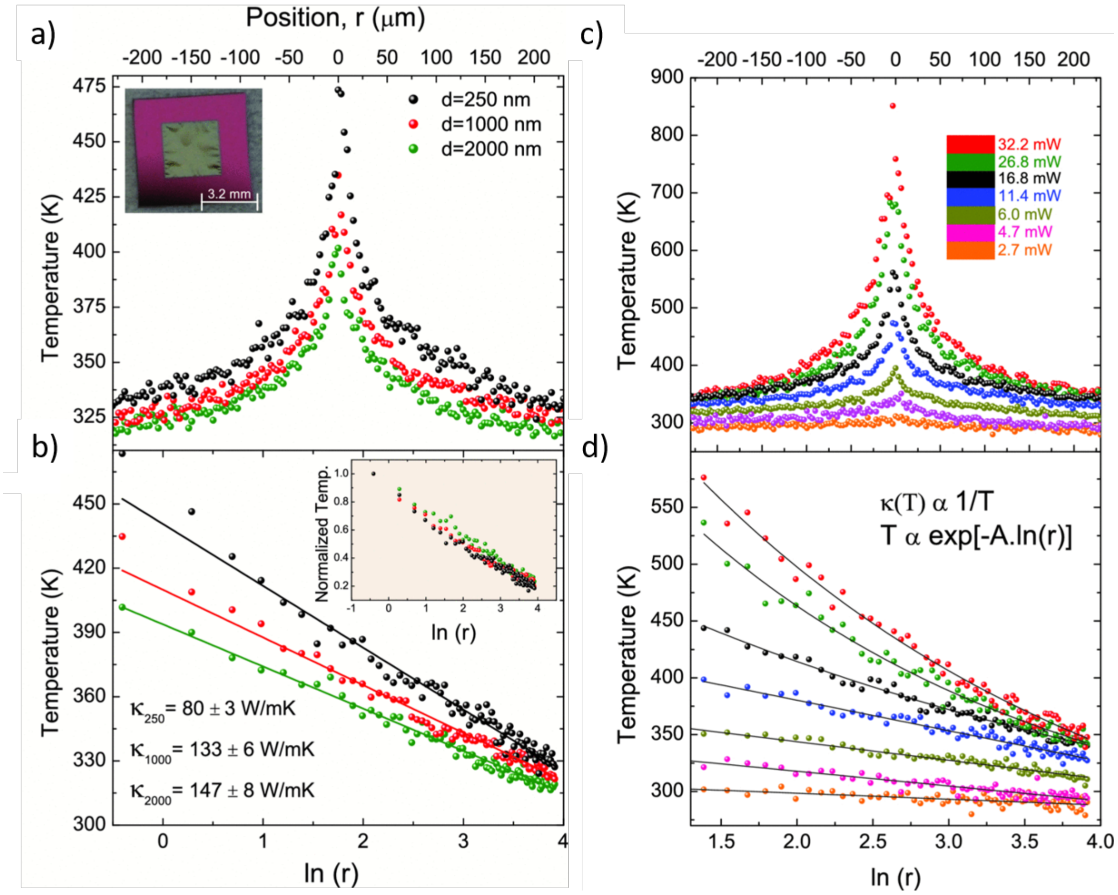

Figure 1.17: **Temperature profile of suspended thin film of Si** [7]: (a) Temperature profile against distance from the hotspot for three different thickness 250, 1000, 2000 nm (b) Temperature profile against ln(r) and linear fittings, it can be seen that for smaller temperature gradient the linear fit works well while for large gradient linear fitting is not justified (c) Temperature profile for 250 nm thin film of Si for different heating laser powers (shown in legend), as expected the peak temperature is raised with increase in the laser power (d) Temperature profile against ln(r) for 250 nm thin film Si measured at different powers, it can be easily observed that as the peak temperature is raised, the linear fit for ln(r) and T is not justified.

For a cylindrical symmetry the Fourier's law predicts that the temperature profile should be logarithmic in space (equation 1.13). Such temperature variation in space has been confirmed by the first reports using line profiles through the hotspot [7]. Reparaz *et al.* showed that using such a setup, one can estimate the thermal conductivity of a thin film [7]. Figure 1.17 show the main summary of their result. They present the temperature profile for different thickness of films in figure 1.17(a) and (b) part shows the log-linear plot between ln(r) with temperature. They show that for small temperature gradient the profile follows the logarithmic dependence, as depicted in figure 1.17(b), but for larger temperature gradients the logarithmic dependence is not followed. Figure 1.17(c) presents the temperature profile for different heating laser powers for a constant thickness of 250 nm thin film. Interestingly, they present that the thermal conductivity is seen to be inversely proportional to temperature since the temperature profile follows polynomial dependence with r (figure 1.17(d)).

Such observation for thin film membrane asserts the need to test the basic assumption of proportionality of gradient of temperature with current (equation 1.12).

Recently, the same group have used the same technique to estimate the thermal conductivity of $MoSe_2$ as well [72]. They monitor the temperature across the suspended membranes through the hotspot, which only gives information about the temperature flow across a selected region of the system. However, we will be using the same technique to monitor the temperature distribution throughout the suspended graphene, in order to be able to follow the thermal transport in two dimensions.

1 laser and 2 laser Raman thermometry: The main difference between the two techniques is that in case of 1LRT, we probe only the hotspot, however in case of 2LRT, we can probe on and away from the hotspot thus enabling the imaging of the thermal transport. 1LRT, owing to its setup, collects the information about the hotspot which cannot be employed to test the applicability of the Fourier's law. On the other hand, 2LRT can be employed to access the spatial thermal transport and thereby can be used to test the applicability of Fourier's law in low dimensional materials.

We would be discussing our results related to suspended graphene under the characterization of 2 laser Raman thermometry in chapter 5.

1.5 Conclusion

2D materials are interesting platforms for exploring fundamental thermal physics. Out of these, graphene has been predicted and estimated to have one of the highest thermal conductivity value. Owing to such high numbers, one can utilize graphene as heat sink in different applications particularly in electronic devices. Since thermal management has been a challenge in the field of reducing the size of different devices, such studies would definitely add to the existing technology. Different approaches have estimated different value of thermal conductivity of graphene. However, existing techniques suffer different drawbacks to estimate the thermal conductivity. We have discussed different techniques and their limitations, it is summarized in figure 1.18.

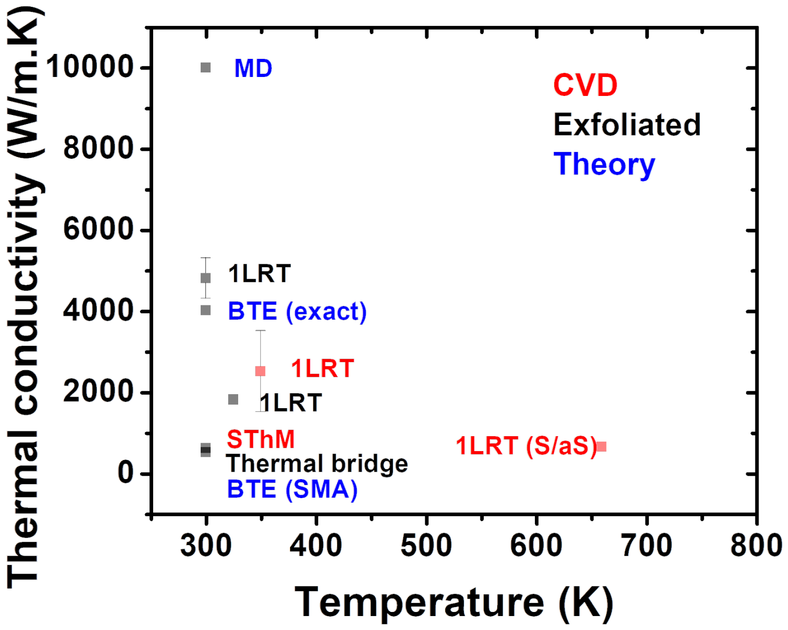

Figure 1.18: **Thermal conductivity estimation of graphene using different methods** [1, 3, 6, 27, 29, 35, 73]: Thermal conductivity estimation using theory and experiments.

Raman scattering is a powerful tool for characterizing 2D materials, despite the low scattering cross-section, due to small sample volume. Raman opto-thermal methods are particularly interesting owing to their non-contact methodology which can be exploited to measure different 2D materials to estimate their thermal properties. Despite the fact that they suffer from large error bars, they can be utilized to study the samples in most fundamental way of heating the samples optically and measure the heat response using optical phonons. Such a technique can be used to eliminate the presented shortcomings in the estimation of thermal conductivity along with testing the heat equation in low dimensions, which has not been tested yet.

Chapter 2

Suspending 2D materials

> We never experiment with just one electron or atom or (small) molecule. In thought experiments we sometimes assume that we do; this invariably entails ridiculous consequences.
>
> Erwin Schrödinger (1952) [74]

The wide range of possibilities for mechanical and electrical properties of graphene drew considerable attention of the scientific community. Mechanically exfoliated graphene sown the seed for this attention [39]. However, these graphene flakes have two major limitations. One is the limited area accessible for experimentation and the other is the need of a support, which affects the intrinsic properties of graphene due to strong substrate-graphene interaction. Regarding the first limitation, roughly four years after the first report of mechanical exfoliation of graphene, Yu *et al.* reported the foundations for growing graphene *via* chemical vapor deposition (CVD) [75]. This has solved the issue of scaling up the size of graphene flakes but yet has limitations such as poly crystalline growth (single crystal growth is still limited to few millimeters) [76]. Second issue was solved by suspending the graphene (which is limited to few 100 of microns) which proved the stability of 2D systems without any support [77, 78]. This started the seeking of intrinsic thermal, mechanical and electrical properties of 2D systems and their use in several applications.

As an ideal surface with no bulk, the properties of 2D materials on a substrate are always influenced by the properties of substrates. The influence can be understood by means of electron or phonon exchange which take place from the coupling. In order to study the intrinsic properties of 2D materials, we must decouple these effects. One way to achieve is, to suspend the 2D materials over holes.

In this chapter, we will focus on explaining the preparation of specially patterned substrates with see-through holes, and integrating 2D materials on such substrates with special emphasis on graphene. We will also describe the strain and doping effects in the resulting samples.

2.1 Substrate preparation

We aim to prepare the substrates with see-through holes for suspending different 2D materials, in a way that it is suited for optical spectroscopy and thermometry. In this section, we shall discuss the strategies and difficulties of the substrate preparation in detail.

2.1.1 Geometrical requirements for thermal study

The geometry of the hole in the substrates is a key factor for observing the thermal transport. If we heat the suspended sample in the center, the heat dissipation would be guided by the geometry of the suspended area. For example, a rectangular geometry would allow anisotropic transport,whereas for a circular case it would be isotropic. The first design used is a rectangular trench (as shown in figure 2.1). In such case, it is relatively easy to completely cover the trench with graphene (empirical observation). But due to the rectangular shape, the heat sink is not equidistant from the center of the hole, which is expected to add symmetry in the heat transport. Explaining such anisotropic systems would require complicated models. To simplify the approach, we then designed circular holes. In the circular case we can assume the thermal transport to be isotropic which will simplify the theoretical model as well.

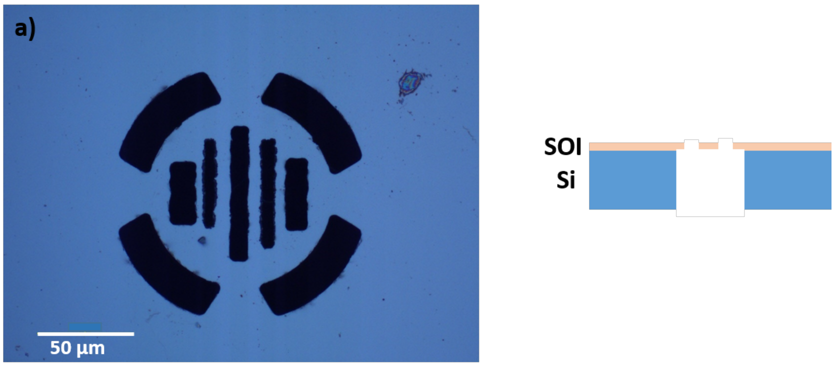

Figure 2.1: **The existing geometry of the rectangular trenches on a SOI membrane**: Optical image of see-through trenches on SOI/Si substrate (shown in schematic)

In order to process the substrates, we designed a pattern as shown in figure 2.2. This pattern consists of circular holes with 10, 15 and 20 μm diameters. As mentioned above the circular design would facilitate an isotropic heat propagation. The elliptical hole is kept for the purpose of direction.

Various range of radii can be incorporated in such design which is helpful to obtain samples with different area of suspension. Distance between each holes is kept in the range of 18-50 μm. Such a distance is adapted to keep the holes from collapsing in each other during fabrication. Another aspect to such range is to observe inter-hole heat transport which is beyond the scope of the present manuscript. Figure 2.2 shows the unit cell of our square lattice of 10x8 dimension

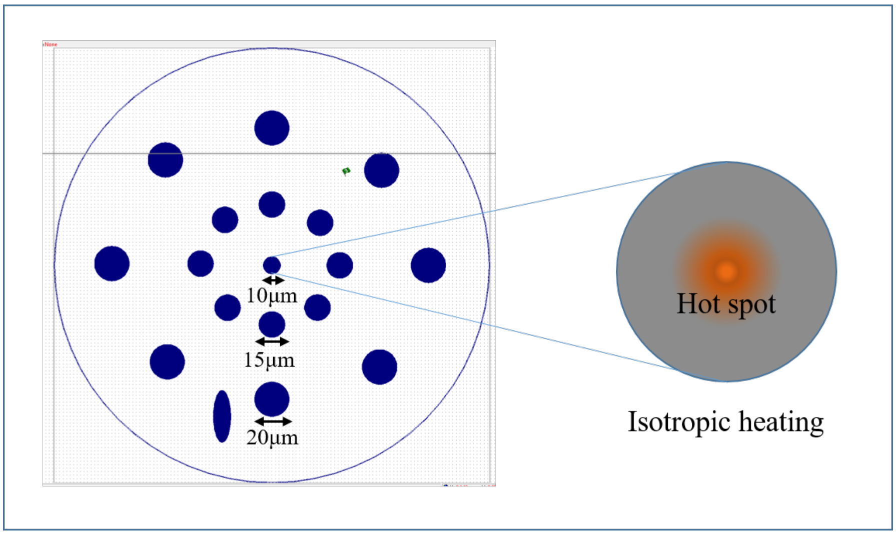

Figure 2.2: **Design of see-through holes**: New design for circular holes in snowflake geometry (left figure-typical representation of isotropic heating when hot-spot is kept at the center of the hole).

with a 300μm pitch. Such a distance would ensure the integrity of the substrate post fabrication and during sample handling. This kind of samples would be useful in observing the effect of the suspended area on the heat transport measurements.

2.1.2 Material requirement of the substrate

Material properties of the substrate for 2D materials play an important role in determining the resulting device efficiency. For example in case of need to isolate the 2D material electrically, we require an insulating substrate such as h-BN , SiO_2 etc. In case of thermal properties it is a real challenge to isolate the system completely from the substrate since the acoustic phonons in almost every materials lie in the energy range of 0-10 cm^{-1} (0-1.2 meV). Since our approach is to observe the thermal transport using the optical phonons, we need a substrate which does not interfere with Raman scattered signal.

To make a good thermal transport observation, we need a supporting substrate with heat sink property. Silicon nitride, silicon or metal coating are some of the available choices in such case to ensure an efficient thermal coupling with the 2D material. But the limitation with these supports for the current case is that they produce huge fluorescence during Raman measurements that dominate the signal and hides the optical phonon signature on the supported part of the sample. We require a material with which we can achieve good Raman signal along with sufficient heat sink property for thermal transport. SiO_2 has shown minimal interference with Raman signal for optical phonons of graphene. Even though the thermal conductivity of SiO_2 is known to be very small (1.3 W/m.K) with respect to predicted for graphene (in the order of 5000 W/m.K) and since we want to compare suspended graphene to the supported one,, it can work as heat sink in our case.

The rectangular trenches are made on bare Si substrates and some measurements can be made on such samples for comparison. We shall discuss about it in later chapters of the manuscript. We shall discuss the details of the fabrication process in the next section.

2.1.3 Fabrication of see-through holes

Fabrication of see-through holes in substrates involves several steps of nanofabrication, which involve laser lithography for top and bottom sides of the wafer, followed by reactive ion etching (RIE) or wet etching methods.

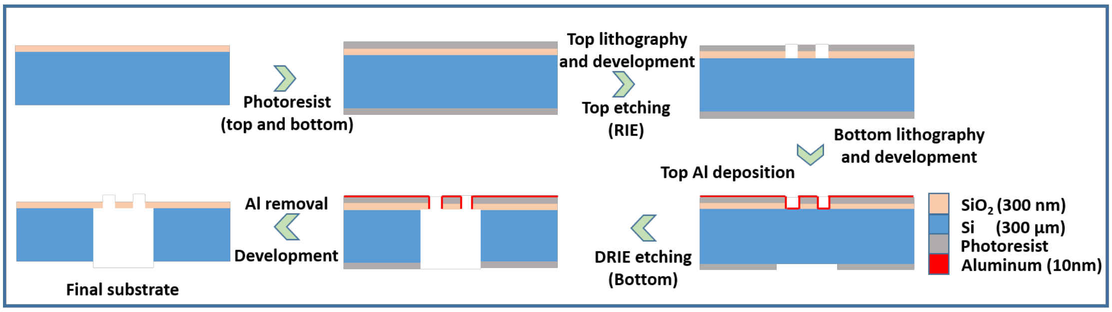

Figure 2.3: **See-through holes using DRIE (Deep Reactive Ion Etching)**: Schematic for creating see-through holes using dry etching.

As shown in figure 2.3, we start with a SiO_2/Si substrate with thickness of 285 nm SiO_2 and 250 μm silicon. Starting with top lithography via a positive photoresist to remove 285 nm SiO_2 from desired places as per the design, using RIE with SF_6 gas. Here, we lay the foundation of SiO_2 membranes (250 μm diameter) with circular holes. Next step is to do bottom lithography with proper alignment using positive photo-resist. Aluminium is used as a mask to protect the top surface from Fomblin oil used to glue the substrate in the DRIE machine. We deposit 10 nm aluminium on the top side for this process.

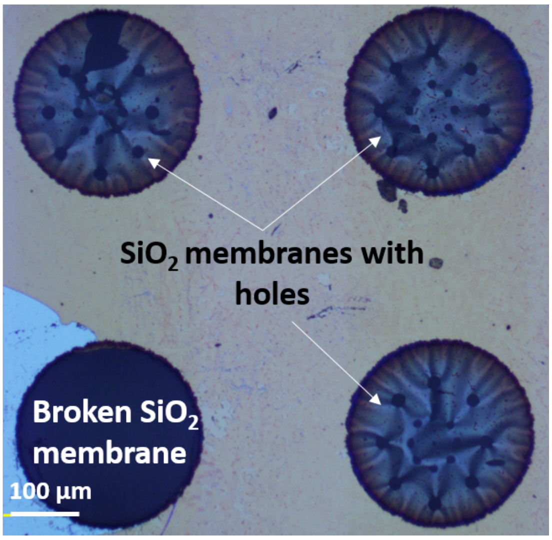

Figure 2.4: **Successful creation of SiO_2 membranes with see-through holes**: Fabrication fo see-through holes with suspended 285 nm SiO_2 membranes using DRIE processing. Wobbles are induced in the suspended SiO_2 membranes due to limited thickness.

After the final step of DRIE, we managed to successfully create the substrates with desired geometry as shown in figure 2.4. It is important to mention here that handling of 285 nm thin SiO_2 membranes in our substrates is delicate, which can easily result in broken membranes as shown in figure 2.4 (special care has to be taken while blow drying the substrates after any kind of liquid treatment during fabrication). We will now discuss some challenges and solutions of the fabrication process of the substrates.

2.1.3.1 Some challenges and solutions

We observe that a diameter of 250 μm of SiO_2 membranes (and thickness being 285 nm) shows non flat membranes (see figure 2.4), which in turn changes optical the focus for different regions of the membranes. As shown in figure 2.5, different focus would be an issue for mapping the surface for a constant height (as is the case for our Raman spectrometer).

Substrates resulting from using dry etching show strange impurity spots on the suspended SiO_2 membranes (see figure 2.5). Additionally we observe huge background during Raman measurements (figure 2.6). We speculate that these strange spots could be responsible for such background. We have tried to etch these spots using HF etching, but we could not remove them.

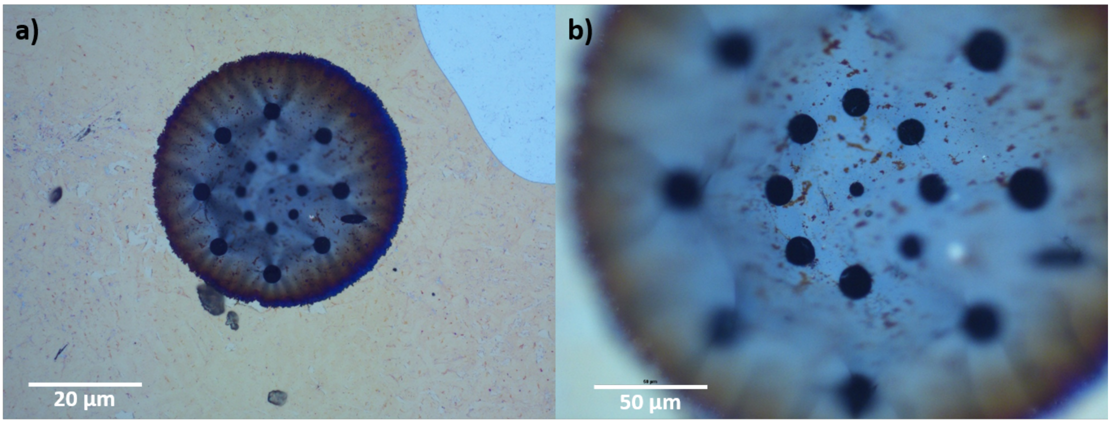

Figure 2.5: **Optical focusing of strained SiO_2 membranes**: Different optical focal plane for different regions of suspended SiO_2 membrane. (a) 20x magnification with 0.4 NA (Numerical Aperture), (b) 50x magnification with 0.75 NA.

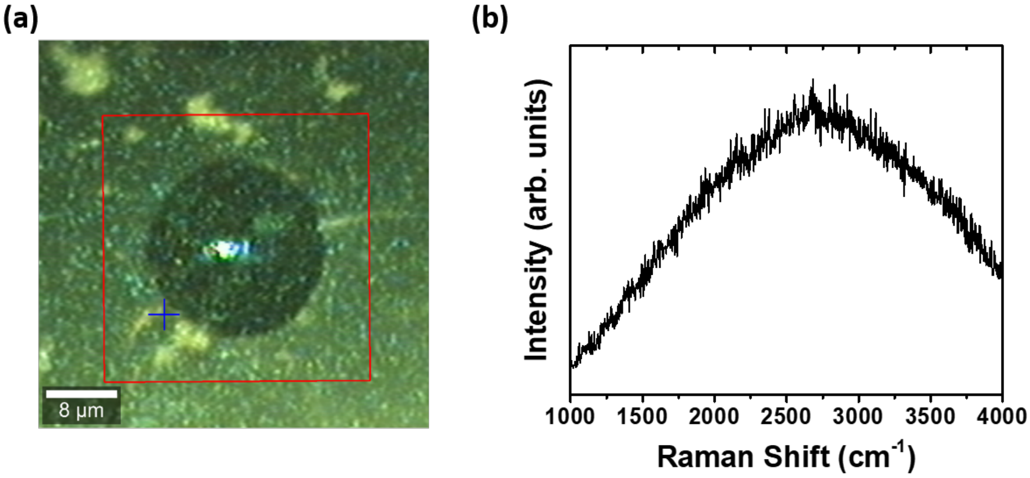

Figure 2.6: **Impurity of the SiO_2 membrane**: Unusual background from SiO_2 membranes in Raman measurements- (a) Optical image (blue cross shows the location of Raman spectrum collected) and (b) Raman spectrum.

However, we speculate that the thermal glue (Fomblin oil) used to perform the DRIE could cause these impurities which means perhaps 10 nm Al layer is not sufficient for the protection. We have tried to remove the glue by using different chemicals with no success. Finally, this issue has been solved by replacing Fomblin oil with crystal bond which is far easier to clean with acetone. We have created clean samples with 50 μm thick silicon with 285 nm SiO_2 using the DRIE process, as shown in figure 2.7. Processing such thin wafers also solved the issue related to strain in the silica membranes. However in this case, the sample is opaque which prevents backside heating with a laser on the supported part of graphene.

In order to totally avoid the glue, we can also use a wet etching process to realize the see-through holes. Schematic for wet etching process is presented in figure 2.8. In this process, we start with both-sides-polished-SiO_2, since silica from the wafer is the only etch mask that can resist to TMAH (Tetra-methylammonium

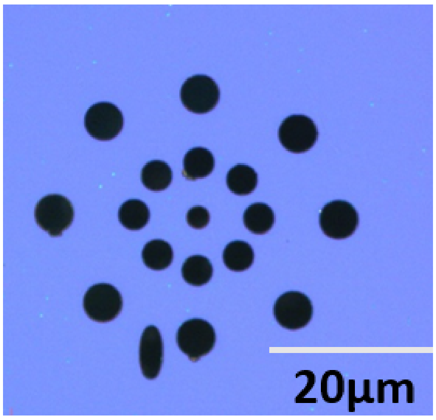

Figure 2.7: **Success with clean substrates**: Clean samples with 285 nm SiO_2/50 μm Si, using crystal bond instead of Fomblin oil

hydroxide). We start with top lithography as in case of dry etching, after etching the top SiO_2 from desired locations we perform the bottom lithography and develop the pattern. Here, we incorporate RIE to etch the backside SiO_2 mask as well.

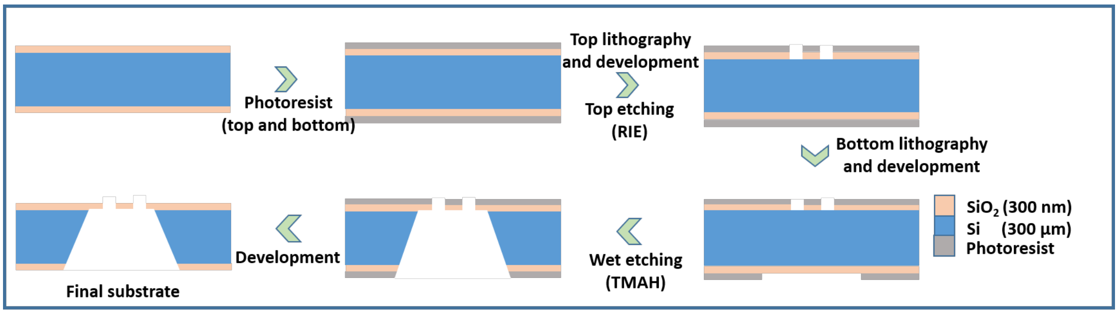

Figure 2.8: **Drilling of holes using wet etching**: Schematics for creating see-through holes using wet etching.

We use TMAH (Tetramethylammonium hydroxide) for etching the silicon. Since, wet etching is preferential in certain direction of crystal structure, we use larger diameter of the bottom lithography to take this into account. TMAH is known to etch silicon, in the direction of 111 plane. It results in 57^o degree to the plane of our substrate. Such a calculation results in the bottom radius value to be tan(57)= 0.48 of the top radius value. However the 285 nm SiO_2 is not thick enough to protect the desired silicon location from getting etched. To solve the issue, we replaced the initial substrate by 2μm thick polished SiO_2 on both sides. This process indeed results in greatly clean substrates, as shown in figure 2.9.

We shall discuss some of the difficulties during these processes. A significantly rigorous step is to align the top and bottom lithography perfectly. In several attempts to fabricate the substrates we encountered misalignment issues from the laser lithography setup, one such example is shown in figure 2.10 (figure corresponds to substrates resulting from DRIE method, however the issue would exist for wet etching method as well). The issue was with the reflection symmetry not

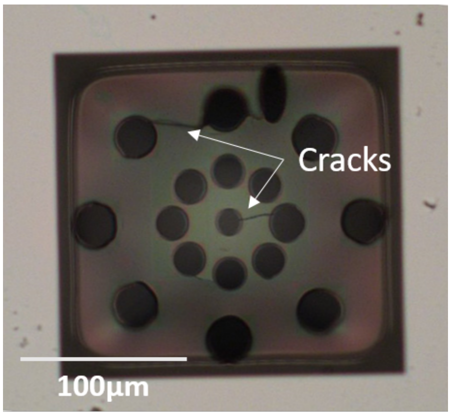

Figure 2.9: **Substrates from wet etching**: 2μm thick SiO_2/Si substrate by wet etching. The square pattern arises due to wet etching of silicon. Processing may induce some cracks in the SiO_2 membrane, as shown.

incorporated in the machine. Since we could realize the misalignment only at the final step, the process becomes very time consuming. This issue was solved using the reflection of the bottom lithography.

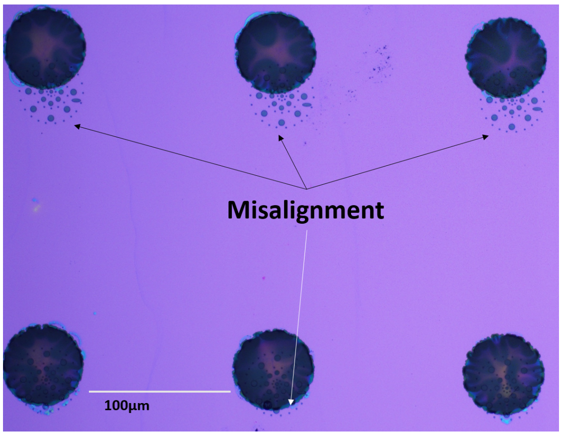

Figure 2.10: **Misalignment issue**: Misalignment of top and bottom lithography after DRIE process.

A particular issue of the wet etching process is the etch rate for TMAH. The observation of initial etch rate for TMAH was found to be 42 μm per hour, which showed rapid increase in the rate (due to reasons we don't understand) due to which the 300 μm substrates were completely dissolved in the TMAH solution within 7 hours. In other samples we monitored the etch rate to be 40 μm per hour which changed after taking out the substrate from the solution in 1 hour interval. We optimized the purity of solution and optimized the etch rate to be 22 μm per hour and substrate with cleaner membranes (figure 2.9). Despite, the clean surfaces, we observe cracks in the SiO_2 membranes, which are yet to be solved as a future prospect.

As discussed above, we can conclude that clean substrates with see-through holes can be created using DRIE, while employing crystal bond for sticking the wafer. Once we have the substrates with desired patterns of holes, we shall discuss the creation of monolayer of 2D materials and thereon their integration onto our substrates. We will dedicate next section for isolation of monolayers of 2D materials (or creation *via* chemical methods).

2.2 Graphene and 2D materials

There can be mainly two ways to create 2D materials. As discussed in the first chapter, primary approach to create monolayer 2D material is to mechanically exfoliate a bulk crystal. We can however, chemically grow some 2D materials with chemical vapour deposition (CVD). The advantage of mechanical exfoliation is the high quality monocrystal samples whereas for the chemically grown samples, we can increase the size of the samples even for the mono-crystals. We will discuss these two approaches in short details in the forthcoming sections.

2.2.1 Mechanical exfoliation of 2D materials

Mechanical exfoliation is the genuine way to create monolayers from the bulk of a layered material, as was first realized by Novoselov *et al.* [39]. Despite the limited size (few 10 s of μm) of sample flake created using the mechanical exfoliation, exfoliated samples show better electronic properties. In the present manuscript, we use different substrates such as fused silica (spectrosil2000), sapphire, thin silica, SiO_2/Si (300 nm/300 μm), PDMS (Polydimethylsiloxane) and glass for exfoliation.

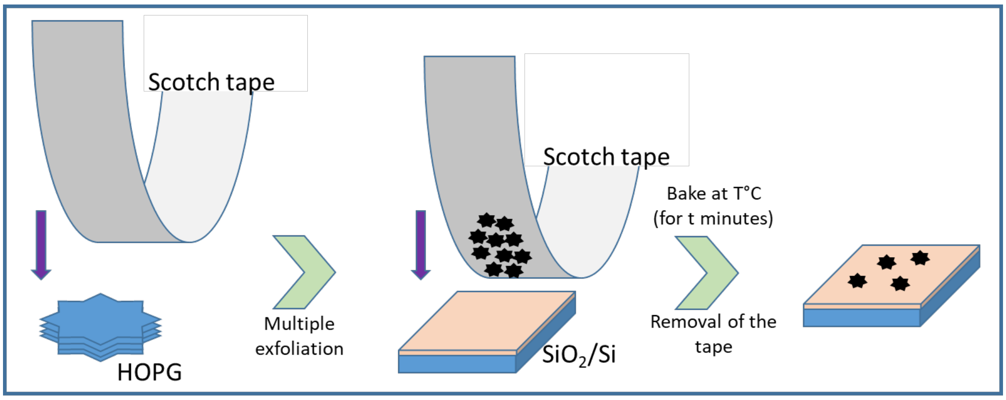

Figure 2.11: **Mechanical exfoliation**: Schematics of exfoliation process (Highly ordered pyrolytic graphite (HOPG) is bulk graphite).

Figure 2.11 shows the schematics of typical exfoliation process. We begin by exfoliating a small chunk of pyrolytic graphite (obtained from *HQ graphene*) on a *3M magic* scotch tape. To prepare the substrate, we start with sonication in acetone for 2 minutes followed by a 10 s oxygen plasma (20 W power), to clean the inorganic and organic impurities respectively. We further exfoliate the chunk until we completely cover the scotch tape by thinner flakes of graphite. Then, we land the scotch tape on the desired substrate and bake the assembly at 38 ^{o}C for the case of graphene. Such temperature would vary with choice of substrate (and

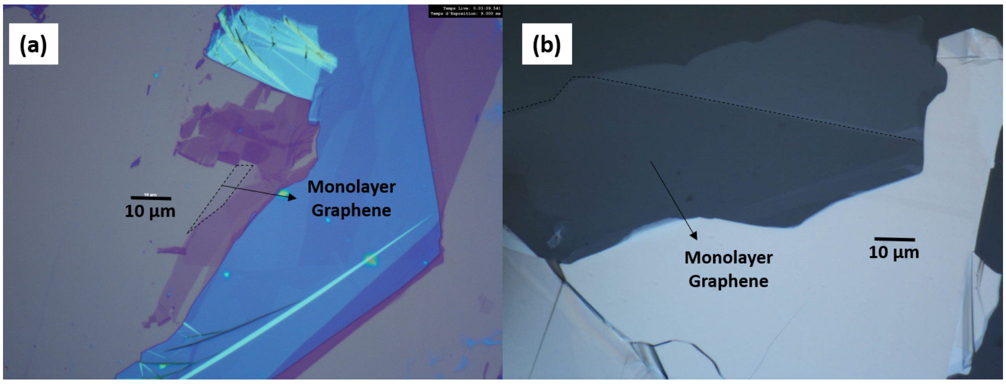

Figure 2.12: **Mechanical exfoliation of graphene**: Exfoliated graphene on (a) SiO_2(300 nm)/Si(300 μm) and (b) thin film SiO_2(200 μm).

other 2D materials), for example while exfoliating on PDMS the additional baking is not needed. The baking time for the case of graphene is nearly 5 minutes, which is followed by removing the scotch tape. This way, we land several flakes on the substrate along with some monolayers. The monolayers can be identified from their color contrast under optical microscope.

The process discussed earlier results in exfoliated graphene on different substrates, as shown in figure 2.12. It is worth noting that a 200 μm SiO_2 baked at 50 ^{o}C results in much larger flakes of monolayer graphene than 300 nm SiO_2/300 μm Si baked at 38 ^{o}C. Even though, we cannot conclusively refer to the reason but it seems only logical that the temperature plays a crucial role for mechanical exfoliation. Same approach can be invoked to be used for exfoliation on PDMS (to be used for dry transfer), sapphire and glass as well.

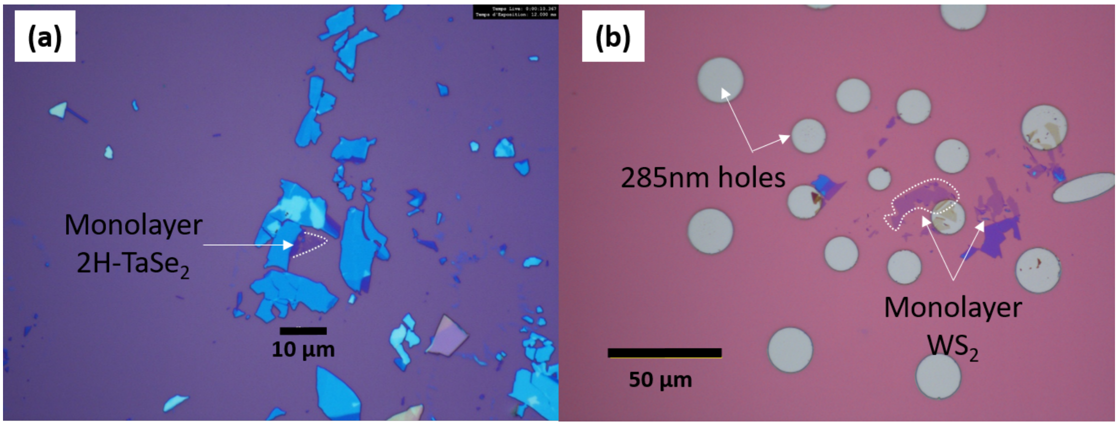

Figure 2.13: **Mechanically exfoliated samples**: Exfoliated monolayer on SiO_2/Si substrate (a) 2H-$TaSe_2$ and (b) WS_2.

We can use the similar protocol for exfoliating TMDCs such as $MoSe_2$, WS_2, WSe_2, 2H-$TaSe_2$ etc. It is crucial to mention that for 2H-$TaSe_2$, a baking at 45 ^{o}C for 5 minutes yields better and larger flakes, whereas for WS_2 the baking is done at 30 ^{o}C for 3 minutes. After the exfoliation, we anneal the samples up to 300 ^{o}C for 6-8 hours in Ar atmosphere of glove box with 1 atm pressure.

As mentioned earlier, despite a clean sample resulting from mechanical exfoliation, such approach suffers a disadvantage of scaling up the sample size, which can be achieved by CVD method. We will discuss the CVD growth of samples in next section.

2.2.2 CVD growth of 2D materials

Large scale production of 2D materials is a necessity for using them at the industrial scale. Chemical vapor deposition turned out to be the answer for such a question. Yu *et al.* and Alfonso *et al.* presented the first reports on the direction of segregating graphene on an insulator and nickel surface[75, 79]. Such an approach was later modified by Arco *et al.* in the following year to synthesize mono-,bi- and few layer graphene and tested field effect transistor devices made out of them [80]. Since then there have been several approaches to create large mono-crystals of graphene [81]. This is an interesting approach which has even been exploited for other TMDC 2D materials such as MoS_2. We will not elaborate on this method in greater detail due to the scope of the manuscript. However the reader can be suggested to read a rather detailed review on the same topic [82].

2.3 Transferring 2D materials on desired substrates

2.3.1 Stamping of exfoliated 2D materials

Stamping (also referred to as dry transfer) the 2D materials on a desired substrate allows to create hetero-structures of 2D materials and the sample can be deposited on a desired location of a substrate [41, 83]. Above all, this section is specially important for creating suspended samples of exfoliated 2D materials. Core idea of the scheme is to exfoliate 2D material on a polymer (PDMS in this case), and then stamp the monolayer on desired location of the substrate. We can divide the whole procedure in 4 steps: 1) exfoliation on a polymer, 2) locating the monolayer (or desired number of layers) *via* optical microscope, 3) aligning the monolayer and desired location of substrate and 4) dropping the monolayer from the polymer on to the substrate (figure 2.14).

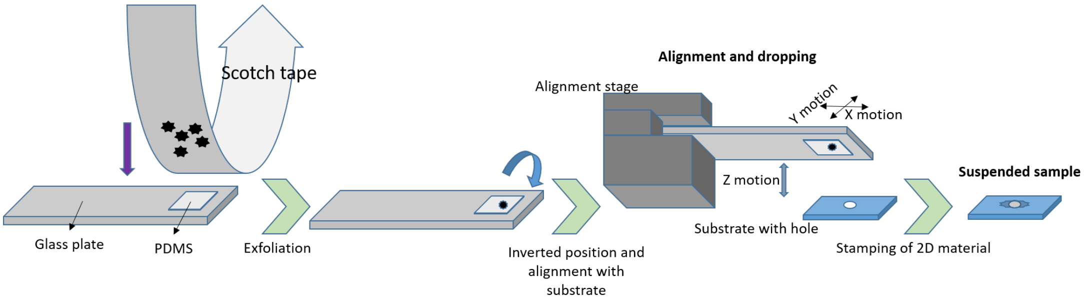

Figure 2.14: **Schematics of stamping**: Typical schematic for stamping of 2D materials.

We attempted several times to stamp exfoliated graphene onto different substrates with holes such as silicon and SiO_2. As a step of standard process we must remove the polymer (third step) after the stamping: the detaching, should be slow (0.2 μm per minute), in order to not exert additional force which might break the graphene flake. Despite several attempts, we did not succeed in suspending exfoliated graphene. However, we notice that there are three important parameters such as force of adhesion with substrate, hole size and area of exfoliated graphene, which play crucial role during the stamping process. In order to achieve the suspended samples (over see-through holes) for exfoliated graphene we need to consider adhesive force for substrate region, which must compensate for the suspended region, where there is no adhesion. The see-through hole has a cylindrical hollow region of 300 μm depth with radius in 10s μm. Adhesion force ($F_{adhesion}$) from the polymer makes it difficult to release the 2D material depending on the substrate used [84]. For instance, we empirically found that for the case of silicon, it is difficult to suspend graphene than on SiO_2 substrate.

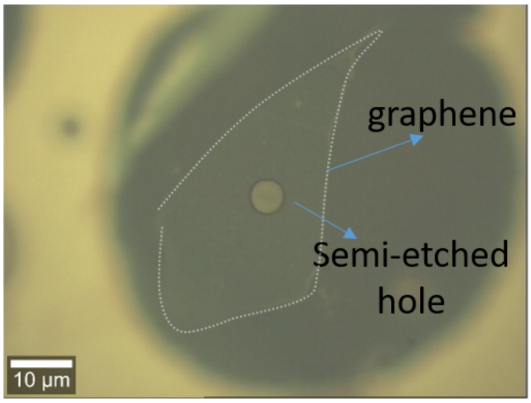

Figure 2.15: **Suspended graphene**: Suspended exfoliated graphene over semi-etched hole. Dotted line shows the region of monolayer graphene. Dark region correspond to the SiO_2 membrane.

To compensate for the $F_{adhesion}$ from the polymer, we need a large area of exfoliated membrane with respect to the hole size (roughly 4 times the area of the hole). However, if the exfoliated flake is larger than 500 μm^2, the flake is seen to break easily during the polymer lift off. Despite many unsuccessful attempt in suspending graphene, we managed to suspend a graphene over a hole of radius 2.5 μm, but the hole was not entirely see-through (semi etched hole) as shown in figure 2.15.

As it can be seen from figure 2.15, the area of exfoliated graphene (500 μm^2) is almost 25 times larger than the area of hole (20 μm^2), such dimensions compensate for $F_{adhesion}$. However, suspension for see through hole was not managed.

An alternative approach is to use the hBN as adhesive substrate for graphene. Since thin films are relatively easier to stamp onto a substrate and graphene can be easily stamped on hBN. We at first stamp a thin (80 nm) film of hBN on a large trench as shown in figure 2.16, and then using FIB (focused ion beam) we can selectively remove disc out from the suspended hBN. Such a hole can later be used to suspend graphene, since hBN and graphene show better adhesion than

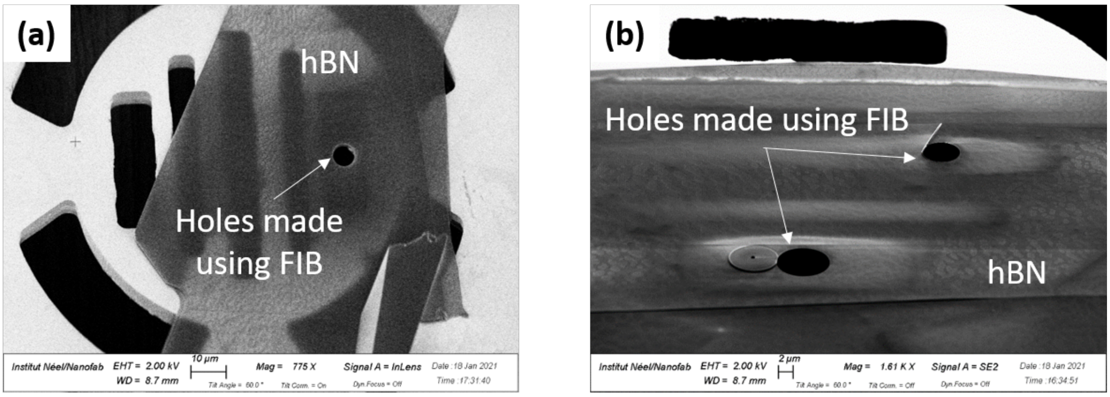

Figure 2.16: **hBN thin film with FIB hole**: hBN thin film suspended over a trench. FIB has been used to drill a see through hole in hBN. This hBN with hole can be used to suspend graphene.

SiO_2. Such an approach can be exploited further in future since the complete transfer was not managed due to lack of time. The obvious disadvantage is the time consumed to create a single hole. As mentioned before that despite the cleaner graphene samples produced by exfoliation, it is difficult to create large area suspended samples. However, we can transfer CVD grown graphene in order to create large area suspended samples. Moreover, using transfer of CVD grown graphene, we can create many suspended samples unlike the exfoliated case where individual flakes are dealt separately. We will now discuss CVD grown graphene transfer in following sections.

2.3.2 Transfer of CVD grown graphene on substrates with holes

Figure 2.17 shows a schematics of steps involved in the standard process for wet transfer of CVD grown graphene on copper films [85]. We begin by spin coating (6000rpm for 2 minutes) a thin polymer (PMMA (polymethyl methacrylate), 50kDa), which adds a layer of nearly 10 nm thickness followed by 3 minutes of heating at 180 ^{o}C, which allows the polymerization of the PMMA. Next step involves spin coating of thick PMMA (950kDa), with same annealing treatment. This process results in 150 nm thick polymer support layer for graphene. O_2 plasma at 20W is performed on the bottom side of the copper foil for 20 seconds, in order to remove the undesired graphene, which acts as a barrier to the copper etching by the ammonium persulphate. The choice of etchant plays a crucial role for the quality of transferred graphene. We have used an ammonium persulphate solution with a concentration of 0.1 g/mL, as optimized by earlier PhD from the lab [86, 68, 87]. The etching can be confirmed by observing the eye based transparency of the graphene/polymer film. We can remove carefully the floating graphene/polymer film from the etching solution and wash it with 8-10 DI water baths in order to get rid of the ions from the acid. At the final DI water bath we can collect the film by placing the patterned substrate below it and lift it up.

The substrate with the graphene/polymer film is left in ambient conditions

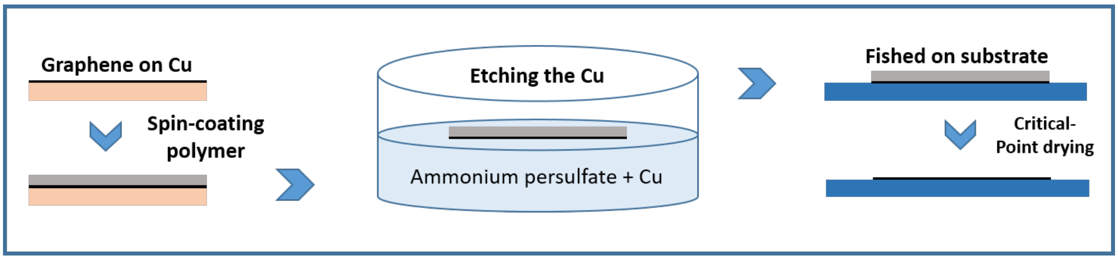

Figure 2.17: **Wet transfer**: Schematics of CVD grown graphene transfer on desired substrate.

for 10-12 hours for letting it dry. In order to ensure maximum removal of water residues, the substrate is heated at 120 °C for 10 minutes. This also allows PMMA to soften and therefore relax some built-in strain. It is then dipped in acetone bath for 2-3 hours, to remove the polymer film. Removal of polymer can also be done in different ways, affecting the quality and yield of the suspended samples, we will discuss them in coming paragraphs. Later on, the substrate is switched to IPA (Isopropyl alcohol) bath. Now a critical step is to dry the sample from the IPA solution. Due to surface tension of IPA, drying the sample in air leads to poor yield of suspended samples (close to 0 %).

2.3.2.1 Drying graphene

In order to dry the sample, we would use supercritical point drying using CO_2 as the media. Figure 2.18 shows the phase diagram of CO_2, which is exploited for the drying process.

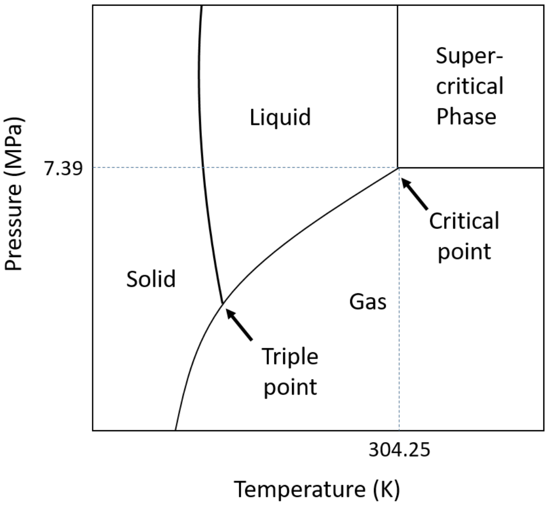

Figure 2.18: **Schematic of CO_2 phase diagram**: Phase diagram of CO_2, on which the critical point drying machine based on.

Supercritical point drying avoids a direct liquid/vapour interface which is a frequent cause of graphene device rupturing due to surface tension and capillary forces. At the critical point of CO_2 (7.39 MPa,304.25 K), it has zero surface tension which can be used to dry the sample of the solvent without rupturing the suspended graphene. We use Tousimis-autosamdri series critical point dryer to achieve the process of critical point drying. The machine is semi-automated, first it lowers the temperature to -5^{o}C and then purges the CO_2 in the system which gradually increases the pressure to enter the liquid phase of CO_2 which replaces the IPA. Since liquid IPA is sufficiently miscible with liquid CO_2, it does not create an issue of difference in capillary forces. Once the pressure is high enough (12-13 MPa), it increases the temperature to reach the critical point. At the critical point the pressure is reduced to enter the vapor phase. The system can now be brought to ambient thermodynamic conditions.

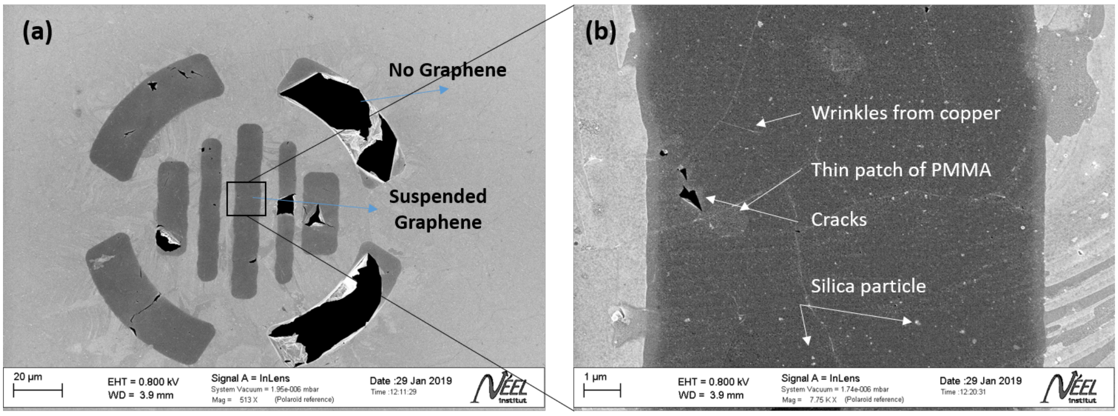

Figure 2.19: **SEM (Scanning electron microscope) image of the suspended graphene by standard transfer process**: (a) 513x and (b) Black rectangle shown in (a) with 7.75kx zoom. Several cracks, silica particles and thin patches of PMMA are visible in (b).

Now, we have successfully created suspended samples. These samples show good quality of SEM images only up to a certain zoom. As shown in figure 2.19, when we further increase the zoom to 7.75k, we observe features such as silica particles, cracks and wrinkles etc. We observe tiny residues of PMMA remnants as well. Since the thermal measurements are highly sensitive to any impurities, it requires an investigation for cleaning the suspended graphene. To do so we shall split the steps mentioned in 2.17 in order to find the source of these impurities, which will be discussed in next subsection.

2.3.3 Optimization for cleanliness of transferred graphene

This manuscript is not the first one to address the cleaning of the graphene [88, 89, 90]. In order to improve the transfer process, we split the process in three major parts, which will be considered one after other while keeping rest of the processes same. The first step of monitoring is the polymer coating on as grown graphene on copper. We will discuss these steps in the reverse order of the schematic presented in figure 2.17, in order to follow a bottom up flow. Firstly we can avoid critical point drying since we had observed impurities resulting from the CO_2 bottle. Second, we can try to replace acetone by other etchant of PMMA in order to efficiently remove the PMMA remnant. Thirdly, we can change the old ammonium persulphate to new batch in order to ensure that aging has not added impurities, which is resulting on the final sample. Another step is that we can change the polymer itself, in order to avoid the tiny remnants of PMMA, this step can be observed as avoidance of PMMA and graphene interface, but since using PDMS did not result in fruitful yield, we would not discuss this step. Alternatively, metals can be used as interface layer between graphene and PMMA, in order to avoid the direct contact of the polymer. We will discuss these processes along with the strain and doping induced by them.

2.3.3.1 1. Avoiding critical point drying step

To achieve the first monitoring step, we have tried :1) to dry the graphene in air after the acetone step , 2) to remove PMMA by heating the sample in ultra high vacuum (10^{-8} bar) at higher temperatures (300-400 ^{o}C) (such approach becomes more useful with H_2/Ar (forming gas) flow, but due to our access limitation we have restrained to ultra high vacuum) [91]. However, annealing can be done in several ways, It was realized that 250 ^{o}C or more can remove the PMMA coated on graphene [92]. In order to achieve this, we annealed our samples in 3 different ways: 1) annealing at 400^{o}C for 8 hours, 2) making temperature steps (annealing at 300 ^{o}C followed by 400 ^{o}C followed by 200 ^{o}C for 6 hours, 4 hours and 2 hours respectively) , 3) annealing at lower temperature (350 ^{o}C for 24 hours).

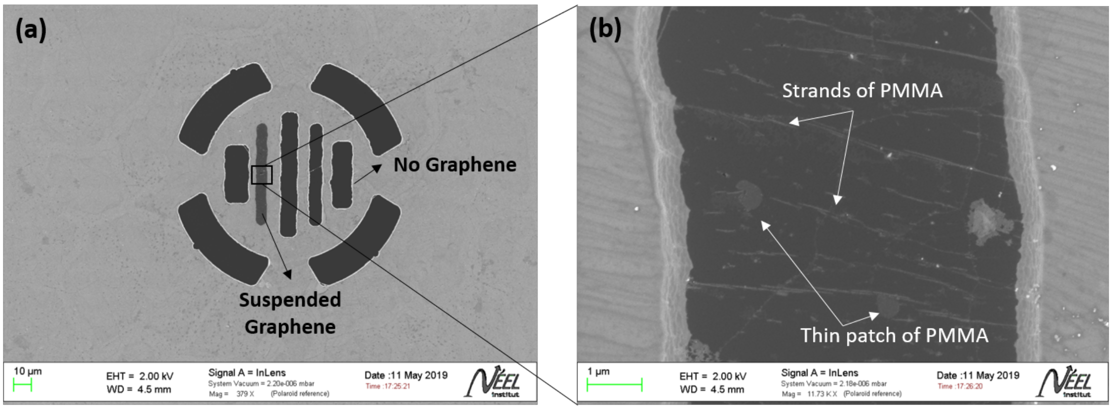

Figure 2.20: **Sample annealed at 400^{o}C**: (a) SEM image of the suspended graphene 379x and (b) Black rectangle shown in (a) with 11.73kx zoom.

Case 1- Annealing samples at 400 ^{o}C resulted in few suspended samples (for example 5-10 suspended holes out of 750) which was better than drying the graphene in air (0-2 suspended holes). Figure 2.20 shows the typical SEM image of suspended graphene resulted by this process. The figure 2.20(a) shows good suspension but the zoomed image still shows remnants of PMMA. However, the density of PMMA residues were relatively lower than that of observed in the earlier case.

Case 2- The need for high temperature to remove the PMMA layer has a disadvantage of providing the graphene a thermal shock. In order to avoid the extent of thermal shock, we used one step of temperature for the rise and the drop. This would however, impact the removal kinetics of PMMA, which is why

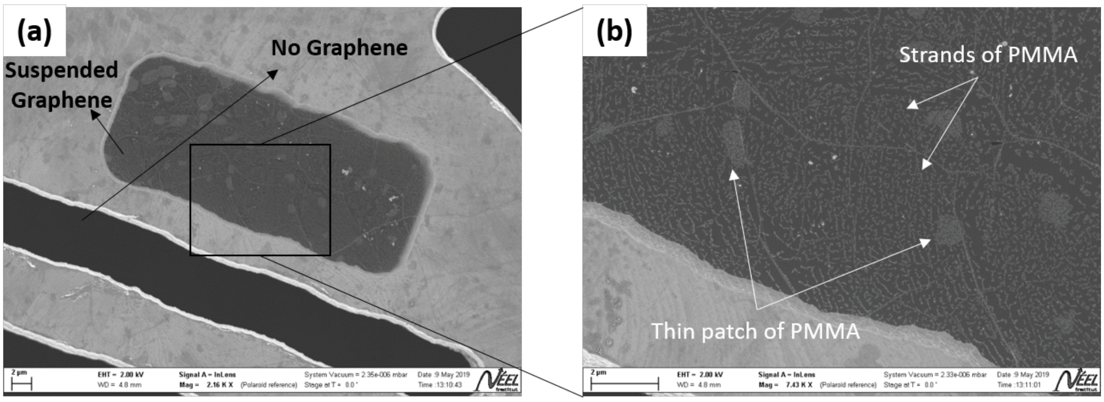

Figure 2.21: **Sample annealed in the steps of 300°C - 400°C - 200°C** (a) SEM image of the suspended graphene 2.16kx and (b) Black rectangle shown in (a) with 7.43kx zoom. Tiny residues of PMMA along with thin patches are visible.

we increased the overall duration. Figure 2.21 presents similar SEM image of the samples resulting from this process. Another empirical observation is that, if we increase the time of annealing the yield of suspended graphene is greatly impacted. A speculation is that keeping the sample at high temperature for longer times facilitates the possibility of the cracks to open up through the defective junctions of graphene.

Comparing the zoomed image of figure 2.20 and figure 2.21 we can infer that the density and pattern of remnant PMMA changes with different thermal treatment. One interesting observation is that PMMA patches are created at regular intervals.

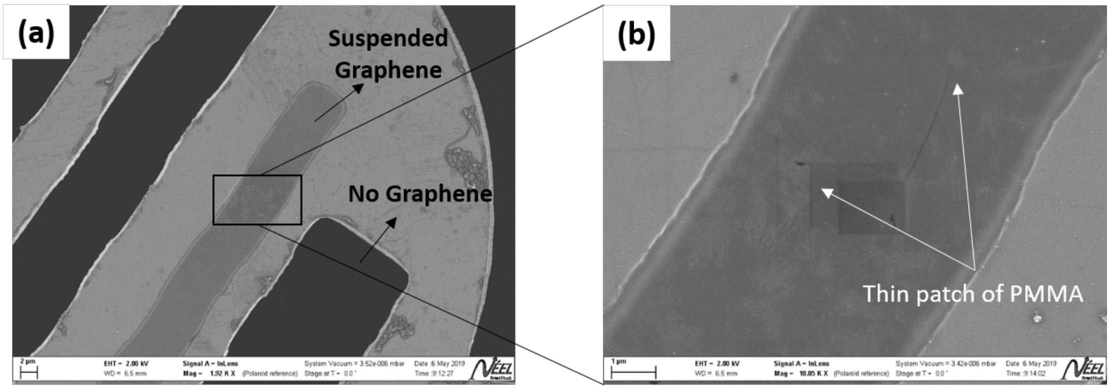

Figure 2.22: **Sample annealed at 350°C**: (a) SEM image of the suspended graphene 1.92kx and (b) Black rectangle shown in (a) with 10.05kx zoom. Thin patches of PMMA are visible in zoom.

Case 3- Another approach to remove the coating of PMMA is to reduce the extent of thermal shock and anneal the sample for longer time. This approach can be achieved by heating the sample at 350 °C for 24 hrs (figure 2.22). Even though we reduce the density of PMMA residues compared to earlier approaches, the size of remnant PMMA droplets is much higher in comparison to case 1 and 2.

To list out some empirical details, we create a table as follows:

Table 2.1: **Empirical parameters from annealing processes**

	Density of PMMA in a constant area	Yield (/750 trenches)
400 ^{o} C	5 (long residues of the length 1- 1.5 μm)	0-5
350 ^{o} C	30-40 (200-400 nm)	2-5
300-400-200 ^{o} C	40+ (50-100 nm)	5-10

As shown in the three different cases, we observe that annealing temperatures play a very crucial role in the kinetics of PMMA removal. A constant temperature and longer annealing times reduces the density of PMMA greatly but creates several big patches of PMMA, where as higher temperature reduces the individual patch volume to tiny residues of PMMA but the density of such residues is very high. With the observation of three different annealing approaches, we can conclude that to remove the final remnants of PMMA we may need to anneal the samples at higher temperatures thereby compromising on the yield of suspended graphene. Another alternative could be to use a forming gas flow during the annealing which can help the kinetics of PMMA removal [91].

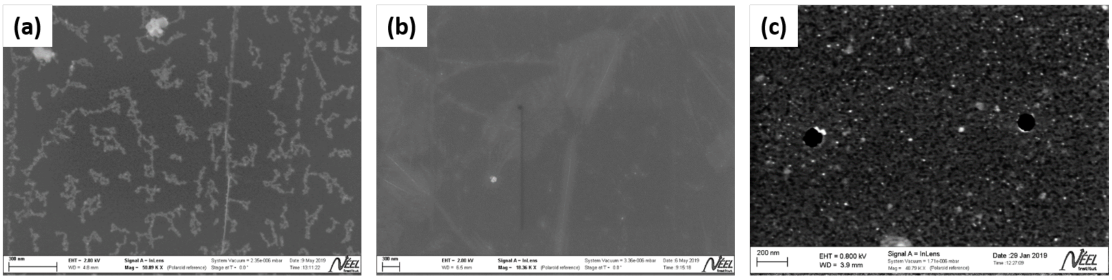

Figure 2.23: **Comparison of sample resulting from three different methods** (a) annealing with three temperature steps (400 ^{o}C - 300 ^{o}C - 200 ^{o}C), (b) annealed at 350 ^{o}C and (c) standard process involving as shown in figure 2.17.

There can be several reasons for low yield of suspended membranes *via* annealing. Low yield of suspended membrane could be reasoned to be affected by the extent of thermal shock presented by the high temperature. The removal of PMMA can be inferred by layered melting and evaporation of PMMA which in turn creates the issue of surface tension difference and hence low yield. This reasoning also explains the fact that same temperature does not allow the smaller residues of PMMA to be removed due to physical kinetics. The nanometer ranged residues would requires much higher temperature for removal, owing to their smaller size hence higher energy kinetics of attachment with the sample surface, which could not be provided by longer times with same temperature. Interestingly, the comparison of these cases with the regular process (see figure 2.23) presents us with a conclusion that remnant PMMA still persists. We can infer that critical point drying machine does not play a role in adding these impurities.

2.3.3.2 2. Replacing the acetone for etching PMMA

Second reason for the impurities could be the etchant of PMMA, in order to test it out one can replace the etchant to be acetic acid, toluene, chloroform or longer treatment of acetone.

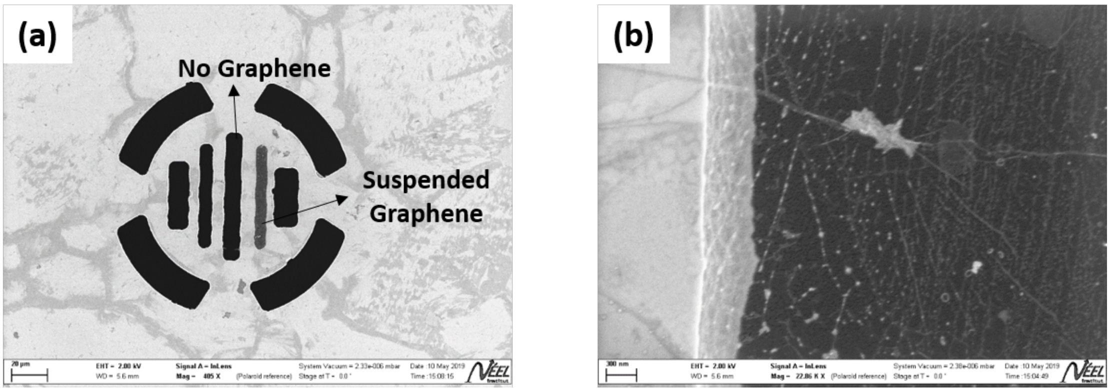

Figure 2.24: **Removing PMMA using toluene treatment for 3 hrs**: (a) SEM image of the suspended graphene 405x and (b) Black rectangle shown in (a) with 22kx zoom. Remnant PMMA is seen in (b) as network of tiny residues.

Figure 2.24 presents the case of toluene treatment for 3 hours followed by steps of standard transfer process. In fact with the use of toluene we create much like a dense network of small residues of PMMA. But interestingly the closer look at the membranes again presents us with small residues of PMMA. To ensure the complete removal we extended the treatment time to overnight (12 hours).

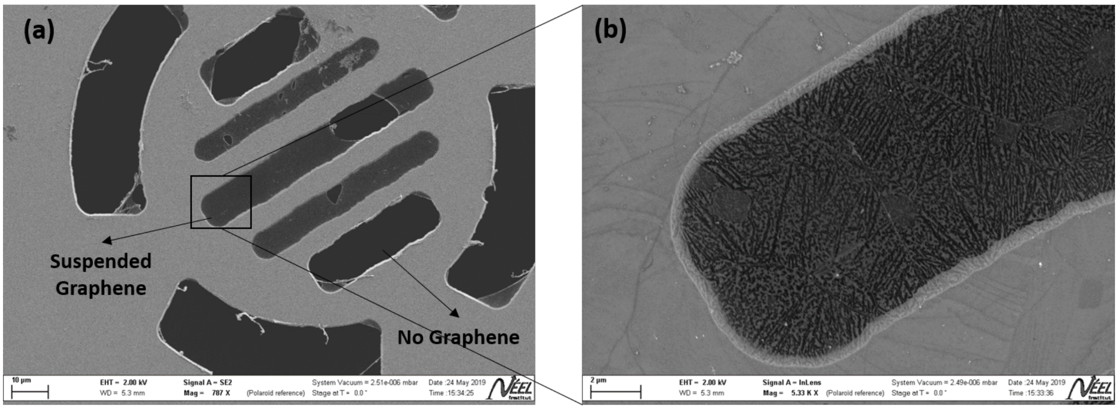

Figure 2.25: **Overnight toluene treatment**: (a) SEM image of the suspended graphene 787x and (b) Black rectangle shown in (a) with 5.33kx zoom. The special patterns are seen in (b) after proper zoom.

Figure 2.25 shows the results after overnight treatment. A specific pattern arises after the overnight treatment. A possible explanation is that chemical bonding occurs between graphene and toluene molecules. It should be noted that toluene has been shown to have electrochemical doping on graphene surface [93, 94]. It could also be a possibility for such observations.

We also tried to observe the results by using chloroform as a solvent along side the overnight acetone treatment, as shown in figure 2.26. The case of chloroform resulted in no efficient removal of PMMA residues but interestingly, we notice similar patterns for the case of overnight acetone treatment.

As discussed in literature, the mechanism of polymerization of the PMMA consists of three distinct stages, nominated, the initiation, depropagation and ter-

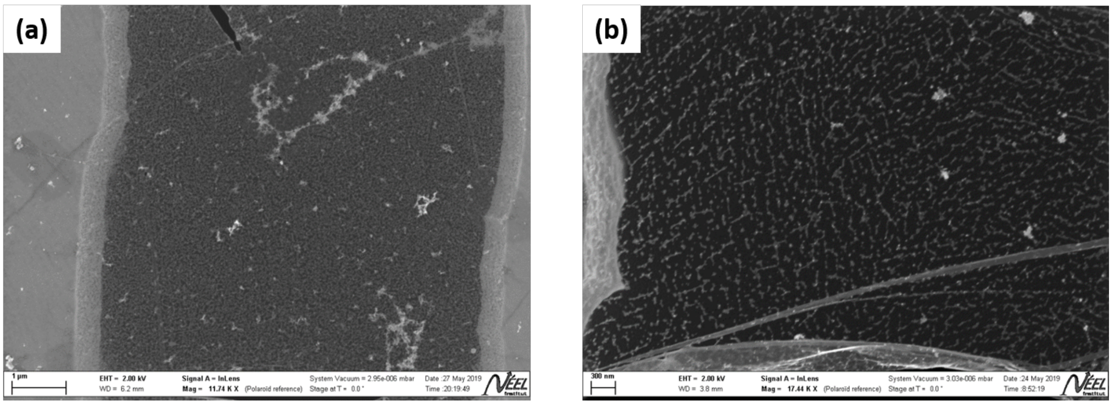

Figure 2.26: **Removing PMMA** *via* (a) 3 hrs of chloroform and (b) overnight acetone treatment. The residues in white are remnant PMMA.

mination [95]. The initiation can occur in three possible ways, 1) breaking of the PMMA chain in monomer and a free radical (chain end scission), 2) two free radical polymer chains (random chain scission) and 3) Initiation in chains with head-head linking's (elimination of metoxicarbonil side-chains) [95]. But these initiations can be inhibited by recombination of two free radicals. Since graphene is a known platform for acting as a catalyst in many cases, it is possible that it provides a room for such recombination which causes the remnants of PMMA. Even though we tried to replace acetone for PMMA removal but we encountered different processes taking place at the graphene surface, with no success in cleaning the graphene.

2.3.3.3 3. Replacing the etchant for Copper

At the third stage, we try to switch the ammonium persulphate solution to a new batch. As presented in figure 2.27, no modification was noted on the resulting suspended membranes thereby leading us to the conclusion that the issue must be addressed at the interface of graphene and PMMA.

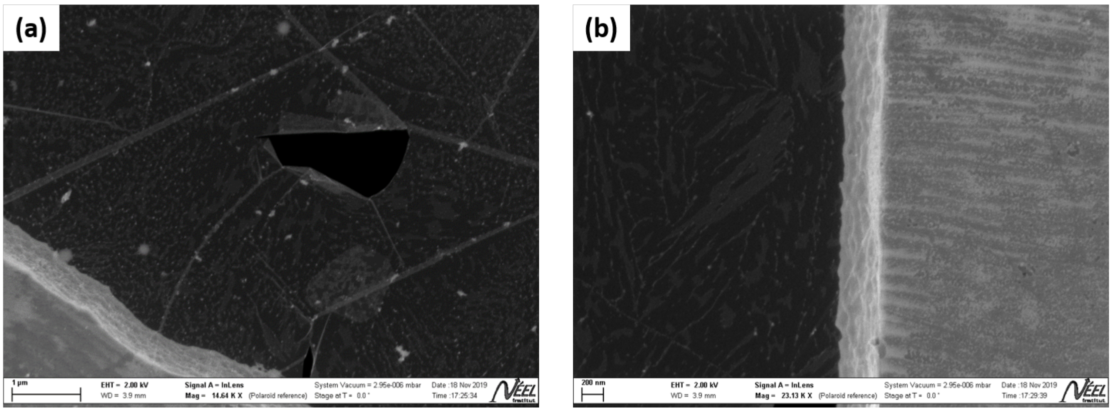

Figure 2.27: **Sample annealed at 400^{o}C**: (a) SEM image of the suspended graphene 379x and (b) Black rectangle shown in (a) with 11.73kx zoom.

2.3.3.4 4. Avoiding PMMA/graphene interface

In order to avoid the PMMA/graphene interface, we could either change the polymer itself or we could introduce another buffer layer between this interface. The trial to use PDMS as alternative polymer resulted in 0 yield of suspended membranes hence we will discuss the buffer layer introduction.

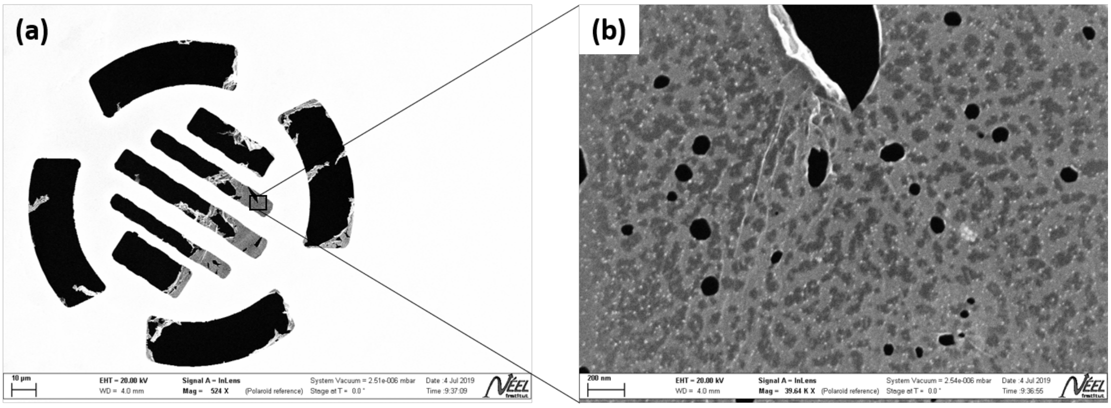

Figure 2.28: **Aluminium mediated suspended samples**: (a) SEM image of the suspended graphene 524x and (b) Black rectangle shown in (a) with 39.64kx zoom.

An approach used in laboratory is to use a metal film (10 nm) as a buffer layer. Interestingly this approach has shown better results in literature [96, 97, 98, 99, 100]. We used deposition of aluminum, on graphene/copper before spin coating the PMMA. This way we would have to introduce NaOH to remove the Al layer after the PMMA removal and before entering the critical point drying step.

As presented in figure 2.28, we observe several tiny holes (10-15 nm) on the suspended membranes. During the removal of Al, the use of NaOH would cause hydrogen release in the form of gas which would make several liquid/gas interface for graphene, which in turn would result in tiny tears in the membrane [$https : //repository.upenn.edu/scn_protocols/59$]. Despite the use of critical point drying machine, yield for such process was quite low for complete suspended membranes. However, we manage several semi suspended membranes with the tiny holes. Due to appearance of holes, we switched to gold metal as buffer layer, since gold has been proven to be better buffer layer for exfoliation of pre-patterned graphene as well meaning by it is compatible with graphene [101].

Interestingly, using gold as a buffer layer removes the undesired dirt seen in all the above cases. As shown in figure 2.29, the small region of broken membrane (which are prone to have impurity due to the assumption that one of the primary reasons for cracks are impurity), are seen to show no impurity even at the 50kx zoom. It would be crucial to mention here that using metals as buffer layer, would make graphene prone to charge doping. We can investigate these by using Raman characterization.

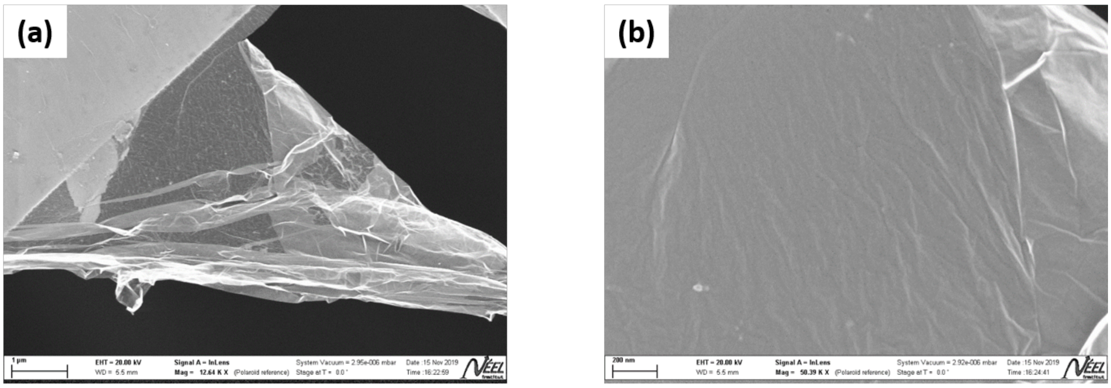

Figure 2.29: **Gold mediated suspended samples**: (a) SEM image of the suspended graphene 12.64kx and (b) 50.35kx zoom.

2.3.4 Strain and doping study in suspended samples

Figure 2.30, presents G and 2D modes of suspended graphene recorded for different processes. for the convenience of the reader these spectra have been presented in two different panels. Panel (a) shows the standard process along with metal mediated process and toluene based transfer, while all the annealing samples have been reported in panel (b).

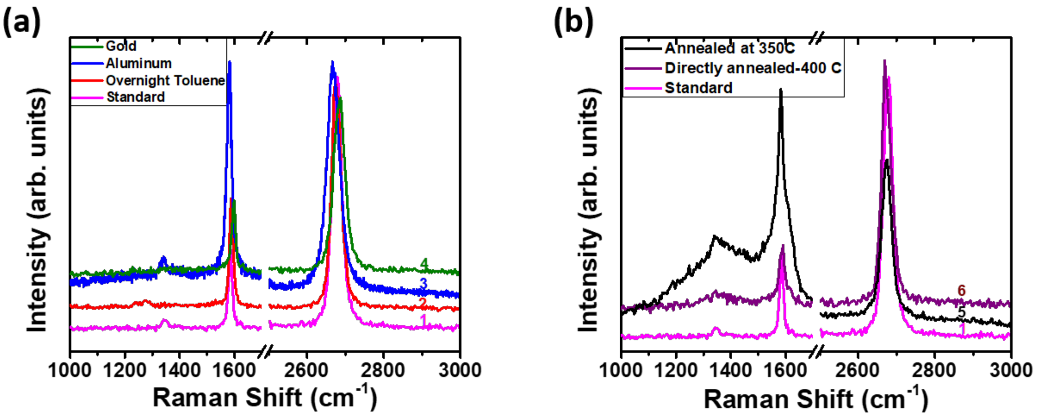

Figure 2.30: **Raman spectra of graphene resulted from different preparation methods**- (a) Metal mediated processes along with overnight Toluene treatment, (b) Annealing methods. Magenta color represent the Raman spectrum resulting from standard process.

The corresponding G and 2D band frequency along with their width is tabulated in table 2.2. The samples yielded by standard process give the G band position at 1585.1 cm^{-1} with a FWHM of 15.3 cm^{-1} and 2D band position at 2678.1 cm^{-1} with a width of 26.6 cm^{-1}. The ratio of area of 2D band to the area of G band shows a value of more than 5, indicating a high quality graphene transfer. Despite the impurities observed in SEM imaging, the Raman measurements present us excellent values of width and position. However, even though annealing process seems to present cleaner samples, the FWHM of G band was

observed to be 27 cm^{-1} (annealed at 400 ^{o}C) and 51 cm^{-1} (annealed at 350 ^{o}C), which are much larger than the theoretical predictions (13, 25 cm^{-1} respectively). We can attribute such observations to changes chemical bonding in graphene, the presence of strong D band supports this hypothesis. Literature have shown such observations of C-C bonds change during the annealing process [102, 103].
We finally look at the numbers of clean graphene obtained via gold mediated transfer, G and 2D band positions are 1590 cm^{-1} and 2681 cm^{-1} with a width of 16 cm^{-1} and 26.7 cm^{-1}, respectively. The area ratio of 2D band to G band is more than 5, which is signature for monolayer graphene.

Table 2.2: **Raman modes for different processes**: The G and 2D band frequency parameters for different processes as observed in Raman spectroscopy

	ω_G	Γ_G	ω_{2D}	Γ_{2D}	I_{2D}/I_G
Standard	1585.1	15.3	2678.1	26.6	5.5
Annealed at 400^{o}C	1586.9	27.4	2673.1	27.2	4.5
Annealed at 350^{o}C	1583.3	50.9	2674.0	28.7	0.5
Overnight Toluene	1588.1	15.1	2676.2	26.0	4.0
Aluminium mediated	1580.8	20.3	2668.2	37.5	2.0
Gold mediated	1590.2	15.9	2680.9	26.7	5.5

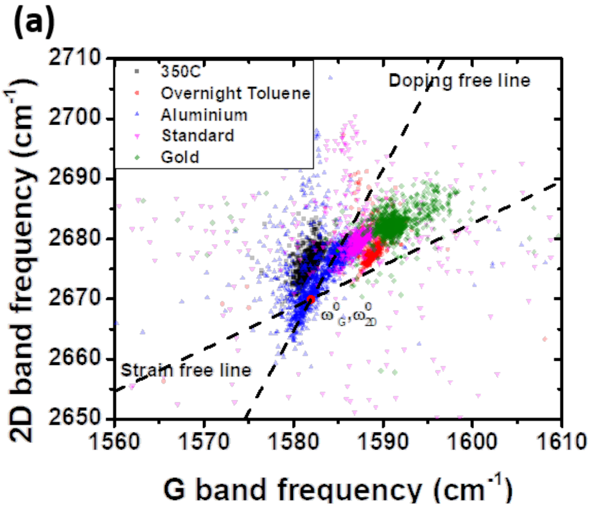

Figure 2.31: **Lee plot**: Lee plot corresponding to different samples preparation methods. Strain and doping free lines are shown by the dashed line. The red dot at the intersection of dashed lines represent the origin of the Lee plot for our samples.

Beyond the SEM observation of cleanliness, it would be important to seek for the effect of the different processes on the strain of resulting suspended samples. We will use the approach of Lee *et al.* (see section 1.4.2.1) to extract the strain information. Figure 2.31 shows the Lee plot for different processes. We notice a compressive strain for gold mediated transfer [63]. Aluminum and gold have lattice parameter of 405 and 408 pm respectively, which is larger than the case of graphene (246 pm), this should result in compressive strain for both the cases but the case of aluminum presents the holey patterns in SEM image which can be held accountable for strain compensation.

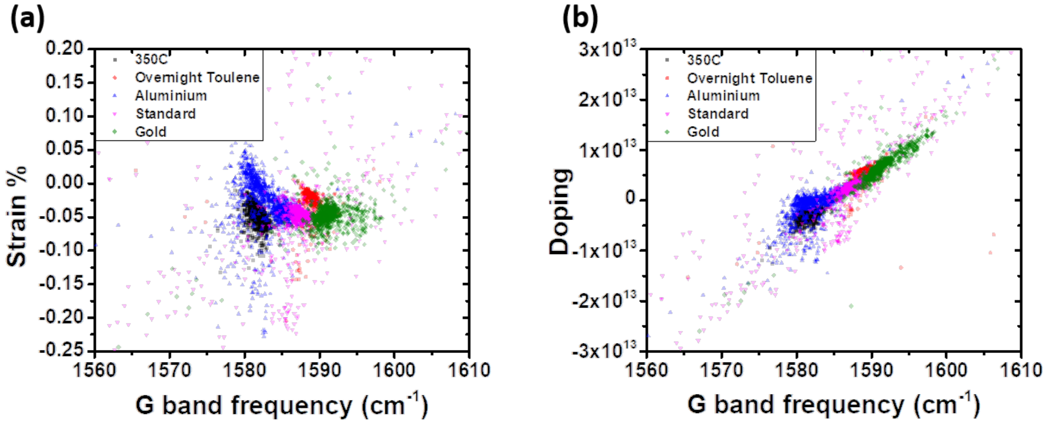

Figure 2.32: **Strain and doping**: (a) Strain with corresponding G band frequency for different processes. (b) Doping with corresponding G band frequency for different processes.

From figure 5.5(a), we also observe that strain induced by suspending the graphene is nearly constant (-0.05%) in all the methods except the overnight toluene treatment (-0.025%). Corroborating this information by the SEM image, one can infer that the specific patterns arising after overnight treatment compensates for the strain in the membrane. The reason for the specific patterns could possibly be arising from the adsorption, which can take place at the graphene surfaces [104, 94].

We expect that when a metal is mediating the transfer, it can easily dope the graphene with additional electrons. It was observed that using continuous gold films produces p-doped graphene [105]. It is discussed in the framework of work-function of gold-graphene (4.89 eV) and graphene (4.69 eV) alone, a positive difference between the two shows lowering of graphene Fermi energy thereby indicating the p doping [105]. We observe similar behavior for gold mediated transfer, whereas aluminium mediation does not show any such effect. The case of aluminium mediation is rather peculiar, owing to noncatalytic properties of aluminium towards graphene [106, 100]. Despite the clean Raman signal from Al mediated transfer, G band width was measured to be 20.3 cm^{-1} (which is unusually high when compared to standard process) which can be attributed to the holes.

We will compare the two interesting method of transfers (Al and Au mediated transfer), from strain and doping information along with the cleanliness of the samples. In order to understand the details and homogeneity of the samples resulting from the two methods, we shall discuss the statistics extracted from Raman mapping. Figure 2.33 presents the statistics of strain and doping for Al and Au mediated processes along with the standard process. For simplicity, we have restricted our data only from suspended region. One can readily observe that the strain contribution from the aluminium mediated transfer shows strain mainly

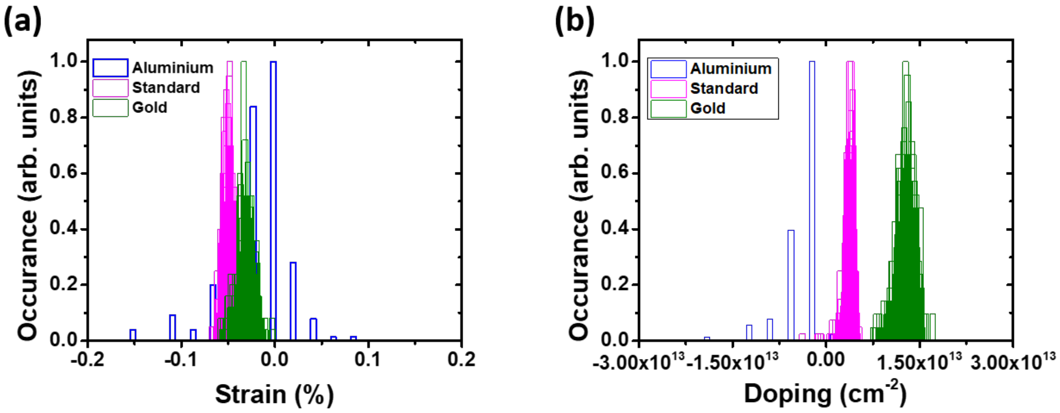

Figure 2.33: **Statistics of strain and doping**: The statistics of (a) strain and (b) doping for the two metal mediation case along with the standard process.

centered to zero %, however, the distribution of strain is rather broader (-0.05-0.05 %) when compared to gold mediated (-0.04-0.01 %) and standard transfer process (-0.06- -0.02%). Furthermore, the gold mediation reduces the average strain of transferred graphene when compared to standard process.

The case of aluminium shows minor n doping, which could be attributed to the lower work-function of the aluminium (4.29 eV) when compared to graphene (4.69 eV). However, such observation is in contrast with literature [100]. Another crucial point which can be raised is the fact that the Lee plot parameters used here are specifically for p-doped graphene (see section 1.4.2.2), whereas Al mediated transfer has shown n doping for this formalism, which is in contrast. It could be a reason for unusual estimations for this process when compared to the SEM observations. In contrast to Al-mediated transfer, gold mediation leads to p doping much larger than the standard process. Such can be attributed to the observations made earlier in literature [105].

We can now discuss the Raman maps of gold mediated transfer, in order to add to the understanding we will be giving numbers from aluminium mediated graphene. The average FWHM of G (2D) band is 18.5 (32.0) cm^{-1} for Al mediated transfer whereas for gold mediated transfer the average is 16.7 (31.8) cm^{-1} hinting towards better sample quality for gold mediated transfer. The tiny holes created in suspended graphene resulting from aluminium mediated transfer lead to inhomogeneity of G and 2D band frequency thereby showing larger G (2D) band FWHM. However, the Raman frequency maps of gold mediated transfer shows very homogeneous distribution of G and 2D band frequencies in the suspended region, as shown in figure 2.34.

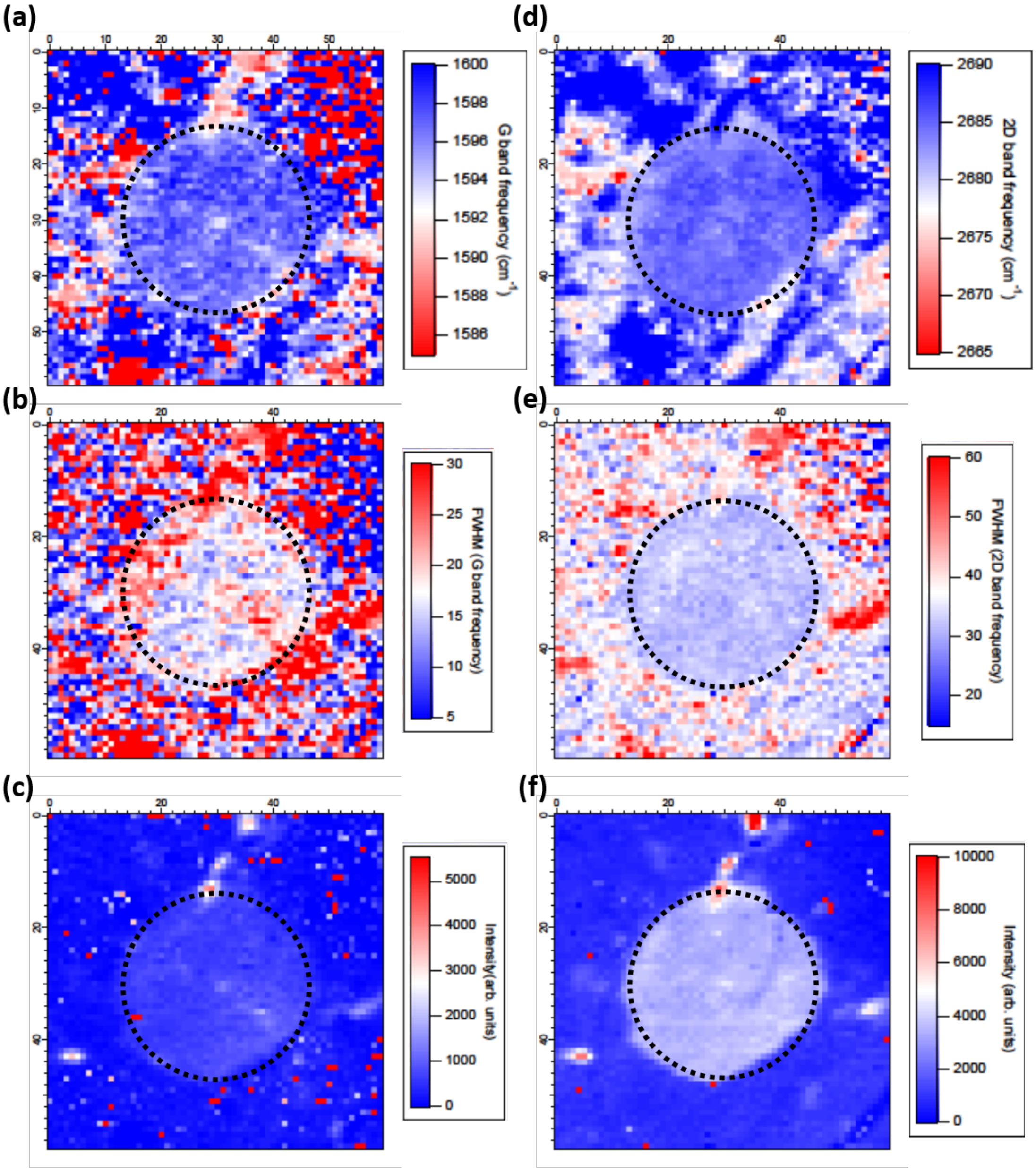

Figure 2.34: **Raman maps**: Raman map for frequency, FWHM and intensity maps for G band (a-c in the same order) and 2D band (d-f). The black dashed line shows the location of the hole.

Similar observation is manifested in intensity maps for both the methods. The homogeneity of the 2D band is more prominent than G band. It could be attributed to the poor signal quality for G band when compared to 2D band. Such condition depicts that the intensity map is much reliable than the frequency or FWHM. It is mainly due to the additional fitting error in the FWHM, while frequency and intensity are less affected owing to the larger value of them. Relying on intensity and frequency maps, we can establish that the suspended graphene is very homogeneous over the suspended region.

The samples created by gold mediated samples can be investigated for thermal transport measurements since we will be using optical heating. However, significant doping can alter the properties used in electron transport. Despite the good numbers of Raman and impurity free SEM image, the case of gold mediated transfer shows graphene with a minor compressive strain, to begin with. We shall discuss the relaxing of these in-situ strains in chapter 3 and 4.

2.4 Conclusion

In conclusion, we present different approaches to pattern holes in substrates designed for suspending 2D materials. We present several samples for the study of thermal effects in various 2D systems. Mechanically exfoliated samples can be easily procured on desired substrates. The suspension of such exfoliated samples would require better support such as hBN. The strategy of hBN can be further explored to suspend different 2D materials.

We have specifically focused on narrowing down the problem of cleaning graphene. To do so, we have investigated different steps of standard wet transfer process. We find that gold mediated transfer can result in cleaner samples with some level of doping and strain in the suspended samples. We have systematically analyzed the strain and doping contributions due to different transfer methods. Even though strain and doping are observed in gold mediated samples, we find high quality of homogeneity in the suspended region of samples which can be used for thermal transport experiments.

Despite all the progress made in the recent years, the field of sample fabrication for 2D systems, seems to have a large room for improvement. We observe that the distribution of CVD transferred graphene samples are not very clean for graphene on substrate. This domain can be area of future optimization. As shown in the substrate fabrication, cleaner substrates have the potential to resolve this issue.

Chapter 3

Thermal conductivity of 2D materials extracted by 1 laser Raman thermometry

As discussed in the last chapter, mechanical exfoliation can provide us with monolayers of 2D materials. There have been several reports to estimate the thermal conductivity of different mono-layer systems using 1 laser Raman thermometry [6, 33, 70, 69, 49]. Moreover, the thermal conductivity measurements for such systems are frequently mentioned in suspended case [51, 107, 72, 49]. In this chapter, we will discuss thermal conductivity of 2D materials supported on different substrates. Actually, there is a need for investigating their thermal properties for their practical applications. Only few such reports have been presented with investigation of thermal conductivity of $MoSe_2$, WSe_2 and h-BN [49, 69, 108]. All these approaches have used the model proposed by Ruoff *et al.* [33] (obtaining the temperature profile using heat diffusion equation), for estimating the thermal conductivity but not the one proposed by Balandin *et al.* (solving radial heat flow equation for two laser powers). Interestingly, the two approaches are based on diffusive heat transport. In 3D systems, we have a relation between electronic properties and thermal properties, which is not clearly studied in 2D materials. Furthermore, in a recent report it was shown that the thermal conductivity of MoS_2 decreases from 40 W/m.K for bulk to 20 W/m.K for monolayer [72, 107]. We know that the electronic structure changes from indirect to direct bandgap semiconductor for the above mentioned case. Similar observations have been made for other TMDCs such as WS_2 and MoS_2 [109]. However, a clear understanding between the relation of electronic structure and thermal property is not known for 2D systems. In the absence of suspended samples for 2LRT, we will attempt to see whether there is any relation between thermal and electronic properties in the available supported 2D materials.

We will investigate the thermal conductivity of different 2D materials (using the approach of Balandin *et al.*) exfoliated on different substrates. We will try to find the best substrates for studying thermal properties of 2D materials. Since the thermal conductivity estimation depends on the $\partial\omega/\partial T$ and $\partial\omega/\partial P_{laser}$, one can look at them as more intrinsic than thermal conductivity. We will try to compare

$\partial\omega/\partial T$ and $\partial\omega/\partial P_{laser}$ on the basis of electronic structure.

3.1 Raman thermometry on semiconductors

As discussed above, we observe a range of electronic band gap in 2D materials and they have been explored separately for their thermal properties [49, 108, 33]. Raman thermometry has been used extensively for estimating the effective thermal conductivity. We have annealed all the samples at 350 ^{o}C under the Ar atmosphere, after the mechanical exfoliation. Such procedure ensures a good adhesion between the substrate and the sample. As mentioned before the basic parameters to estimate the thermal conductivity are $\partial\omega/\partial T$ and $\partial\omega/\partial P_{laser}$, ω being the thermometer mode phonon frequency. We will at first discuss about these parameters and their extraction from experiments, starting with the case of $MoSe_2$.

3.1.1 Effect of global heating

After the mechanical exfoliation (as discussed in section 2.2.1), we use the optical properties of the monolayer TMDC to characterize it. Since monolayer $MoSe_2$ is a direct bandgap semiconductor, we can easily identify it using PL (photoluminescence) spectroscopy. Owing to its band gap around 1.58 eV [110], we can image the desired location of the sample using the Raman spectrometer in PL configuration. Figure 3.1 shows the optical image and a PL image (centered at 1.58 eV) of exfoliated $MoSe_2$ on SiO_2/Si substrate (100 nm SiO_2). The laser power used is 50 μW and acquisition time for each spectra is 5 seconds. The PL image with strong signal confirms the presence of monolayer and a weak signal in the image shows the location of bilayer (encircled in figure 3.1(right)), which is connected to few layer $MoSe_2$ (Red circle of figure 3.1(right) and white circle in figure 3.1(left)).

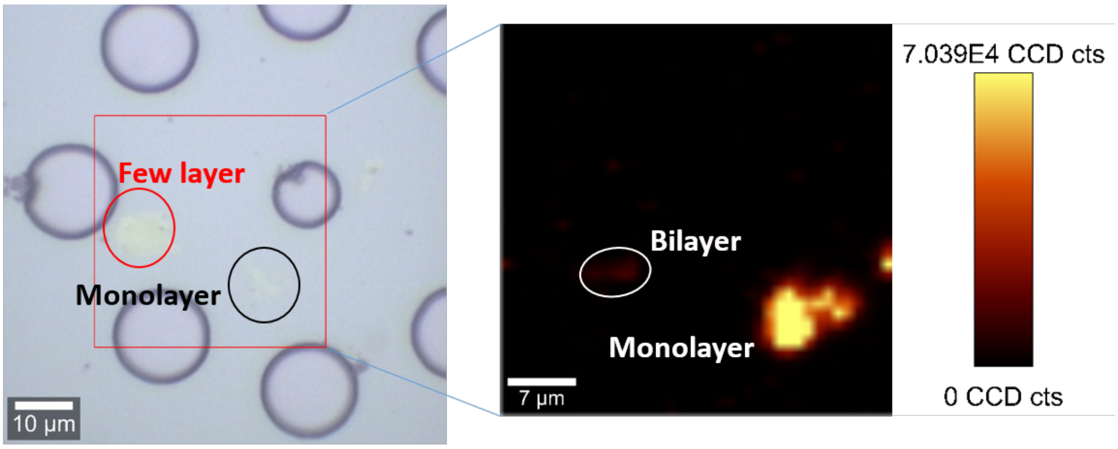

Figure 3.1: **Characterization of exfoliated $MoSe_2$**: (a) Optical image and (b) PL image of exfoliated $MoSe_2$ sample at room temperature. The bright yellow region in PL image shows the monolayer $MoSe_2$ while a feeble reddish tinch in (b) shows the bilayer (encircled in white). The PL spectra is observed at 50 μW.

Figure 3.2 presents the Raman and PL spectra of exfoliated $MoSe_2$ at ambient conditions. We observe the A_{1g} (out of plane) mode around 242 cm^{-1} for mono-, bi- and few layer $MoSe_2$ [49]. The signal around 305 cm^{-1} is due to the optical fiber of the collection optics (section 1.4.2.1), which hinders the weak in-plane E_{2g} mode of $MoSe_2$ [111, 49, 112]. So, we will focus on the A_{1g} mode for all our observations. The Raman signal from few layer $MoSe_2$ is stronger than mono- and bilayer due to increased sample volume. Figure 3.2(b) shows the strong PL signal at 1.58 eV (corresponding to A exciton) from the monolayer whereas bilayer has a weak peak at 1.55 eV (corresponding to B exciton) [110, 113]. Few layer $MoSe_2$, on the other hand does not show any PL signal (see figure 3.2(b)) owing to its indirect bandgap [114]. Interestingly, the PL peak position here also corresponds to direct band gap of monolayer $MoSe_2$.

With the confirmation of the number of layers, we would observe the global heating (using hotplate setup mentioned in section 1.4.2.3) response by monitoring the PL peak position and the A_{1g} mode from the monolayer $MoSe_2$ [49].

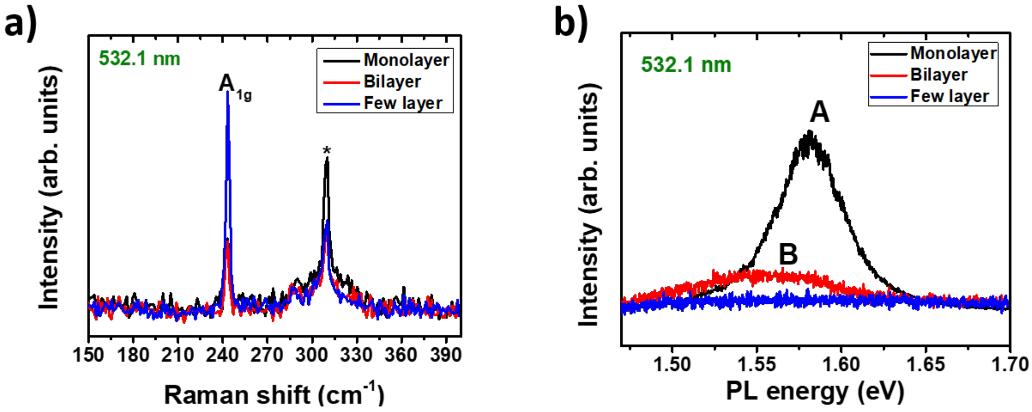

Figure 3.2: **Characterization of exfoliated $MoSe_2$ on SiO_2/Si**: (a) Raman and (b) PL spectra of mono-, bi- and few layer MoSe2 at room temperature. Sample is annealed at 350^{o}C under Ar gas glove box for 3 hrs. The * peak is an artifact arising from the optical fiber in (a). The power used for the measurement is 50 μW and acquisition time for each spectra is 5 seconds.

Figure 3.3(a) shows temperature dependent evolution of A_{1g} frequency. A clear red shift is observed as reported in literature [49]. In the first approximation the linear fit gives the $\partial\omega/\partial T$ value to be -0.008 cm^{-1}/K, which is not far from the reported value (-0.01 cm^{-1}/K). The red shift can be attributed to the phonon-phonon interaction and the lattice expansion of the material. With increase in temperature, the population of phonons would increase thereby increasing phonon-phonon scattering. The increase in phonon-phonon scattering leads to anharmonicity contributing to the observed redshift [49]. On the other hand, we know that the lattice expansion of the 2D material is severely affected by the thermal expansion coefficient (TEC) of the substrate, which is SiO_2 in this case. The TEC for $MoSe_2$ is 1.95x10^{-5} /K [115], whereas TEC for SiO_2 is reported to be 0.6x10^{-6} /K. The TEC mismatch being 1 order of magnitude will resist the intrinsic lattice expansion of $MoSe_2$ thereby reducing the extent of redshift. We can say that TEC mismatch and phonon anharmonicity are competing against each other. Since the substrate-MoSe$_2$ coupling would be deciding factor for the extent of contribution from TEC mismatch (a good coupling leads to strong contribution), it should be given special attention for studying heating effects.

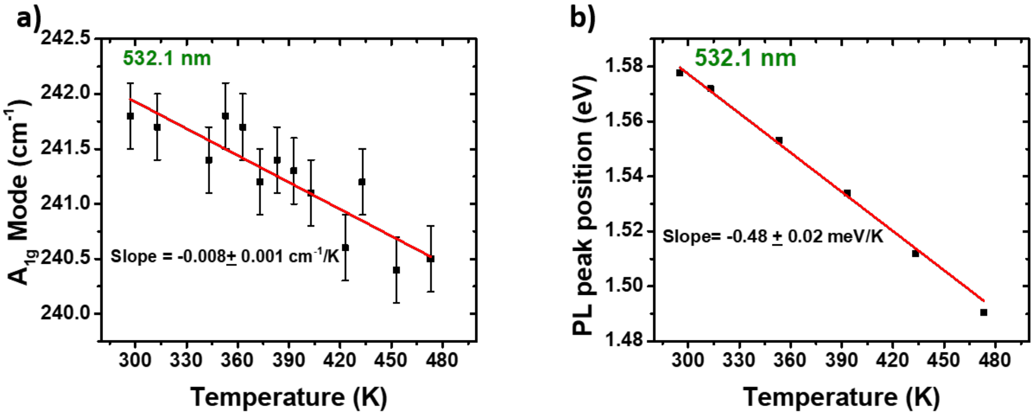

Figure 3.3: **Temperature dependence of optical properties**: (a) Temperature dependence of optical phonon energy and (b) Temperature dependence of PL energy. Red line shows the linear fit.

Figure 3.3(b) shows the thermal response of the optical band gap, which can be explained by Varshni relation (E$_g$ = E$_0$ - αT^2/(T+β), where E$_g$ is bandgap, E$_0$ is bandgap at 0 K and α,β are constants) [116]. This relation holds good for 3D systems, however, it has been shown in literature that it applies well for monolayer MX$_2$ [117]. It clearly depicts that the increase in temperature decreases the PL energy and reduction of band gap can be observed as expected.

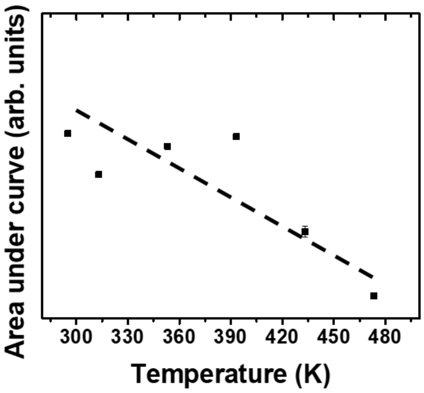

Figure 3.4: **Temperature dependence of PL intensity**: Temperature dependence of area under the curve of PL peak, dashed line is eye to guide line.

Non-radiative recombinations can hint upon the phonon population in a system and area under the curve of a PL peak can hint upon the probability of radiative recombination in a system. So using the area under the curve of PL peak, we can monitor the phonon population qualitatively. Figure 3.4 shows the evolution for the area under the curve with temperature. With the increase in temperature, we observe a decrease in area under the curve which is a signature for the non-radiative recombination increase. Thus the the red shift observed can be attributed to the phonon anharmonicity in the system.

It is important to mention that the $\partial\omega/\partial$T values for other materials with similar band gaps such as MoS_2, WS_2 and WSe_2 (taken from literature) are reported to be -0.016, -0.006 and -0.006 cm^{-1}/K respectively [49, 70, 69]. These values are very close to each other, interestingly these materials have very close range of band gaps as well. This observation in the first approximation may hint upon a relation between the thermal properties between 2D materials and their electronic band structure.

Owing to their direct band gap, these materials show stronger absorption (>5 %) than other 2D materials such as graphene (2.3 %). It is why the effect of optical heating is expected to be more prominent for these materials. However the effect of substrate can affect this observation depending of the efficiency of heat dissipation. In order to understand these effects, we would investigate the local heating in next section.

3.1.2 Effect of local heating

As mentioned in earlier section (section 3.1.1), we shall follow the in-plane A_{1g} vibrational mode to observe the heat response of $MoSe_2$. Figure 3.5(a)shows the evolution of A_{1g} mode with laser power. We notice a weak heating effect contrary to the stronger absorption values reported in literature [49]. A total of 0.4 cm^{-1} was observed during a total power change of 6.5 mW. Since the absorption of monolayer $MoSe_2$ is reported to be 5.7 % [49], the total heat absorbed should be around 370 μW. In a recent report regarding similar measurement, total of 0.5 cm^{-1} shift was observed for an absorption of nearly 50 μW laser power [49]. The discrepancy observed here is nearly 7 fold. As discussed earlier, one of the crucial factor for heating effects is the substrate-$MoSe_2$ coupling. It is important to mention that the reported absorption value is measured for suspended samples, however the absorption can change strongly depending on the strength of substrate-$MoSe_2$ coupling.

It should be reminded from section 2.2.1 that the exfoliated samples are annealed in Ar atmosphere for 3 hours, immediately after the exfoliation. Hence, we can assume a good coupling between the monolayer $MoSe_2$ and the substrate. In order to test this hypothesis, we performed local heating experiments on few layer $MoSe_2$ sample, which was present next to the monolayer (see figure 3.1). Figure 3.5(b) shows the evolution of A_{1g} mode for few layer $MoSe_2$. A linear fit immediately tells that the few layer sample was heated more efficiently than the monolayer. The $\partial\omega/\partial P_{laser}$ value is twice as observed for monolayer confirming the efficient heating *via* laser power. Such observation is consistent with the hypothesis that the substrate-$MoSe_2$ coupling for monolayer is very prominent which results in easier heat dissipation whereas the heat dissipation is weaker for few layer $MoSe_2$ leading.

In addition, we correlate our data with the observations made by Zhang *et al.*

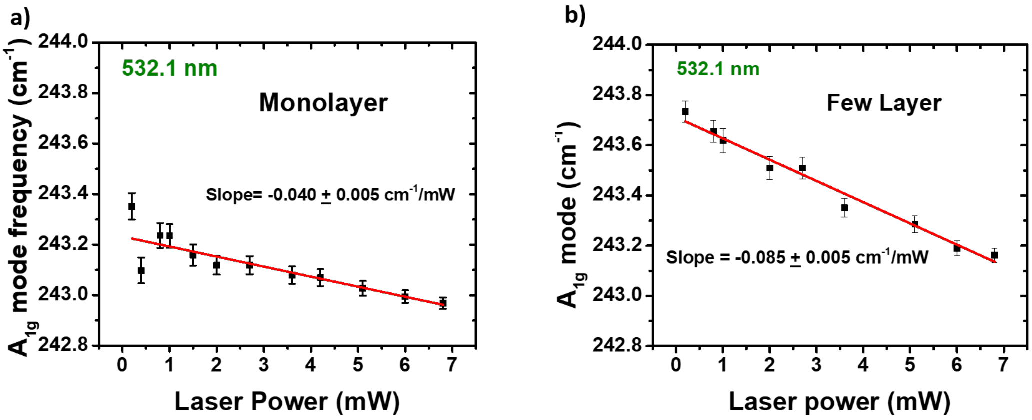

Figure 3.5: **Laser power dependence of optical phonons of exfoliated MoSe$_2$**: (a) Power dependence of A$_{1g}$ mode for monolayer and (b) Power dependence of A$_{1g}$ mode for few layer. The power mentioned on X axis is the incident laser power, red line shows the linear fit.

[49]. They report the optical absorption for bilayer MoSe$_2$ to be 9.7 %, which is much higher than the reported value for monolayer. Despite higher optical absorption they measure smaller $\partial\omega/\partial P_{laser}$ (0.03 cm^{-1}/μW) for bilayer than that of monolayer (0.044 cm^{-1}/μW) suggesting the contrary of our observation. Moreover, they report similar trend for suspended samples. Interestingly, in a very recent report by Reig *et al.* [72], it is shown that the $\partial\omega/\partial P_{laser}$ trend, for suspended mono- and bilayer, is consistent with [49] but if the number of layers are increased further, the $\partial\omega/\partial P_{laser}$ value starts to increase suggesting that the increase in absorption directly affects the heating efficiency (optical absorption for bulk MoSe$_2$ is found to be nearly 30%).

We can hence conclude that regarding only the absorption aspect for heating effect the $\partial\omega/\partial P_{laser}$ value should increase with the number of layers. However, for monolayer MoSe$_2$, the coupling between MoSe$_2$ is strong and the heat is efficiently dissipated by the substrate thereby decreasing the observed $\partial\omega/\partial P_{laser}$. However, to understand the case of few layer MoSe$_2$, we can refer to a recent report by Jiang *et al.* [118]. Jiang *et al.* showed by using pump-probe thermoreflectance measurements that the out of plane thermal conductivity for MoSe$_2$ is far lesser than in plane thermal conductivity [118]. Using their observations we can say that as the number of layers are increased the out-of-plane thermal conduction prohibits the efficient heat propagation to the substrate resulting in efficient heating effect, which explains the steeper $\partial\omega/\partial P_{laser}$ for few layer sample. In addition, since the A$_{1g}$ mode is out-of-plane, strong coupling with substrate would directly affect its dynamics.

Despite the fact that, we understand qualitatively that the substrate effect is playing an important role for our observation of less heating, we need more experiments to quantitatively validate reason behind such observation. A very important experiment could be to directly measure the optical absorption in our case which would hint upon the strain induced modification of optical absorption. Moreover, we observe similar effect of efficient heat dissipation from the substrates in studying WSe_2 and WS_2 (not shown). All these experiments hint toward the fact that the substrate coupling can be an issue for studying thermal transport in 2D materials. Furthermore, it was shown by Reig *et al.* that the out of plane heat dissipation is very efficient in case of $MoSe_2$ and must be taken into account during these experiments [72]. We can perform same experiment in vacuum to avoid the heat loss due to air.

We observe that the heating effect in 2D materials on substrate can be very complex problem. Hence, a careful and systematic study is necessary for any robust conclusion.

3.1.3 Thermal conductivity

In order to calculate the effective thermal conductivity we can use the data from above sections. As argued by Ruoff *et al.*, the model proposed by Balandin *et al.* needs a modification due to the fact that the 100 % laser power is not used to heat the system. We will use the model from Balandin *et al.* [6] with modification of considering the absorbance to compensate for the fact that only absorbed laser power is being used for heating of the sample. As discussed in chapter 1 (see section 1.4.2.3), we will use the following equation to estimate the effective thermal conductivity:

$$\kappa = \frac{\chi}{2\pi h}\frac{\partial P_{laser}}{\partial \omega}(\frac{\partial P_{abs}}{\partial P_{laser}}) \tag{3.1}$$

where χ is temperature coefficient obtained from the global heat experiment (fig 3.7), h denotes the thickness of the material and P_{laser} represents the laser power, ω is the frequency of the thermometer mode and P_{abs} is the absorbed laser power.

The thickness of monolayer $MoSe_2$ is taken from literature, which is of the order of 1 nm. Using the value of slope -0.008 cm^{-1}/K and -0.04 cm^{-1}/mW for global and local temperature dependence of the A_{1g} mode frequency, along with the optical absorption of 5.7 % [49] for 532.1 nm laser would result in the effective thermal conductivity of 1814 W/m.K. The effective thermal conductivity obtained with such approach is very high, which does not compare well with the numbers of theoretical predictions (54 W/m.K) by calculating the Boltzmann transport equation [119]. An investigation on the Joule heating could add to our knowledge for confirming the device application and heating issues, which could be a future prospect of this study.

In the next section we will try to explore insulating samples in order to add more to the understanding of possible problems which may arise during such studies.

3.2 Raman thermometry on insulators

Insulating 2D materials are of great importance to be used as dielectrics for device fabrication with 2D materials. Such an example turns out to be hexagonal boron nitride (h-BN). h-BN acts as one of the best substrate for graphene and other

2D materials. It isolates the 2D material from the substrate effect (for example doping). However, it does not isolate the 2D material from the substrate, thermally. In almost every electronic devices, thermal losses reduce the efficiency and the life time of devices. This reason makes it a crucial player to understand the thermal properties of h-BN on substrate. To reach this goal, we study CVD grown h-BN, which is not much reported in the literature regarding thermal properties [120, 121]. h-BN mono-, bi- and tri-layer grown on sapphire are obtained from our collaborator Prof. Hyeon Suk Shin's group (South Korea). Samples were grown on sapphire via chemical vapour deposition method [122]. These CVD grown samples are shown to be wrinkle free. These h-BN samples grown on a transparent substrate (sapphire) are difficult to measure (with Raman spectroscopy) due to large band gap, most of the light is transmitted which causes difficulty in optical focusing.

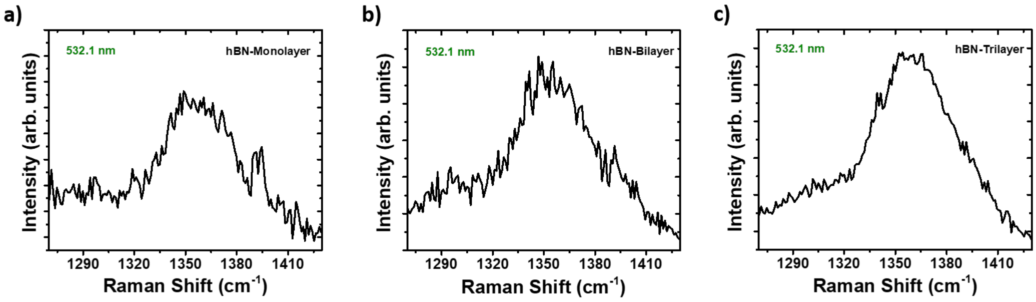

Figure 3.6: **CVD grown h-BN on sapphire**: Raman spectrum of (a) Mono-, (b) Bi- and (c) Tri-layer of h-BN on sapphire.

Another difficulty is that very small back-scattered light is collected at the spectrometer, owing to higher transmission of the substrate. For a comparison of signal collection, typical graphene measurement takes 8-10 seconds whereas h-BN samples required 1800 seconds for comparable signal to noise ratio with the same laser power. We will now discuss the effect of global and local heat in these samples.

3.2.1 Effect of global heating

In this section, we will discuss the global heating experiments done on h-BN mono-, bi- and trilayer samples. Figure 3.7(a) shows the temperature dependent E_{2g} mode frequency evolution for CVD grown mono-, bi- and trilayer h-BN on sapphire, respectively. Linear fitting is adopted to extract the first order temperature coefficient ($\partial\omega/\partial$T). We observe that the $\partial\omega/\partial$T is -0.025±0.003, -0.044±0.003 and -0.063±0.007 cm^{-1}/K for mono-, bi and trilayer h-BN respectively. Our observation shows that the $\partial\omega/\partial$T increases with number of layers. The reported $\partial\omega/\partial$T for mono- and bilayer CVD grown h-BN (grown on Ni and subsequently transferred on 10 nm Au on Si) are -0.034 and -0.032 cm^{-1}/K and reaches -0.038 cm^{-1}/K for 9 layers of CVD grown h-BN [120]. Moreover, another report for CVD grown few layer h-BN has $\partial\omega/\partial$T value to be -0.022 cm^{-1}/K (grown on Cu foil and transferred on SiO_2/Si) [121]. Considering the range of values reported for CVD grown h-BN samples, our values are well consistent.

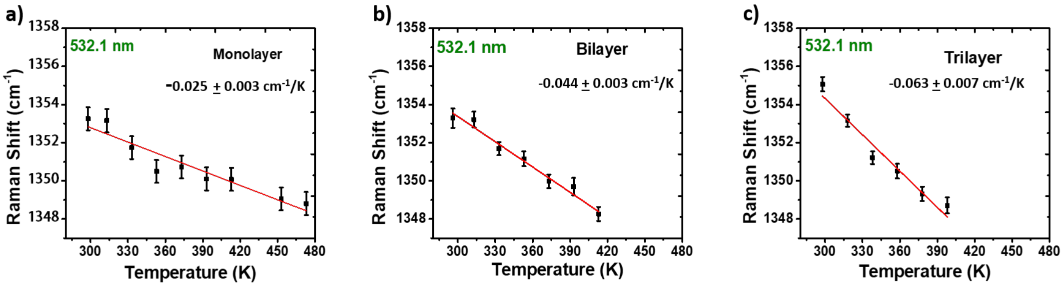

Figure 3.7: **Global heating of CVD grown hBN on sapphire**: Temperature dependence for E_{2g} mode of (a) Mono-, (b) Bi- and (c) Tri-layer of hBN on sapphire, red lines show the linear fit.

Interestingly, Cai *et al.* observe that $\partial\omega/\partial T$, for mechanically **exfoliated** mono-, bi- and trilayer h-BN on SiO_2/Si, decreases with increasing number of layers, which are -0.056, -0.048 and -0.038 cm^{-1}/K for mono-, bi- and trilayer h-BN/SiO_2. However, we can attribute the differences observed by us to the nature of h-BN along with the SiO_2 substrate they have used. Considering the wide range of numbers for thermal parameters, we will mainly discuss the reports from CVD grown h-BN.

The downshift observed would have two major contributions: (1) phonon-phonon anharmonic interactions,(2) thermal expansion coefficient mismatch between the h-BN lattice and sapphire lattice. It is found that the TEC for h-BN decreases with increase in number of layers (from -3.6 to -1.7x10^{-6}/K for mono and tri-layer, respectively) [108] (in the absence of experimental value for CVD samples, we will take the values from exfoliated sample assuming that it will not be drastically different). The increase in number of layers would hence decreases the mismatch between the TEC of substrate and h-BN (difference decrease from -10.8 to -8.9x10^{-6}/K), which would reduce the tensile strain and hence add to the downshift observation. The large mismatch would reduce the free lattice expansion of h-BN in turn leading to a tensile strain and hence more red-shift and consequently more slope.

In addition, the thermal conductivity of sapphire is strongly temperature dependent in the relevant temperature range (300-420 K) [123]. For example, it reduces from 35 W/m.K to 23 W/m.K from 300 to 420 K, which amounts to 35 % change. Such change would affect the heat dissipation and in turn would change the observation of associated temperature dependence of h-BN mode for our case. Since phonon anharmonicity is associated with the phonon relaxation time, which is inversely proportional to temperature, with the increase in temperature the anharmonic interactions with the substrate will increase (owing to lower thermal conductivity of sapphire).

In order to estimate the thermal conductivity of these samples, we would investigate about the local heating effects in our samples.

3.2.2 Effect of local heating

Local heating is investigated *via* laser heating by varying the laser power (see section 1.4.3). Figure 3.8 shows the power dependent E_{2g} frequency evolution. A downshift is observed as in case of global heat. It is however, interesting to note that the slope of bi-layer sample does not follow the monotonic behavior with the number of layers. The power dependent slope for mono- and tri-layer is almost the same (-1.63 and -1.68 cm^{-1}/mW respectively) but the slope for bi–layer h-BN (-0.7 cm^{-1}/mW) is lesser than the former.

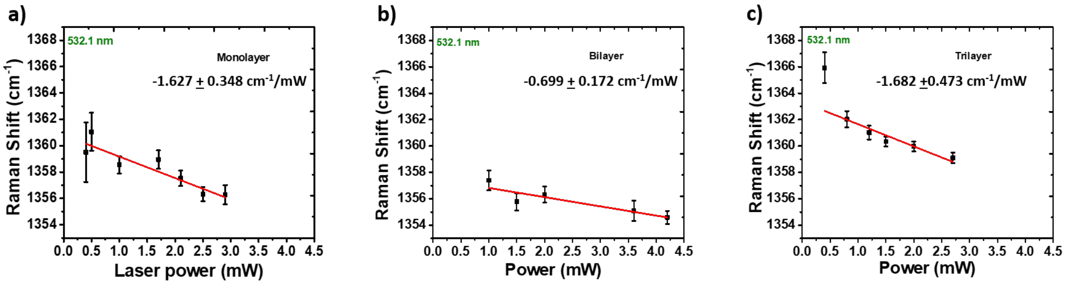

Figure 3.8: **Local heating of CVD grown h-BN on sapphire**: Power dependence for E_{2g} mode of (a) Mono-, (b) Bi- and (c) Tri-layer of h-BN on sapphire, red lines show the linear fit for each graph.

When compared to literature, we find that for CVD grown 9L suspended h-BN, the $\partial\omega/\partial P_{laser}$ value is -1.13 cm^{-1}/mW using a laser excitation of 514.5 nm [120]. In addition, another report for few layer suspended h-BN sample shows $\partial\omega/\partial P_{laser}$ to be -0.45 cm^{-1}/mW [121]. Interestingly, we observe the $\partial\omega/\partial P_{laser}$ values in both range meaning that mono- and trilayer (1.62 and -1.68 cm^{-1}/mW) shows closer value to [120] and bilayer (0.699 cm^{-1}/mW) shows similar value to [121]. We should remind that our samples are directly grown on the substrate and hence must be in good thermal contact with the sapphire. Owing to the TEC of the h-BN and sapphire, we must expect different strain for our samples than the suspended case. In other words, the substrate effect would be a a crucial parameter for defining the heat dissipation during the local heating experiment.

To understand the differences in slope values resulting from different layers we should consider the absorption values resulting for these samples. The observation for the absorption was made *via* UV-vis spectrometer. Figure 3.9 shows the absorption spectra in the range of 500 to 600 nm for mono-, bi- and tri-layer hBN on sapphire.

To our surprise we observe that monolayer has the strongest absorption (0.20 %) where as the bilayer is showing the smallest absorption of 0.09%. The trilayer h-BN however, shows an absorption of 0.17%. The higher values of thermal conductivity reported for CVD grown h-BN samples have always taken the absorption to be either 10 % [120] or 6 % [121]. First, this comes from the fact that their substrate is not transparent, allowing the light to be reflected and absorbed twice. Still these values are very high compared to graphene (2.3%) which is a good absorber as a zero gap semiconductor. Alternatively, it could be due to the fact that they had thicker samples. However, Cai *et al.* [108], showed that for 514.5

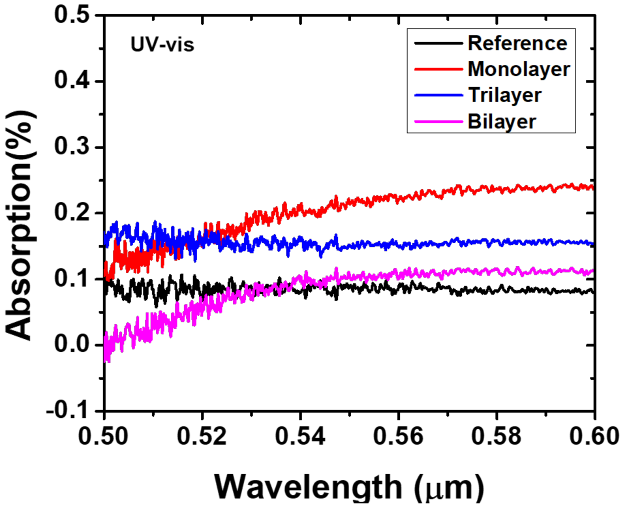

Figure 3.9: **Optical absorption of CVD grown h-BN on sapphire**: Absorption spectrum of 1-3 layers of h-BN on sapphire and sapphire alone as reference (black)

nm wavelength the absorbance values (0.35 ± 0.14%, 0.62 ± 0.19%, and 1.04 ± 0.10%) increase with number of layers (1-3 layers) respectively. Despite the clear discrepancy we can say that the range of absorption values for us are closer to the values reported by Cai *et al.*. Even though, we observe the physically plausible absorbance value in the literature [108] (since the number of the layers increase the sample volume hence more absorbance), it is important to mention that the h-BN layers were transferred via PMMA mediated transfer, which can induce difference in absorption values due to the remnant PMMA residues. Whereas in our experiments, the samples are directly grown on sapphire using CVD method, hence residue effect from wet transfer can be ruled out. Despite the observation of absorbance for 1-3 layers of h-BN on sapphire is strange, it is consistent with the $\partial\omega/\partial \mathrm{P}_{laser}$ values found in figure 3.8. Bilayer being the least absorbing sample gives least slope (absolute value of the slope). On the other hand, the reduced absorption value measured for bilayer sample cannot be explained.

In order to understand better the sample, we refer to the sample fabrication of the h-BN on sapphire [122]. The growth technique discusses few layer h-BN grown on sapphire. Using HRTEM it was shown that h-BN growth has taken place in the half Al terminated end of the sapphire, which makes the h-BN 30 ^{o} rotated to the orientation of sapphire. In addition, presence of corrugation is also a possibility. The growth report has also predicted the possibility of Moiré pattern between the half terminated Al and h-BN layer. With Moiré possibility the additional layer could play a strong role in modifying the optical properties and could explain our absorption measurements.

This is future prospect of this investigation to suspend the h-BN samples and make similar measurements in the absence of sapphire substrate. Based on our observations we can, however, estimate the thermal conductivity of mono-, bi- and trilayer h-BN.

3.2.3 Thermal conductivity

We use equation 3.1 to estimate the effective thermal conductivity. We estimate the effective thermal conductivity for mono- and bi-layer h-BN on sapphire to be 14 and 10 W/m.K. For tri-layer sample the effective conductivity turns out to be 7 W/m.K. The thermal conductivity of CVD grown few layer and 9L h-BN was reported to be more than 200 W/m.K [121, 120]. The difference between our measurements and the reported values can be explained on the basis of two reasons, 1) owing to thicker samples the absorption coefficient taken in literature is much stronger than our observation (in the order of 10% whereas we observe in the order of 0.1) and 2) our samples are supported which are under strong substrate effect whereas the reported samples are suspended. Moreover their growth substrates are metallic (Ni and Cu) and subsequently transferred on to (SiO_2/Si and 10 nm Au/Si) substrate which can lead to strong influence on the thermal dissipation.

As suggested above, we would like to transfer these samples over holes to estimate the thermal conductivity closer to intrinsic h-BN atomic layers. This would be seen as a future perspective of this investigation.

3.3 Raman thermometry: semi-metals and metals

Semi-metallic and metallic 2D materials are of great importance when it comes to device fabrication for applications. As mentioned earlier the heat loss in electronic devices are of great concern and hence we would aim to study the thermal response of these materials. 2H-TaSe2 is one of the layered material which shows rich charge density wave phase transitions. In this section, we will aim to study 2D semi metals and metals.

3.3.1 The case of semi-metal: graphene

3.3.1.1 Global heating

We have shown in chapter 2 that we can suspend graphene (see section 2.3.2), we will look at the thermal properties of suspended graphene. The heating is performed by an external hot plate. As a universal trend the G and 2D band frequencies show red shifts with increase in temperature.

Figure 3.10 shows the temperature dependent G and 2D band frequency for suspended graphene. The redshift observed with increase in temperature is consistent with literature [**?**, 124]. We fitted the data presented in figure 3.10, linearly in the first approximation. $\partial\omega_{G/2D}/\partial$T is found to be -0.026 ± 0.003 (-0.054 ± 0.002) cm^{-1}/K for G (2D) band frequency, which is consistent with literature [**?**].

In general the redshift observed in the case of graphene is guided by three factors, 1) TEC mismatch, 2) lattice expansion, 3) phonon anharmonicity. The three factors are dependent on each other. We can however, ignore the first factor since we are in suspended case. Interestingly, we observe the $\partial\omega_{2D}/\partial$T is nearly twice the $\partial\omega_G/\partial$T. We attribute this to the 2 phonon origin of 2D band, which enhances

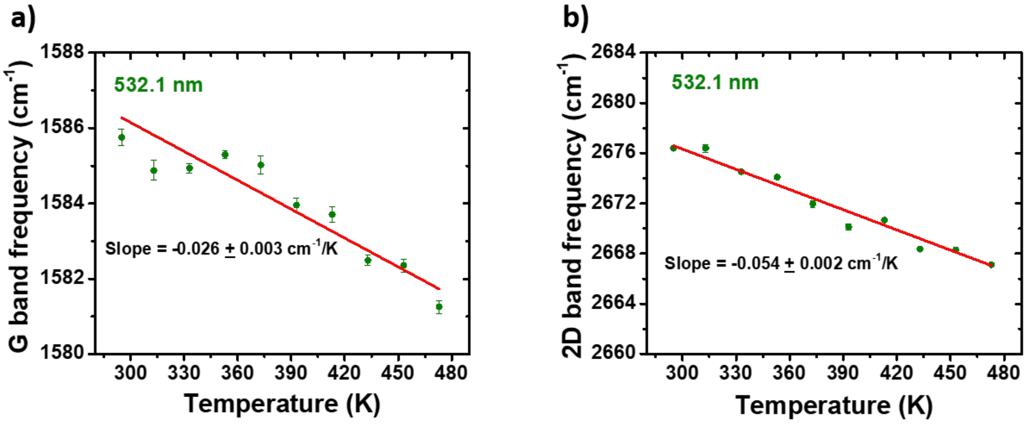

Figure 3.10: **Temperature evolution for optical phonons of suspended graphene**: Temperature dependence of (a) G band frequency and (b) 2D band frequency. The red line shows the linear fitting of the data.

the phonon anharmonicity contribution. The lattice expansion however, directly relates to the vibration at Γ point of graphene. We will detail this observation in chapter 4.

We will now discuss the effect of local heating of graphene on different substrates in order to study the substrate effect, which we will discuss in next section. We have divided the next section in 2 parts, CVD grown graphene suspended and mechanically exfoliated graphene on different substrates.

3.3.1.2 Local heating: suspended graphene

Figure 3.11 shows the evolution of G and 2D band frequency for local heating in suspended graphene. Typical redshift is observed for both G and 2D band frequency as reported in literature [6]. We fit the data linearly in first approximation as we did for global heating.

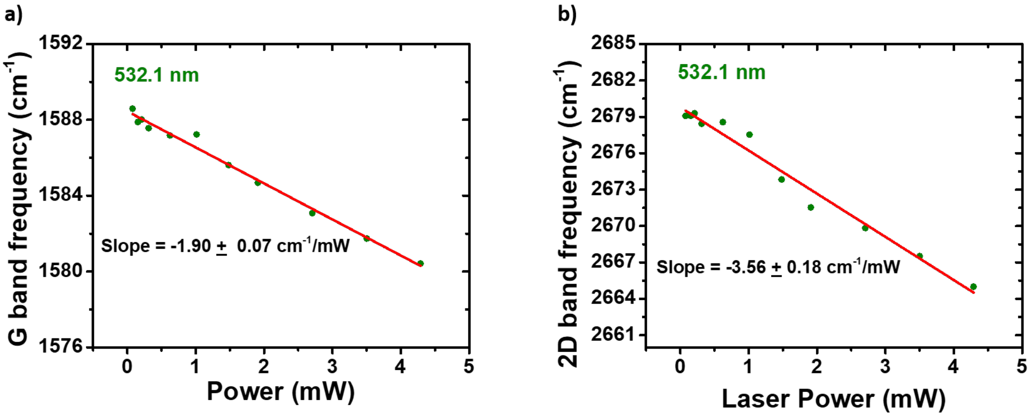

Figure 3.11: **Local heating of suspended graphene**: Laser power dependence of (a) G band frequency and (b) 2D band frequency. Red line shows the linear fit.

The $\partial\omega_{G/2D}/\partial \mathrm{P}_{laser}$ is obtained from the linear fitting. We observe similar trend as in case of global heating meaning by the $\partial\omega_{2D}/\partial \mathrm{P}_{laser}$ is nearly twice the value reported for $\partial\omega_{G}/\partial \mathrm{P}_{laser}$ which is consistent with reported literature [1, 2]. In fact the reason for such observation can be attributed to the similar reasons as in case of global heat.

We observe the $\partial\omega_{G}/\partial \mathrm{P}_{laser}$ to be -1.90 cm^{-1}/mW, which is slightly larger than the value reported by Balandin *et al.* (-1.29 cm^{-1}/mW). We attribute this difference to the nature of graphene, since we use CVD grown graphene whereas the reported value is mentioned for mechanically exfoliated sample. For the 2D band we observe that $\partial\omega_{2D}/\partial \mathrm{P}_{laser}$ is -3.56 cm^{-1}/mW which compares well with the unique data reported for 2D modes (-3.0 cm^{-1}/mW) [2].

Interestingly, we would like to add that the case of suspended graphene is reported in literature regarding local heat whereas the reports of local heating of graphene on different substrates is not available. We would be discussing it in next section.

3.3.1.3 Exfoliated graphene on different substrates

Now we will try to investigate the substrate dependence of exfoliated graphene regarding the local heat [28]. We try to understand the $\partial\omega_{G}/\partial \mathrm{P}_{laser}$ for exfoliated graphene on different substrates to realize the effective way of heating. A crucial observation in some cases is the degeneracy of G band is lifted due to the substrate interaction: sapphire and fused silica (now on it will be called spectrosil2000) are two such substrates. But in case of sapphire the splitting of G band takes place at higher laser power (1.0 mW) value than for spectrosil2000 (0.2 mW). These non-degenerate G bands frequencies are named as G^{-} and G^{+} according to their frequency value.

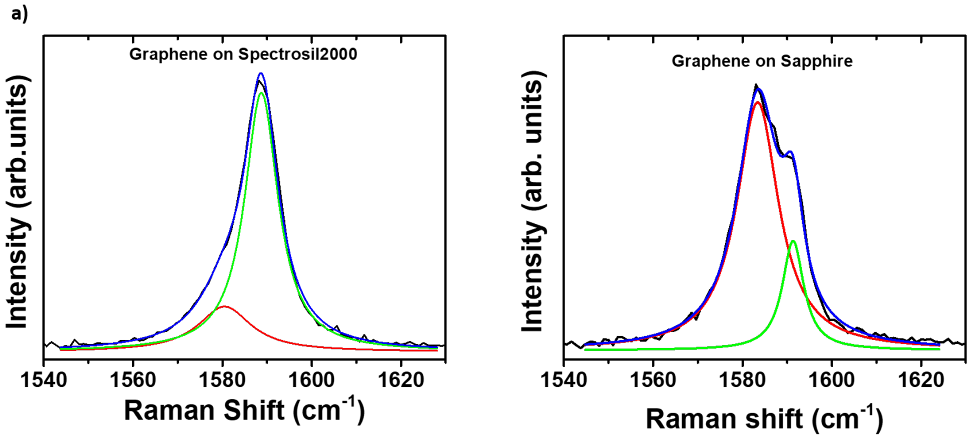

Figure 3.12: **Raman Spectrum of G band**: Raman Spectrum of G band for mechanically exfoliated graphene on (a) spectrosil2000 and (b) sapphire, the fitting function is Lorentz.

Figure 3.13(a) shows the G band frequency evolution with power for mechanically exfoliated graphene on different substrates. Figure 3.13(b) shows the corresponding $\partial\omega_{G}/\partial \mathrm{P}_{laser}$ values with different substrates. The case of suspended graphene shows the highest value of $\partial\omega_G/\partial P_{laser}$, which is -1.90 cm^{-1}/mW indicating the efficient heating. On the other hand we observe range of values for different substrate. From no slope on h-BN to -1.48 cm^{-1}/mW (closest to suspended case among all) for SiO_2/Si. Interestingly, G^+ resulting from graphene on sapphire shows similar slope value on SiO_2/Si. However, we know that the splitting of G peak already indicates the deviation of sample from its isolated properties, hence we cannot rely on such substrate. Spectrosil2000 shows nearly $1/3^{rd}$ of the slope observed in case of suspended samples. The splitting of G band suggests that strain induced by these substrates lifts the degeneracy of G band thereby the phonon propagation becomes anisotropic. It can be interesting to study such effects with spatial imaging in order to check this hypothesis and clarify the role of the substrate on thermal properties of graphene.

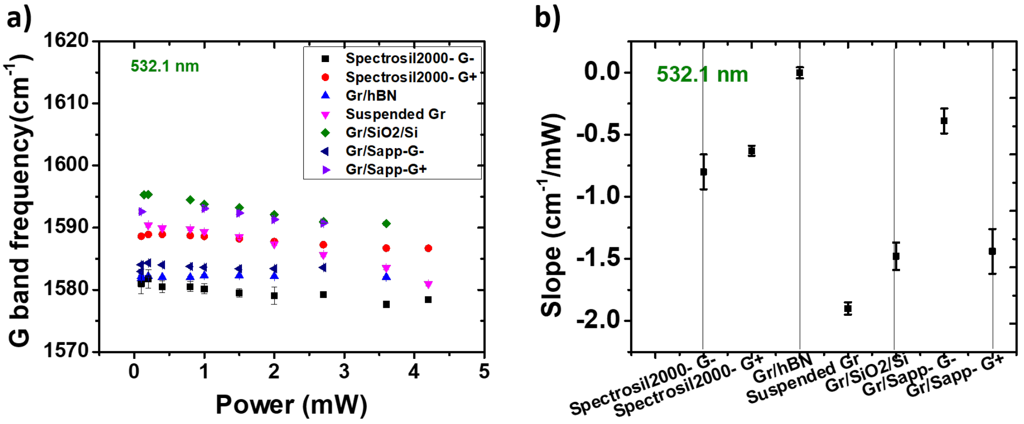

Figure 3.13: **Local heating of mechanically exfoliated graphene on different substrates**: (a)Substrate dependent G frequency variation with power (using 532.1 nm), (b) Slope of G band on different substrates.

We can clearly conclude that to isolate graphene thermally from the environment, the best possible way is to suspend it. Any other substrate immediately couples with it thereby affecting its behavior. The effect of substrate is very strong for observing the local heating in graphene. From the above study we can infer that in order to investigate the intrinsic thermal properties of 2D materials, it would be ideal to suspend them. We will see in chapter 5 that the samples on transparent substrates can also be studied under 2LRT.

3.3.2 The case of metals: 2H-$TaSe_2$

3.3.2.1 Global heating

2H-$TaSe_2$ is a 2D material with metallic properties. In fact, bulk 2H-$TaSe_2$ has a unique complex phase diagram: it exhibits an incommensurate CDW transition at 120 K, followed by a lock-in transition into a 3 × 3 commensurate CDW phase at 90 K, in which superconductivity emerges at extremely low Tc = 0.14 K. Moreover, in theoretical calculations it was shown that in the 2D limit 2H-$TaSe_2$ shows strong CDW effects and the predicted T_c was calculated to be 2.2 K [125, 126]. Due to its rich electronic landscape, it attracts attention for its thermal properties as well. Figure 3.14 shows an exfoliated image of mono- and bilayer 2H-TaSe$_2$, along with Raman spectra taken at room temperature for bilayer sample. We would study the bilayer sample here since the monolayer samples show too weak signal to be detected. Figure 3.15 shows the E$_{2g}$ and A$_{1g}$ mode dependence on temperature for bilayer 2H-TaSe$_2$. A linear behavior is observed except at 373K and 298K. Since the location of the probed spot changes with increase in temperature due to thermal expansion of heating stage, we attribute it to sample inhomogeneity. Excluding these points, we obtain consistent $\partial\omega_G/\partial$T values for E$_{2g}$ and A$_{1g}$ mode with temperature as mentioned in literature [127].

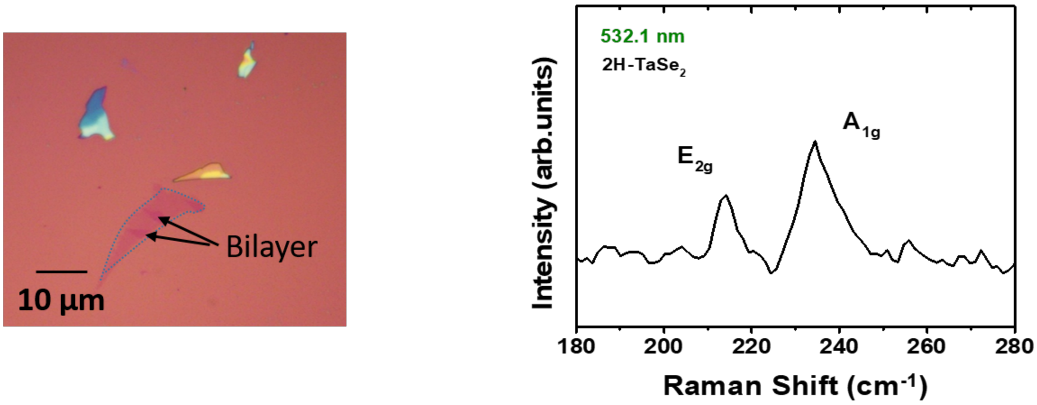

Figure 3.14: **Mechanically exfoliated 2H-TaSe$_2$**: (left) Exfoliated mono- and bilayer 2H-TaSe$_2$ on SiO$_2$/Si, bilayers are shown by arrow and blue dashed contour shows the monolayer region, (right) typical Raman spectrum of bilayer 2H-TaSe$_2$ at room temperature.

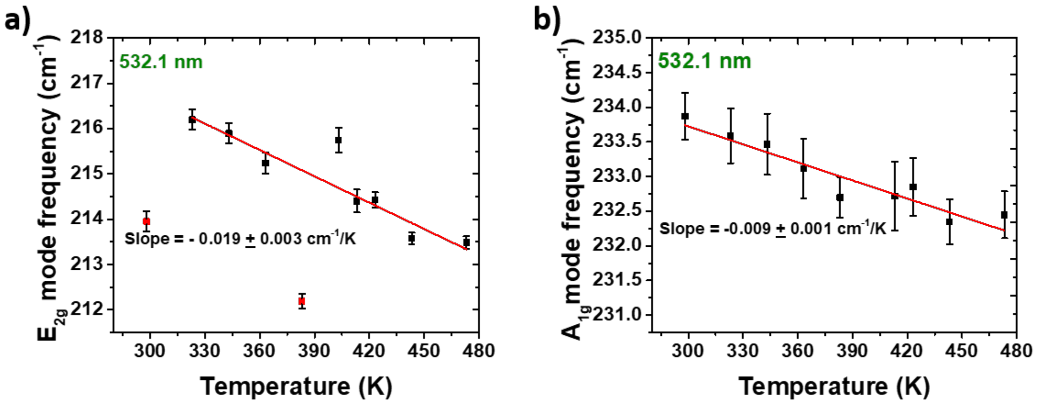

Figure 3.15: **Temperature dependent Raman modes of mechanically exfoliated 2H-TaSe$_2$**: Temperature dependence of (a) E$_{2g}$ and A$_{1g}$ mode of 2H-TaSe$_2$, red points have been intentionally left for the fitting purposes.

Since the samples are exfoliated on the substrate, we shall have 3 major contributors to the red shift observed, which are thermal expansion coefficient mismatch , lattice expansion and phonon anharmonicity. Thermal expansion coefficient (TEC) mismatch could be a major role player since TEC for 2H-TaSe$_2$ (bulk) is reported -8x10 $^{-6}$/K [128] and for SiO$_2$ (bulk) it is 0.5x10^{-6}/K. The difference in TEC is nearly one order of magnitude which would cause a tensile strain on 2H-TaSe$_2$. As observed in case of h-BN, we expect that the tensile strain may reduce the temperature coefficient. It is however, important to point out that the TEC value used here is for bulk system which could be different in the case of bilayer TaSe$_2$ and thus change our understanding of this behavior. We can study same samples under suspended condition to understand the TEC contributions, which can be scope of future work. We can add to our understanding from local heat information, which shall be discussed in next section.

3.3.2.2 Local heating

Now we will discuss the local heating experiment in case of 2H-TaSe$_2$. Mahajan *et al*, observed that the PL for thin film 2H-TaSe$_2$ is around 2.08 eV [129]. Since the observed PL energy is closer to 1.96 eV (632.8 nm wavelength) we would use this wavelength for our measurements.

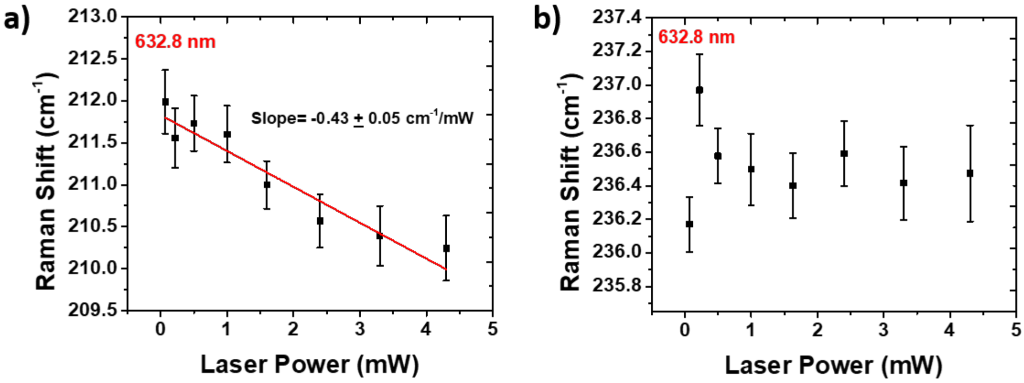

Figure 3.16: **Local heating of mechanically exfoliated 2H-TaSe$_2$ using different excitations**: Power dependence for few layer 2H-TaSe$_2$ (a) E$_{2g}$ mode using 632.8 nm excitation and corresponding (b) FWHM.

Interestingly, an article shows a heating effect using 2 different laser powers for thin film of 2H-TaSe$_2$ while using an excitation of 632.8 nm [127].

Figure 3.16(a,c) shows the E$_{2g}$ mode frequency with laser power. It is noteworthy that the case of 632.8 nm shows us a redshift trend. Local heating via 632.8 nm laser shows a linear slope of -0.43±0.03 cm^{-1}/mW. In the literature, Balandin *et al.* present a slope value of -1.34 cm^{-1}/mW, which is 3 times that of our observation, it is also important to mention that his observation is result of mere 2 points of power so we can ignore this discrepancy [127]. We can attribute the redshift to the resonance effect of the laser line with the bandgap, which ensures effective heating thereby leading to redshift.

3.3.3 Thermal conductivity

We estimate the effective thermal conductivity values in case of suspended graphene using the G band slopes. Using our measured absorption values for suspended graphene samples (2.9% , see chapter 4, section 4.3), we can estimate the thermal conductivity to be 187 W/m.K which doesn't match (underestimation, u.e.) with reported experimental value (2500 W/m.K) by Ruoff *et al.* and 5000 W/m.K by Balandin *et al.* (as discussed in chapter 1, section 1.4.2.3).
However, the estimation of the thermal conductivity of 2H-TaSe$_2$ cannot be done since we are using 2 different wavelengths for global and local heating and the absorption values are different in these two wavelengths [129].

We will now look into the possible association of electronic structure and $\partial\omega/\partial \mathrm{P}_{laser}$, $\partial\omega/\partial \mathrm{T}$.

3.4 Electronic structure and thermal response

To include all the observations of above-mentioned experiments along with literature values, we can discuss the results in two parts, first discussing the first order thermal coefficient $\partial\omega/\partial \mathrm{T}$ (global heat) and second discussing the $\partial\omega/\partial \mathrm{P}_{laser}$.

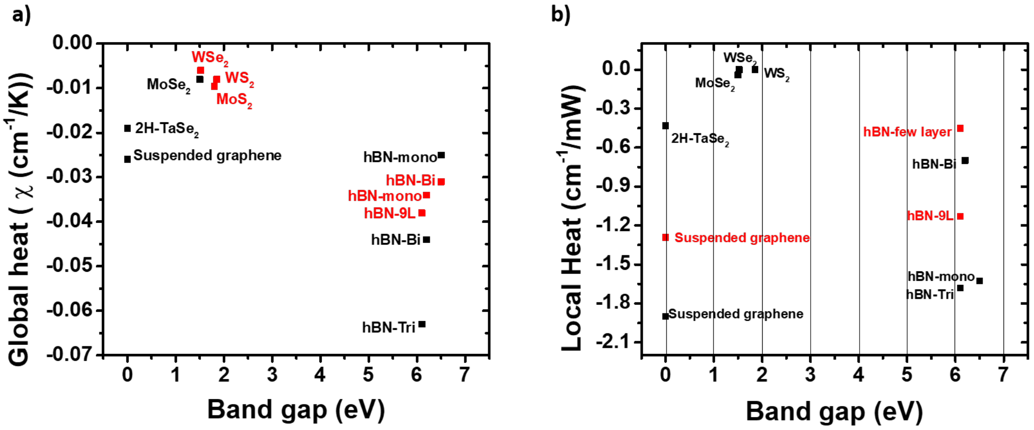

Figure 3.17: $\partial\omega/\partial \mathbf{T}$ **and** $\partial\omega/\partial \mathbf{P}_{laser}$ **with electronic structure**: Bandgap otted against (a) $\partial\omega/\partial \mathrm{T}$ and (b) $\partial\omega/\partial \mathrm{P}_{laser}$, red points correspond to literature [70, 69, 49, 121, 120, 6].

From the figure 3.17(a) we plot the $\partial\omega/\partial \mathrm{T}$ against the bandgap of corresponding to the materials investigated. Interestingly, we notice that the samples with low bandgap present a narrow range of temperature coefficients (-0.006 to -0.02 cm^{-1}/K). For insulators, however, we observe a wide range of temperature coefficient (-0.025 to -0.063 cm^{-1}/K).

It is crucial to mention that such an association (between global and local heating and electronic structure) cannot be established due to several other parameters at play, for instance the substrates for rest of the samples are not same as the case of insulators (in our case). However, if we incorporate the values from literature (samples on SiO$_2$, same as rest of the samples in our case), the observation remains same due to the fact the $\partial\omega/\partial \mathrm{T}$ values are very close to our observations (see figure 3.17(a)). Despite initial hint that there is an association of electronic structure and $\partial\omega/\partial$T, we need a more thorough investigation to establish a clear dependence.

Table 3.1: **Different thermal parameters of various materials** : Thermal conductivity of different materials using Balandin *et al.* formalism (o.e.- overestimation and u.e.- underestimation). *, †, + show the SiO_2/Si, sapphire and 10 nm Au/Si substrates, respectively.

	$\partial\omega/\partial$T	$\partial\omega/\partial P_{laser}$	Absorption (%)	κ (W/m.K)
Monolayer $MoSe_2^*$	-0.008	-0.04	5.7[49]	1814.3 (o.e.)
hBN-mono†	-0.025	-1.627	0.202	14
hBN-mono$^+$	-0.034 [120]	N/A	0.35 [108]	751
hBN-bi†	-0.044	-0.699	0.09	10
hBN-bi$^+$	-0.031 [120]	N/A	0.62 [108]	646
hBN-tri†	-0.063	-1.682	0.165	7
hBN-tri*	-0.038 [108]	N/A	1.04	602
Suspended graphene	-0.03	-1.90	2.9	187 (u.e.)
2H-$TaSe_2^*$	-0.019 (532.1nm)	-0.43 (632.8nm)	N/A	N/A

Figure 3.17(b) shows the $\partial\omega/\partial P_{laser}$ against the bandgap. Such dependence does not show similar pattern as figure 3.17(a). However, it is interesting to notice that the heating mechanisms for each of the cases described above have different origins. For instance, the case of direct bandgap semiconductor does not result in comparable values of $\partial\omega/\partial P_{laser}$ when seen with other samples due to the strong radiative re-combinations. The case of graphene is entirely different, here a strong electron phonon coupling ensures a strong optical heating effects even at very low powers (0-2 mW). Whereas the substrate for insulator is heavily straining the sample which changes the mechanism of heating. Interestingly, if we monitor only the insulator case, three cases present different range of values which makes it difficult to comment on any pattern seen in the graph.

The scattered nature of slope values hints towards the fact there is no clear dependence of $\partial\omega/\partial P_{laser}$ on the bandgap of material. However, it would require some material such as MoO_2 which has a bandgap of 3.85 eV, in order to establish dependence of bandgap and $\partial\omega/\partial P_{laser}$ as well as $\partial\omega/\partial$T. Such a proposition can be taken for future prospects of this work.

3.5 Conclusion

In this chapter we have tried to study different materials on various substrates for their thermal properties. We have determined the effective thermal conductivity of different systems based on their electronic properties using Raman thermometry. Table 3.1, sums up our observations, we have systematically observed the estimation of effective thermal conductivity using the formalism of Balandin *et al.*. Underestimation for the case of insulators and semi-metals is observed whereas the model overestimates the effective thermal conductivity for semiconductors (table 3.1). It is another hint that we need an alternative and robust approach to estimate the effective thermal conductivity for 2D materials. On the other hand, we can argue that the relation given by Balandin *et al.* is based on linear Fourier equation, and since the cases studied here may not follow this condition, owing to their limiting thickness, we cannot apply this relation directly to such cases. We will try to further our observations in radially symmetric conditions in chapter 4.

We have also investigated effect of local heating for mechanically exfoliated graphene on different substrates. We observe that different substrates affect the graphene differently, thereby we notice different $\partial\omega_G/\partial\mathrm{P}_{laser}$ for different substrates. Alternatively, it can be inferred that a good adhesion must be ensured for electronic devices fabricated out of these materials in order to better manage the heating issues. In addition to the process of studying the thermal effect of 2D materials on various substrates, we learn that the best configuration to study the minimally disturbed thermal property of 2D material is suspended case. Now we will turn our attention to strain contributions (during global and local heating) in suspended samples or its dependence on geometry, which we shall be doing in chapter 4.

Chapter 4

Effect of geometry on heat response of suspended graphene

As we discussed in the last chapter, the model considered by Balandin *et al.* does not reliably estimate the thermal conductivity for different 2D materials. Such experiments have been used to calculate thermal conductivity of suspended 2D materials starting from graphene [6]. Since the modelling used by these approaches are based on Fourier law, an investigation of the parameters involved in these studies is required. A careful study of the two experiments (global and local heat) can be done for studying the thermal properties of 2D material.

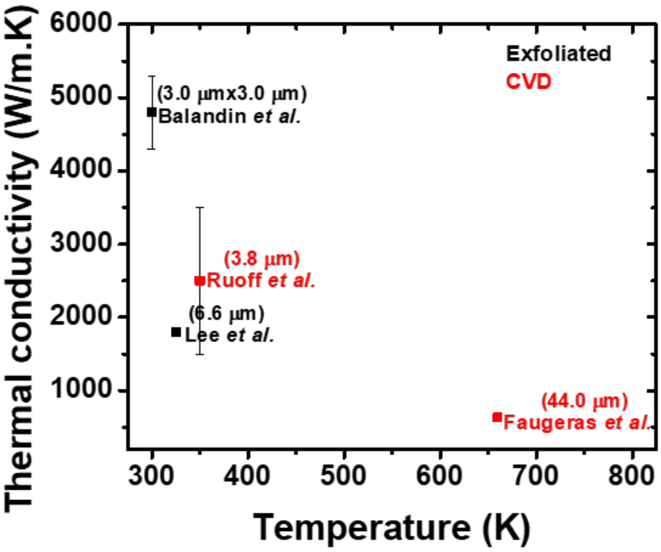

Figure 4.1: **Thermal conductivity of suspended graphene using optothermal methods**: Different groups have used different models in order to estimate the thermal conductivity. Balandin *at al.* used a trench geometry, whereas other groups used circular geometry (diameter of suspended part is mentioned in μm). Except Lee *et al.*, all the other values reported are using G band as thermometer mode. Faugeras *et al.* have used Stokes-anti Stokes intensity ratio for temperature estimation.

There are several parameters which can affect the heat response of single layer graphene, such as the size of the suspended graphene. The size of the suspended graphene has a direct relation to the nature of transport in graphene. Theoretical predictions have been made regarding ballistic thermal transport in graphene [29]. The interest in suspended graphene over different hole size dependence of thermal conductivity was investigated by Ruoff *et al.* and Bae *et al.*. The latter group measured the thermal conductivity in different sizes (45-260 nm) of exfoliated graphene nano-ribbons (on SiO_2/Si substrate) *via* using a local temperature-dependent electrical resistance as the thermometer (heater-sensor approach, discussed in section 1.4.1.1) [4]. They show that the thermal conductivity scales as square of the width of the nano-ribbons ($\propto W^2$). In this paper, they also estimate the mean free path about 100 nm, which was claimed to be 35% of the theoretical ballistic flow limit. The Raman optothermal method has been used by several groups for estimation of thermal conductivity, as shown in figure 4.1. It is important to mention that we cannot compare the findings of Bae *et al.* with rest of the reports since the studies made by Bae *et al.* are done on substrate. Ruoff *et al.* measured samples with disk radius in the range of 1.5 to 4.9 μm [73], where they found no dependence of thermal conductivity on the suspended area. However, it can be argued that the error bars of the estimation were too high to establish a conclusion. Faugeras *et al.*, however, estimated the thermal conductivity of suspended graphene of relatively large radius of 22 μm [27]. As discussed in chapter 1, the thermal conductivity reported by Faugeras *et al.* was nearly 1/10 th of the values reported by Ruoff *et al.*. Such discrepancy was attributed to the high laser power used by Faugeras *et al.* (see section 1.4.2.3).

However, a systematic study of thermal conductivity estimation for the sample sizes between the radius 4.9 (largest sample of Ruoff *et al.*) and 22 μm (sample size of Faugeras *et al.*) is missing in literature. Both articles consider G band frequency as the thermometer mode for extracting thermal conductivity. 2D mode can also be used as thermometer [2] and it was shown that the 2D mode has resulted in similar values of thermal conductivity as the G band. Lee *et al.* has demonstrated that using 2D band, one can estimate the thermal conductivity of 1800 W/m.K, which is closer to the value estimated by Ruoff *et al.*. These studies invoke different approaches of modelling (however, they all rely on the assumption of applicability of Fourier's Law) to extract thermal conductivity, which makes it difficult to compare them, which shows that the debate of thermal conductivity is not settled. One can, however, monitor the laser power dependence of G and 2D band frequencies to the size of suspended graphene, in order to answer the question of 'what is the nature of thermal transport?'. Despite the fact that, with these observations one cannot conclusively establish the transport regime, one can always qualitatively get hints for diffusive or non-diffusive transport.

Owing to their Fourier like modelling approaches, we need a systematic study to look at the coefficients involved in the laser heating and hotplate experiments. In this chapter, we focus on analyzing the effect of global and local heating on different radius (in the range of 1.6-7 μm) of suspended graphene and extracting a thermal calibration for temperature profiles. We will also show that by relating the thermal evolution of 2D band frequency to laser power evolution, we will show that the optical power dependence of 2D band frequency is a consequence of heat.

4.1 Effect of global heating in suspended graphene

As discussed in section 1.4.2.3, one first needs to record the Raman response of suspended graphene in a given range of temperature before being able to conclude on the response to thermal excitation from a focused laser (also known as 1 laser Raman thermometry). It is therefore needed to heat the sample globally with a hotplate at a well-known set-point temperature. We use a suspended graphene with circular disk geometry as discussed in chapter 2 (section 2.3.4). In this section we shall detail the effect of global heat on different radius of suspension. Since we heat the whole sample in case of global heating, the response of graphene comes from phonon- phonon interaction and lattice dynamics [130]. Electron-phonon contribution remains constant throughout the experiment due to the fact that we do not apply electrical biases and thermal effects do not contribute to it [130]. Generally G band of graphene is considered to be thermometer mode. We will follow both G and 2D band frequencies in order to extract the thermal behavior of monolayer suspended graphene.

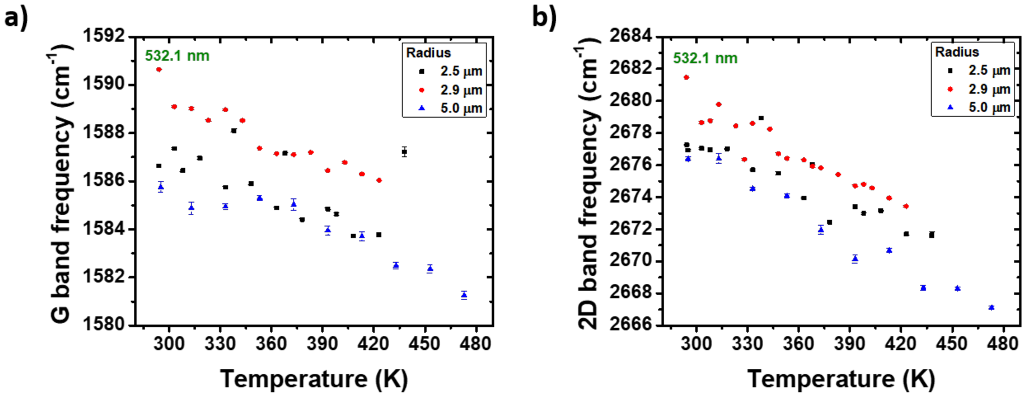

Figure 4.2: **Frequency *vs* temperature for different radius of suspended graphene**: (a) G band frequency vs temperature, (b) 2D band frequency vs temperature. The measurements are done at the center of the suspended graphene. The error bars are within the shown points.

Figure 4.2 presents the frequency of G and 2D band plotted against temperature for different radius of suspended graphene. Redshift was observed as reported in literature [124] [130]. It is worth noting that the different suspended samples have different initial G and 2D band frequencies. The change in initial frequency of the G and 2D bands may depend on the sample fabrication conditions since the fabrication process of suspended graphene leads to different strain and doping (section 2.3.4). These parameters being very locally dependent, induce a statistical response of initial frequency of G and 2D band, even for the same batch of graphene. Thus we will not focus on initial conditions as important parameters but only on the red shift observed for graphene optical phonons which is universal with temperature. Let's now discuss the $\partial\omega/\partial$T (first order temperature coefficients) for G and 2D band frequency.

4.1.1 Evolution of G and 2D bands

Effect of global heat and corresponding $\partial\omega_{G/2D}/\partial$T have been widely reported in literature [?]. The ranges of values reported for the slope of G (2D) band is -0.015 to -0.070 (-0.070 to -0.100) cm^{-1}/K [?]. The reason for these dispersions has been attributed to number of parameters such as the quality of graphene, substrate used and the environment of the graphene [131].

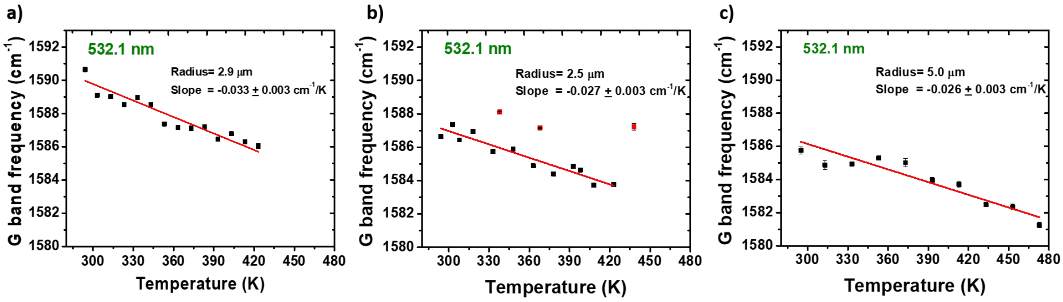

Figure 4.3: **Linearly fitted G band frequency with temperature for different radius**:(a) 2.5μm, (b) 2.9μm, (c) 5.0μm. The measurement is performed at the center of the suspended graphene. Red dots represent the frequency recorded while cooling the sample. The error bars are within the experimental points.

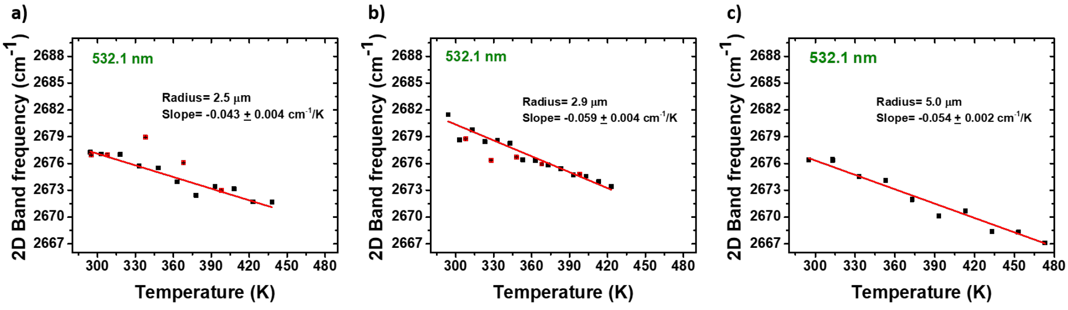

Figure 4.4: **Linearly fitted 2D band frequency with temperature for different radius**:(a) 2.5μm, (b) 2.9μm, (c) 5.0μm. The measurement is performed at the center of the suspended graphene. Red dots represent the frequency recorded while cooling the sample. The error bars are within the experimental points.

The data presented in fig 4.2 are fitted linearly (consistent with literature) which is shown in fig 4.3 and 4.4 for each radius. Red points correspond to frequency during the cool down, which indicate some hysteresis in the sample. The issue of hysteresis has been discussed in literature [?], we will not discuss them here. With three different radius ranging from 2.5 to 5.0 μm, we observe a range of slope values for G (-0.026 to -0.033 cm^{-1}/K) and 2D (-0.043 to -0.059 cm^{-1}/K) band. Our experimentally extracted values of $\partial\omega_G/\partial$T and $\partial\omega_{2D}/\partial$T are indicated in fig 4.3 and 4.4, which match well with reported literature [**?**]. Such a narrow range can be attributed to the same source of CVD grown graphene.

The red shift observed in optical phonons under global heating can be explained by anharmonicity in which one can distinguish two contributions: phonon-phonon interactions and lattice expansion as discussed by Bonini *et al.*[130]. Phonon-phonon interactions have major contributions from 3-phonon and 4-phonon processes. It is important to note that the lattice expansion causes a blue-shift and the phonon-phonon interactions cause a red-shift. The overall red shift can be attributed to the prominent phonon-phonon interaction as proposed by Bonini *et al.* [130]. It is also worth mentioning that the change in G band frequency above 300 K can be approximated to a linear response (which is not possible for temperature below 300 K) [130]. It justifies the linear fitting of our measured data.

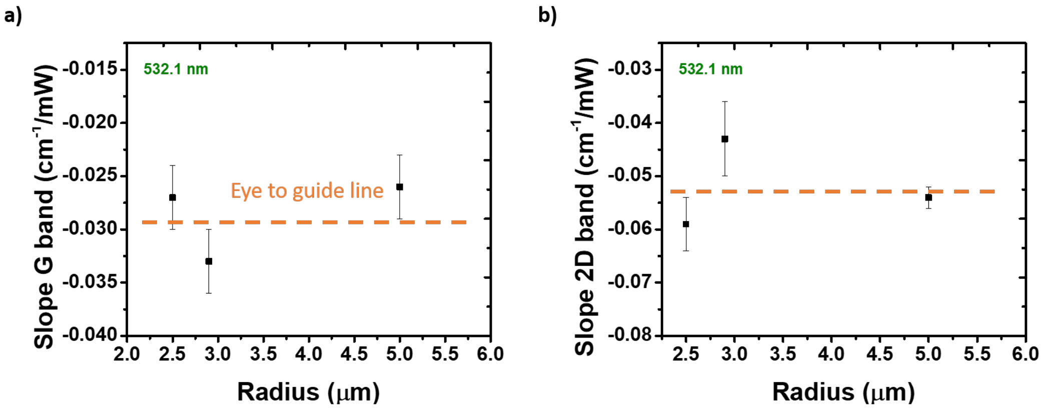

Figure 4.5: **Radius dependence**: Slope of (a) G band and (b) 2D band for global heating. The measurement is performed at the center of the suspended graphene. A slope number resulting from linear fit for temperature evolution is shown for different radius of hole size.

Figure 4.5 shows the radius versus slope of G and 2D band frequencies, obtained from the linear fitting. Since the values obtained in our experiments are nearly constant within the error bar of measurement, without loss of generality we can assume that the global heat coefficient found in our samples can be averaged and taken as a universal number: for G (2D) bands, it is -0.029 cm^{-1}/K (0.053 cm^{-1}/K). Nearly constant value of thermal coefficient shows that quality of CVD grown samples is consistent from batch to batch.

We observe that the slope of the 2D mode is roughly twice the slope of the G mode. This is consistent with the literature[**?**]. This observation can be explained by considering the fact that the 2D band results from a 2-phonon Raman processes [61]. Effect of heat on each phonon is additive for a 2 phonon process, which enhances the overall effect of global heat twice (see figure 4.6). With an extent of universality in the ratio of 2D to G mode slope, we can hypothesize that the 2D mode thermal dependency is mainly due to heat, such a hypothesis has been demonstrated for G and 2D band in literature [2]. However, a systematic study for using the 2D mode as a thermometer is missing in literature.

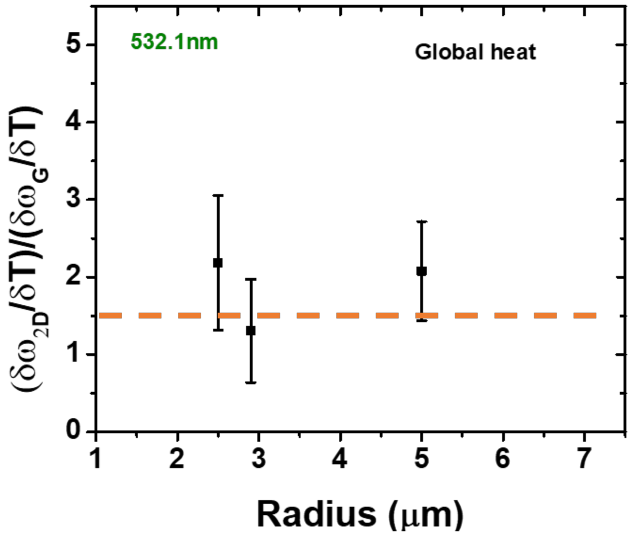

Figure 4.6: **Radius dependent slope ratio of 2D band to G band**: The ratio is calculated from taking ratio from individual slope values corresponding to each radius of hole size.

On a different note, it is important to mention that the samples with large radius (larger than 10μm) broke at the temperature range of 450-500K. As discussed before since these measurements are done in air, several parameters can be responsible for such observation. Large area membranes with radius larger than 10 μm are difficult to handle due to their sensitivity to airflow and temperature gradients. One of the hypothesis could be that strain evolution due to global heat would be key factor in this case. We will dedicate next section to discuss the strain in detail in order to understand the role of strain for membrane stability over different radius.

4.1.2 Strain analysis

In this section, we are going to discuss the strain evolution of graphene with temperature under global heating. The details of strain evaluation using the correlation plot for G and 2D band is done in chapter 1 (section 1.4.2.2). We shall use the same approach to estimate the strain and follow its evolution with temperature. Zero strain-zero doping point in the graph (which will be referred to as the origin ω_{G0}, ω_{2D0}) of corresponding Lee plot is estimated by suspending graphene on SiO_2 pillars [87]. This origin value of G and 2D band was found to be 1582 cm^{-1} and 2670 cm^{-1}, respectively [87]. Since the CVD growth process of graphene remains same, we can assume the same origin for our strain calculations.

Fig 4.7 presents the Lee plot with G and 2D band frequency evolution with temperature. Here the black (purple) dashed line represents the constant doping (strain) line (chapter 1). As discussed earlier, we see different starting position for different samples. Interestingly, all the samples show similar trend with increase in temperature. The initial negative strain indicates the compressive strain in

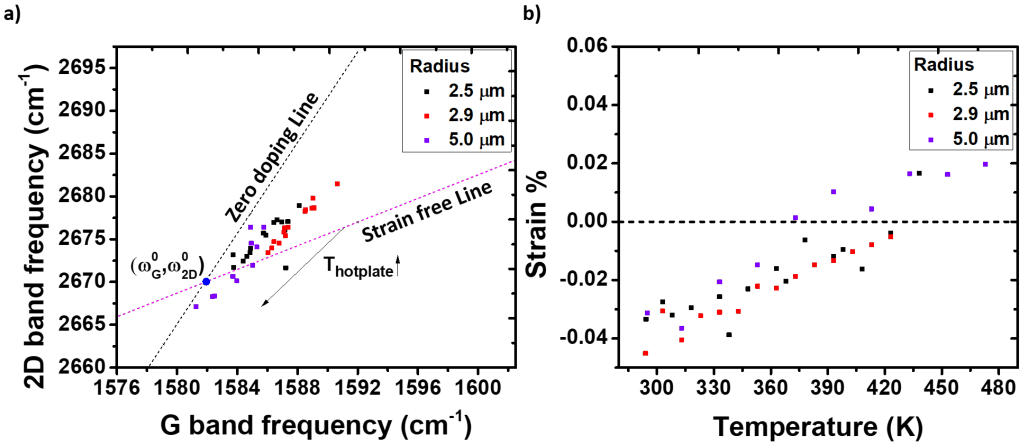

Figure 4.7: **Temperature dependent strain evolution for different hole size**: (a) Lee plot evolution with temperature, (b) Strain variation with temperature. The observations are made at the center of the suspended graphene. Lee plot shows the movement of the G and 2D band frequency towards the origin hinting upon the strain relaxation in suspended graphene. Corresponding to the estimated strain using Lee plot, shows a linear increase in strain with temperature.

the suspended membranes. With the temperature increasing, the G and 2D band frequencies approach the origin, which indicates increasing the temperature relaxes the membrane as a consequence of tensile strain. Interestingly, we observe that beyond certain temperature, the tensile strain goes beyond origin for sample with hole radius 5 μm (see figure 4.7(a)). Figure 4.7(b) shows the strain evolution with temperature. An empirical observation affirms a linear increase in tensile strain with temperature. Initial strain values show that samples have negative strain indicating a compressive strain. It is well known that annealing is one of the ways to relax strain in membranes [68]. The observed linear increase in strain with temperature can be attributed to the thermal relaxation.

We observe that the temperature at which the membrane is fully relaxed may depend on its radius. If we plot the $\partial\epsilon/\partial T$ against each radius, we see the strain evolution is constant, 3x10^{-4} %/K, with the size of suspended graphene as depicted in figure 4.8. We establish that for each 100 K increment in the sample, the strain relaxation is around 0.03 %. This number can be useful for sample fabrication process, to use annealing methods for producing strain-free suspended graphene. Experiments should be performed at 400 K, if we want to observe the behavior of a strain-free suspended graphene.

Since strain is an outcome of disturbance in mechanical equilibrium of structure and heat propagation also induces such stress, it is important to rule out the strain dominance in the studies of thermal transport. We can estimate the temperature induced strain in graphene by following the Grüneisen parameter. In a recent report, it is shown that Grüneisen parameter for graphene on Cu show no change in the temperature range of 300-800 K [?], our temperature range (300-480 K) falls well within this temperature range. Graphene supported by a substrate is always under some strain due to the substrate, however suspended graphene

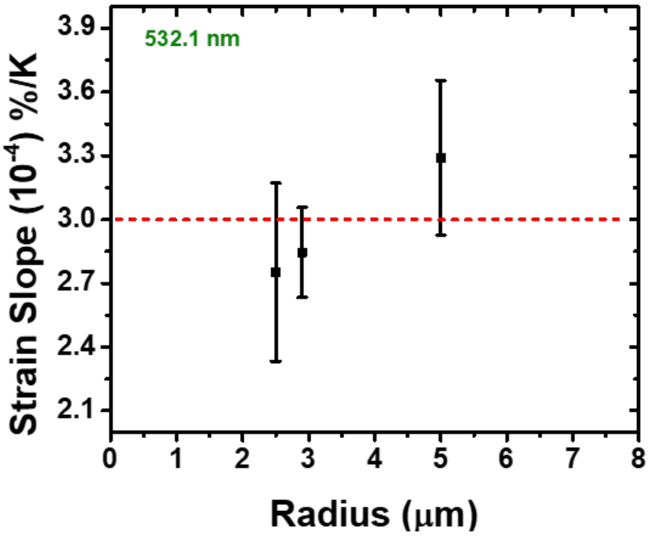

Figure 4.8: $\partial\epsilon/\partial$T **dependence on radius of hole size**: Strain evolution with temperature is fitted linearly using the data from figure 4.7(b).

has been shown to have least strain ($\sim 10^{-1}$ %) [87]. Therefore it is safe to assume that in our case of suspended graphene, Grüneisen parameters would remain constant throughout the experiment. The consequence of constancy of Grüneisen parameters is two fold: 1) the Lee plot can be used for all our data even at different temperatures, 2) even though the effect of thermal transport would always be affected by the strain in the system, we can assume dominance of thermal propagation over the mechanical strain for suspended graphene.

One of the crucial information is to understand the strain after the annealing experiment. In order to understand the reversibility of strain, we did the strain estimation by recording the G and 2D band frequency during the cool down. Figure 4.9 shows estimated strain with different temperature for 2 different radius (purple points show the points during the cool down). We can clearly observe the restoration of initial strain as the temperature is brought down to ambient value. However, we must notice that the strain evolution remain constant until 350K, we can infer that in this temperature range the strain contribution remains constant.

Global heating is a classical way to anneal the system, as discussed earlier in case of suspended graphene, we are required to anneal the samples at 400 K in order to release the initial strain in our samples. Furthermore, we can heat graphene locally using optical means. Local heating allows the heat to dissipate through the sample, which is why such experiment would shed more light about the thermal effects in suspended graphene.

4.2 Effect of local heating on suspended graphene

The advantage with local heating is that it is directly linked to the transport problem due to the local hot spot and the heat sink (the SiO_2). In order to

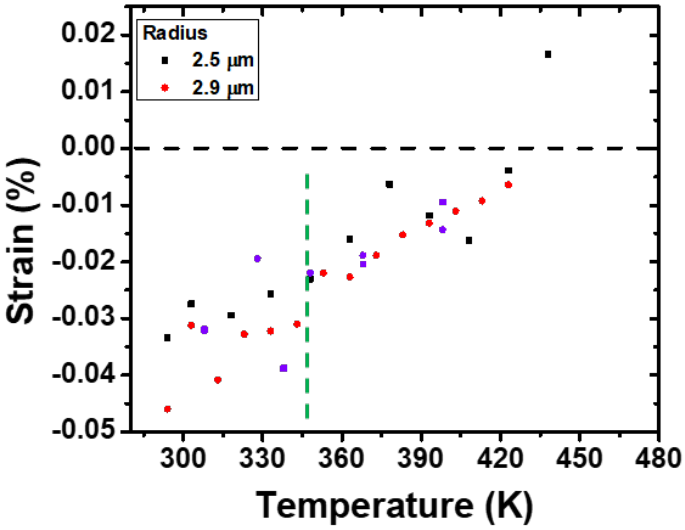

Figure 4.9: **Strain during the cool down**: Reversibility of strain for two different hole size. Red and black color represents the strain evolution with increasing temperature and purple color represents the points during the cool down experiment.

understand the thermal effects in suspended graphene, we would setup our problem from basic theoretical understanding. For simplicity, we take the classification of thermal transport as two regimes: diffusive and non-diffusive transport. In case of local heating, the hot-spot is kept in the center of the membrane. We can change the distance from hot-spot to the heat sink in 2 ways, 1) changing the radius of the sample, 2) changing the location of the hotspot by moving the laser or sample.

In the first case, as discussed before, the radius gives an estimate of 'how far' the heat sink (substrate) is from the heat source (hot-spot). Qualitatively, the $\partial\omega_G/\partial \mathrm{P}_{laser}$ can be related to how far heat is carried to the heat sink from the hot-spot. For instance, a smaller distance between heat sink and hot-spot, it should allow easier heat dissipation, compared to larger samples. In the second case, the motion of laser spot with respect to the sample would control the distance between the heat sink and hot-spot. For such case, $\partial\omega_{G/2D}/\partial \mathrm{P}_{laser}$ can be monitored with the spatial location of hot-spot.

We have dedicated these two types of experiments in two different sections (namely case 1 and case 2). We will mention them one by one, beforehand and try to analyze them under the diffusive model of transport (as discussed in figure 4.2).

4.2.1 Case 1: Dependence of G and 2D mode with hole size

As discussed in chapter 3, local heating can be induced by injecting the laser power at a desired spot of the sample, which is the topic developed in this section. Figure 4.11 presents raw data of laser power dependent heating for suspended samples of

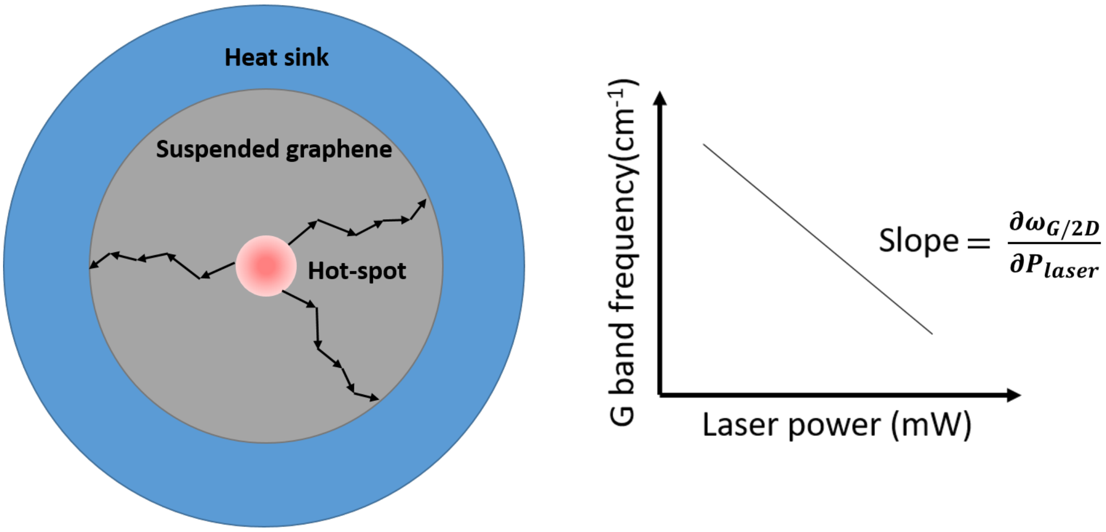

Figure 4.10: **Schematic of transport during local heat under diffusive model**: (Right) Blue region depicts the SiO_2 membrane, Grey region is suspended graphene and the red spot shows the laser spot (the hot-spot). The arrows represent the possible path taken by the phonons to carry the heat to the heat sink (SiO_2 in this case), head of the arrows represent a scattering event. (Left) With icreasing power we should observe the red shift of optical phonon frequency, which can be associated with slope after linear fitting as performed in literature [6].

different radius. A general trend of red-shift for G band frequency can be easily observed as in the reported literature [6]. The trend of 2D band frequency is also observed to be red-shifted.

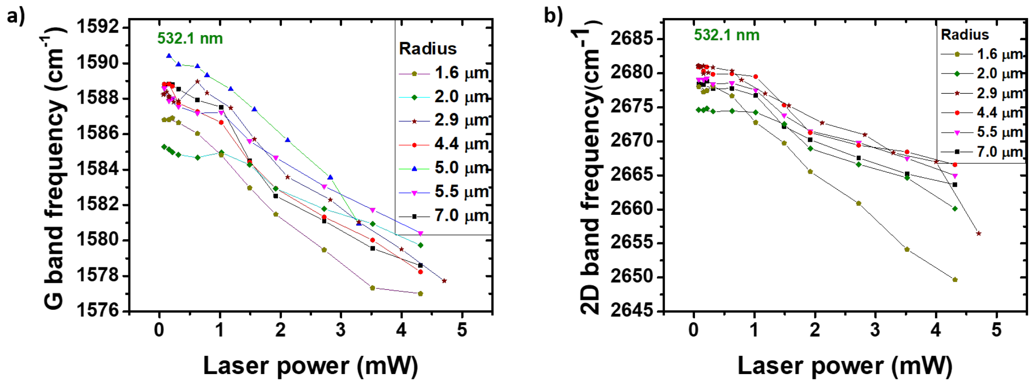

Figure 4.11: **Laser power dependent evolution for different radius of suspended graphene**: (a) G band frequency, (b) 2D band frequency. Different samples correspond to different transfer. Maximum power is adapted to not break the suspended membranes.

Like we observe a range of $\partial\omega_G/\partial\mathrm{T}$ ($\partial\omega_{2D}/\partial\mathrm{T}$) for global heating (4.1.1) for different hole sizes, similar observations would be made in case of local heating as well. The red shift observed for G band frequency is linear in the first approximation. Such approximation have been made in literature [6]. Figure 4.11(b) shows the trend of 2D band with power. 2D band frequency shows two regimes: a constant frequency with laser power (close to 1.0 mW) followed by a linear drop (laser power greater than 1.0 mW). We attribute this observation to the anharmonic nature of 2D band, which has been shown theoretically by Apostolov *et al.* and Bonini *et al.* [132, 130]. Following their model, there are two contributions to the frequency shift: 1) the 4-phonon processes and 2) electron-phonon coupling contribution.

As discussed by Apostolov *et al.* and Bonini *et al.*, the contribution of electron-phonon coupling leads to blue-shift of these frequencies however, 4-phonon processes strongly contribute to the red-shift of these modes. The competition of the two processes results in the strong temperature dependence [132]. 2D band being a result of 2 phonon process, it has stronger contribution of 4 phonon processes resulting in larger red-shift of 20 cm^{-1} (and stronger anharmonicity which is effectively seen as 2D frequency is constant at low power (less than 1.0 mW)) in comparison to the G band (red-shift of 10 cm^{-1}). We have only taken the linear contribution into account (laser power larger than 1.5 mW), for fitting purposes. We will discuss the slope dependence of G and 2D band frequency with hole radius in next section.

4.2.1.1 Evolution of G and 2D bands with laser power

As depicted in figure 4.11 the red shift is universal for G and 2D bands. With linear fitting we extract the slope for G and 2D band frequencies with laser power. Figure 4.12 shows the radius against the $\partial\omega_G/\partial P_{laser}$. It is interesting to note that we observe the $\partial\omega_G/\partial P_{laser}$ (-2.53 cm^{-1}/mW) is independent of the radius as well as the initial G band frequency. We tried to determine the radius dependence of initial frequency of G band but it does not show a clear dependence on radius of suspended membrane as well. Such observation would be interesting to discuss along with similar plot for 2D band frequency.

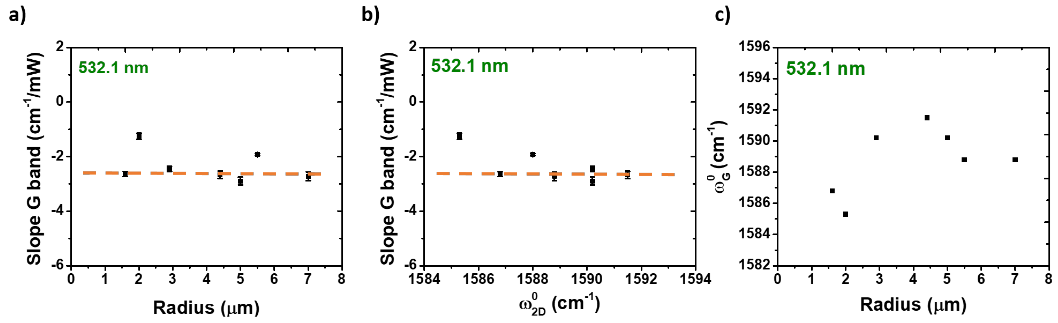

Figure 4.12: **Interdependence of $\delta\omega_G$/dP, Initial G band frequency and radius** (a) $\delta\omega_G$/dP *vs* radius, (b) Slope of G band frequency *vs* initial G band frequency and (c) Initial G band frequency *vs* radius. Slope is estimated by the linear fitting of the data shown in figure 4.11(a). Initial G band frequency is taken at the minimum laser power of 0.27 mW.

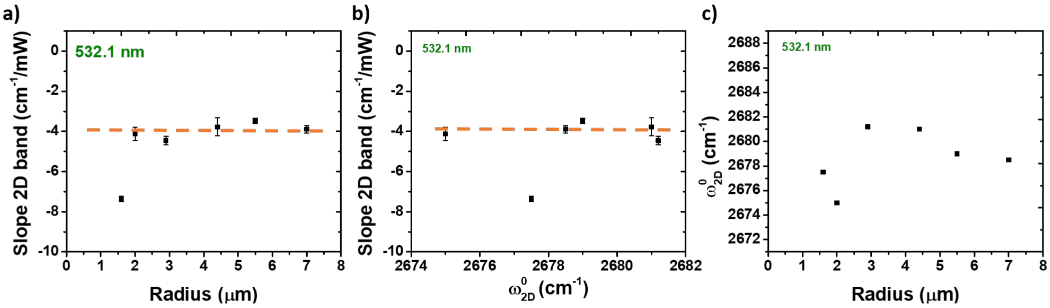

Figure 4.13: **Interdependence of 2D band slope, Initial 2D band frequency and radius** (a) slope of 2D band frequency *vs* radius, (b) Slope of 2D band frequency *vs* initial 2D band frequency and (c) Initial 2D band frequency *vs* radius. Slope is estimated by the linear fitting of the data shown in figure 4.11(b). Initial 2D band frequency is taken at the minimum laser power of 0.27 mW.

Analogous to figure 4.12, similar observation was made corresponding to 2D band. Figure 4.13 depicts the radius dependence of 2D band slope. Similar to G band results, independence of slope (-4.0 cm^{-1}/mW) from radius and initial 2D band frequency was observed. However, when we compare the trend of initial 2D band frequency with radius of suspended samples, we notice similar behavior as the case of G band frequency.

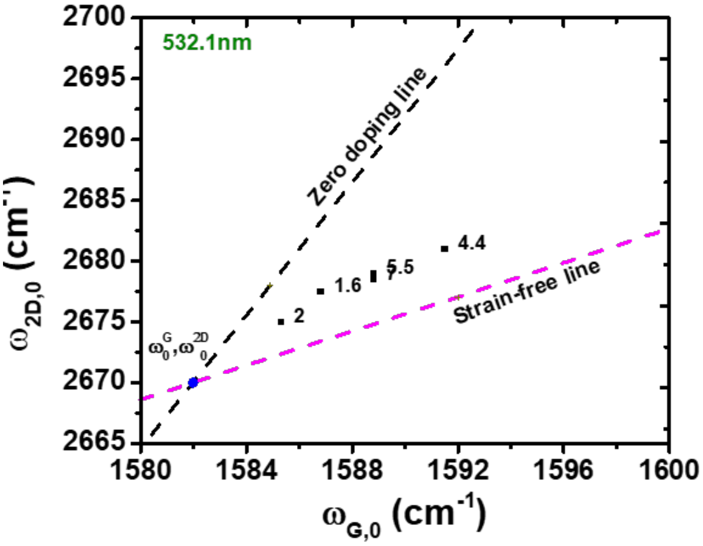

Figure 4.14: **Initial G and 2D band frequency for different hole size**: Initial values of G and 2D band frequency on a lee plot is shown with varying radius of hole. Labels represent the radius in μm. The measured location is in the center of the suspended graphene.

In order to understand this observation, we refer to figure 4.14, the Lee plot shows that as the radius of the suspension is reduced, (ω_G, ω_{2D}) moves closer to the strain-free and doping free point (origin of the Lee plot). Such observation is

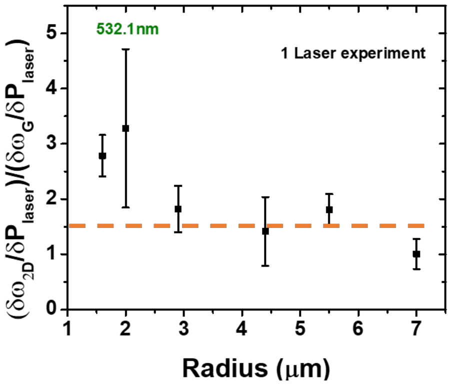

Figure 4.15: **Radius dependence of** $(\partial\omega_{2D}/\partial\mathbf{P}_{laser})/(\partial\omega_G/\partial\mathbf{P}_{laser})$: The ratio is calculated by taking the ratio of values taken from figure 4.13(a) and 4.12(a). Dashed line is an eye to guide line depicting the ratio to be 1.5.

physical, as we know that the strain in the system reduces with the increase in area of suspension. It is worth mentioning the outlying point for slope of 2D band at radius 1.6 μm (which is not a peculiar point regarding the G band), this can be due to local impurity (such as chemical impurity) on the sample since 2D band is more sensitive than G band, towards local environment [63].

Figure 4.15 shows the slope ratio (2D band to G band) against radius. We observe that the slope of 2D band is nearly 1.5±0.5 times the slope of G band which is not far from 2. We however notice that for 1.6 and 2.0 μm radius the ratio deviates from 1.5, since, as from figure 4.12 and 4.13, the slope values for these 2 samples are deviated in 2D and G band slopes, respectively. The value of $(\partial\omega_{2D}/\partial\mathrm{P}_{laser})/(\partial\omega_G/\partial\mathrm{P}_{laser})$ is same as in the case of global heat (1.5±0.5) so it can be said without the loss of generality that the effect of 2D band red shift is due to heat.

The constant value of slope ratio from 2D band to G band (for radius $>3\mu$m) matching with the global heat, hints upon the fact that even *via* laser power, dominant heating effects are induced. To confirm our hypothesis we must analyze the evolution of Lee plot and strain with laser power. We will elaborate on this in the next section.

4.2.1.2 Strain analysis

We know from global heating experiments that the strain is released during a heating experiment. We can utilize the Lee-plot for monitoring such observations. However, global heating experiments are different from this case since here we do not heat all the sample (substrate and graphene) but a local region is heated. We will focus on the evolution of strain and how the unheated region can play a role in such cases, but before that we must address some qualitative questions such as optical doping. The question of optical doping concerns our study deeply owing to the fact that our experiments are done in air, and these effects can cause the optical phonons to change their frequency which would in turn affect our conclusions. There have been reports of optical doping in graphene [133], it would be interesting to rule out such effects in order to ensure that the effects measured are intrinsically due to thermal properties. In the literature, it was shown that the optical doping effectively becomes relevant while irradiating the sample at low power (nearly 0.2 mW) [133], whereas at higher power optical heating is dominant. Interestingly, our laser power has been in the range of 0.2 mW to 4.3 mW, hence we should consider the possibility of optical doping in our measurements for the lower laser powers.

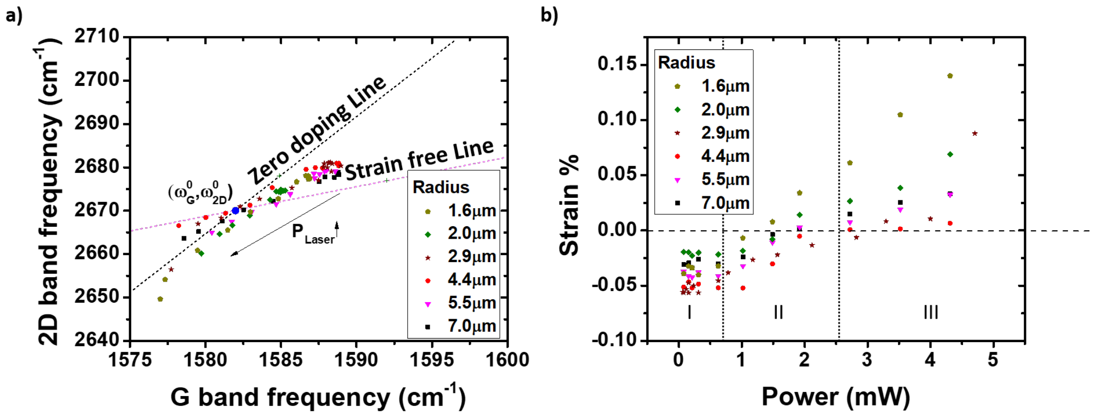

Figure 4.16: **Lee plot and strain estimation for different hole size**: (a) Lee plot with increasing laser power, (b) estimated strain with laser power (dashed line represent the zero strain). Individual points are measured at the center of the suspended membrane. An empirical observation can classify the strain evolution in three regimes: 0.2-0.6 mW (constant strain), from 0.6-2.5 mW (linear increase) and 2.5-4.3 mW (saturation in strain). This observation does not hold good for smaller samples with hole size 1.6 and 2 μm.

Figure 4.16(a) depicts the power dependent Lee plot of different radius samples. With increase in laser power, G and 2D band frequencies move towards the origin of Lee plot, as observed in case of global heat. In comparison to global heat, we observe that with 4.3 mW of laser power, it is possible to move the G and 2D band frequencies beyond the origin of the Lee plot. Following the findings of Lee *et al.*, the effect of substrate perturbs the strain evolution of the suspended graphene on smaller hole size (radius 1.3 μm), hence it is inconclusive for our case [2]. With a direct comparison we can argue that with such power we reach higher in temperature than the case of global heat (450 K). This does not, however , affect the linearity assumption according to the calculations of Bonini *et al.* [130]. It is worth noting that the case of 1.6 μm is particular, as with the same power of 4.3 mW, it is possible to go far away from the origin and the evolution is non-linear. However, in literature it has been discussed that for smaller holes the effect of substrate hinders the effect observed at the center while using local heating *via* laser [2]. We can attribute the exceptional behavior to the substrate hindrance induced at higher heating.

Since local heating allows the heat propagation through the membrane of graphene (from the hot-spot to the heat sink), it would be interesting to observe the strain evolution. To understand the strain evolution, fig 4.16(b) is presented with estimated local strain against laser power, for samples with different radius. Different samples have different local strain values to begin with. It can be seen that after approaching the strain-free value (0.0 %), the evolution of strain stops (>2.5 mW) for larger than 3.0 μm membranes. We observe a constant strain values in lower power (<0.6 mW) and higher power range (>2.5mW). We attribute the constant behavior of strain at lower power to the influence of optical doping. It has been shown that at higher power optical doping does not interfere with the optical heating, we can ignore this effect beyond 0.6 mW laser power.

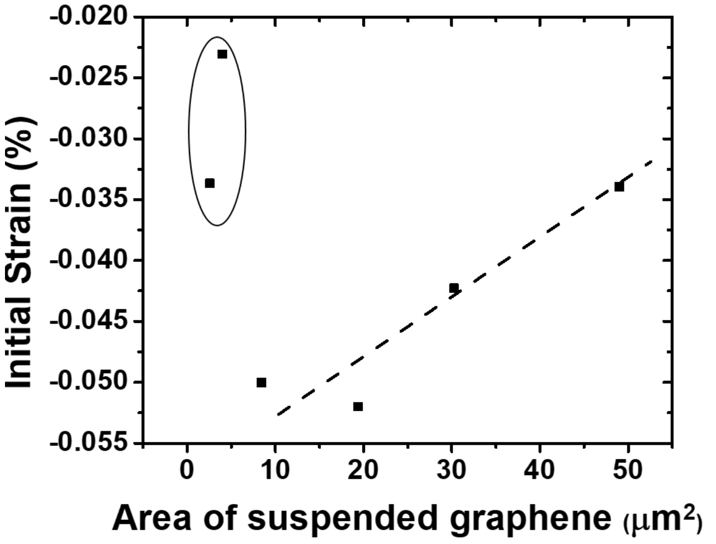

Figure 4.17: **Initial strain for different hole size**: Estimated initial strain with area of suspended graphene. Individual points are measured at the center of the suspended membrane. An empirical observation can classify the strain evolution in two regimes: small radius (encircled) and larger holes (shown by eye to guide-dashed line).

To understand the first regime of smaller radius samples, we refer to initial strain for different hole size. Figure 4.17 shows that with increase in area of suspended graphene the initial compressive strain decreases. We hypothesize that initial constancy of strain can be associated with the limited heat available due to low laser power. The strain relaxation from the initial compressive strain results from the competition of the strain at the hot-spot (which is being relaxed by the optical heating) and the rest of the suspended graphene which is not under direct influence of optical heat. However, we cannot rely on this hypothesis for smaller radius samples as shown in figure 4.17.

In the second regime the strain evolution takes places linearly, which is similar to seen in case of global heat. On the other hand, for smaller membranes, the linear increase in the strain continues even at higher powers (>2.5 mW). This observation relates to figure 4.12 and 4.13, where both these sample have shown discrepancies, which was attributed to substrate effect [2]. Since we know that even in the suspended graphene, the substrate around it plays a role in determining the strain [134] on the suspended region, it can be inferred that membranes smaller than 3 μm radius have strain from substrate reaching till the center throughout the experiment. However, the effect of substrate to the suspended graphene plays less significant role for larger than 3 μm radius samples. It can be argued that such effects would affect the thermal conductivity estimations done by Ruoff *et al.*, as they use membranes with smaller radius in their primary article [1]. Owing to the strain effects being prominent, it would change the temperature estimated and consequently the thermal conductivity, hence one can question the estimated thermal conductivity in the report of Ruoff *et al.*.

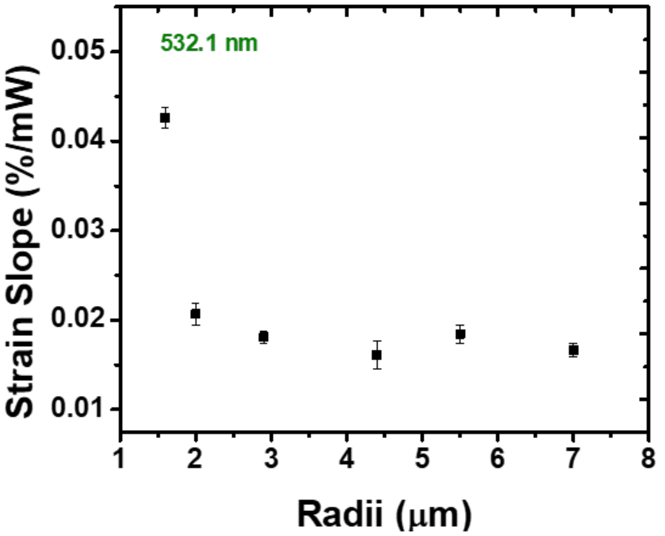

Figure 4.18: **Dependence of $\partial\epsilon/\partial\mathbf{P}_{laser}$ on radius of hole size**: A positive $\partial\epsilon/\partial\mathrm{P}_{laser}$ shows that laser power initiates a tensile strain. The measurements correspond to center of the suspended graphene. The value for smallest radius of 1.6 μm is an outlier.

The power dependence of strain is fitted with a line, in the first approximation. Figure 4.18 shows the linearly fitted strain-slope vs the radius. We can infer that strain release for each mW of laser power is around 0.02 % independently from the radius value. It is interesting to note that for similar strain relaxation we require 50 K of temperature change in case of global heat. It is also worth mentioning that for smaller radius of hole size, we observe a deviation which can be attributed to the strong presence of strain for smaller samples. We shall be utilizing this fact to address the transport studies in next chapter.

Above mentioned study completes the observations for case 1, now we will focus on studying the second case as discussed in section 4.2.

4.2.2 Case 2: Dependence G and 2D mode with spatial location of hot spot

To monitor the change of $\partial\omega_{2D}/\partial \mathrm{P}_{laser}$ and $\partial\omega_{G}/\partial \mathrm{P}_{laser}$ values with respect to spatial location of hot-spot, we perform another experiment to move the laser spot in the steps of nearly 500 nm (by controlled motion of the piezo stage). This way we will vary the distance from the heat sink to the hot-spot. To achieve the $\partial\omega_{G}/\partial \mathrm{P}_{laser}$ at each point, we performed line scans with different power. Such set of line scans can be used to extract the $\partial\omega_{2D}/\partial \mathrm{P}_{laser}$ and $\partial\omega_{G}/\partial \mathrm{P}_{laser}$ values, corresponding to their respective spatial locations.

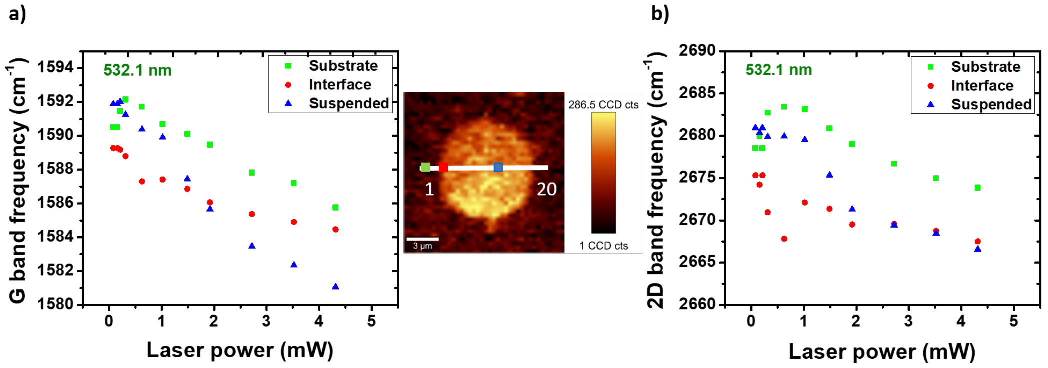

Figure 4.19: **Effect of substrate on optical phonon frequency with laser power**: (a) G band frequency on substrate, interface and suspended regions, (b) 2D band frequency on substrate, interface and suspended regions. (Inset figure shows the location of three regions on the Raman map of 2D band intensity. The dark yellow region represent the intense 2D band, as depicted by the scale bar in the numbers of CCD counts. Graphene on substrate reduces the intensity of optical phonons due to the loss incurred by the substrate.)

Figure 4.19 presents the raw data for substrate, interface and suspended part of graphene. The observation of substrate and suspended region is easily understandable whereas the case of interface is relatively difficult. As discussed in the fabrication section, the interface of holes is never perfect which adds to the strain induced in the suspended 2D materials, we will not discuss this strain, since the interface of hole is vastly statistical due to fabrication process. G band frequency is larger in case of suspended region (1592.0 cm^{-1}) compared to the supported region (1590.5 cm^{-1}), such observation is unusual [135]. This observation becomes rectified with small application of laser power of 0.4 mW. Such an observation could be associated with the strain release *via* laser heat and hence the unusual observation of G band frequency on substrate and suspended region.

In case of interface, we notice that initially the red shift of G band remains largely in between the supported and suspended regions, which is obvious since the interface carries the contribution from the two regions. Figure4.19(b) shows the 2D band frequency trend with laser power increase. Similar observation as for G band frequency is noticed here. Importantly, we observe two regimes of trend for substrate, suspended and interface. For lower power (<1.0 mW), the 2D band shows non-linear trend and then it follows the linear evolution but the case of G band shows this behavior only up to 0.4 mW. In order to avoid the strain contribution, we have fitted the data from higher power for 2D band.

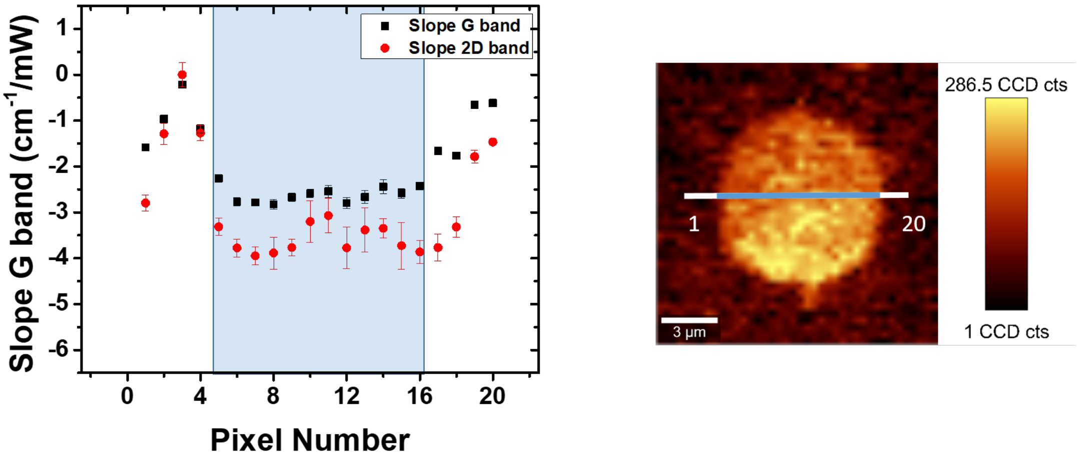

Figure 4.20: **Spatial dependence**: $\partial\omega_{G/2D}/\partial\mathrm{P}_{laser}$ across the diameter of a suspended graphene (left), location of the line scan on the Raman map (Inset figure shows the location of three regions on the Raman map of 2D band intensity. The dark yellow region represent the intense 2D band, as depicted by the scale bar in the numbers of CCD counts (right). The blue region represents the suspended graphene. The length of the line is 12 μm, which has been divided in 20 pixels. The region of suspended graphene is 8.8 μm.

The spatial dependence of $\partial\omega_{2D}/\partial\mathrm{P}_{laser}$ and $\partial\omega_{G}/\partial\mathrm{P}_{laser}$ values (which are -3.74 and 2.66 cm^{-1}/mW) can be observed from figure 4.20. The light blue region represents the suspended graphene. The graph shows that G band slope is independent of spatial location of the hot-spot. However, the $\partial\omega_{G}/\partial\mathrm{P}_{laser}$ across the laser power sweep is sharper in case of suspended graphene (-2.66 cm^{-1}/mW) than the supported region (-1.31 cm^{-1}/mW). Since substrate acts as heat sink it is obvious to expect the difference in the two regimes. The $\partial\omega_{G}/\partial\mathrm{P}_{laser}$ value, however, is constant within the error bar of the slope. The $\partial\omega_{G/2D}/\partial\mathrm{P}_{laser}$ values on the substrate are varying, which is attributed to the fact that the $\mathrm{SiO_2}$ membrane is not stress-free (discussed in chapter 2, section 2.1.3), overall we can observe the slope of suspended region is roughly twice the values in the supported region.

4.2.2.1 Analysis of case 1 and 2

In order to understand the two observations let's consider two cases as follows: 1) mean free path in the range of few μm (case 1) and 2) means free path in the range of few 100 nm (case 2).

For the first case, since the mean free path is assumed to be in the order of few μm, we can expect to observe no change in the $\partial\omega_{G/2D}/\partial\mathrm{P}_{laser}$ with the hole radius lesser than the mean free path. Such observation would be justified from the fact that heat taken to the heat sink would encounter similar number of scattering events hence not influencing the $\partial\omega_{G/2D}/\partial\mathrm{P}_{laser}$ values. However, for hole radius larger than the expected mean free path, $\partial\omega_{G/2D}/\partial\mathrm{P}_{laser}$ would show a dependence with hole radius, since here the number of scattering events would scale with the radius of the hole size. Hence, for a diffusive transport we should expect a radius dependence of $\partial\omega_{G}/\partial\mathrm{P}_{laser}$, for a mean free path lesser than the radius of the suspended sample (few μm). The independence of the $\partial\omega_{G}/\partial\mathrm{P}_{laser}$ from radius would give an indirect hint towards the non diffusive transport. As per our observation in figure 4.12 and 4.13, it can be inferred that there is a hint of non-diffusive transport observed in our samples. However, to estimate the mean free path one has to observe $\partial\omega_{G/2D}/\partial\mathrm{P}_{laser}$ for larger suspended samples.

Another explanation for such independence could be the fact that the mean free path is very small compared to the sample size which qualitatively leads to same number of scattering events for all the samples and hence the resulting $\partial\omega_{G/2D}/\partial\mathrm{P}_{laser}$ values are same. In order to test this explanation, we can discuss the second part of experiment, where we can control the distance of heat sink to hot-spot much smaller that few μm.

For the second case, we have to compare the data from substrate and suspended region first. Sharper slope of suspended region shows that the thermal dissipation in the suspended region is better than in the supported one. It is also noteworthy that the slope of 2D band is nearly 1.5 times the slope of G band, which agrees with earlier observations. The independence of slope for spatial location of hot-spot is consistent with radius independence of slope. As discussed earlier, for the case of diffusive transport, closer the heat sink, easier should be the heat dissipation. For hot-spot closer to heat sink, phonons would encounter lesser scattering events before reaching the heat sink, than the case of larger distances. Our observations suggest the contrary, which hints towards the non- diffusive transport of heat in graphene.

In the present case, we move the hot-spot in the steps of 500 nm which does not show any variation in $\partial\omega_{G/2D}/\partial\mathrm{P}_{laser}$, hence it can be concluded that either the mean free path should be smaller than 100 nm, or shall be larger than 7 μm (largest radius of the sample). However, despite the substrate influence smallest value of mean free path estimation is nearly 100 nm [4], so we can discard the possibility of mean free path being smaller than 100 nm, since we are in suspended case. An estimate of $\sim$100 nm as mean free path value was made in experiments performed by Bae *et al.* for the sample size corresponding to 0.25 μm on substrate supported graphene. Other studies by Balandin *et al.* and Ruoff *et al.* estimated the mean free path around 700 nm in their experiments. However, Fugallo *et al.* talks about the possibility of mean free paths in the range of 100 μm for suspended samples, in their theoretical report [29]. This could be a future prospect of the current study to perform similar measurements on larger samples, in order to test the above mentioned contradictory hypothesis for observing the mean free path.

This study hints towards the possibility of non-diffusive transport in our samples. Notwithstanding the limitations of Balandin's model, it would be an interesting exercise to estimate the thermal conductivity from our measurements using

Balandin *et al.* approach.

4.3 Extraction of thermal conductivity

Using the data of local and global heating experiments one can derive an effective thermal conductivity of graphene using the model given by Balandin *et al.* [6]. As discussed in chapter 1 (section 1.4.2.3), we will take into account the optical absorption value of graphene. The right hand side of figure 4.21 shows the schematic of the experiment performed to estimate the optical absorption. We directly measure the power after the sample using a thorlabs digital power meter. In order to calibrate the power meter we use a hole with same radius without suspended graphene. This calibrated data are used as abscissa for our graph. The power values obtained by using 'non covered hole' against 'with suspended graphene hole', results in the value of optical absorption to be around 2.9 ± 0.9%. This value matches well with reported literature [33]. The thickness of monolayer graphene is commonly estimated to be around 0.335 nm, we can use the $\partial\omega_G/\partial\mathrm{T}$ and $\partial\omega_G/\partial\mathrm{P}_{laser}$ from the above mentioned experiments to estimate the thermal conductivity. Using the modified relation of model given by Balandin *et al.*, we arrive at effective thermal conductivity value of 125 W/m.K ± 85 W/m.K. We can also use the 2D slope values, that results in the thermal conductivity of 148 W/m.K ± 85 W/m.K, which is fairly close to the value obtained for the G mode calculation. However, the values estimated by us are very low compared to all the other values reported in literature (see figure 4.22) [33, 6].

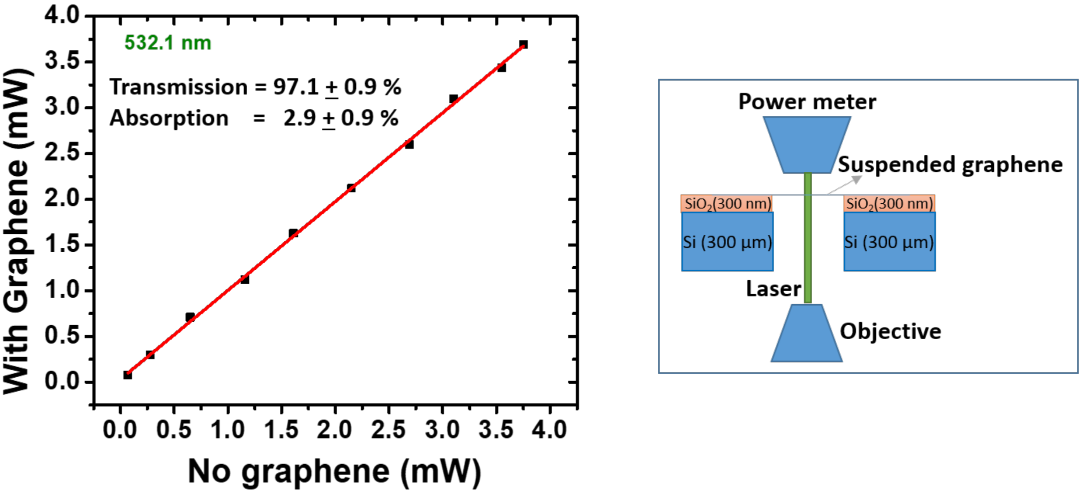

Figure 4.21: **Transmission for 532.1 nm laser through suspended graphene** (Inset shows the measurement scheme): Abscissa- laser power measured after a hole (with radius r) without suspended graphene, ordinate- laser power measured after a hole (with radius r) with suspended graphene.

The estimated difference in the thermal conductivity of our samples relative to the value reported by Balandin *et al.* is attributed to the additional term of

optical absorption. In addition, the $\partial\omega_G/\partial$T value used in Balandin *et al.* report is taken from exfoliated graphene on SiO_2/Si substrate however the $\partial\omega_G/\partial P_{laser}$ value obtained was from suspended sample. For our results all the numbers are taken for suspended graphene. If we do not consider the optical absorption, the thermal conductivity turns out to be nearly 3685 W/m.K, which is in fair agreement with the values reported by Balandin *et al.* [6]. Similar number was arrived by Lee *et al.*, when assumed the same approach as Balandin *et al.*, so it will be fair to assume that we would reach similar numbers if used their model. Moreover, our $\partial\omega_{2D}/\partial P_{laser}$ value (-4.0 ± 0.5 cm^{-1}/mW) compares well with Lee *et al.* (-2.7 ± 0.7 cm^{-1}/mW) (considering the fact that they used mechanically exfoliated graphene compared to our CVD grown graphene), which indirectly hints towards the agreement of our observation.
As argued by Ruoff *et al.*, the method of Balandin *et al.* severely overestimates the thermal conductivity [33]. Ruoff *et al.* uses a different approach to model the thermal conductivity by incorporating the slope values of global and local heat using two different spot sizes and thereby simulating the heat flow.

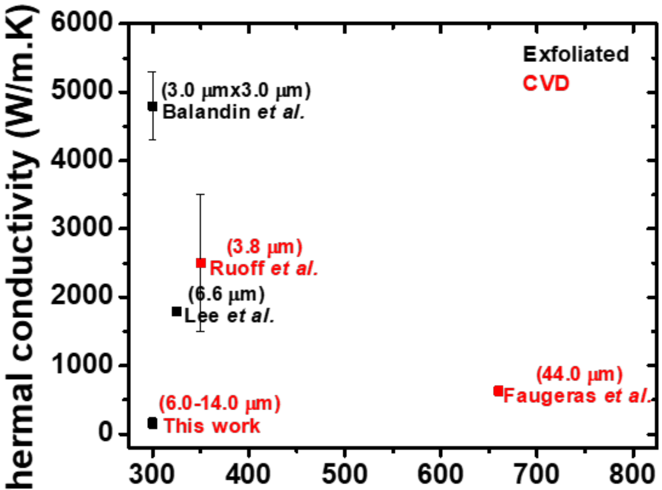

[H]

Figure 4.22: **Thermal conductivity of suspended graphene using optothermal methods**: Different groups have used different models in order to estimate the thermal conductivity. Balandin *at al.* used a trench geometry, whereas other groups used circular geometry (diameter of suspended part is mentioned in μm). Except Lee *et al.*, all the other values reported are using G band as thermometer mode. Faugeras *et al.* have used Stokes-anti Stokes intensity ratio for temperature estimation.

In both the models, the presumption of diffusive behavior keeps the conclusion in question. To model an appropriate approach, it is important to test the applicability of Fourier's law. In order to achieve this objective, we require the estimated temperature about the unheated region of the suspended membrane. With information about the locally distributed temperature around the hot-spot, one can observe the temperature flow in the suspended graphene. This gives rise to the need for a transport map of locally heated suspended graphene with information of spatial temperature. One way to achieve this goal is to split the objective in two parts, one to extract the temperature information from the frequency and second to create a temperature map which is easily available with the 2 Laser Raman thermometry. We shall discuss the temperature estimation in the following section and use it to achieve the second goal that shall be discussed in next chapter.

4.4 Temperature determination by optical phonons

As mentioned in the beginning of this chapter, the two types of experiment mentioned in earlier sections can help us create a calibration curve to estimate the temperature of the suspended graphene. This can be achieved with the help of data collected in the hotplate experiment as a reference for temperature estimation. To convert the power used during optical heating experiment into a temperature, we will use the global heating experiment. The main principle here is the fact that the frequency of optical phonons (G and 2D band) can be represented as a function of power in one case and temperature in the other. As discussed in earlier sections we have managed to put these two functions to be linear under certain power and temperature regimes. Now in order to make the correspondence, due to the linear nature of both the functions, we can simply take the ratio of the slopes resulting from global and local heating experiments. With such an approach, we find that the $(\partial\omega_{G/2D}/\partial \mathrm{P}_{laser})/(\partial\omega_{G/2D}/\partial \mathrm{T})$ results in 12.1 μW/K for G band whereas it becomes 13.3 μW/K for 2D band.

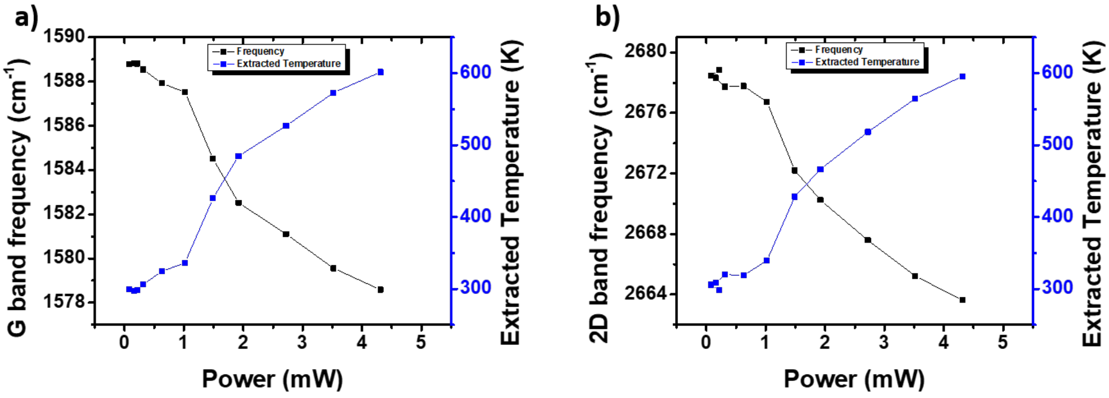

Figure 4.23: **Temperature estimation**: (a) G band frequency, (b) 2D band frequency and estimated temperature against the laser power, using the relation 4.2 for $\partial\omega_{G/2D}/\partial \mathrm{P}_{laser}$, we arrive at same estimated temperature. Here, it is assumed that the base temperature of the graphene is at 298 K (experimental condition). The estimated uncertainty in the temperature is 20 K.

The linear fitting allows us to model the power dependent evolution of G mode as given by equation

$$\frac{\omega_{G/2D} - (\omega_{G/2D})_0}{\chi_{P_{laser}}} = \partial P_{laser} \tag{4.1}$$

Where ω_G is frequency of G mode at certain power, $(\omega_G)_0$ represents the initial G band frequency, χ_P is $\partial\omega_{G/2D}/\partial\mathrm{P}_{laser}$ and $\partial\mathrm{P}_{laser}$ is laser power change. $\partial\mathrm{P}_{laser}$ can be replaced by the $(\partial\omega_{G/2D}/\partial\mathrm{P}_{laser})/(\partial\omega_{G/2D}/\partial\mathrm{T})$ value, which will result the expression in terms of temperature. The resulting equation 4.2 would give us the local temperature information of the sample.

$$(\frac{\partial\omega_{G/2D}/\partial P_{laser}}{\partial\omega_{G/2D}/\partial T})\frac{\omega_G - (\omega_{G/2D})_0}{\chi_{P_{laser}}} = \partial T \tag{4.2}$$

Using the above mentioned strategy, figure 4.23 shows the extracted temperature from G and 2D mode for a sample of 7 μm radius. It is physical to consider that the temperature extracted by G band and 2D band should be same since the measurement duration (60 s for a spectra) allows the whole system to be in a steady state. The extracted temperature with G and 2D band match within 10 K difference, however the uncertainty in each estimated temperature is 20 K owing to the uncertainty of the Raman shift. The temperature range of our experiment is 300-600 K for a laser power change up to 4 mW, which corresponds to 75 K temperature change for each mW of laser power change.

With this method, we can estimate the local temperature of a 2D material. A Raman image can hence be converted into a local temperature map which in turn can be used for understanding the thermal transport. We shall be discussing this in chapter 5.

4.5 Conclusion

In this chapter, we successfully observe the effect of radius of the suspended graphene membranes on global and local heating measurements. We observe a narrow range of values for $\partial\omega_G/\partial$T and $\partial\omega_{2D}/\partial$T for our suspended graphene samples. We also analyze the temperature dependence of the strain, for the first time. A linear strain evolution is observed within the set temperature range (300 - 450 K). The radius independence of $\partial\omega_G/\partial$T and $\partial\omega_{2D}/\partial$T shows the intrinsic nature of these numbers. A detailed analysis is presented for using 2D band as better option of exploring thermal effects owing to the sensitivity of 2D band frequency towards the heat (due to the involvement of 2 phonon-process).

In the experiments of local heat, We have shown that 2D band evolution with laser power is a consequence of temperature similar to the hotplate experiment. We have also analyzed the strain evolution for the case of 1 laser experiments which is lacking in literature. The strain evolution has been taken into account in order to observe the thermal effects remaining least affected by strain. Despite the fact that, it is very difficult to disentangle the contribution of thermal effects and strain, this analysis provides more insight about the physics of strain and local heat. The observations made in local heating experiments, have shed light towards the possibility of non- diffusive nature of heat transport in suspended graphene. Comparing our observations, we could say that there is a hint towards the larger value of mean free path of the phonons for suspended graphene.

We have also shown that with this study we can estimate the local temperature in graphene samples by using the optical phonon frequency. We would be using the approach developed in this chapter, in creating the thermal transport map for suspended graphene.

Chapter 5

Thermal transport beyond Fourier regime

Even though we have reviewed the state of the art for thermal measurements in 2D materials, we will briefly review the state of the art again from graphene point of view. The estimation of thermal conductivity for graphene is a long sought quest in the field of 2D materials. Several groups have made efforts towards the progress in such measurements. First such report was made by Balandin *et al.* using Raman optothermal method, who reported the thermal conductivity to be in the range of 4800-5300 W/mK for exfoliated graphene near room temperature suspended over a trench of 3 μm [6]. Faugeras *et al.*, estimated the thermal conductivity to be around 630 W/mK for CVD grown graphene suspended over a hole of diameter 44 μm in a Corbino geometry by estimating the local temperature using Stokes/anti-Stokes ratio of Raman intensities [27]. In the same timeline, Ruoff *et al.* presented series of experiments, showing different parameters (such as C atom isotope percentage, environment, temperature and hole size) affecting the thermal conductivity values [1, 33, 73]. At 350 K, Ruoff's group estimated the thermal conductivity to be around 2500-3000 W/m.K [1]. Ruoff *et al.* attributed the low thermal conductivity estimated by Faugeras *at al.*, to the temperature increase due to the higher laser power used for measuring the Raman intensities.

All these reports used G band frequency as thermometer. However, Cheong *et al.* presented a radius dependent study, using 2D band frequency as thermometer [2]. Despite a close range of diameter values of 2.6-6.6 μm, they managed to report a diameter dependence of $\partial\omega_{2D}/\partial\mathrm{P}_{laser}$. Using 2D band as thermometer, resulted in thermal conductivity estimation of around 1800 W/mK for exfoliated graphene measured at 325 K, which is not far away from the values reported using G mode. There is though a consensus about the high thermal conductivity, but not on the exact value nor about the transport regime. Actually, the method of estimation of thermal conductivity has to be questioned since it supposes the applicability of the Fourier law *i.e.* a diffusive thermal equation. Fourier theory relies on the gradient of temperature, which depends on the cross section of the sample, but cross section cannot be well defined for monolayer graphene since it's difficult to define the thickness of a 2D material. All the estimations mentioned above are based on the Fourier theory of heat transport, which can be questioned due to limited thickness for the case of 2D materials.

In the literature, Bae *et al.* reported a diffusive to ballistic crossover for range of graphene samples with different size. They claimed to have reached 35% of ballistic regime in exfoliated supported graphene samples with 250 nm width [4]. They estimated the mean free path of acoustic phonon to be nearly 100 nm which can be interpreted as quasi-ballistic regime of thermal transport. Another report by Xu *et al.*, presented similar observations for CVD grown samples with different lengths [136]. They presented length dependence in thermal conductivity (for 2D systems) which can be attributed to consequence of non-diffusive transport, they also reported the mean free path to be 240 nm. These reports re-opened the question of the determination of thermal conductivity regarding the thermal regimes in such 2D materials in case of graphene and other 2D materials.

Soon after these reports, theoretical models (such as exact solution to Boltzmann transport equation solved using DFT and molecular dynamics) were used in order to calculate the mean free path, and thermal conductivity spectra over different temperatures were estimated [29]. Fugallo *et al.* showed that using Boltzmann transport equation, one can estimate the thermal conductivity to be around 4000 W/m.K [29, 137]. Interestingly, it was also shown that the mean free path of the phonon could be estimated to be in the range of 100 μm, in the same study. Later computational works suggested the possibility of hydrodynamic type of heat transport of graphene [30, 31]. The specificity about hydrodynamic transport comes from the momentum loss mechanism which is mainly due to boundary diffused scattering hence allowing the phonons to flow like a fluid.

As we discussed in last chapter, we observe deviation from diffusive model of thermal transport in suspended graphene. Such observation could be possibly a consequence of mean free path of phonon comparable to the device length. The case of graphene has spectacularly wide range of speculations for heat transport. However, in order to add more towards narrowing the debate, it would be interesting to image the thermal transport on a completely suspended graphene membrane. This is possible by using spatial Raman imaging but in the case of 2 laser Raman thermometry, where one laser is the heater and the other one is the probe (as discussed in 1.4.2.4). Indeed, in all the works discussed above, information on thermal transport were deduced on the basis of temperature measured at the same spot in which it is heated.

As discussed in chapter 1 (see section 1.4.2.4), the two laser Raman thermometry was established in 2014 for silicon films [7], but in that case samples (thin film silicon, 250, 1000, 2000 nm) showed measurements which can be interpreted within a standard Fourier-law approach. On the other hand, temperatures maps on graphene membranes have been reported in the last few months [138], but these were taken within a one-laser experiment approach, that is a set-up which does not allow the measurement of the temperature outside the heated spot.

In this chapter, we would elaborate on the thermal transport imaging of suspended graphene *via* 2LRT thereby interpreting the observations away from the heated spot. With such information, we would attempt to contribute to a better description of the heat propagation and of thermal conductivity estimation.

5.1 Measurement scheme

5.1.1 Wavelength of heating laser

To optimize the wavelength of heating laser, we need to discuss the setup with respect to optical properties of different elements. Figure 5.1 presents a schematics of 2LRT setup. As discussed earlier, a heater laser is connected with the piezo stage where the sample is placed, so that the collective motion of heater-sample assembly could be ensured. First, the heating laser enters from the bottom of the sample, through a 20x objective after getting collimated. With such an arrangement, we measure the laser spot size to be 0.8 μm, using two different ways namely razor blade technique and linear scan involving the piezo stage [139] (Appendix C). Second, the probe laser enters from the top of the sample, after getting reflected by a dichroic mirror angled at 45^o. The probe laser is collimated and kept in a circularly polarized state. The Raman signal is measured in back-scattered geometry. In this configuration, the heating laser beam can happen to enter in the collection optics, which is why it is a crucial to choose a heating laser wavelength such that it will not interfere with Raman signal collected by the spectrometer.

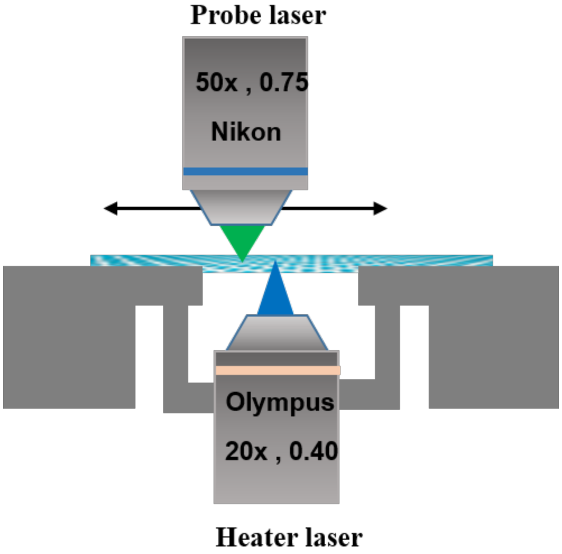

Figure 5.1: **Schematic of 2-laser Raman thermometry**: Typical schematic of 2LRT setup. The probe laser is connected to a conventional Raman spectrometer (WITec alpha 500). The sample stage is screwed onto an external piezo stage which controls the motion of sample along with the heating laser.

Two crucial components of the setup to filter the Raman signal of probe laser from the heating laser (and the Raman signal due to heating laser) are the dichroic mirror and the edge filter. The probe laser wavelength is fixed at 532.1 nm. As shown in figure 5.2(b), transmission profile of dichroic mirror suggests that we need the heating wavelength to be lower than the probe laser (532.1 nm). As the transmission of wavelength lower than 532.1 nm is close to zero percent, choice of lower wavelength for heater would help to filter the Raman signal. The edge filter adds to this objective, as it would further cut the optical signal lower than 532.1 nm wavelength. It is important to mention that heating laser would be transmitted by the dichroic mirror towards the spectrometer, which may interfere with the signal. This is why we must have an edge filter in the collection optics hence we cannot obtain Stokes signal in this configuration. We have selected 488.0 nm wavelength for heating purpose.

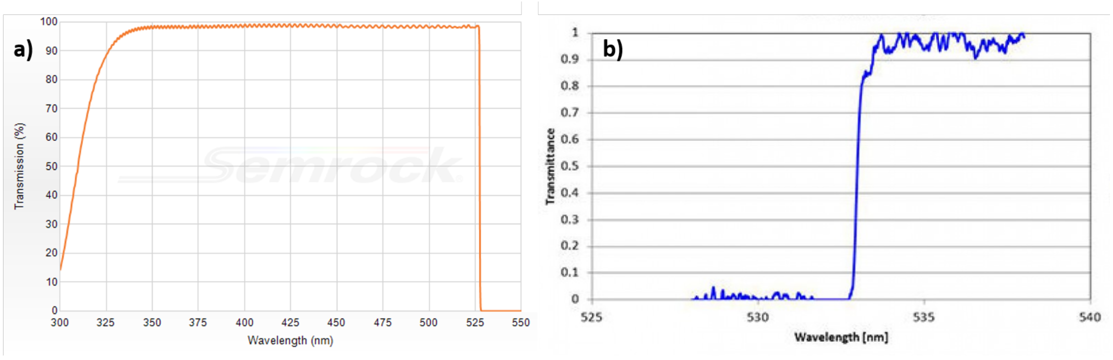

Figure 5.2: **Transmission profile** of (a) Edge filter and (b) Dichroic mirror. It is crucial that the profiles of dichroic and edge filter are such that they cut the wavelengths of heating laser. In other cases, the heating laser may interfere with the Raman signal of the probe laser. (Profiles adapted from Thorlabs)

Another crucial factor to rule out interference from Raman signal of probe laser is the Raman signal induced by the heating laser. In case of graphene samples, there are mainly 2 signals, G and 2D band frequencies. The G and 2D band wavelengths scattered from 488 nm laser correspond to 529 nm and 561 nm, respectively. The same values for 532.1 nm excitation correspond to 581.2 nm and 620.5 nm, respectively. As a matter of fact these values are larger than 532.1 nm hence, would not be blocked by the edge filter. However, the difference between these values ensure that the Raman signal from heating laser would not interfere with Raman signal from probe laser. As a matter of fact the chosen CCD window is such that the G and 2D band wavelength from heater laser lies out of the window for G and 2D wavelength from probe laser.

Similarly, G and 2D band wavelengths for 632.8 nm are around 703.5 and 762.0 nm. Hence we can also use 632.8 nm as probe and 532.1 nm as heater. But for such combination, one needs to consider the scattering cross section, which is inversely proportional to the fourth power of the wavelength. Hence, probing the system with 632.8 nm wavelength would require more time in comparison to 532.1 nm. Keeping all these points in mind we use 532.1 nm wavelength as probe and 488.0 nm as heating laser. Another important parameters is the absorption of graphene with respect to different wavelengths, but we measure absorption of graphene to be same (3 ±1 %) for both the wavelengths (which is in accordance with the literature [140]), hence this issue can be safely ignored. All these parameters would be same for all the maps presented in this chapter.

5.1.2 Motion stage

For 2-laser Raman thermometry, we require a special sample stage to accommodate the schematics discussed in chapter 1. The details of the setup require us to have a translation controlled stage for sample, which is coupled with heating laser. Such a stage (shown in figure 5.3) was designed and built in our mechanical workshop by Laurent Del Rey (Pôle Ingénierie Expérimentale).

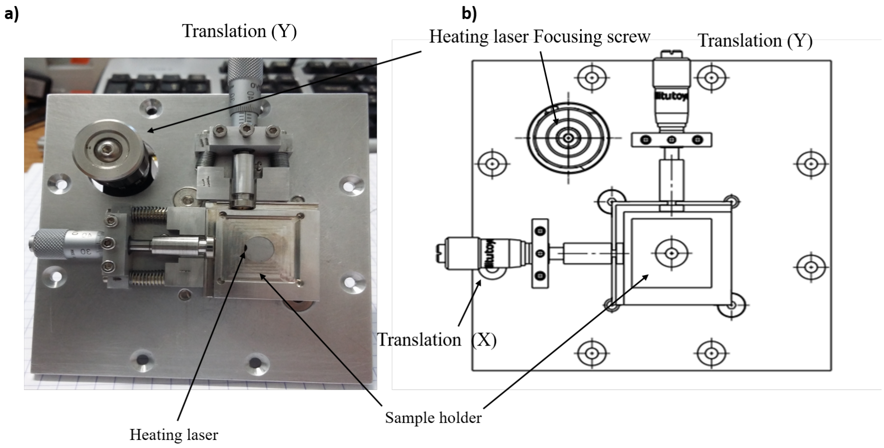

Figure 5.3: **Sample stage for 2LRT**: (a) The stage designed at Institut N*é*el for measuring the 2LRT, the heating laser comes from the bottom plane of the stage shown where an objective along with a collimating assembly is attached to the sample stage. (b) A schematic of sample stage designed in solid works.

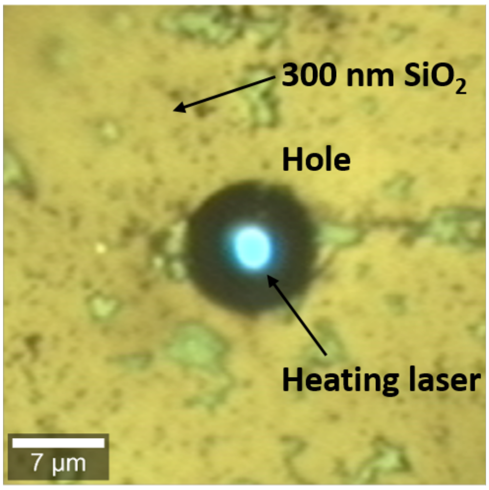

Figure 5.4: **Optical image of suspended graphene**: A typical optical image of suspended graphene with heating laser in the center. The bright white spot shows the saturation of the optical camera. The laser is not focused for the optical camera.

Heating laser is supposed to be stationary, as it is used to heat the sample at a fixed point. In order to do that, we fixate the heating laser with the sample stage, while the whole assembly is free to move *via* the motion of connected piezo stage as shown in figure 5.4. With this setup one can perform 2LRT for different suspended samples. We will be discussing the first few experiments performed on suspended graphene, using this setup.

5.2 2 Laser Raman thermometry in suspended graphene

5.2.1 Observations

In this section, we will discuss the thermal transport maps obtained by recording the frequency of the Raman modes of the graphene membrane using Raman imaging, to our knowledge this has not been reported in the literature yet. As mentioned before (see section 1.4.2.4), we use two different lasers, one to heat (488.0 nm) on a certain spot and the other to probe (532.1 nm) the suspended graphene membrane on different locations. We will present, transport heat maps for different heating powers and for different samples having different radius. The grating of Raman spectrometer is 1800 grooves/mm which gives us the standard error bar of 0.1 cm^{-1} in frequency measured. A typical Raman spectra collection takes nearly 4-6 seconds. Since a typical Raman map takes up to 1600 pixels (40x40 for size of 15x15 μm^2, which correspond to 0.14 μm^2 per pixel), the amount of time to record one map is around 2-3 hours, therefore to finish one set of experiment may take few days. The spot size of the heating laser is measured to be 0.8 μm. On the other hand, the probe laser has a spot size (half width of the Gaussian profile) of $\approx$ 300 nm, which results in a probed area of 0.28 μm^2. Such a scheme would result in overlap between two pixels in the thermal transport map. The probe map will cover the entire membrane without leaving an unprobed region of suspended graphene. Hence the local frequency information and estimated temperatures are a statistical average of carbon atoms assembled in the area of 0.28 μm^2 of the sample, corresponding to each pixels. This area corresponds to roughly 10^7 carbon atoms and we assume that local temperature is a well defined parameter in these limits.

Before discussing the transport maps it is crucial to mention the strain and doping estimated according to Lee-plot approach (described in section 1.4.2.2) of the sample [63]. Figure 5.5 presents the strain and doping of the graphene membrane which would be analyzed later in terms of thermal transport. As discussed in chapter 2, we observe a p-doping (see figure 5.5(a)) due to the gold mediated transfer (section 2.3.4). The doping level in the suspended region is nearly constant at 10^{13} /cm^2. Since the devices are electrically floating hence we can assume that the doping contribution remains constant. However, we can observe inhomogeneity in the substrate region. It is important to mention here that inhomogeneity would contribute to the noise for the temperature estimation, since the shift in thermometer mode cannot be deconvoluted for thermal effect or inhomogeneity.

From figure 5.5(b), we determine the strain levels of the graphene membrane before heating. In the suspended region the strain is mostly present at the interface along with a specific location at the top-right of the region. Thus we can conclude

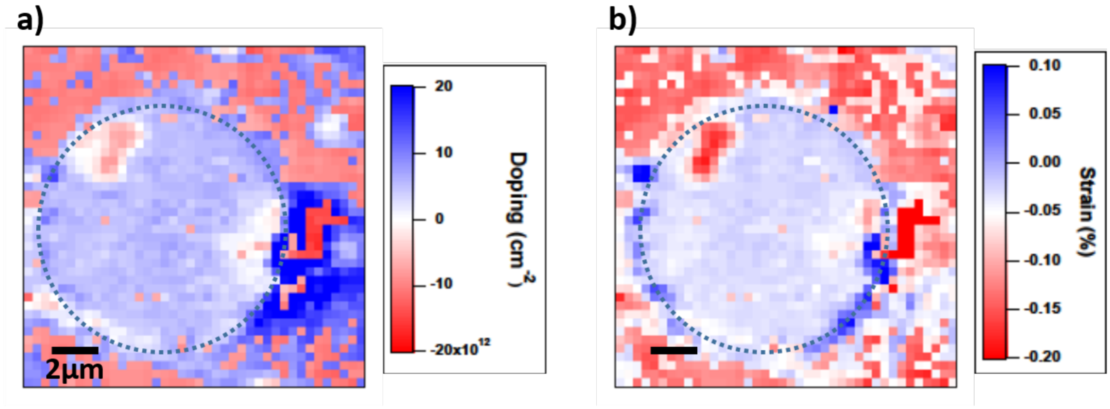

Figure 5.5: **Initial strain and doping of suspended graphene**: The estimated (a) strain and (b) doping of the suspended graphene before the 2LRT (the estimation is based of Lee plot as discussed in 1.4.2.2). The dashed circle shows the optical location of the hole thereby suspended graphene.

that most of the suspended region shows a constant strain whereas the substrate regions shows a distribution of strain probably due to the inhomogeneity of the graphene adhesion on SiO_2. We will show that the local strain might play crucial role for further analyzing the thermal effects.

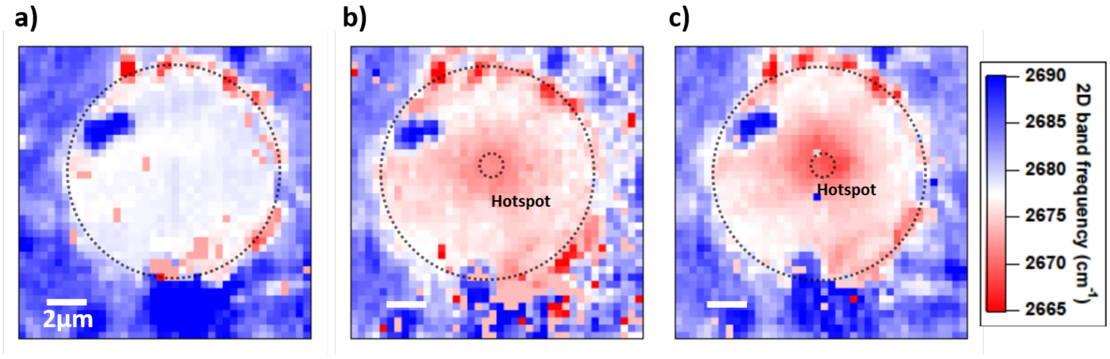

Figure 5.6: **2D band frequency map of suspended graphene in 2LRT configuration**: 2D band frequency for suspended graphene (dashed circle) with a heating laser in the center of the membrane (dashed circle shows the hotspot). The scale bar is 2 μm shown in first map. From left to right the heating power is increasing from (a) 0.0 mW, (b) 1.6 mW and (c) 2.3 mW.

Figure 5.6 shows an example of the frequency (2D mode) map of a suspended graphene over a hole of 5.3 μm radius. A typical frequency map obtained with the two-laser set-up shows that in the center, there is the hot spot which corresponds to the minimum of frequency, then from the hot spot the frequency increases towards the periphery where it reaches the values of the unheated membrane. The diameter of the hotspot is $\sim$ 1.5 μm. The frequency increases smoothly, as we go from the hotspot to the periphery of the membrane, showing a sudden jump at the border of the suspended region (see figure 5.6), where the membrane is in touch with the substrate. To our knowledge this is the first example of such an experiment (two laser approach) reported for graphene and an established framework for its interpretation is not available.

In the ideal situation of a perfectly circular and uniform membrane with centered hotspot the frequency profile should have radial symmetry. This is not the overall case mainly because of the presence of localized anomalous spots which can be attributed to localized strained region in the membrane and which are very well reproducible in experiments done at different times. Moreover, due to the limitations of setup the hotspot is not exactly in the center. AFM image of this sample is shown in figure 5.7, where such localized spots can be seen as the locally strained regions. This sample non-uniformity is similar to that reported also in [138]. However, if we exclude certain specific region, we can say that the profile has an overall radial symmetry and we will try to drive some conclusions on the basis of this assumption.

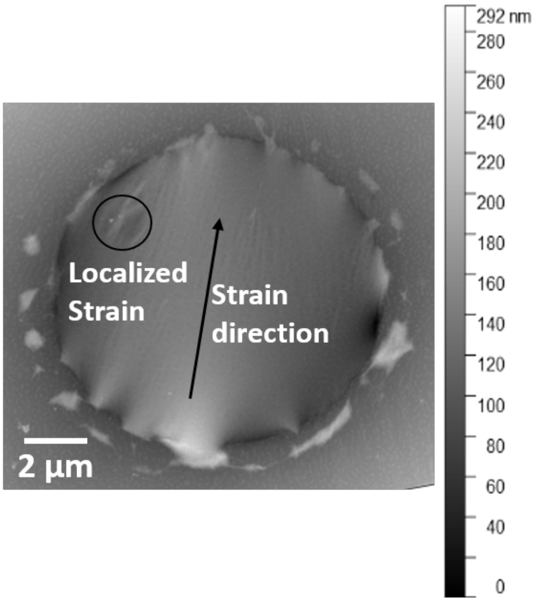

Figure 5.7: **AFM profile of the suspended sample**: Height profile of the suspended graphene on 285 nm SiO_2 films with holes. The locally strained graphene is shown encircled. The arrow depicts the direction of the strain in the sample which is evident from the light ripple formation in the direction of the arrow. The edge of the hole presents different adhesion links such as some locations are smooth whereas some location show some clipping behavior of the graphene.

From the frequency, we can extract the temperature maps as described before (equation 4.1). Figure 5.8 shows the corresponding temperature evolution with heating laser power. We notice a temperature drop around the hotspot followed by saturation of temperature within the suspended region. Interestingly, the direction of strain does not dictate the temperature profile around the hotspot which is almost radially symmetric around the hotspot.

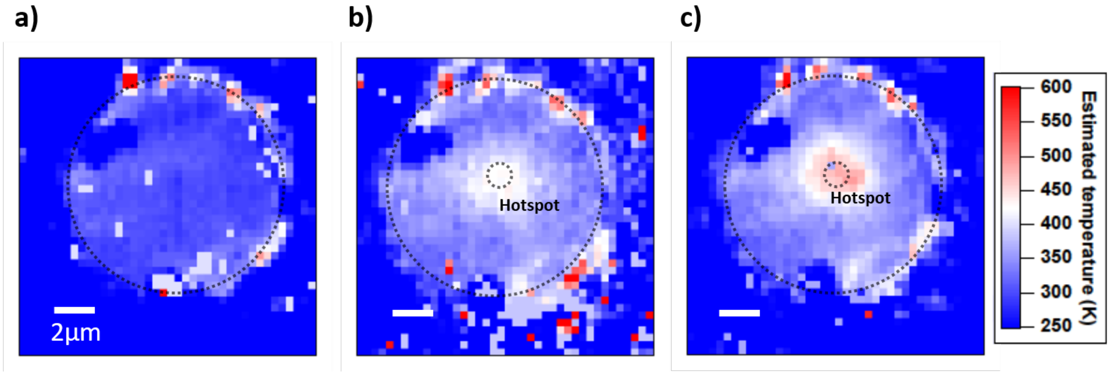

Figure 5.8: **Estimated temperature maps of suspended graphene in 2LRT configuration**: Local estimated temperature maps for suspended graphene (dashed circle) with a heating laser fixed in the center of the membrane (dashed circle shows the hotspot). The scale bar is 2 μm. The temperature estimation is done by using the frequency information from figure 5.6. From left to right the heating power is increasing from (a) 0.0 mW, (b) 1.6 mW and (c) 2.3 mW.

5.2.2 Extracting the temperature profiles

We now discuss how the temperature T changes as a function of the distance r from the center of the hot-spot: $T(r)$. The reader should keep in mind that we will only describe what is happening within the suspended region. Moreover, since special care has been devoted to the measurement of the radius of the heating laser spot we can state that above a radius of 0.8 μm from the center of the hotspot, no power is injected on the membrane by the heating laser. T is obtained from the Raman frequency using the proportionality relation $T = -C(\omega - \omega_0) + T_0$, where the coefficient C=18.86 K/cm^{-1} is the one previously determined (chapter 4), $T_0 = 300$K and the reference frequency ω_0 (2678.5 cm^{-1}) is the average frequency on the studied region obtained with a previous zero-power measurement (without heating laser). The profiles shown in figure 5.9, correspond to a specific radial direction selected by an angle θ and are the angular average:

$$T(r) = \frac{1}{\theta_2 - \theta_1} \int_{\theta_1}^{\theta_2} T(r, \theta') d\theta' \tag{5.1}$$

where $T(r, \theta)$ is the temperature map in two-dimensional polar coordinates referred for the hot-spot center. $T(r, \theta)$ is obtained from the raw measured data with a simple bi-linear interpolation without smoothing. We are performing an angular average on a "wedge" of the membrane.

Fig 5.9 reports the experimental profiles $T(r)$ obtained for the different wedges. Because of the imperfections of the sample and experimental error-bar, the profiles of the different wedges are not identical. However, if we exclude certain specific wedges (e.g. IV, VI and VII, which are, according to the 2D maps, associated with the presence of strain/imperfections), all the profiles are remarkably similar and display common features, which we can thus assume are due to the radial symmetry of the geometry. In the following we will discuss only wedge I (as shown in figure

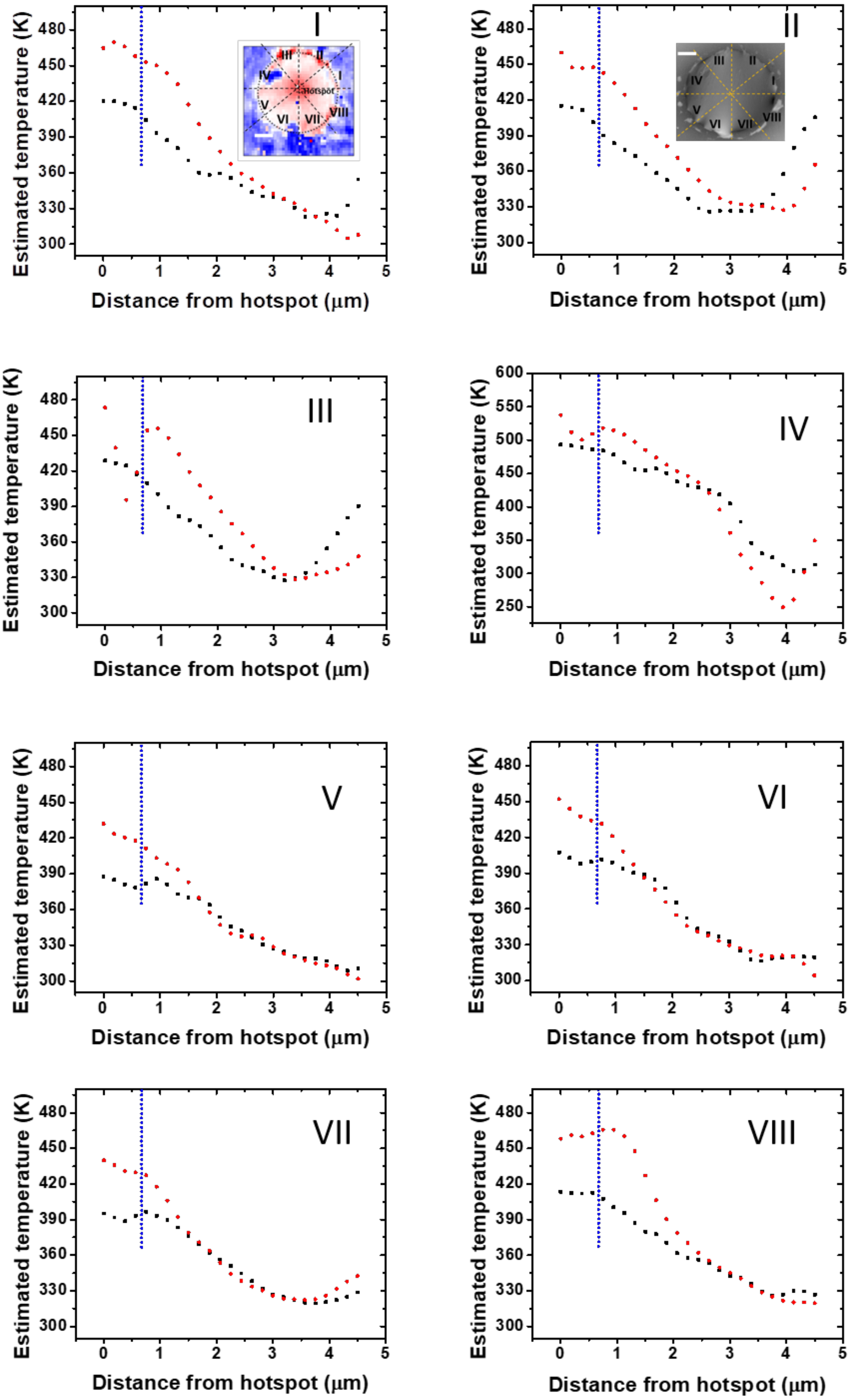

Figure 5.9: **Temperature profile (T(r)) for different wedges**: The roman numbers represent the wedge number corresponding to the inset shown in wedge VII. Wedge IV, VI and VII are affected by locally strained regions seen in AFM profile (inset of wedge II). Red points represent the data at 2.3 mW heating laser power and black points represent the data at 1.6 mW heating power. The blue dashed line shows the edge of the hotspot.

5.10) which is considered as representative. This choice has been made after the inspection of a much wider set of data on different samples and experiments (5 different samples) than those presently shown.

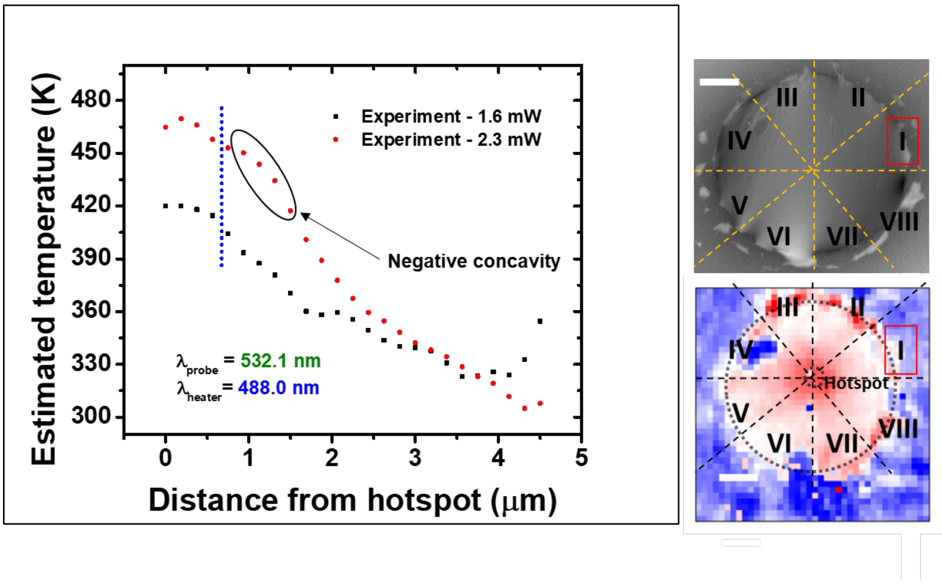

Figure 5.10: **Representative profile of T(r) with distance**: The graph shows a typical T(r) profile for a wedge (wedge I in this case). Location of different wedges are shown in right hand side, where the top image correspond to the AFM height profile oriented with the 2D frequency map shown below. Red color represent 2.3 mW heating laser power and black color represent the 1.6 mW heating power. The boundary of hotspot is shown by the blue dashed vertical line.

Figure 5.10 shows a representative observation for our measurements. As we go away from the hotspot (separated by the vertical dashed blue line), the gradual decrease of temperature is noticed followed by saturation to room temperature. We observe presence of a region with negative concavity ($T(r)$ profile for the distance of 1.0-1.8 μm, highlighted by encircled region in figure 5.10) well beyond the heated region (the boundary of hotspot is shown by the blue dashed line in figure 5.10) in the $T(r)$ profile. We will focus the discussion on this negative concavity, keeping in mind that this is robust and reproducible characteristics of the present measurements observable in this and other samples (see Appendix B). We remind that the values of the graphene thermal conductivity reported so far are the result of interpretations relying on the Fourier law, resulting from 1 laser experiments. Since the 1 laser experiment by its design is limited to only the heated region, it cannot account for this observation of negative concavity. We will now show that the present data cannot be interpreted by making some additional assumptions under the linearized Fourier law.

5.2.3 Analysis under Fourier's formalism

We will now apply the Fourier formalism to our data. Let us consider a two-dimensional (2D) system with radial symmetry and inject the laser power in a localized region near the origin with radius $< r_0$ (radius of the hotspot). The continuity equation relates the radial current density $J(r)$ at a distance r to the total injected power W with $2\pi r J(r) = W$. First, let us consider the Fourier law: according to the Fourier law the thermal current density J is proportional to the gradient of the temperature.

$$\vec{J} = -\kappa \vec{\nabla} T, \tag{5.2}$$

κ being the thermal conductivity. In the case of radial symmetry, combining with the continuity equation, it gives:

$$\kappa \frac{dT}{dr} = -\frac{W}{2\pi r}. \tag{5.3}$$

The conductivity κ can, in turn, depend on T and for sufficiently high temperatures (diffusive regime), when thermal carriers are mainly phonons, this is expected to be $\kappa = a/T$ (as discussed in [7]). By using equation 5.3, one then finds that $T(r) \propto r^{-\alpha}$, with $\alpha = W/(2\pi a)$. This law has been used to describe, successfully, two laser experiments in Si thin films [7].

Already by naked eye one can tell that this law cannot be used to interpret the present measurements (see figure 5.10). Indeed, the function $T(r) \propto r^{-\alpha}$ displays positive concavity ($d^2T/dr^2 > 0$), while present measurements do not. Negative concavity ($d^2T/dr^2 < 0$) can be present only within the hot-spot region, where the heating laser injects external power, owing to the Gaussian profile of the laser. We can associate the negative concavity (within the hotspot) with the shape of the Gaussian profile of the laser, which is the power injected within the hotspot and thereby translates into the temperature profile of similar concavity. But negative concavity is clearly visible for $r > 0.8\ \mu$m, which is well outside the hot-spot region. If we wanted to interpret the present data within the framework of the Fourier law (Eq. 5.2), we then need to assume that one of the previous hypothesis does not hold. For example, one could claim that κ has a different dependence on T than $1/T$ and use the present data to fit this hypothetical new $\tilde{\kappa}(T)$. With this goal, if call $y = ln(r)$. Eq. 5.3 reads:

$$\tilde{\kappa}(T) dT/dy = \text{const.} \tag{5.4}$$

and

$$(d\tilde{\kappa}/dT) dT/dy + \tilde{\kappa} d^2T/(dy)^2 = 0 \tag{5.5}$$

This implies that a negative concavity of the $T(r)$ profile in logarithmic scale would be associated to a positive value of $d\tilde{\kappa}/(dT)$.

Figure 5.11(a) shows $T(r)$ profile in logarithmic scale for a representative wedge. Indeed, by plotting the $T(r)$ profile in logarithmic scale (see figure 5.11(a)) one can see that the inflexion point is still present (encircled region of figure 5.11(a)). In the figure 5.11(a), the concavity becomes negative for $T > 400K$

meaning that this reasoning implies the use of a $\tilde{\kappa}(T)$ which decreases with temperature ($d\tilde{\kappa}/dT$) for $T < 400$K (as usual) and increases ($d\tilde{\kappa}/dT$) for $T > 400$K thanks to the presence of an unconventional temperature-activated mechanism. We judge this hypothesis unlikely since, from the present measurements, the inflexion point for measurements done at different injected power (compare the black and red curves in Fig 5.11(a)) do not appear to occur at the same temperature (the figure shows a temperature window near 390 K in which the black curve as negative concavity while the red one has a negative concavity around 450 K) as it would be expected for a temperature activated phenomenon.

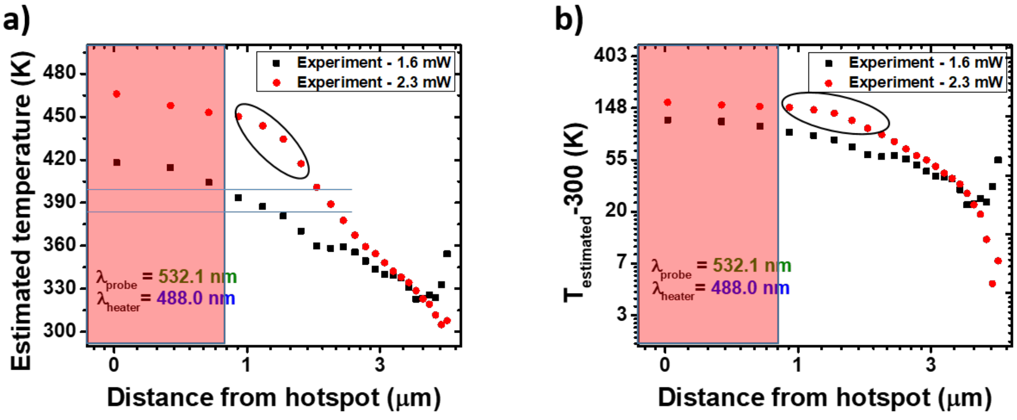

Figure 5.11: **Representative logarithmic profile for T(r)**: (a) The semi-log profile for T(r), corresponding to two different heating laser powers. (b) The log-log profile for T(r), corresponding to two different heating laser powers. Red region represents the hotspot. Encircled region shows the negative concavity.

A second alternative (if we wanted to keep Eq. 5.2 applicable) would be to release the conservation of energy hypothesis, meaning that, in Eq. 5.3, W should not be considered as a constant but as a function of r. Let us call $W(r)$ as the power (used for heating the graphene) globally injected on the membrane within the radius r. Ideally, $W(r)$ should be constant for $r > 0.8\mu m$. Here, for the sake of discussion, we are assuming that it is not and some power is injected beyond the hot-spot radius. Assuming as usual that $\kappa = a/T$, Eq. 5.3 becomes:

$$\frac{dln(T)}{dln(r)} = -\frac{W(r)}{2\pi a}. \tag{5.6}$$

This equation tells that by looking at the concavity of the $T(r)$ profile in logarithmic plot one can derive the behavior of $W(r)$. In particular, when the concavity is negative (that is, when the logarithmic derivative is decreasing by increasing r, as can be seen in figure 5.12) the injected power $W(r)$ is increasing by increasing r. On the contrary, when the concavity is positive (when the the logarithmic derivative is increasing by increasing r), the injected power $W(r)$ is decreasing by increasing r. So, the encircled region in figure 5.11(b)) displays a negative concavity and should be associated to a mechanism allowing $W(r)$ to increase with r. Negative concavity can be observed in the region of the hotspot due to the external energy injection unlike the present case where it spreads beyond the hotspot. (we remind the reader that in the present work, according to direct measurements, at all the used powers the heating laser present a constant spot size of ~0.8 μm and it has a fixed position all over the experiment).

Same authors [72] have observed in a similar experiment but on different system that radiative dissipation effects are relevant. According to the previous reasoning, radiative dissipation (which we cannot exclude) results in a decrease of $W(r)$ beyond the hot-spot radius (0.8 μm) and are thus associated to a positive concavity, meaning that, if we include these effects the anomalous observed negative concavity will result enhanced. Radiative dissipation [72] cannot, thus, explain the present findings. The present findings could be explained assuming that not all the power is actually released to the system within the hot-spot region. This could happen because of a convective mechanism, in which the air molecules heated by the laser can heat the graphene far from the hotspot. Alternatively, $W(r)$ can increase by increasing r if we assume that not all the power (that is used to heat the graphene) is actually released to the acoustic phonons (which determines the frequency shift that we are actually measuring and interpreting as a temperature) but it is stored in a second "reservoir" and then gradually released to the acoustic phonon as r is increased. The second "reservoir" could be associated to the motion of the excited optical phonons, which could involve a region larger than the hot-spot region ($r < 0.8$ μm). It could also be associated to a partially ballistic motion of the heat carriers (whose energy is not directly detected) which gradually becomes diffusive (and thus detectable) as r is increased.

We expect that these phenomena would be associated to an increase of $W(r)$ obeying exponential laws (e^{-r} or e^{-r^2}). The implementation of these models did not, however, provide a satisfactory agreement (to fit the observed negative concavity) with the observed results, the main reason being that the present data seem to be associated to a sudden decrease of the logarithmic derivative at a given distance (near 1.2 μm) from the hotspot and not to a smooth decrease on a wider region (this is already visible in Figure 5.12(b)) as expected by any of the described hypothetical mechanisms. Because of this we judge that these or similar mechanism are unlikely to explain the present findings.

Moreover, the issue of parasitic heat loss, which is discussed in literature by Ruoff *et al.* [33] using 1LRT. They report that at low absorbed power (figure 2(a) of the said reference), heat loses can be ignored. Thus, in our case (2.3 mW, which correspond to $\approx$ 0.07 mW absorbed power), we can ignore these effect.

To further clarify the above discussed concepts, let us consider the different possible behaviors of W(r).

- **A**- W(r) is constant beyond the hotspot region (all the power is released within the hot-spot).
- **B**- W(r) decreases due to a heat loss mechanisms such as radiative loss or similar.

- **C-** W(r) increases beyond the hotspot because of heat injection, for example due to convection of air molecules, or other means of unknown origin.

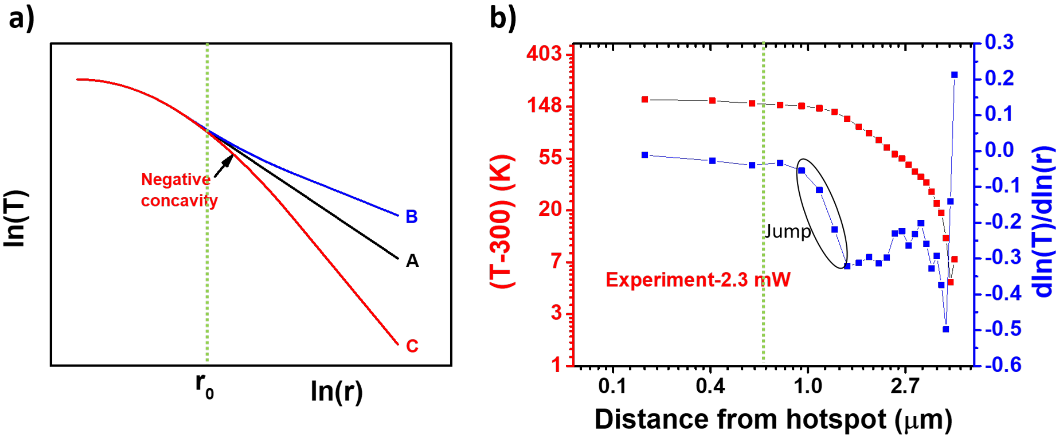

Figure 5.12: **Schematics for different W(r) behaviors and our observation**: (a) Schematic of different behaviors of W(r) and its variation in ln-ln scale. (b) Our measured data for 2.3 mW heating laser power and logarithmic derivative of T.

Fig. 5.12(a) reports the schematic curves obtainable by using Eq. 5.6. In the case A, the profile is linear outside the hotspot region (as in the plots reported in ref [7]). In case B, the profile shows in a certain region an increase of the logarithmic derivative (positive concavity) before becoming linear. In case C, the concavity is negative in a region wider than that of the hot-spot one. Then, if Eq. 5.6 is considered as valid, case C is the only one that can explain the present measurements. However, let us look at Fig. 5.12(b), reporting in a double-logarithmic scale, a representative temperature profile together with its logarithmic derivative.
The logarithmic derivative, which according to Eq. 5.6 is proportional to the injected power up to that radius, displays a sudden drop near 1.2 μm (which is well outside the hot-spot region). The same sudden drop is observed in other wedges of the same sample and in other samples as well. This observation is crucial, if you want to compare with the mechanism of external heat injection due to convection *via* air molecules. This mechanism should operate *gradually* in a region outside the hotspot. Indeed, in the present case the change observed is not gradual (figure 5.12(b)). Considering that, in the present experiments, heating due to air convection should, for some reasons, operate only for radii smaller than 1.2 μm and then suddenly disappear beyond that radius, seems to us unlikely.

At this point, we need to conclude that the standard Fourier law, Eq. 5.3, cannot be used to interpret the present measurements. This is by itself not surprising since the Fourier law is a local response, meaning that $\vec{J}$ on a specific location is entirely determined by $\vec{\nabla}T$ at the same location and it is obvious that at a sufficiently small length scale this assumption may fail because of the occurrence of non-local effects. Several discussions are available in literature on the non-local corrections to the Fourier law needed for transient problems (describing temperature profiles evolving in time) [55, 141]. Some authors have dealt also with the static problem (describing a steady-state situation as the present one) providing microscopic models to deal with specific problems mainly on the basis of analysis based on the linearized Boltzmann transport equation [142, 143]. We will see in the next section that these kind of treatment do not provide the corrections necessary to describe the present measurements.

5.2.4 Phenomenological theory of non-local and non-linear thermal transport

At sufficiently small scales the local approximation, Eq. 5.3 has to be substituted with the more general form:

$$\vec{J}(\vec{x}) = -\int K(\vec{x}, -\vec{y})\vec{\nabla}T(\vec{x}+\vec{y})d^n y, \tag{5.7}$$

where we have explicited the dependence of $\vec{J}$ and $\vec{\nabla}T$ on the position $\vec{x}$, $\int d^n y$ is the integration in the $n-$dimensional space (three in general, two in our specific case). The response function $K(\vec{x}, \vec{y})$ is usually called "Kernel", in general K is a tensor but here it can be considered as a scalar (with the assumption of isotropic and radially symmetric system). The main idea, implicit in the use of the local approximation of Eq. 5.3, is that the gradient has a smooth dependence on $\vec{y}$, while the kernel is localized in $\vec{y}$ (it is different from zero only for short distances). Assuming

$$K(\vec{x}, -\vec{y}) \sim \kappa^{(0,0)}(\vec{x})\delta(\vec{y}) \tag{5.8}$$

being $\delta(\vec{y})$ the Dirac distribution, the local Fourier law is recovered as

$$\vec{J}(\vec{x}) \sim \kappa^{(0,0)}(\vec{x})\vec{\nabla}T(\vec{x}) \tag{5.9}$$

When the system is translationally invariant, K does not depend on $\vec{x}$, and when the system is isotrope K can be assumed to depend just on $y = |\vec{y}|$. Thus, for many problems one can substitute $K(\vec{x}, \vec{y})$ with a simpler form $K(y)$. Developing $K(y)$ in term of localized functions as

$$K(y) \sim \kappa^{(0,0)}\delta(\vec{y}) + \kappa^{(0,2)}\triangle\delta(\vec{y}) \tag{5.10}$$

(the first order term is absent since $K(y)$ must be an even function of y) and inserting it in Eq. 5.7 one obtains a correction to Eq. 5.3 as a term proportional to $\triangle\vec{\nabla}T$. The coefficients $\kappa^{(0,0)}$ and $\kappa^{(0,2)}$ can be derived from the development in Taylor series of the Fourier transform $K(\vec{k})$ of $K(y)$:

$$K(\vec{k}) = \kappa^{(0,0)} + \kappa^{(0,2)}k^2 + \mathcal{O}(k^4) \tag{5.11}$$

If we want to compare with the microscopic theory of Allen (2018) [142] we should expand Equation 17 of that paper as a function of $\vec{k}$.

Actually, it is known that $K(\vec{k})$ can diverge for small k [144]. Following [142], the diverging terms of $K(\vec{k})$ can however be factorized as $1/Z(\vec{k})$ to have

$$Z(\vec{k})\vec{J}(\vec{k}) = -\tilde{K}(\vec{k})\vec{\nabla}T(\vec{k}). \tag{5.12}$$

This is a linear Fourier law written as function of the reciprocal space coordinate $\vec{k}$ and a development in Taylor series of $\vec{k}$ is possible for both left- and right-hand side kernels. In real space, this will correspond to adding corrective terms to the Fourier law proportional to $\triangle\vec{J}$ (left kernel) and $\triangle\vec{\nabla}T$ (right kernel). The $\triangle\vec{J}$ correction is usually referred as the Guyer and Krumhansl model [145] and it has been used to interpret recent experiments [146]. However, in the present geometry (2D radial symmetry), in the region (beyond the hotspot), where the energy is conserved $\vec{\nabla}\cdot\vec{J} = 0 \Rightarrow \vec{J} \propto \hat{r}/r$ and $\triangle(\hat{r}/r) = 0$. Thus, in the present geometry, the possible occurrence of this effect is filtered-out and not observable. The inclusion of a $\triangle\vec{\nabla}T$ term is no more able to reproduce the present measurements, since it introduces an oscillatory behavior in the resulting $T(r)$ which is not observed.

In order to go beyond existing models, we remark that the simplification $K(\vec{x}, \vec{y}) \sim K(y)$ cannot be applied straightforwardly in the thermal problem. Indeed, besides the obvious fact that K depends on the temperature at the point $\vec{x}$, when non-local effects are observable one should also expect a dependence on the temperature at the point $\vec{x} + \vec{y}$ ($\vec{y}$ is a small distance from $\vec{x}$), which can be included as a dependence on $\vec{\nabla}T$:

$$K(\vec{x}, \vec{y}) \sim K(T(\vec{x}), \vec{\nabla}T(\vec{x}), \vec{y}) \tag{5.13}$$

The development of K in localized functions that includes the linear term on $\vec{\nabla}T$ is then

$$K(\vec{y}) \sim \kappa^{(0,0)}\delta(\vec{y}) + \kappa^{(1,1)}\vec{\nabla}T \cdot \vec{\nabla}\delta(\vec{y}) \tag{5.14}$$

where we have hidden for clarity the dependence on $\vec{x}$ of the various terms. By inserting this terms into Eq. 5.7 we have,

$$\vec{J} = -\kappa^{(0,0)}\vec{\nabla}T + \kappa^{(1,1)}\vec{\nabla}T \cdot \vec{\nabla}\vec{\nabla}T. \tag{5.15}$$

This generalization of the Fourier law uses only the first order derivative $\vec{\nabla}T$ but is not linear in $\vec{\nabla}T$ and reproduces remarkably well the anomalous behavior of the temperature profiles presently obtained (see figure 5.13 for a representative curve and figure 5.14 for other wedges). We can thus use Eq. 5.15 to fit the experimental data and measure the coefficients $k^{(0,0)}$ and $k^{(1,1)}$.

We will use the following conventions. $k^{(0,0)}$ is the 2D graphene thermal conductivity, which is expected to go as $1/T$. In literature, it is customary to divide this coefficient by the graphite interlayer spacing $d_0 = 3.32$Å[29], to have a quantity with the dimensions of a 3D thermal conductivity. If we call κ_{3D} this 3D conductivity obtained at room temperature $T_R = 300$ K, $k^{(0,0)} = \kappa_{3D}d_0T_R/T$. By assuming that $\kappa^{(1,1)}$ also has $1/T$ behavior (a different assumption does not improve or worsen the present result in a detectable way), we will express it as a function of the length l_1 as $k^{(1,1)} = \kappa_{3D}d_0l_1^2/T$, this expression having only conventional meaning. Rewriting Eq. 5.15 in 2D radial coordinates for a radial symmetry problem and using $J(r) = -W/(2\pi r)$ we have that (outside the hot-spot region) the radial temperature profile $T(r)$ should obey

$$T'' = \beta\left(\alpha\frac{T}{rT'} + 1\right), \tag{5.16}$$

where T' and T'' are its first and second derivatives with respect to r with $\alpha = W/(2\pi T_R \kappa_{3D} d_0)$ and $\beta = T_R/l_1^2$. We used this formula to fit the measured $T(r)$, the calculated profiles being obtained by a simple numerical implementation of the Newton finite-differences approach. Besides the conditions at the border for T and T', the only fitting parameters are the two parameters k_{3D} and l_1. For a given wedge we fit in parallel two different profiles (obtained for two different heating laser powers W) by using the same k_{3D} and l_1 values and imposing the constraint that $T(r_b) = 300$ K where r_b is the border of the membrane ($r_b = 5.6$ μm in the figure).

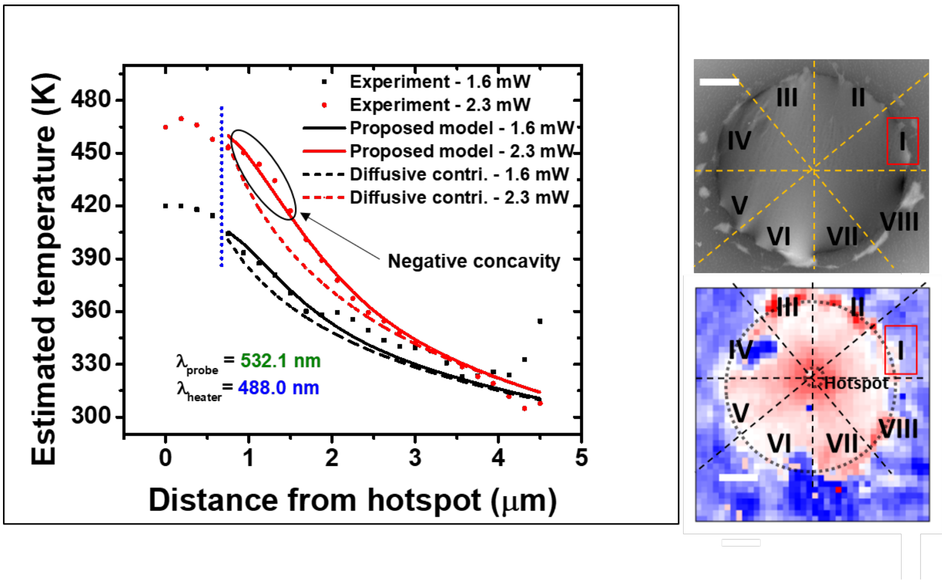

Figure 5.13: **Representative profile of T(r) with distance**: The graph shows a typical T(r) profile for a wedge (wedge I in this case). Location of different wedges are shown in right hand side, where the top image correspond to the AFM height profile oriented with the 2D frequency map shown below. The dashed line shows the profile obtained with diffusive contribution and solid lines represent the proposed new model. Red color represent 2.3 mW heating laser power and black color represent the 1.6 mW heating power. The boundary of hotspot is shown by the blue dashed vertical line.

Eq. 5.7 captures very well the most important features of the measured profiles and, considering the simplicity of the model and minimal use of fitting parameters the agreement is extremely good. The representative fit is shown in figure 5.13 and other wedges are shown in figure 5.14. It can readily be seen that the model fits for almost all the wedges except for wedge IV, VI and VII which are heavily affected by local strain. In general the 2.3 mW curve is better reproduced, mainly because the 1.6 mW is more noisy. We have shown in chapter 4 (see section 4.2.1.2) that laser power can be used to relax the graphene membrane, we argue that the strain relaxation due to 1.6 mW power is not enough to suppress the noise whereas

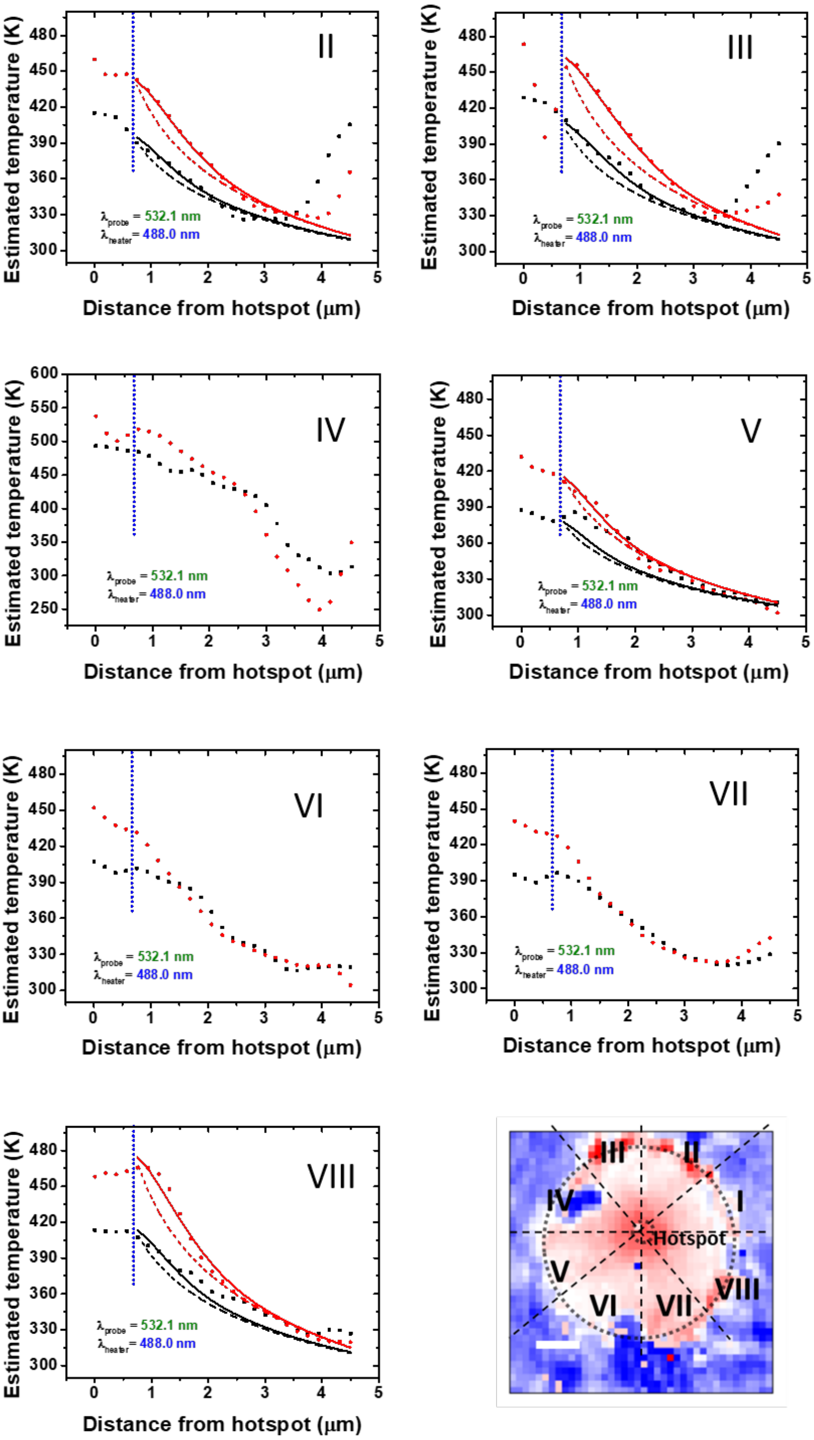

Figure 5.14: **Fits with proposed model for T(r) profile of different wedges**: The roman numbers represent the wedge number corresponding to the bottom image. Wedge IV, VI and VII do not represent the typical T(r) profiles owing to the defects seen in the AFM image. The dashed line shows the profile obtained with a diffusive model and solid lines represent the proposed new model. Red color represent 2.3 mW heating laser power and black color represent the 1.6 mW heating power.

wedge # :	κ_{3D}	l_1
I	516	1.62
II	568	1.57
III	516	1.80
V	671	1.40
VIII	481	1.44

Table 5.1: The extracted parameters from the proposed model (κ_{3D} is in $Watt/K/m$, l_1 is in μm).

2.3 mW laser power relaxes the strain, enough to regain the representative curve. These figures also show the comparison of the profile obtained from the standard Fourier model as dashed lines.

The fitted values for κ_{3D} and l_1 are reported in the table 5.1. Note also that the values obtained for the different wedges are reasonably similar implying that the radial symmetry assumption has a sufficient degree of validity. With the values reported in table 5.1, the average thermal conductivity (κ_{3D}) for the present graphene sample is 550 $W/m.K$. Such number is far lesser than the values reported by earlier Raman optothermal reports [1, 6, 2]. By comparing this value to literature, one should keep in mind that besides the fact that the samples are different, the present approach to determine the conductivity is far more direct (since it estimates the conductivity directly from the data collected rather than depending on modelling on diffusive equation) and should thus be considered more reliable. It is due to the fact that earlier estimations were based on the information extracted from the hotspot while we have taken the information far beyond the hotspot. In earlier approaches, the temperature information estimated from the hotspot were used to model the temperature beyond the hotspot based on diffusive equation. As we demonstrated here that the diffusive equation is not applicable, the models used in earlier approaches is not correct. Despite the fact that our estimation is far lesser than earlier reports, it is still considerably higher than most of the materials known for their thermal conductivity such as silver which has thermal conductivity of 430 $W/m.K$.

5.2.5 2LRT by heating the substrate

A second set of experiments was dedicated to heating the graphene membrane on the supported region and thereon to monitor the temperature profile through the suspended region. It is important to mention here that the geometry of the setup is such that one needs suspended graphene or on a transparent substrate in order to perform the 2LRT. Our graphene samples have been suspended on the 285 nm thin film of SiO_2 membranes. With such samples, we can manage to focus the heating laser onto graphene even on the SiO_2 membrane and record the response on the suspended region. Figure 5.15 presents the temperature maps for substrate heating experiment on a sample with hole size 3.6 μm radius. The hotspot is kept 0.5 μm aside of the suspended membrane shown by the dashed circle.

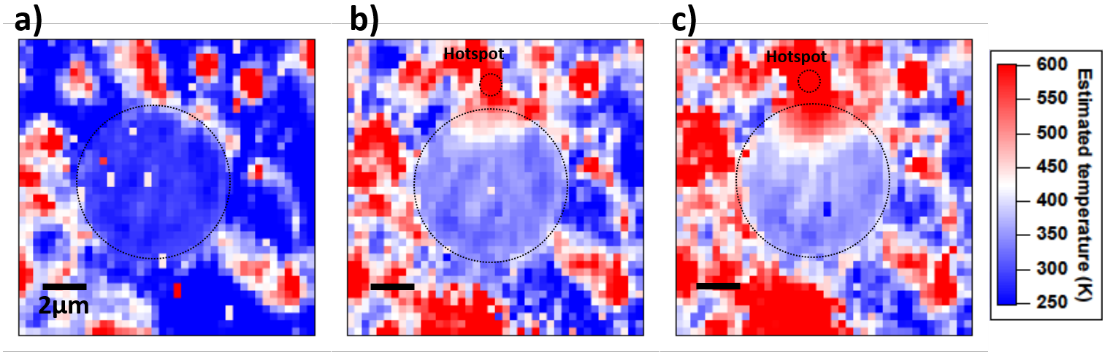

Figure 5.15: **Estimated temperature maps of suspended graphene in 2LRT configuration while the hotspot is on the substrate**: A heating laser is fixed at the top of the membrane (dashed circle shows the hotspot). From left to right the heating power is increasing from 0.0 mW, 2.2 mW and 3.3 mW.

We observe that increasing the laser power shows increase in temperature on and around the hotspot. It can also be noticed that the gradual temperature increase starting from the hotspot flows through the suspended region in a clearly detectable way. The flow looks similar to the propagation of a wavefront through a medium. It is important to remind that the temperature estimation for the substrate region is not reliable owing to the doping and inhomogeneity in strain and weaker Raman signal, which causes much noise in the estimated temperature. However, we can clearly see the evolution of the temperature in the suspended region, as the heating power in increased.

To monitor the propagation through the suspended region, figure 5.16 presents the $T(r)$ profile with distance from the hotspot. The data in the white background represent the temperature from the suspended region. Without the loss of generality it can be said that the effect of the hotspot translates to different r (distance from the hotspot) values for different heating laser powers. It is interesting to mention that the border of the hole induces only a slight change in the slope of the estimated temperature. It would be interesting to confirm if such effect is owing to the thermal propagation, by observing similar measurements on different samples.

The analysis of these data is more complex than the previous one since, because

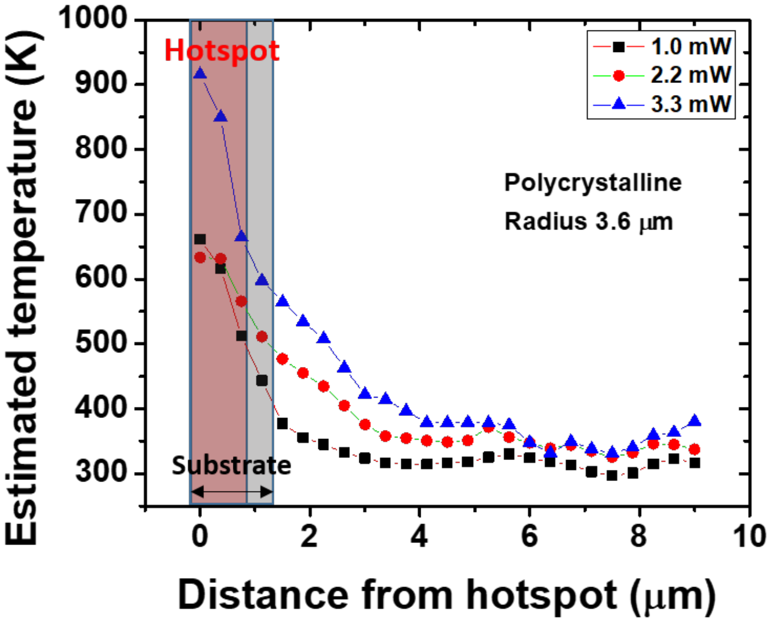

Figure 5.16: **Temperature profile with distance**: The estimated temperature (for three different heating laser powers) across the hotspot through the center of the suspended graphene. Red region represents the location of the hotspot and the light blue region corresponds to the substrate.

of the absence of radial symmetry, it cannot be reduced to a one dimensional problem. It has been performed only at a preliminary level and the first results indicate that also in this geometry measurements display a detectable deviation from the Fourier law. The next, perspective work, will be to test the proposed model in this alternative geometry. There are certain advantages with the substrate heating experiment, such as one can observe the heating effects for higher heating powers without directly affecting the graphene membrane and risking rupture. We can extend our studies for different layers of graphene and other 2D materials thanks to the dedicated state of the art 2 laser Raman thermometry setup.

5.3 Conclusion

We have successfully performed 2 laser Raman thermometry on suspended graphene. We have managed to record the thermal transport maps on graphene suspended over holes with different radius. We show that our observations cannot be explained by the standard linear Fourier law and we propose a non-local non-linear phenomenological correction. This correction can well explain the present measured temperature profiles by adding only one phenomenological parameter at the expense of introducing a nonlinear dependence on the temperature gradient. In spite of the present lack of a microscopic justification for this correction, the correction is introduced as a very general model which can be tested, as a perspective work, in different geometries and, possibly, different materials. The implications of such investigation will be reflected in the study of thermal transport in 2D materials. Since earlier studies have been making the estimations on the basis of the information collected from the hotspot, which would render inaccurate results, the approach presented here is a solution to the problem. We can conclude that the very high thermal conductivity of graphene reported earlier in literature is due to the approach of using diffusive heat equation and the use of temperature measured on the hotspot. We can use the 2LRT setup for other 2D materials either exfoliated on substrates or suspended as done in this chapter. The future prospect is to apply the said model in different experiments in order to test it.

Chapter 6

Conclusions and perspectives

In this manuscript, we have attempted to fabricate and study the thermal properties of different 2D materials with special focus on the case of graphene. We have focused on optical probes to access the local temperature of the phonon bath, by using Raman spectroscopy. To isolate the effect of substrate on the 2D materials we have designed special substrates with see-through holes and then integrated the graphene onto these holes. Such methods are established *via* a standard technique of wet transfer. At first we have demonstrated that the standard method of transferring graphene on different substrates can be modified using a metallic interface. Using a gold interface we showed that the transfer of clean graphene could be achieved. Secondly we have systematically studied the effect of such mediation on strain and doping of the resulting samples. From the information obtained by our characterization process, there are a large number of possibilities to be explored in optimizing the transfer of a clean 2D material. We also showed the mechanically exfoliated 2D materials on different substrates such as sapphire, SiO_2/Si and fused silica etc. However, suspending the exfoliated graphene was not managed for see-through holes. Another solution was proposed by using h-BN as interface, which can be drilled by FIB for suspending the exfoliated graphene. This experiment could be a good perspective in the light on current manuscript to continue and observe the heat transport in suspended exfoliated samples.

Fabrication of exfoliated samples is followed by the study of these samples using 1 laser Raman thermometry and estimation of the thermal conductivity under the formalism of Balandin *et al.*. We demonstrate that this formalism is inefficient to estimate the thermal conductivity for different materials such as $MoSe_2$, WS_2, WSe_2, h-BN and 2H-$TaSe_2$. We also try to understand the thermal properties of these materials (such as $\partial\omega/\partial\mathrm{T}$, $\partial\omega/\partial\mathrm{P}_{laser}$) in accordance to the electronic structure of materials. It is shown that a broader class of samples on same substrate is required to observe a conclusive dependence of above said parameters on the electronic structure. Such is the future scope of this investigation. Furthermore, we also study the effect of different substrates for heating effects, we concluded that to study the heating effect, the ideal environment is to suspend them since substrate-sample coupling leads to prominent heat dissipation. Interestingly we notice the hint of anisotropic thermal propagation in certain substrates (such as sapphire and spectrosil2000). Study of such effect with spatial imaging of thermal transport is an interesting perspective.

We systematically demonstrated that the 2D band of graphene can be used as thermometer mode. We have also demonstrated that $\partial\omega/\partial\mathrm{T}$, $\partial\omega/\partial\mathrm{P}_{laser}$ do not change with the radius of hole size for suspended graphene in the range of 2.5-7.0 μm, for both G and 2D bands. Such observation was attempted to be understood within the diffusive formalism. We conclude that there is a possibility of large mean free path of acoustic phonons involved in carrying the heat for suspended graphene. Following the hint of non-diffusivity, we performed 2LRT on different suspended graphene samples.

To perform the 2LRT we have designed and set up a 2 laser Raman setup and demonstrated the working of it for suspended graphene samples. With 2LRT, we manage to report the spatial imaging of thermal transport of suspended graphene heated in the center by estimating the local temperature from the frequency of the Raman modes. We demonstrate that radial evolution of the temperature cannot be explained under the linear Fourier model. We extended the Fourier formalism only phenomenologically, in order to explain the $T(r)$ profiles by introducing nonlinear and nonlocal terms. With this phenomenological model, we report the thermal conductivity of graphene to be around 550 W/m.K. The estimated thermal conductivity does not suffer from the fact that the estimation has been based on what happens on the hotspot which has been the case for all the experimental reports using Raman thermometry up to now. This approach does not only solve this issue but also provides a generalized way to estimate the thermal conductivity of different 2D materials, which is a future perspective of the manuscript.

We also present alternative experiment to observe the thermal transport in suspended graphene, which is to heat the substrate aside the graphene membrane. Such experiment involves a non-radial symmetry. In the perspectives of the proposed model, we could extend our phenomenological theory to explain the observations of this alternative experiment.
Another advantage of the 2LRT setup designed in the framework of the manuscript is the fact that it does not necessarily require a suspended sample, however, a transparent substrate is needed. With this advantage, one of the most promising perspective is to use 2LRT for recording the thermal transport imaging for different 2D/1D materials such as carbon nanotubes which exhibit resonant Raman scattering. While the samples are on transparent substrate, strain would be a key player while recording the transport maps. One can attempt to study the effect of strain on thermal transport by comparing the transport on suspended and supported samples.
A perspective from the instrumentation point of view is to design the setup to be used in vacuum and at low temperatures. The observation of thermal transport in graphene at low temperature could enhance our understanding for it to be used in different applications such as bolometers.

It would also be interesting to complement our findings with alternative measurements such as optomechanical measurements. One could heat the suspended graphene with one laser and map the optomechanical response of graphene depending on the dimension of the samples.

To conclude generally, we have studied different 2D materials for their thermal properties with special emphasis on graphene. We have used Raman optothermal methods in order to provide a general way of estimating the thermal conductivity for 2D materials. These studies show the limitation of existing approaches and provide a common solution. A nonlocal nonlinear thermal transport observed here, is an exciting result which still requires microscopic interpretation that would add to our understanding of thermal transport in low dimensions and open new future prospects in thermal physics in 2D and 1D materials.

Appendix A

The appendix discusses different Raman processes involved in monolayer graphene based on the literature and the phonon dispersion of monolayer graphene [62, 147].

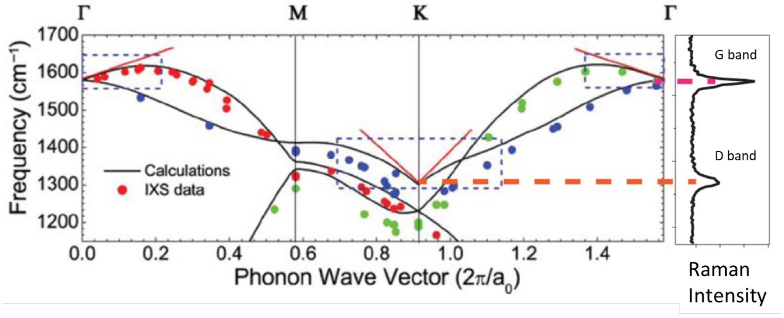

Figure 1: **Phonon dispersion in monolayer graphene, adapted from [147]**: Solid lines represent the calculated phonon dispersion and experimental points are taken from [148]. Inset on the right hand side shows the G and D band position at Γand K points respectively.

Figure **??** shows the typical phonon dispersion in monolayer graphene. 2 Key Raman process happen at Γand K points, which are called G and D bands. A crucial fact is that the G band is a consequence of two degenerate vibrations at Γ point. Asymmetric strain can ne used to lift this degeneracy. It can also be explored by using different wavelength of light excitation. The 2D peak results from various processes at K points, which shall be detailed in next figure.

Figure 2 shows different Raman processes in graphene. The two modes which we have considered throughout this work are G and 2D mode respectively. G mode is a consequence of Raman scattering at Γ point as shown in figure 2(a). On the other, 2D mode phonon is a consequence of 2 phonon process at K and K'point. There are different contributions to the 2D phonon process as shown in figure 2 (i,j,k), however, major contribution comes from the process shown in (i). The two phonons are created in opposite directions (represented by wave vectors) connecting the valleysof K and K' point. Owing to involvement of two phonons we have seen higher sensitivity of 2D mode with respect to temperature and laser power.

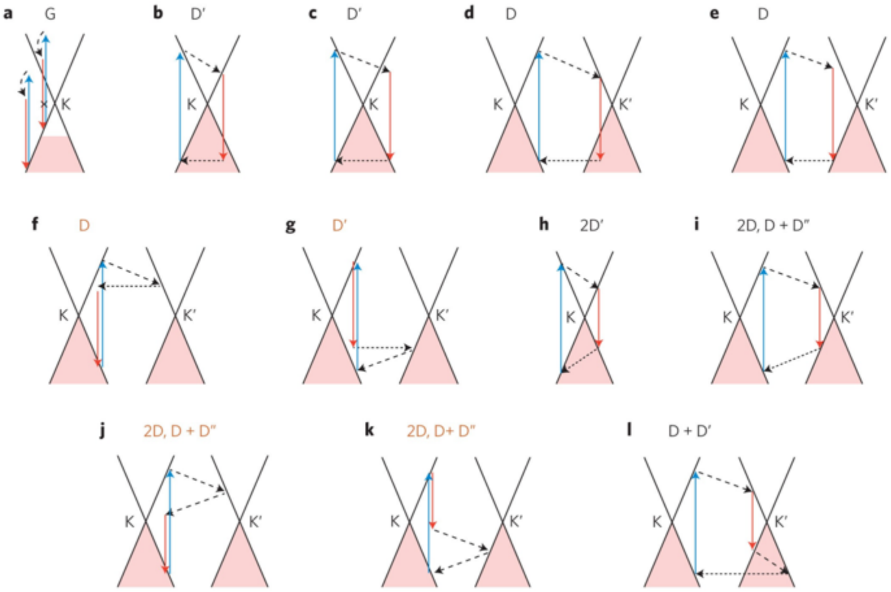

Figure 2: **Raman processes of suspended monolayer graphene [62]**: Electron dispersion (solid black lines), occupied states (shaded areas), interband transitions neglecting the photon momentum, accompanied by photon absorption (blue arrows) and emission (red arrows), intraband transitions accompanied by phonon emission (dashed arrows), electron scattering on a defect (horizontal dotted arrows). a, One-phonon processes responsible for the G peak, which interfere destructively. Some processes can be eliminated by doping, such as the one that is crossed out. b–g, In the presence of defects, the phonon wave vector need not be zero, producing the D' peak for intravalley scattering (b,c), and D peak for intervalley scattering (d–g). Besides the eh or he processes, where the electron and the hole participate in one act of scattering each (b–e), there are contributions (ee, hh) where only the electron (f) or the hole (g) are scattered. h–k, For two-phonon scattering, momentum can be conserved by emitting two phonons with opposite wave vectors, producing the 2D' peak for intravalley scattering (h) and the 2D, D + D" peaks for intervalley scattering (i–k). The ee and hh processes are shown in j,k. l, With defects, one intravalley and one intervalley phonon can be emitted, producing the D + D' peak. The processes (f,g,j,k) give a small contribution, as indicated by the orange peak labels.

Appendix B

The appendix shows the transport maps taken on suspended graphene samples for different hole sizes. The heating laser is 488.0 nm and probe laser is 532.1 nm.

.1 Holesize: Radius 3.6 μm

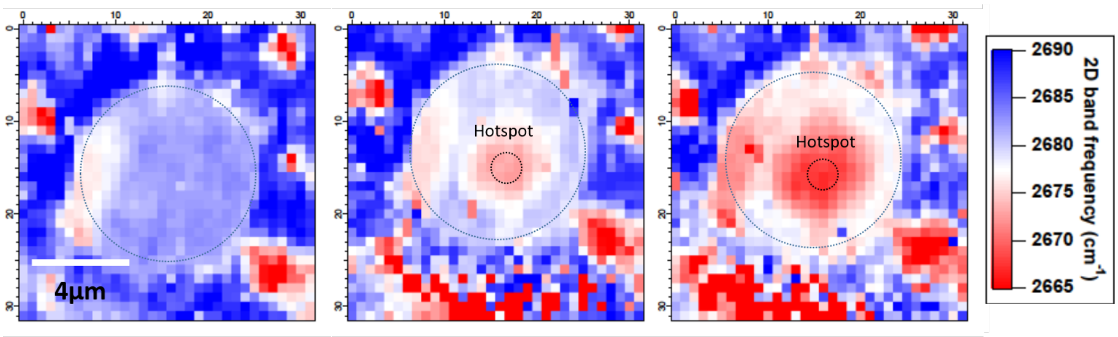

Figure 3: **2D band frequency map of suspended graphene in 2LRT configuration**: 2D band frequency for suspended graphene (dashed circle) with a heating laser in the center of the membrane (dashed circle shows the hotspot). The scale bar is 4 μm shown in first map. From left to right the heating power is increasing from 0.0 mW, 1.6 mW and 2.3 mW.

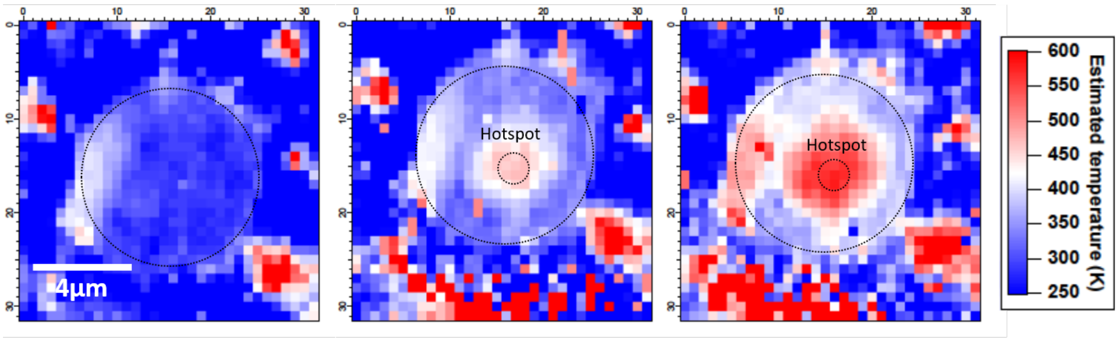

Figure 4: **Estimated temperature maps of suspended graphene in 2LRT configuration**: Local estimated temperature maps for suspended graphene (dashed circle) with a heating laser fixed in the center of the membrane (dashed circle shows the hotspot). The scale bar is 4 μm. From left to right the heating power is increasing from 0.0 mW, 1.6 mW and 2.3 mW.

.2 Holesize: Radius 5.3 μm

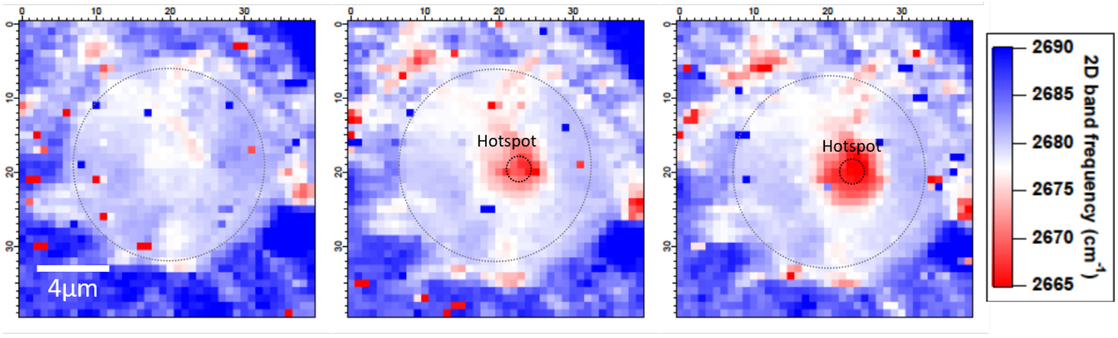

Figure 5: **2D band frequency map of suspended graphene in 2LRT configuration**: 2D band frequency for suspended graphene (dashed circle) with a heating laser in the center of the membrane (dashed circle shows the hotspot). The scale bar is 4 μm shown in first map. From left to right the heating power is increasing from 0.0 mW, 1.6 mW and 2.3 mW.

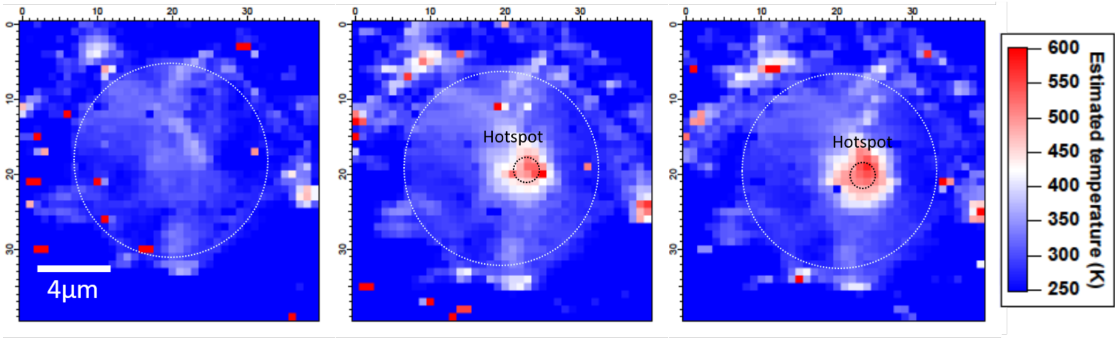

Figure 6: **Estimated temperature maps of suspended graphene in 2LRT configuration**: Local estimated temperature maps for suspended graphene (dashed circle) with a heating laser fixed in the center of the membrane (dashed circle shows the hotspot). The scale bar is 4 μm. From left to right the heating power is increasing from 0.0 mW, 1.6 mW and 2.3 mW.

.3 Holesize: Radius 8.3 μm

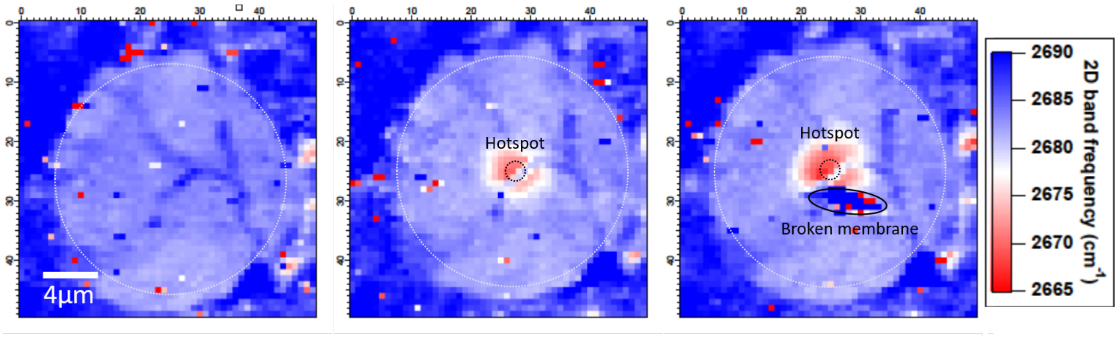

Figure 7: **2D band frequency map of suspended graphene in 2LRT configuration**: 2D band frequency for suspended graphene (dashed circle) with a heating laser in the center of the membrane (dashed circle shows the hotspot). The scale bar is 4 μm shown in first map. From left to right the heating power is increasing from 0.0 mW, 1.6 mW and 2.3 mW.

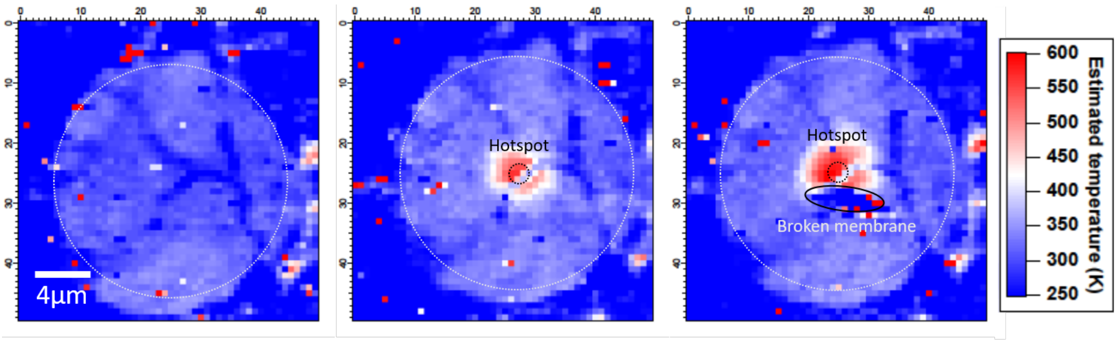

Figure 8: **Estimated temperature maps of suspended graphene in 2LRT configuration**: Local estimated temperature maps for suspended graphene (dashed circle) with a heating laser fixed in the center of the membrane (dashed circle shows the hotspot). The scale bar is 4 μm. From left to right the heating power is increasing from 0.0 mW, 1.6 mW and 2.3 mW.

.4 Temperature profiles

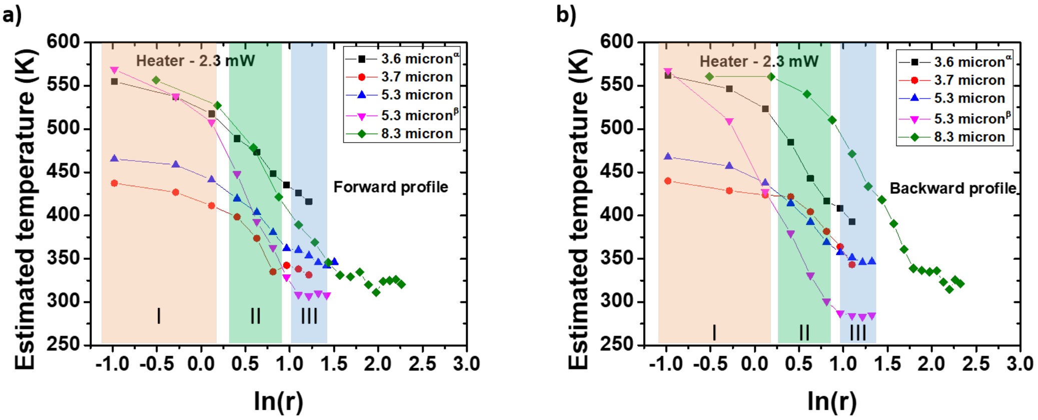

Figure 9: Averaged temperature profile along different cuts through hotspot, plotted in semi-log scale. The representative curve discussed in chapter 5 is reproducible in all the samples. α shows the experiment corresponding to solid state laser. β corresponds to monocrystal graphene sample.

The final figure shows the averaged temperature profile for forward and backward profiles of the bell curve seen in a typical cut through the hotspot. We observe the representative curve discussed in chapter 5 is reproducible in every sample. The red color represents the location of hotspot, green region shows the presence of negative concavity. The green region does change from sample to sample depending on the radius of the hole size.

Appendix C

This appendix describes the spot size determination of 488.0 nm (heating laser) by two different techniques.

.5 Razor blade technique

We use a razor edge to monitor the intensity of the Gaussian profile of heating laser after the 20x objective (used in the 2LRT setup). The 2LRT setup is taken out of the Raman spectrometer and the intensity profile of the optically focused beam is analyzed at different distances from the objective lens (as shown in figure 10).

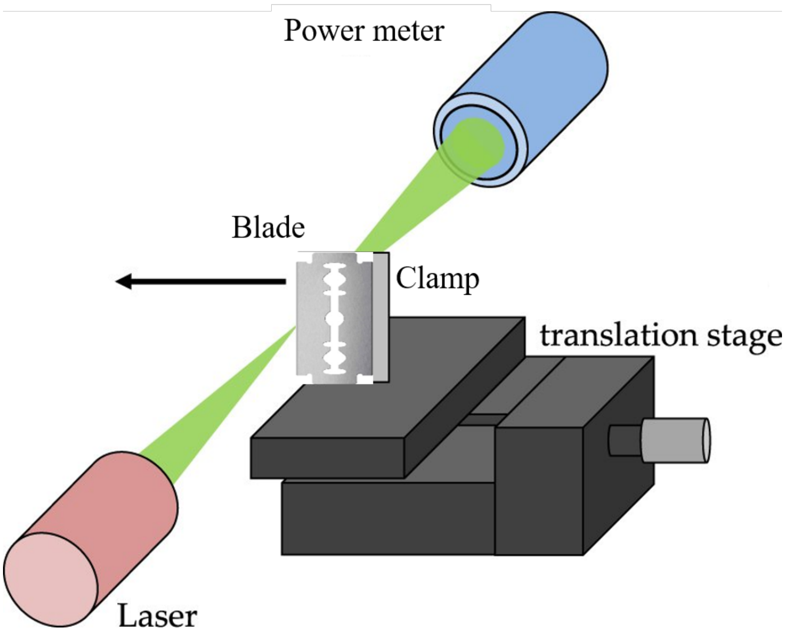

Figure 10: **Schematic of measuring the spot size**: Figure is adapted from [139]

The intensity profile is observed by monitoring the intensity of the laser while moving the blade in the perpendicular direction of the beam. Each point in figure 11 correspond to one such profile, which gives the information of the waist size at each point.

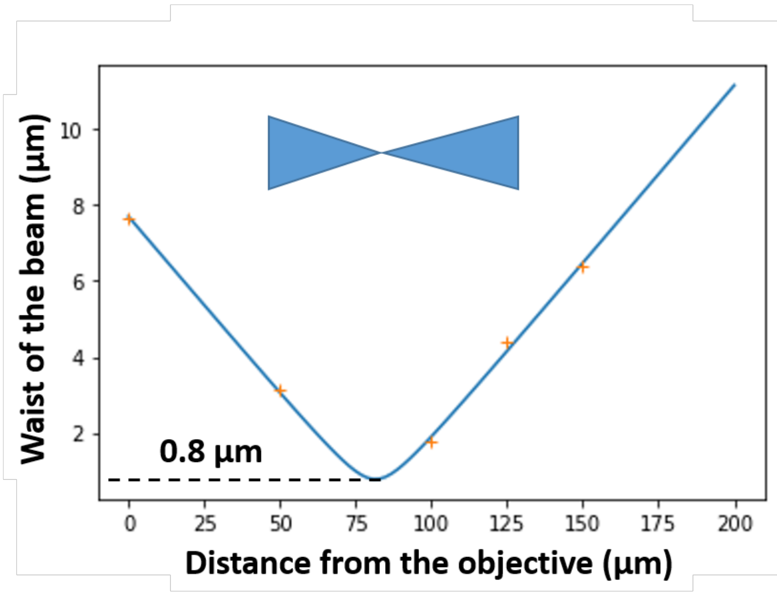

Figure 11: **Spot size of heating laser using razor edge technique**: The inset shows the schematic of the laser beam after the objective.

Fitting the resulting values with different waist size gives the spot size of 0.8 μm.

.6 Piezo scan method

In this method the motion stage of the 2LRT setup is used to scan the fixed heating laser spatially. We collect the laser signal from the collection optics of the Raman spectrometer. By analyzing the intensity profile for each step, we observe a Gaussian profile which can then be fitted to result in the spot size of 0.7±0.1 μm.

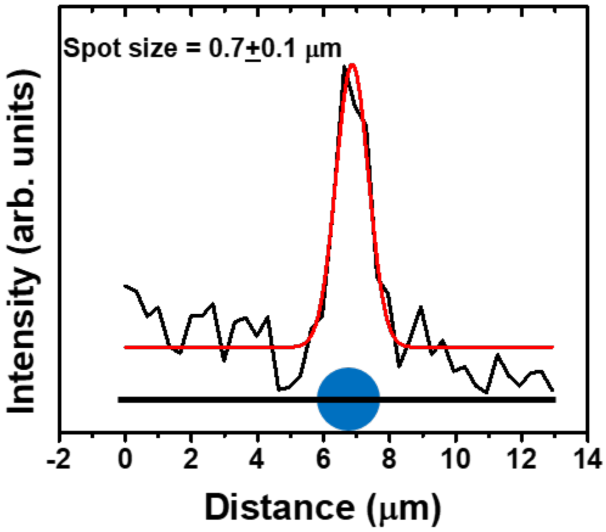

Figure 12: **Spot size of heating laser by using linear scan of piezo stage**: Black curve shows the data collected and red curve is a Gaussian fit. The blue circle represents the hot spot and the solid black line shows the scan direction.

Bibliography

[1] W. Cai, A. L. Moore, Y. Zhu, X. Li, S. Chen, L. Shi, and R. S. Ruoff. Thermal transport in suspended and supported monolayer graphene grown by chemical vapor deposition. *Nano Letters*, 10(5):1645–1651, 2010.

[2] J. U. Lee, D. Yoon, H. Kim, S. W. Lee, and H. Cheong. Thermal conductivity of suspended pristine graphene measured by Raman spectroscopy. *Phys. Rev. B*, 83:081419, 2011.

[3] G. Hwang and O. Kwon. Measuring the size dependence of thermal conductivity of suspended graphene disks using null-point scanning thermal microscopy. *Nanoscale*, 8:5280–5290, 2016.

[4] M. H. Bae, Z. Li, Z. Aksamija, P. N. Martin, F. Xiong, Z. Y. Ong, I. Knezevic, and E. Pop. Ballistic to diffusive crossover of heat flow in graphene ribbons. *Nature Communications*, 4(1):1734, 2013.

[5] P. Kim, L. Shi, A. Majumdar, and P. L. McEuen. Thermal transport measurements of individual multiwalled nanotubes. *Phys. Rev. Lett.*, 87:215502, 2001.

[6] A. A. Balandin, S. Ghosh, W. Bao, I. Calizo, D. Teweldebrhan, F. Miao, and C. N. Lau. Superior thermal conductivity of single-layer graphene. *Nano Letters*, 8(3):902–907, 2008.

[7] J. S. Reparaz, E. Chavez-Angel, M. R. Wagner, B. Graczykowski, J. Gomis-Bresco, F. Alzina, and C. M. Sotomayor Torres. A novel contactless technique for thermal field mapping and thermal conductivity determination: Two-laser Raman thermometry. *Review of Scientific Instruments*, 85(3):034901, 2014.

[8] UNESCO, Memory of the world. `http://www.unesco.org/new/en/communication-and-information/flagship-project-activities/memory-of-the-world/register/full-list-of-registered-heritage/registered-heritage-page-7/rigveda/#c190310`, 2007.

[9] Rigveda, Sanskrit/English. `https://www.wisdomlib.org/hinduism/book/rig-veda-english-translation/d/doc828866.html`, 2007.

[10] D.V. Schroeder. *An Introduction to Thermal Physics*. Addison Wesley, 2000.

[11] J.B.J. Fourier. *Théorie analytique de la chaleur.* CHEZ FERMIN DIDOT, PÈRE ET FILS, 1878.

[12] J. Lee, J. Lim, and P. Yang. Ballistic phonon transport in holey silicon. *Nano Letters*, 15(5):3273–3279, 2015.

[13] Z. Cheng, W. Lu, J. Shi, D. Tanaka, N. H. Protik, S. Wang, M. Iwaya, T. Takeuchi, S. Kamiyama, I. Akasaki, H. Amano, and S. Graham. Quasi-ballistic thermal conduction in 6H-SiC, 2021. 2102.07683.

[14] M. Sledzinska, B. Graczykowski, J. Maire, E. Chavez-Angel, C. M. Sotomayor-Torres, and F. Alzina. 2d phononic crystals: Progress and prospects in hypersound and thermal transport engineering. *Advanced Functional Materials*, 30(8):1904434, 2020.

[15] J. Chaste, A. Saadani, A. Jaffre, A. Madouri, J. Alvarez, D. Pierucci, Z. Ben Aziza, and A. Ouerghi. Nanostructures in suspended mono- and bilayer epitaxial graphene. *Carbon*, 125:162–167, 2017.

[16] S. Lin and M. J. Buehler. Thermal transport in monolayer graphene oxide: Atomistic insights into phonon engineering through surface chemistry. *Carbon*, 77:351–359, 2014.

[17] Z. Han and A. Fina. Thermal conductivity of carbon nanotubes and their polymer nanocomposites: A review. *Progress in Polymer Science*, 36(7):914–944, 2011. Special Issue on Composites.

[18] P. Kim, L. Shi, A. Majumdar, and P. L. McEuen. Thermal transport measurements of individual multiwalled nanotubes. *Phys. Rev. Lett.*, 87:215502, 2001.

[19] S. Volz. *Thermal Nanosystems and Nanomaterials.* Topics in Applied Physics. Springer Berlin Heidelberg, 2009.

[20] H.A. Schafft, J.S. Suehle, and P.G.A. Mirel. Thermal conductivity measurements of thin-film silicon dioxide. In *Proceedings of the 1989 International Conference on Microelectronic Test Structures*, pages 121–125, 1989.

[21] J. Krempaský. New methods of measuring thermal and thermoelectric characteristics of substances, particularly semi-conductors on samples of undefined shape. *Cechoslovackij Fiziceskij Zurnal B*, 14(7):533–554, 1964.

[22] K. Termentzidis, T. Barreteau, Y. Ni, S. Merabia, X. Zianni, Y. Chalopin, P. Chantrenne, and S. Volz. Modulated SiC nanowires: Molecular dynamics study of their thermal properties. *Phys. Rev. B*, 87:125410, 2013.

[23] K. Termentzidis, J. Parasuraman, C. A. Da Cruz, S. Merabia, D. Angelescu, F. Marty, T. Bourouina, X. Kleber, P. Chantrenne, and P. Basset. Thermal conductivity and thermal boundary resistance of nanostructures. *Nanoscale Research Letters*, 6(1):288, 2011.

[24] C. Abs da Cruz, K. Termentzidis, P. Chantrenne, and X. Kleber. Molecular dynamics simulations for the prediction of thermal conductivity of bulk silicon and silicon nanowires: Influence of interatomic potentials and boundary conditions. *Journal of Applied Physics*, 110(3):034309, 2011.

[25] R. Prasher. Thermal boundary resistance and thermal conductivity of multiwalled carbon nanotubes. *Phys. Rev. B*, 77:075424, 2008.

[26] K. Komatsu. Theory of the specific heat of graphite II. *Journal of the Physical Society of Japan*, 10(5):346–356, 1955.

[27] C. Faugeras, B. Faugeras, M. Orlita, M. Potemski, R. R. Nair, and A. K. Geim. Thermal conductivity of graphene in Corbino membrane geometry. *ACS Nano*, 4(4):1889–1892, 2010.

[28] Y. Y. Wang, Z. H. Ni, T. Yu, Z. X. Shen, H. M. Wang, Y. H. Wu, W. Chen, and A. T. Shen Wee. Raman studies of monolayer graphene: The substrate effect. *The Journal of Physical Chemistry C*, 112(29):10637–10640, 2008.

[29] G. Fugallo, A. Cepellotti, L. Paulatto, M. Lazzeri, N. Marzari, and F. Mauri. Thermal conductivity of graphene and graphite: Collective excitations and mean free paths. *Nano Letters*, 14(11):6109–6114, 2014.

[30] S. Lee, D. Broido, K. Esfarjani, and G. Chen. Hydrodynamic phonon transport in suspended graphene. *Nature Communications*, 6(1):6290, 2015.

[31] A. Cepellotti, G. Fugallo, L. Paulatto, M. Lazzeri, F. Mauri, and N. Marzari. Phonon hydrodynamics in two-dimensional materials. *Nature Communications*, 6(1):6400, 2015.

[32] S. Ghosh, I. Calizo, D. Teweldebrhan, E. P. Pokatilov, D. L. Nika, A. A. Balandin, W. Bao, F. Miao, and C. N. Lau. Extremely high thermal conductivity of graphene: Prospects for thermal management applications in nanoelectronic circuits. *Applied Physics Letters*, 92(15):151911, 2008.

[33] S. Chen, Q. Wu, C. Mishra, J. Kang, H. Zhang, K. Cho, W. Cai, A. A. Balandin, and R. S. Ruoff. Thermal conductivity of isotopically modified graphene. *Nature Materials*, 11:203–207, 2012.

[34] T. Feng, X. Ruan, Z. Ye, and B. Cao. Spectral phonon mean free path and thermal conductivity accumulation in defected graphene: The effects of defect type and concentration. *Phys. Rev. B*, 91:224301, 2015.

[35] T. Ma, P. Chakraborty, X. Guo, L. Cao, and Y. Wang. First-principles modeling of thermal transport in materials: Achievements, opportunities, and challenges. *International Journal of Thermophysics*, 41(1):9, 2019.

[36] Konstantinos Termentzidis and Samy Merabia. Molecular dynamics simulations and thermal transport at the nano-scale. In L. Wang, editor, *Molecular Dynamics*, chapter 5. IntechOpen, Rijeka, 2012.

[37] W. Paul. Electromagnetic traps for charged and neutral particles. *Rev. Mod. Phys.*, 62:531–540, 1990.

[38] N. D. Mermin. Crystalline order in two dimensions. *Phys. Rev.*, 176:250–254, 1968.

[39] K. S. Novoselov, A. K. Geim, S. V. Morozov, D. Jiang, Y. Zhang, S. V. Dubonos, I. V. Grigorieva, and A. A. Firsov. Electric field effect in atomically thin carbon films. *Science*, 306(5696):666–669, 2004.

[40] K. S. Novoselov. Nobel lecture: Graphene: Materials in the flatland. *Rev. Mod. Phys.*, 83:837–849, 2011.

[41] A. K. Geim and I. V. Grigorieva. Van der waals heterostructures. *Nature*, 499(7459):419–425, 2013.

[42] G. Yang, L. Li, W. B. Lee, and M. C. Ng. Structure of graphene and its disorders: a review. *Science and Technology of Advanced Materials*, 19(1):613–648, 2018.

[43] A. H. Castro Neto, F. Guinea, N. M. R. Peres, K. S. Novoselov, and A. K. Geim. The electronic properties of graphene. *Rev. Mod. Phys.*, 81:109–162, Jan 2009.

[44] M.F. Craciun, S. Russo, M. Yamamoto, and S. Tarucha. Tuneable electronic properties in graphene. *Nano Today*, 6(1):42–60, 2011.

[45] A. Rycerz. Wiedemann–franz law for massless dirac fermions with implications for graphene. *Materials*, 14(11), 2021.

[46] A. Principi and G. Vignale. Violation of the wiedemann-franz law in hydrodynamic electron liquids. *Phys. Rev. Lett.*, 115:056603, 2015.

[47] D. L. Nika, E. P. Pokatilov, A. S. Askerov, and A. A. Balandin. Phonon thermal conduction in graphene: Role of umklapp and edge roughness scattering. *Phys. Rev. B*, 79:155413, 2009.

[48] K. Matsuda. Optical properties of atomically thin layered transition metal dichalchogenide. *Journal of the Physical Society of Japan*, 84(12):121009, 2015.

[49] X. Zhang, D. Sun, Y. Li, G. H. Lee, X. Cui, D. Chenet, Y. You, T. F. Heinz, and J. C. Hone. Measurement of lateral and interfacial thermal conductivity of single- and bilayer MoS_2 and $MoSe_2$ using refined optothermal Raman technique. *ACS Applied Materials & Interfaces*, 7(46):25923–25929, 2015.

[50] Han Zhang, Xiao-Li Fan, Yi Yang, and Pin Xiao. Strain engineering the magnetic states of vacancy-doped monolayer $MoSe_2$. *Journal of Alloys and Compounds*, 635:307–313, 2015.

[51] X. Liu and Y. W. Zhang. Thermal properties of transition-metal dichalcogenide. *Chinese Physics B*, 27(3):034402, 2018.

[52] K. Zhang, Y. Feng, F. Wang, Z. Yang, and J. Wang. Two dimensional hexagonal boron nitride (2d-hbn): synthesis, properties and applications. *J. Mater. Chem. C*, 5:11992–12022, 2017.

[53] X. Xu, J. Chen, and B. Li. Phonon thermal conduction in novel 2d materials. *Journal of Physics: Condensed Matter*, 28(48):483001, 2016.

[54] S. Gomès, P. Newby, B. Canut, K. Termentzidis, O. Marty, L. Fréchette, P. Chantrenne, V. Aimez, J.M. Bluet, and V. Lysenko. Characterization of the thermal conductivity of insulating thin films by scanning thermal microscopy. *Microelectronics Journal*, 44(11):1029–1034, 2013. Thermal investigations of integrated circuits in systems at THERMINIC'11.

[55] G. Chen. Nonlocal and Nonequilibrium Heat Conduction in the Vicinity of Nanoparticles. *Journal of Heat Transfer*, 118(3):539–545, 1996.

[56] P. G. Klemens. Theory of thermal conduction in thin ceramic films. *International Journal of Thermophysics*, 22(1):265–275, 2001.

[57] Wikipedia: Raman scattering. `https://fr.wikipedia.org/wiki/Diffusion_Raman#/media/Fichier:Ramanscattering.svg`.

[58] A. Cantarero. Review on Raman scattering in semiconductor nanowires: I. theory. *Journal of Nanophotonics*, 7(1):1 – 29, 2013.

[59] E. Garmire, M. Cardona, J.M. Hammer, H. Kogelnik, T. Tamir, and F. Zernike. *Light Scattering in Solids 1*. Topics in Applied Physics. Springer Berlin Heidelberg, 2013.

[60] L.M. Malard, M.A. Pimenta, G. Dresselhaus, and M.S. Dresselhaus. Raman spectroscopy in graphene. *Physics Reports*, 473(5):51–87, 2009.

[61] D. M. Basko. Theory of resonant multiphonon Raman scattering in graphene. *Phys. Rev. B*, 78:125418, 2008.

[62] A. C. Ferrari and D. M. Basko. Raman spectroscopy as a versatile tool for studying the properties of graphene. *Nature nanotechnology*, 8(4):235–246, 2013.

[63] J. E. Lee, G. Ahn, J. Shim, Y. S. Lee, and S. Ryu. Optical separation of mechanical strain from charge doping in graphene. *Nature Communications*, 3(1024):1–8, 2012.

[64] A. Das, S. Pisana, B. Chakraborty, S. Piscanec, S. K. Saha, U. V. Waghmare, K. S. Novoselov, H. R. Krishnamurthy, A. K. Geim, A. C. Ferrari, and A. K. Sood. Monitoring dopants by Raman scattering in an electrochemically top-gated graphene transistor. *Nature Nanotechnology*, 3(4):210–215, 2008.

[65] A. Das, B. Chakraborty, S. Piscanec, S. Pisana, A. K. Sood, and A. C. Ferrari. Phonon renormalization in doped bilayer graphene. *Phys. Rev. B*, 79:155417, 2009.

[66] F. Ding, H. Ji, Y. Chen, A. Herklotz, K. Dörr, Y. Mei, A. Rastelli, and O. G. Schmidt. Stretchable graphene: A close look at fundamental parameters through biaxial straining. *Nano Letters*, 10(9):3453–3458, 2010.

[67] F. Ding, H. Ji, Y. Chen, A. Herklotz, K. Dörr, Y. Mei, A. Rastelli, and O. G. Schmidt. Stretchable graphene: A close look at fundamental parameters through biaxial straining. *Nano Letters*, 10(9):3453–3458, 2010.

[68] C. Schwarz. *Propriétés optomécaniques, vibrationelles et thermiques de membranes de graphène suspendues.* PhD thesis, 2016.

[69] T. C. V. Carvalho, F. D. V. Araujo, C. Costa dos Santos, L. M. R. Alencar, J. Ribeiro-Soares, D. J. Late, A. O. Lobo, A. G. Souza Filho, R. S. Alencar, and B. C. Viana. Temperature-dependent phonon dynamics of supported and suspended monolayer tungsten diselenide. *AIP Advances*, 9(8):085316, 2019.

[70] M Thripuranthaka and D. J. Late. Temperature dependent phonon shifts in single-layer WS_2. *ACS Applied Materials & Interfaces*, 6(2):1158–1163, 2014.

[71] S. Ghosh. *Thermal Conduction in Graphene and Graphene Multilayers.* PhD thesis, 2009. UC Riverside Electronic Theses and Dissertations.

[72] D. Saleta Reig, S. Varghese, R. Farris, A. Block, J. D. Mehew, O. Hellman, P. Woźniak, M. Sledzinska, A. El Sachat, E. Chávez-Ángel, S. O. Valenzuela, N. F. Van Hulst, P. Ordejón, Z. Zanolli, C. M. Sotomayor Torres, M. J. Verstraete, and K. J. Tielrooij. Unraveling heat transport and dissipation in suspended $MoSe_2$ crystals from bulk to monolayer, 2021. arxiv:2109.09225.

[73] S. Chen, A. L. Moore, W. Cai, J. W. Suk, J. An, C. Mishra, C. Amos, C. W. Magnuson, J. Kang, L. Shi, and R. S. Ruoff. Raman measurements of thermal transport in suspended monolayer graphene of variable sizes in vacuum and gaseous environments. *ACS Nano*, 5(1):321–328, 2011.

[74] E. Schrödinger. Are there quantum jumps? part ii. *The British Journal for the Philosophy of science*, 3(11):233–242, 1952.

[75] Q. Yu, J. Lian, S. Siriponglert, H. Li, Y. P. Chen, and S.S. Pei. Graphene segregated on Ni surfaces and transferred to insulators. *Applied Physics Letters*, 93(11):113103, 2008.

[76] V. Miseikis, D. Convertino, N. Mishra, M. Gemmi, T. Mashoff, S. Heun, N. Haghighian, F. Bisio, M. Canepa, V. Piazza, and C. Coletti. Rapid CVD growth of millimetre-sized single crystal graphene using a cold-wall reactor. *2D Materials*, 2(1):014006, 2015.

[77] C. K Lee, Y Hwangbo, S. M. Kim, S. K. Lee, S. M. Lee, S. S. Kim, K. S. Kim, H. J. Lee, B. I. Choi, C. K. Song, J. H. Ahn, and J. H. Kim. Monatomic chemical-vapor-deposited graphene membranes bridge a half-millimeter-scale gap. *ACS Nano*, 8(3):2336–2344, 2014.

[78] A. Reserbat-Plantey, D. Kalita, Z. Han, L. Ferlazzo, S. Autier-Laurent, K. Komatsu, C. Li, R. Weil, A. Ralko, L. Marty, S. Guéron, N. Bendiab, H. Bouchiat, and V. Bouchiat. Strain superlattices and macroscale suspension of graphene induced by corrugated substrates. *Nano Letters*, 14(9):5044–5051, 2014.

[79] A. Reina, X. Jia, J. Ho, D. Nezich, H. Son, V. Bulovic, M. S. Dresselhaus, and J. Kong. Large area, few-layer graphene films on arbitrary substrates by chemical vapor deposition. *Nano Letters*, 9(1):30–35, 2009.

[80] L. Gomez De Arco, Y. Zhang, A. Kumar, and C. Zhou. Synthesis, transfer, and devices of single- and few-layer graphene by chemical vapor deposition. *IEEE Transactions on Nanotechnology*, 8(2):135–138, 2009.

[81] S. Bae, H. Kim, Y. Lee, X. Xu, J. S. Park, Y. Zheng, J. Balakrishnan, T. Lei, H. Ri Kim, Y. I. Song, Y. J. Kim, K. S. Kim, B. Özyilmaz, J. H. Ahn, B. H. Hong, and S. Iijima. Roll-to-roll production of 30-inch graphene films for transparent electrodes. *Nature Nanotechnology*, 5(8):574–578, 2010.

[82] C. Mattevi, H. Kim, and M. Chhowalla. A review of chemical vapour deposition of graphene on copper. *J. Mater. Chem.*, 21:3324–3334, 2011.

[83] A. C. Gomez, M. Buscema, R. Molenaar, V. Singh, L. Janssen, H. S. J. van der Zant, and G. A. Steele. Deterministic transfer of two-dimensional materials by all-dry viscoelastic stamping. *2D Materials*, 1(1):011002, 2014.

[84] Y. He, W. Yu, and G. Ouyang. Effect of stepped substrates on the interfacial adhesion properties of graphene membranes. *Phys. Chem. Chem. Phys.*, 16:11390–11397, 2014.

[85] M. Chen, R. C. Haddon, R. Yan, and E. Bekyarova. Advances in transferring chemical vapour deposition graphene: a review. *Mater. Horiz.*, 4:1054–1063, 2017.

[86] D. Kalita. *Graphene produced by chemical vapor deposition : from control and understanding of atomic scale defects to production of macroscale functional devices.* Phd thesis, Université Grenoble Alpes, 2015.

[87] N. Bendiab, J. Renard, C. Schwarz, A. Reserbat-Plantey, L. Djevahirdjian, V. Bouchiat, J. Coraux, and L. Marty. Unravelling external perturbation effects on the optical phonon response of graphene. *Journal of Raman Spectroscopy*, 49(1):130–145, 2018.

[88] Y. C. Lin, C. C. Lu, C. H. Yeh, C. Jin, K. Suenaga, and P. W. Chiu. Graphene annealing: How clean can it be? *Nano Letters*, 12(1):414–419, 2012.

[89] J. D. Wood, G. P. Doidge, E. A. Carrion, J. C. Koepke, J. A. Kaitz, I. Datye, A. Behnam, J. Hewaparakrama, B. Aruin, Y. Chen, H. Dong, R. T. Haasch, J. W. Lyding, and E. Pop. Annealing free, clean graphene transfer using alternative polymer scaffolds. *Nanotechnology*, 26(5):055302, 2015.

[90] V.S. Prudkovskiy, K.P. Katin, M.M. Maslov, P. Puech, R. Yakimova, and G. Deligeorgis. Efficient cleaning of graphene from residual lithographic polymers by ozone treatment. *Carbon*, 109:221–226, 2016.

[91] K. Kumar, Y. S. Kim, and E. H. Yang. The influence of thermal annealing to remove polymeric residue on the electronic doping and morphological characteristics of graphene. *Carbon*, 65:35–45, 2013.

[92] B. Zhuang, S. Li, S. Li, and J. Yin. Ways to eliminate pmma residues on graphene-superclean graphene. *Carbon*, 173:609–636, 2021.

[93] A.A. Kaverzin, S.M. Strawbridge, A.S. Price, F. Withers, A.K. Savchenko, and D.W. Horsell. Electrochemical doping of graphene with toluene. *Carbon*, 49(12):3829–3834, 2011.

[94] H. Pinto, R. Jones, J. P. Goss, and P. R. Briddon. Unexpected change in the electronic properties of the Au-graphene interface caused by toluene. *Phys. Rev. B*, 82:125407, 2010.

[95] Nsingi Ngoma, João Carlos Bordado, Carlos Moura Bordado, and Doutor Carlos Carvalheira. Study of the mechanisms of thermal despolimerization of the poli(methyl methacrylate) selection of solvent compatible with PMMA. 2007.

[96] A. Matruglio, S. Nappini, D. Naumenko, E. Magnano, F. Bondino, M. Lazzarino, and S. Dal Zilio. Contamination-free suspended graphene structures by a Ti-based transfer method. *Carbon*, 103:305–310, 2016.

[97] J. Choi, H. Kim, J. Park, M. Waqas Iqbal, M. Z. Iqbal, J. Eom, and J. Jung. Enhanced performance of graphene by using gold film for transfer and masking process. *Current Applied Physics*, 14(8):1045–1050, 2014.

[98] M. Jang, T. Q. Trung, J. H. Jung, B. Y. Kim, and N. E. Lee. Improved performance and stability of field-effect transistors with polymeric residue-free graphene channel transferred by gold layer. *Phys. Chem. Chem. Phys.*, 16:4098–4105, 2014.

[99] M. T. Ghoneim, C. E. Smith, and M. M. Hussain. Simplistic graphene transfer process and its impact on contact resistance. *Applied Physics Letters*, 102(18):183115, 2013.

[100] A. Hsu, H. Wang, K. K. Kim, J. Kong, and T. Palacios. Impact of graphene interface quality on contact resistance and RF device performance. *IEEE Electron Device Letters*, 32(8):1008–1010, 2011.

[101] L. Song, L. Ci, W. Gao, and P. M. Ajayan. Transfer printing of graphene using gold film. *ACS Nano*, 3(6):1353–1356, 2009.

[102] Y. L. Shen, P. Zhou, L. H. Wang, Q. Q. Sun, Q. Q. Tao, P. F. Wang, S. J. Ding, and D. W. Zhang. The annealing effect of chemical vapor deposited graphene. In *2013 IEEE 10th International Conference on ASIC*, pages 1–4, 2013.

[103] G. Pillet, A. Sapelkin, W. Bacsa, M. Monthioux, and P. Puech. Size-controlled graphene-based materials prepared by annealing of pitch-based cokes: G band phonon line broadening effects due to high pressure, crystallite size, and merging with D$'$ band. *Journal of Raman Spectroscopy*, 50(12):1861–1866, 2019.

[104] A.A. Kaverzin, S.M. Strawbridge, A.S. Price, F. Withers, A.K. Savchenko, and D.W. Horsell. Electrochemical doping of graphene with toluene. *Carbon*, 49(12):3829–3834, 2011.

[105] Y. Wu, W. Jiang, Y. Ren, W. Cai, W. H. Lee, H. Li, R. D. Piner, C. W. Pope, Y. Hao, H. Ji, J. Kang, and R. S. Ruoff. Tuning the doping type and level of graphene with different gold configurations. *Small*, 8(20):3129–3136, 2012.

[106] M. Cao, Y. Luo, Y. Xie, Z. Tan, G. Fan, Q. Guo, Y. Su, Z. Li, and D. B. Xiong. The influence of interface structure on the electrical conductivity of graphene embedded in aluminum matrix. *Advanced Materials Interfaces*, 6(13):1900468, 2019.

[107] J. Chaste, A. Missaoui, S. Huang, H. Henck, Z. Ben Aziza, L. Ferlazzo, C. Naylor, A. Balan, A. T. C. Johnson Jr, R. Braive, et al. Intrinsic properties of suspended MoS_2 on SiO_2/Si pillar arrays for nanomechanics and optics. *ACS nano*, 12(4):3235–3242, 2018.

[108] Q. Cai, D. Scullion, W. Gan, A. Falin, S. Zhang, K. Watanabe, T. Taniguchi, Y. Chen, E. J. G. Santos, and L. H. Li. High thermal conductivity of high-quality monolayer boron nitride and its thermal expansion. *Science Advances*, 5(6):eaav0129, 2019.

[109] N. Peimyoo, J. Shang, W. Yang, Y. Wang, C. Cong, and T. Yu. Thermal conductivity determination of suspended mono- and bilayer WS_2 by Raman spectroscopy. *Nano Research*, 8(4):1210–1221, 2015.

[110] J. S. Ross, S. Wu, H. Yu, N. J. Ghimire, A. M. Jones, G. Aivazian, J. Yan, D. G. Mandrus, D. Xiao, W. Yao, and X. Xu. Electrical control of neutral and charged excitons in a monolayer semiconductor. *Nature Communications*, 4(1):1474, 2013.

[111] D. Nam, J.U. Lee, and H. Cheong. Excitation energy dependent Raman spectrum of $MoSe_2$. *Scientific Reports*, 5(1):17113, 2015.

[112] P. Tonndorf, R. Schmidt, P. Böttger, X. Zhang, J. Börner, A. Liebig, M. Albrecht, C. Kloc, O. Gordan, D. R. T. Zahn, S. M. Vasconcellos, and R. Bratschitsch. Photoluminescence emission and Raman response of monolayer MoS_2, $MoSe_2$, and WSe_2. *Opt. Express*, 21(4):4908–4916, 2013.

[113] X. Lu, M. I. B. Utama, J. Lin, X. Gong, J. Zhang, Y. Zhao, S. T. Pantelides, J. Wang, Z. Dong, Z. Liu, W. Zhou, and Q. Xiong. Large-area synthesis of monolayer and few-layer $MoSe_2$ films on SiO_2 substrates. *Nano Letters*, 14(5):2419–2425, 2014.

[114] M. Koperski, M. R. Molas, A. Arora, K. Nogajewski, A. O. Slobodeniuk, C. Faugeras, and M. Potemski. Optical properties of atomically thin transition metal dichalcogenides: observations and puzzles:. *Nanophotonics*, 6(6):1289–1308, 2017.

[115] B. Peng, H. Zhang, H. Shao, Y. Xu, X. Zhang, and H. Zhu. Thermal conductivity of monolayer MoS_2, $MoSe_2$, and WS_2: interplay of mass effect, interatomic bonding and anharmonicity. *RSC Adv.*, 6:5767–5773, 2016.

[116] Y.P. Varshni. Temperature dependence of the energy gap in semiconductors. *Physica*, 34(1):149–154, 1967.

[117] Y. Uchiyama, K. Watanabe, T. Taniguchi, K. Kojima, T. Endo, Y. Miyata, H. Shinohara, and R. Kitaura. Indirect bandgap of hbn-encapsulated monolayer MoS_2. *arXiv: Mesoscale and Nanoscale Physics*, 2019.

[118] P. Jiang, X. Qian, X. Gu, and R. Yang. Probing anisotropic thermal conductivity of transition metal dichalcogenides MX_2 (M = Mo, W and X = S, Se) using time-domain thermoreflectance. *Advanced Materials*, 29(36):1701068, 2017.

[119] X. Gu and R. Yang. Phonon transport in single-layer transition metal dichalcogenides: A first-principles study. *Applied Physics Letters*, 105(13):131903, 2014.

[120] H. Zhou, J. Zhu, Z. Liu, Z. Yan, X. Fan, J. Lin, G. Wang, Q. Yan, T. Yu, P. M. Ajayan, et al. High thermal conductivity of suspended few-layer hexagonal boron nitride sheets. *Nano Research*, 7(8):1232–1240, 2014.

[121] Z. Lin, C. Liu, and Y. Chai. High thermally conductive and electrically insulating 2D boron nitride nanosheet for efficient heat dissipation of high-power transistors. *2D Materials*, 3(4):041009, 2016.

[122] A. R. Jang, S. Hong, C. Hyun, S. I. Yoon, G. Kim, H. Y. Jeong, T. J. Shin, S. O. Park, K. Wong, S. K. Kwak, N. Park, K. Yu, E. Choi, A. Mishchenko, F. Withers, K. S. Novoselov, H. Lim, and H. S. Shin. Wafer-scale and wrinkle-free epitaxial growth of single-orientated multilayer hexagonal boron nitride on sapphire. *Nano Letters*, 16(5):3360–3366, 2016.

[123] D. G. Cahill, S.M. Lee, and T. I. Selinder. Thermal conductivity of κ-Al_2O_3 and α-Al_2O_3 wear-resistant coatings. *Journal of Applied Physics*, 83(11):5783–5786, 1998.

[124] I. Calizo, A. A. Balandin, W. Bao, F. Miao, and C. N. Lau. Temperature dependence of the Raman spectra of graphene and graphene multilayers. *Nano Letters*, 7(9):2645–2649, 2007.

[125] C.S. Lian, C. Heil, X. Liu, C. Si, F. Giustino, and W. Duan. Coexistence of superconductivity with enhanced charge density wave order in the two-dimensional limit of $TaSe_2$. *The Journal of Physical Chemistry Letters*, 10(14):4076–4081, 2019.

[126] M. Lee, M. Šiškins, S. Mañas-Valero, E. Coronado, P. G. Steeneken, and H. S. J. van der Zant. Study of charge density waves in suspended 2H-TaS_2 and 2H-$TaSe_2$ by nanomechanical resonance. *Applied Physics Letters*, 118(19):193105, 2021.

[127] Z. Yan, C. Jiang, T. R. Pope, C. F. Tsang, J. L. Stickney, P. Goli, J. Renteria, T. T. Salguero, and A. A. Balandin. Phonon and thermal properties of exfoliated $TaSe_2$ thin films. *Journal of Applied Physics*, 114(20):204301, 2013.

[128] D. Maclean and M. H. Jericho. Effect of the charge-density-wave transition on the thermal expansion of 2H-$TaSe_2$, $NbSe_3$, and o-TaS_3. *Phys. Rev. B*, 47:16169–16177, 1993.

[129] M. Mahajan, S. Kallatt, M. Dandu, N. Sharma, S. Gupta, and K. Majumdar. Light emission from the layered metal 2H-$TaSe_2$ and its potential applications. *Communications Physics*, 2(1):88, 2019.

[130] N. Bonini, M. Lazzeri, N. Marzari, and F. Mauri. Phonon anharmonicities in graphite and graphene. *Phys. Rev. Lett.*, 99:176802, 2007.

[131] L. M. Malard, R. L. Moreira, D. C. Elias, F. Plentz, E. S. Alves, and M. A. Pimenta. Thermal enhancement of chemical doping in graphene: a Raman spectroscopy study. *Journal of Physics: Condensed Matter*, 22(33):334202, 2010.

[132] A. T. Apostolov, I. N. Apostolova, and J. M. Wesselinowa. Temperature and layer number dependence of the G and 2D phonon energy and damping in graphene. *Journal of Physics: Condensed Matter*, 24(23):235401, 2012.

[133] A. Tiberj, M. Rubio-Roy, M. Paillet, J. R. Huntzinger, P. Landois, M. Mikolasek, S. Contreras, J. L. Sauvajol, E. Dujardin, and A. A. Zahab. Reversible optical doping of graphene. *Scientific Reports*, 3, 2013.

[134] S. Tian, Y. Yang, Z. Liu, C. Wang, R. Pan, C. Gu, and J. Li. Temperature-dependent Raman investigation on suspended graphene: Contribution from thermal expansion coefficient mismatch between graphene and substrate. *Carbon*, 104:27–32, 2016.

[135] S. Shivaraman, R. A. Barton, X. Yu, J. Alden, L. Herman, MVS Chandrashekhar, J. Park, P. L. McEuen, J. M. Parpia, H. G. Craighead, and M. G. Spencer. Free-standing epitaxial graphene. *Nano Letters*, 9(9):3100–3105, 2009.

[136] X. Xu, Luiz F. C. Pereira, Y. Wang, J. Wu, K. Zhang, X. Zhao, S. Bae, C. Tinh Bui, R. Xie, J. T. L. Thong, B. H. Hong, K. P. Loh, D. Donadio, B. Li, and Barbaros Özyilmaz. Length-dependent thermal conductivity in suspended single-layer graphene. *Nature Communications*, 5(1):3689, 2014.

[137] L. Lindsay, D. A. Broido, and Natalio Mingo. Flexural phonons and thermal transport in multilayer graphene and graphite. *Phys. Rev. B*, 83:235428, 2011.

[138] O. Braun, R. Furrer, P. Butti, K. R. Thodkar, I. Shorubalko, I. Zardo, M. Calame, and M. L. Perrin. Spatially mapping the thermal conductivity of graphene by an opto-thermal method, 2021. 2101.12238.

[139] C. Westgate. How to determine the laser-induced damage threshold of 2-d imaging arrays. SPIE, 2019.

[140] F. Bonaccorso, Z. Sun, T. Hasan, and AC Ferrari. Graphene photonics and optoelectronics. *Nature Photonics*, 4(9):611–622, 2010.

[141] A. A. Joshi and A. Majumdar. Transient ballistic and diffusive phonon heat transport in thin films. *Journal of Applied Physics*, 74(1):31–39, 1993.

[142] P. B. Allen. Analysis of nonlocal phonon thermal conductivity simulations showing the ballistic to diffusive crossover. *Phys. Rev. B*, 97:134307, 2018.

[143] B. Vermeersch, J. Carrete, N. Mingo, and A. Shakouri. Superdiffusive heat conduction in semiconductor alloys. I. theoretical foundations. *Phys. Rev. B*, 91:085202, 2015.

[144] G. D. Mahan and F. Claro. Nonlocal theory of thermal conductivity. *Phys. Rev. B*, 38:1963–1969, 1988.

[145] R. A. Guyer and J. A. Krumhansl. Solution of the linearized phonon Boltzmann equation. *Phys. Rev.*, 148:766–778, 1966.

[146] S. Alajlouni, A. Beardo, L. Sendra, A. Ziabari, J. Bafaluy, J. Camacho, Y. Xuan, F. X. Alvarez, and A. Shakouri. Geometrical quasi-ballistic effects on thermal transport in nanostructured devices. *Nano Research*, 14(4):945–952, 2021.

[147] S. Piscanec, M. Lazzeri, Francesco Mauri, A. C. Ferrari, and J. Robertson. Kohn anomalies and electron-phonon interactions in graphite. *Phys. Rev. Lett.*, 93:185503, Oct 2004.

[148] J. Maultzsch, S. Reich, C. Thomsen, H. Requardt, and P. Ordejón. Phonon dispersion in graphite. *Phys. Rev. Lett.*, 92:075501, Feb 2004.

Abstract

This thesis investigates the fabrication and study of the thermal properties of different 2D materials under the formalism of existing literature and beyond. The thesis can be broadly divided in three parts. The first part discusses sample fabrication involving making of see-through holes in substrates followed by integrating CVD grown graphene over the patterned holes. It also discusses the mechanical exfoliation of different 2D materials on substrates. The process of standard transfer for suspending graphene is optimized and characterized using Raman spectroscopy, atomic force microscopy and scanning electron microscopy. We successfully suspended graphene on hole size of 2-10 µm radius. Second part of thesis discusses the estimation of thermal conductivity of different 2D materials on substrates using 1 laser Raman thermometry. It presents an attempt to understand the role of temperature and optical power on the evolution of optical phonon frequencies with the electronic structure of the material. In the final part, it discusses the characterization of the suspended graphene using 1 and 2 laser Raman thermometry. It shows the effect of geometry on the parameters of 1 laser Raman thermometry and thereby discussing the possibility of non-diffusive thermal transport in suspended graphene. It presents the first thermal transport spatial imaging of suspended graphene using the 2 laser Raman thermometry setup by heating the graphene at the center of the suspended region. The experiments show a deviation from linearized Fourier law in suspended graphene, which hasn't been reported experimentally up to our knowledge. A phenomenological model using nonlocal nonlinear term is proposed to successfully fit the observed thermal transport behavior in suspended graphene. Using this model, this work reports a high thermal conductivity of 550 W/m.K for suspended graphene, which is one of the highest among existing materials. Such approach presents a better formalism to correctly estimate the thermal conductivity of 2D materials by incorporating a generalized Fourier law.